INVESTIGATION OF THE NO-LOAD PERFORMANCE OF A MODEL THREE-PHASE THREE-LIMB LAMINATED TRANSFORMER CORE OPERATING UNDER SINUSOIDAL AND PWM VOLTAGE EXCITATION

BY

XIAO GUANG YAO

A Thesis Submitted to Cardiff University
in Candidature for the degree of
Doctor of Philosophy

Wolfson Centre for Magnetics
School of Engineering
Cardiff University
Wales, United Kingdom

March 2010

ProQuest LLC
789 East Eisenhower Parkway
P.O. Box 1346
Ann Arbor, MI 48106-1346

DECLARATION

This work has not previously been accepted in substance for any degree and is not concurrently submitted in candidature for any degree.

Signed Xiao Guang Yao (姚晓光) (candidate) Date 29/03/2010

STATEMENT 1

This thesis is being submitted in partial fulfillment of the requirements for the degree of PhD.

Signed Xiao Guang Yao (姚晓光) (candidate) Date 29/03/2010

STATEMENT 2

This thesis is the result of my own independent work/investigation, except where otherwise stated. Other sources are acknowledged by explicit references.

Signed Xiao Guang Yao (姚晓光) (candidate) Date 29/03/2010

STATEMENT 3

I hereby give consent for my thesis, if accepted, to be available for photocopying and for inter-library loan, and for the title and summary to be made available to outside organisations.

Signed Xiao Guang Yao (姚晓光) (candidate) Date 29/03/2010

STATEMENT 4: PREVIOUSLY APPROVED BAR ON ACCESS

I hereby give consent for my thesis, if accepted, to be available for photocopying and for inter-library loans **after expiry of a bar on access previously approved by the Graduate Development Committee**.

Signed Xiao Guang Yao (姚晓光) (candidate) Date 29/03/2010

To my beloved parents Cheng Kai Yao and Xue Yong Chen who have always believed in me, to my old sister Dong Mei Yao and my dearest wife Lei Wang for the laughter we share.

ACKNOWLEDGEMENTS

This research work has been carried out at Wolfson Centre for Magnetics, School of Engineering, Cardiff University, to which I am grateful for providing the resources needed to complete this project.

First, I wish to express appreciation to my supervisors, Professor A. J. Moses for his guidance and valuable discussions, and Dr. F. J. Anayi for his contribution and patience throughout this research work. Thank you both for your continuous help and support.

I would like to express my gratitude to Professor P. Beckley and Professor S. E. Zirka who have given me the stimulation and assistance to enhance part of subject.

I should also like to thank Cogent Power Ltd for providing electrical steel laminations to assemble the model power transformer core.

Finally, I feel very much indebted to several colleagues who have assisted me one way or another, especially Mr. Ming Chuan Huang, Mr. Sakda Somkun, Dr. P. Marketos and Dr. S. Zurek in challenging me with alternative views.

SUMMARY

Transformers subjected to PWM voltage excitation are becoming more and more common in industrial applications and renewable energy supply systems. Therefore, the assessment and improvement in the performance of transformer cores under PWM voltage excitation have become prominent. This project intends to characterise the no-load performance, total power loss and acoustic noise level, of a model three-phase, three-limb laminated transformer core, operating under sinusoidal and PWM voltage excitation.

Measurements of total power losses and localised flux density in the joint regions of the core under sinusoidal and PWM voltage excitation for assigned modulation index m_a with switching frequency f_s varied from 1 kHz to 3 kHz, has been carried out. The analysis highlights the form factor K_f of the secondary induced voltage as a key parameter in controlling the performance of eddy-current component loss in the core. The estimate localised rotational losses due to rotating flux and planar eddy-current losses due to normal flux density in the joints have been analysed, also the analysis of measurement results contributes towards a better understanding of the influence of m_a and f_s.

Moreover, the acoustic noise level of the core and the corresponding vibration at investigated points on the core surface has been measured under sinusoidal and PWM voltage excitation. Measurement results show that the values of acoustic noise and core vibration under PWM voltage excitation were much higher than under corresponding sinusoidal voltage condition. Also, the magneto-mechanical resonant phenomenon of the core under PWM voltage excitation has been observed, which was due to switching frequency f_s close to the resonance vibration frequency of the core laminations that is a possible cause of increasing acoustic noise. The measurement results inferred that the resonant phenomenon could possibly occur in cores with different length laminations leading to variability of noise output according to how close the magnetising frequency or predominant harmonics are to the resonant frequency.

CONTENTS

Appendixes

Aims of the Investigation

It is well known that transformers play a very important role in power generation, transmission and distribution systems. Two most significant characteristics of transformer cores are the no-load power losses and acoustic noise resulting from vibration partly caused by the magnetostriction of the core material. The large increase in energy costs and the rise in demand for electric power call for more efficient transformers. Moreover, increased environmental consciousness has called for low acoustic noise from transformers, which is one of the major environmental concerns of the highly industrialised world.

It is known that energy supply systems have undergone some major changes due to the growing role of power electronic techniques in the grid through power flow conditioners and converters of electricity. Therefore, transformers subjected to PWM voltage excitation are becoming more common; assessment and improvement in the performance of transformers under PWM voltage excitation are increasingly prominent. Limited research has been reported on non-sinusoidal voltage excitation of transformer cores, most previous research has been carried out on the no-load performance under sinusoidal voltage excitation.

This research project aims to investigate the no-load performance of a model three-phase, three-limb laminated transformer core, assembled from grain-oriented, 3% silicon electrical steel laminations, operating under sinusoidal and PWM voltage excitation. Also, the main aims of the investigation can be summarised as follows:

a). To measure the magnetostriction of grain-oriented, 3% silicon electrical steel in the form of Epstein strips, using a single-point laser vibrometer method, to compare and analyse the measurement results under sinusoidal and PWM voltage excitation, and also to explain mechanical resonance phenomena in material subjected to PWM voltage excitation.

b). To measure the total iron losses and localised flux density within the laminations in transformer core joints using a computerised measurement system, to estimate localised rotational and planar eddy-current losses under sinusoidal and PWM voltage excitation, and to obtain a better understanding of the influence of modulation index and switching frequency.

c). To measure the acoustic noise level and vibration of the same model transformer core, using another computerised measurement system, to compare and analyse the measurement

results under sinusoidal and PWM voltage excitation, and also to explain the magneto-mechanical resonance phenomenon of the core under PWM voltage excitation.

Chapter 1 General Introduction and Theoretical Basis

1.1 Introduction

Transformers are widely used to change *ac* electric power at one voltage level to *ac* electric power at another voltage level. Generally, a transformer consists of two or more conducting coils wrapped around a ferromagnetic core. The only link between the coils is the common magnetic flux present within the core. One winding is connected to a source of *ac* electric power, and the second windings supplies power to a load. The transformer winding connected to the power source is the primary or input winding, and the winding connected to the load is the secondary or output winding.

The first power distribution system in the United States was a 120-V *dc* system invented by Thomas A. Edison to supply power for incandescent light bulbs. Edison's first central power station went into operation in New York City in September 1882.Unfortunately, this power system generated and transmitted power at such low voltages that very large currents were necessary to supply significant amounts of power. These high currents caused large voltage drops and power losses in the transmission lines, severely restricting the service area of a generating station. The fact that power could not be transmitted far with low-voltage *dc* power systems meant that generating stations had to be small and localised and so were relatively inefficient [*1.1*].

The invention of the transformer and the concurrent development of *ac* power sources eliminated these restrictions on the range and power level of power systems. Therefore, *ac* electric power can be generated at one central location, its voltage stepped up for transmission over long distances at very low losses, and its voltage stepped down again for final use. Since the transmission losses in the lines of a power system are proportional to the square of the current in the lines, raising the transmission voltage and reducing the resulting transmission currents by a factor of 10 with transformers reduces power transmission losses by a factor of 100.

In general, in a modern power system, electric power is generated at voltages of 12 kV to 25 kV. Transformers step up the voltage to between 110 kV and nearly 1000 kV for transmission over long distances at very low losses. The voltage is then stepped down to the range of 12

kV to 34.5 kV for local distribution and allowing the power to be used safely at low voltage [*1.1*].

1.2 Pulse Width Modulation (PWM) basics

Three-phase static converters are usually used in industrial applications such as induction motors, permanent-magnet synchronous motors drives [*1.2*]-[*1.6*]; and also in active power line conditioners and renewable power supply systems, which lead the transformers subjected to PWM voltage excitation to become more common [*1.7*]-[*1.10*].

A PWM voltage waveform is obtained by comparing a reference voltage waveform (modulating signal, usually sinusoidal waveform) with a carrier voltage waveform (carrier signal, usually triangular waveform). The reference voltage frequency is usually 50 Hz or 60 Hz; moreover, in motors speed control applications, at low frequencies the motor speed tends to be jerky, at high frequencies the motor's inductance becomes significant and power is lost; therefore, frequencies of 30 – 200 Hz are commonly used. The carrier voltage frequency (switching frequency) is normally varied from 0.5 kHz to 20 kHz [*1.11*] [*1.12*]. A PWM output voltage waveform with synthesis of two voltage waveforms is illustrated in fig. 1-1 [*1.13*].

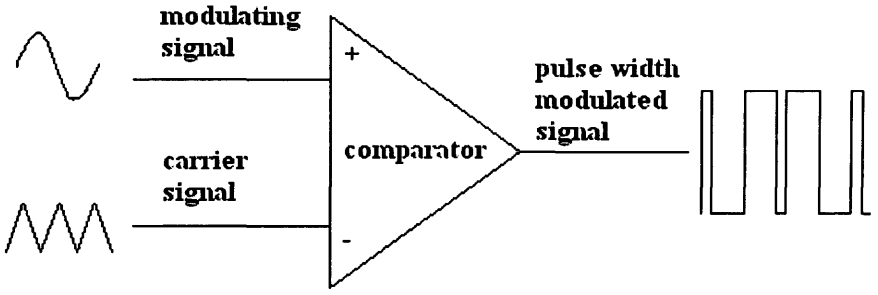

Fig. 1-1 PWM waveform produced by comparison between sinusoidal control signal and carrier (triangular) signal [*1.13*]

Several significant parameters determine the performance of PWM inverters. One is the adjustment of the *ac* output voltage of the inverter that is achieved by adjusting the amplitude modulation ratio or index m_a, defined in (1.1), where $\hat{V}_{control}$ is the peak amplitude of the control signal (modulating signal) and $\hat{V}_{tri}$ is the amplitude of the triangular waveform (carrier signal), respectively. In PWM inverters, the switches are controlled based on the comparison of $v_{control}$ and v_{tri}, and the output voltage will depend on the circuit configuration

of the inverter. Boglietti et al, had shown that the modulation index m_a had an effect on iron losses in electrical steels [*1.14*].

$$m_a = \frac{\hat{V}_{control}}{\hat{V}_{tri}} \tag{1.1}$$

The inverter switching frequency f_s is generally kept constant along with its amplitude $\hat{V}_{tri}$. The sinusoidal modulating voltage signal $v_{control}$ is used to modulate the switch duty ratio and has a frequency f_1, which is the desired fundamental frequency f of the inverter voltage output (f_1 is also called the modulating frequency), recognising that the inverter output voltage will not be a perfect sinusoidal waveform [*1.15*]. The ration between switching frequency f_s and fundamental frequency f is defined as frequency modulation ratio m_f (1.2) defining the frequencies at which the harmonics occur.

$$m_f = \frac{f_s}{f} \tag{1.2}$$

Moreover, f_s is another key parameter of PWM inverter supplies that affects iron losses in magnetic materials [*1.16*]. Because of the relative ease in filtering harmonic voltages at high frequencies, it is desirable to use as high a switching frequency as possible, except for one significant drawback: higher power switching losses in the inverter power transistor switches increase proportionally with the f_s. The development of power electronics has allowed increasing switching frequency in PWM inverters. If the optimum switching frequency (based on the overall system performance) is in the 6 to 20 kHz range, then the disadvantages of increasing it to 20 kHz are often outweighed by the advantage of no audible noise with the switching frequency of 20 kHz or greater [*1.17*].

1.2.1 Three-phase PWM inverter

In applications such as uninterruptible *ac* power supplies and *ac*-motor drives, three-phase inverters are commonly used to supply three-phase loads. The most frequently used three-phase inverter circuit consists of three legs, one for each phase, as shown in fig. 1-2 [*1.15*]. The output of each leg, for example v_{AN} (with respect to the negative *dc* bus) depends on V_d,

which is the *dc* bus value in the input of the inverter, and the switch status; the output voltage is independent of the output load current since one of the two switches in a leg is on at any instant [*1.15*].

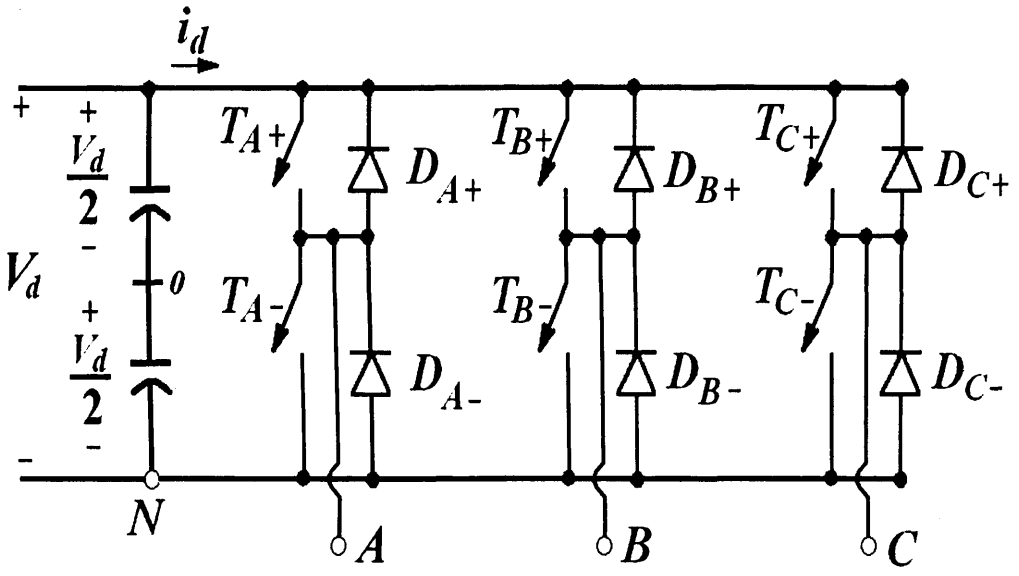

Fig. 1-2 Three-phase inverter [*1.15*]

The objective in a pulse-width modulated three-phase system is to shape and control three-phase *ac* output voltages in magnitude and frequency with an essentially constant magnitude input *dc*-link voltage V_d. To obtain balanced three-phase output voltages in a three-phase PWM inverter, the same triangular voltage waveform is compared with three sinusoidal control voltages that are 120^0 out of phase, as shown in fig. 1-3 (plotted for m_f = 15) [*1.15*].

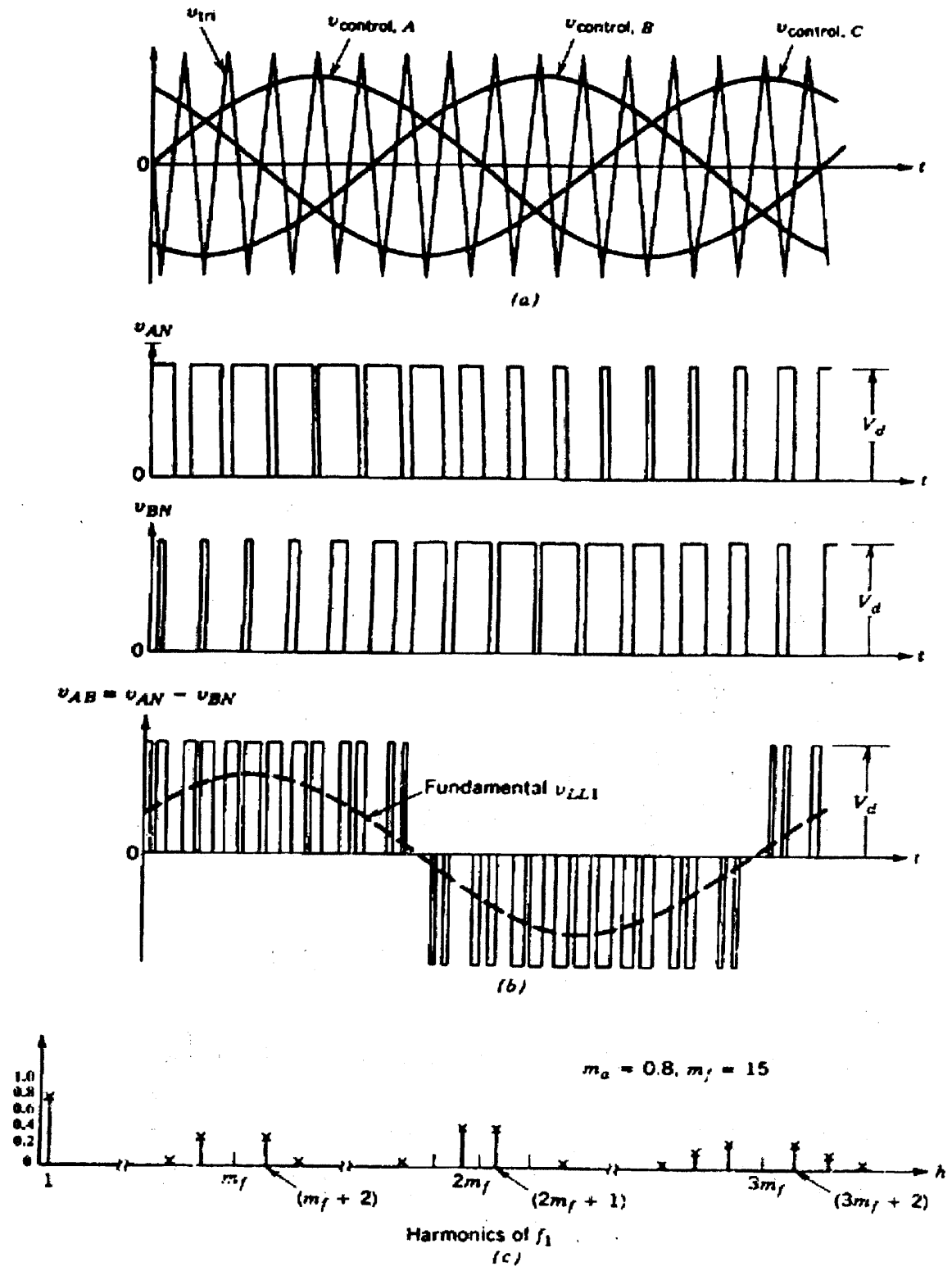

Fig. 1-3 Three-phase PWM waveforms and harmonic spectrum [*1.15*]

1.2.2 Linear modulation ($m_a \leq 1.0$) and over-modulation ($m_a > 1.0$) [*1.15*]

In the linear region ($m_a \leq 1.0$), the fundamental frequency component of the output voltage varies linearly with m_a. In the over-modulation region ($m_a > 1.0$), the peak value $\hat{V}_{control}$ exceeds the peak value of the triangular $\hat{V}_{tri}$, unlike the linear region, in this mode of operation the fundamental frequency voltage magnitude does not increase proportionally with m_a. Fig. 1-4 shows the *rms* value of the fundamental frequency line-to-line voltage V_{LL_1} plotted as a function of m_a. For a sufficiently large value of m_a, the PWM degenerates into a square-wave inverter waveform.

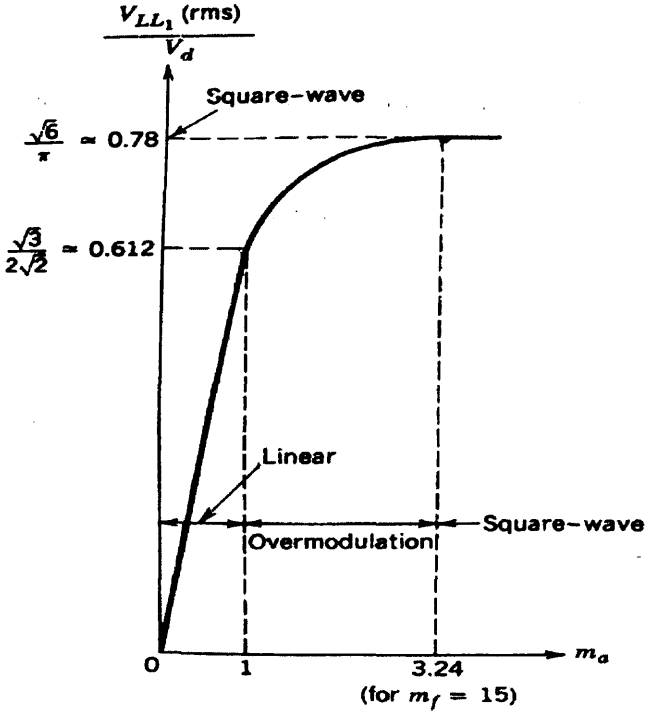

Fig. 1-4 Three-phase inverter $V_{LL_1}(rms)/V_d$ ratio as a function of m_a, where V_{LL_1} is fundamental frequency line-to-line voltage and V_d is the *dc* bus voltage [*1.15*]

1.3 Transformer theory and performance

The most important aspects of transformer action could be brought out by idealising the transformer. Fig. 1-5 shows an elementary model of ideal single-phase transformer, having two windings with N_1 and N_2 turns, respectively, on a common magnetic circuit.

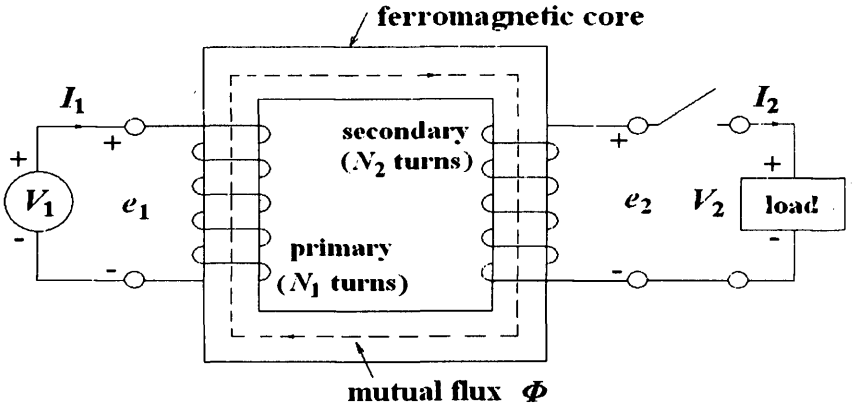

Fig. 1-5 Ideal single-phase transformer core [*1.18*]

Therefore, the voltage induced in a single turn of each winding is equal and the induced voltages in the primary and secondary windings are directly proportional to the number of turns, which is defined by

$$\frac{V_1}{V_2} = \frac{N_1}{N_2} = \frac{I_2}{I_1} = a \qquad [1.18] \qquad (1.3)$$

where V_1 and V_2 are the primary and secondary voltages, I_1 and I_2 are the primary and secondary currents, a is the turns ratio.

1.3.1 Measurement of the core flux density

The scalar form of Faraday's law is given by

$$e = -\frac{d\phi}{dt} \qquad [1.18] \qquad (1.4)$$

where

$$\phi = \iint_S \overline{B} \bullet d\overline{S} \qquad [1.18] \qquad (1.5)$$

where ϕ is the magnetic flux in webers (Wb) passing across an arbitrary surface.

Consider an ideal single-phase transformer shown in fig. 1-5 with a supply voltage for magnetising the coil to generate a value of ϕ at a steady frequency f. Since there is no leakage flux for the ideal transformer, the instantaneous $e.m.f$ induced in N_2 is given by

$$e_2 = N_2 \frac{d\phi}{dt} \tag{1.6}$$

therefore, the *e.m.f* induced in the secondary windings by the flux variation will be,

$$e_2(t) = N_2 \frac{d\phi(t)}{dt} \tag{1.7}$$

It might be expected that the distribution of magnetic flux at every point in the cross-sectional area A of the core is uniform, if so, the magnetic flux density $B(t)$ could be found as uniform by (1.8)

$$B(t) = \frac{\phi(t)}{A} \tag{1.8}$$

from equations (1.7) and (1.8), it can be seen that,

$$e_2(t) = N_2 \frac{d\phi(t)}{dt} = N_2 A \frac{dB(t)}{dt} \tag{1.9}$$

by using the above definition, the instantaneous flux density $B(t)$ can be expressed as

$$B(t) = \frac{1}{N_2 A} \int e_2(t) dt \tag{1.10}$$

1). ***Measurement of the core flux density under sinusoidal voltage excitation*** **[*1.18*]**

In the case where the waveforms of the applied voltage and the flux are sinusoidal, the flux as a function of time is given by

$$\phi(t) = \phi_{peak} \sin \omega t \qquad [1.18] \tag{1.11}$$

where ϕ_{peak} is the peak value of the flux in the core, ω is $2\pi f$. Then, the secondary induced voltage is given by

$$e_2(t) = N_2 \frac{d\phi(t)}{dt} = \omega N_2 \phi_{peak} \cos \omega t \qquad [1.18] \tag{1.12}$$

therefore, the *rms* value of the secondary induced *e.m.f* is given by

$$e_{rms} = \frac{2\pi}{\sqrt{2}} fN_2\phi_{peak} = 4.44\, fN_2\phi_{peak} \qquad [1.18] \qquad (1.13)$$

for an alternating and sinusoidal variation of flux density,

$$B(t) = B_{peak} \sin \omega t \qquad (1.14)$$

where B_{peak} is the peak value of the flux density in the core. By introducing equations (1.8) and (1.12), it can be shown that

$$e_2(t) = \omega N_2 A B_{peak} \cos \omega t \qquad (1.15)$$

so that, the *rms* value of the secondary induced *e.m.f* is also given by

$$e_{rms} = 4.44\, fN_2 AB_{peak} \qquad (1.16)$$

to determine the average value of the secondary induced voltage over a period of time,

$$e_{av} = \frac{2}{T}\int_0^{T/2} e_2(t)\,dt \qquad (1.17)$$

hence, the average secondary induced voltage can be easily calculated from

$$e_{av} = 4\, fN_2 AB_{peak} \qquad (1.18)$$

Therefore, equations (1.16) or (1.18) can be used to set a desired peak flux density in a magnetic core under sinusoidal voltage excitation.

2). ***Measurement of the core flux density under PWM voltage excitation***

Equations (1.16) and (1.18) are not valid when the waveforms of the applied voltage and the flux are non-sinusoidal unless Fourier expansion of the secondary induced voltage is implemented. Under non-sinusoidal flux density condition, the instantaneous secondary induced voltage can be expressed as:

$$e_2(t) = \sum_n e_n Sin(2n\pi f + \varphi_n) \quad (n = odd; \varphi_1 = 0) \quad [1.17] \qquad (1.19)$$

where e_n and φ_n are the amplitude and phase of the n^{th} harmonic component.

A PWM voltage waveform is a discrete function so it can be defined over half a cycle by:

$$e(t) = \begin{cases} V \sum \tau_i \neq 0 \\ 0 \sum \tau_i = 0 \end{cases} \qquad [1.17] \qquad (1.20)$$

where $\sum_1^n \tau_i$ and V are the sum of pulse widths in a half cycle and inverter constant output voltage, respectively. Hence, from equation (1.10), $B(t)$ of the core under PWM voltage excitation can be obtained from Faraday's law in discrete form as:

$$B(t) = \frac{1}{N_2 A} \int e_2(t) dt \approx \frac{V}{N_2 A} \sum \tau_i \qquad [1.17] \qquad (1.21)$$

Under PWM voltage excitation, the peak value of flux density can be expressed as:

$$B_{peak} = \frac{V}{2N_2 A} \sum \tau_i \qquad [1.17] \qquad (1.22)$$

This can be used to find the B_{peak} value in a core provided that, the number of turns of the secondary winding, core cross sectional area and the PWM inverter parameters are known.

1.3.2 Three-phase transformer connections

The windings of three-phase transformers can be connected in either wye (star or Y) or delta (mesh or Δ). Four possible combinations of connections for the three-phase, two-winding transformers are: Y - Δ, Δ - Y, Δ – Δ and Y - Y.

The Y - Δ connection is commonly used in high-voltage transmission systems to step down the voltage. A common arrangement in distribution circuits is the 208 (line-to-line)/120 (line-to-neutral)-voltage system supplied by the Y-connection on the low-voltage side, with the

high-voltage side of the transformer connected in Δ. The neutral point of the Y is usually grounded.

The Δ - Y connection is popularly used for stepping up to a high voltage. The Y-connection on the high-voltage side provides a neutral for grounding and reduces insulation requirements.

The Δ - Δ connection is generally used in medium voltage systems since the windings operate at full line-to-line voltage. In the case of a bank consisting of three single-phase transformer units, one of the advantages of the Δ - Δ connection is that if one transformer fails it can be removed from the circuit and reduced three-phase output supplied by the other two units connected in open - delta. The open - delta connection is also known as V-connection. The rating of the V - V connection will only be about 58% of that of Δ- Δ connection without overheating.

The Y - Y connection may be used in high-voltage applications because the voltage across the transformer winding is only $1/\sqrt{3}$ of the line-to-line voltage. However, it is seldom used because of the difficulties with the exiting current phenomena. In cases where Y - Y transformation is utilized, it is quite common to incorporate a third winding, known as a tertiary winding, connected in delta.

1.3.3 No-load core loss measurement using wattmeter method

No-load core or iron losses are usually less than 1% of the power rating of a transformer. These losses do not vary with load and can be obtained from a no-load test, using wattmeter method.

1.3.3.1 Principle of power loss measurement using wattmeter method

The principle of the wattmeter measurement was developed by Steinmetz [*1.19*]. The wattmeter measures the scalar product of the magnetising current, which is proportional to the magnetising field and the time derivative of the flux density. This is equivalent to the induced voltage and forms an exact expression of the power loss, which was described previously [*1.20*]. The wattmeter reading gives a direct indication of the total iron loss of the specimen. This technique has been widely adopted for the measurement of the total iron loss in

commercial material, and it could be used in conjunction with any magnetic circuit configuration, such as the Epstein square or a transformer core [*1.20*].

1.3.3.2 Measurement circuit of three-phase transformer core

The number of wattmeter's required and the connections of the voltage and current elements are dictated by Blondel's Theorem – "The total power delivered to a load system by means of n conductors is given by the algebraic sum of the indications of n wattmeters so inserted that each of the n wires contains one wattmeter current-coil, its potential coil being connected between that wire and some point of the system in common with all the other potential coils; if that common junction of all the potential leads is on one of the n wires, the total power is obtainable from the indications of $n-1$ wattmeter elements" [*1.21*]. I.e. for a three-phase, four-wire system three elements are required; and for a three-phase, three-wire system two elements are required.

The current element of each wattmeter is connected to one of the lines, and the corresponding voltage element is connected between that line and a common point. Total power is determined by summing the readings of the wattmeters. The three-wattmeter method states that to measure the no-load total power loss of three-phase transformer core, three wattmeters are required as shown in fig. 1-6 [*1.22*].

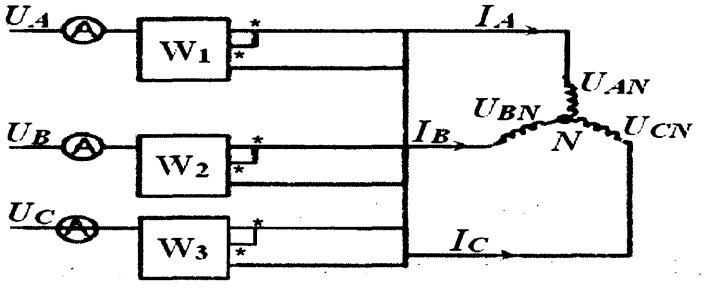

Fig. 1-6 Three wattmeter's circuit [*1.22*]

Fig. 1-6 shows the voltages and currents that define the total instantaneous power and that also determine the individual wattmeter readings. The effects of various circuit conditions can be evaluated by examining the equations that govern the voltages and currents. The total instantaneous power P_{total} measured by the three wattmeters is calculated from

$$P_{total} = U_{AN} I_A + U_{BN} I_B + U_{CN} I_C \tag{1.23}$$

$$P_1 = U_{AN} I_A \tag{1.24}$$

$$P_2 = U_{BN} I_B \tag{1.25}$$

$$P_3 = U_{CN} I_C \tag{1.26}$$

therefore

$$P_{total} = P_1 + P_2 + P_3 \tag{1.27}$$

where P_{total} is the sum of the active power indicated by three wattmeters P_1, P_2 and P_3, and U_{AN}, U_{BN}, U_{CN} are the phase-to-neutral voltages across the wattmeter voltage elements, I_A, I_B, I_C are the line currents (and the currents in the wattmeter current elements).

According to Blondel's Theorem, three-phase power can be measured by means of only two wattmeters having a common potential junction on any one of the three lines in which there is no current coil. This is the two-wattmeter method as shown in fig. 1-7.

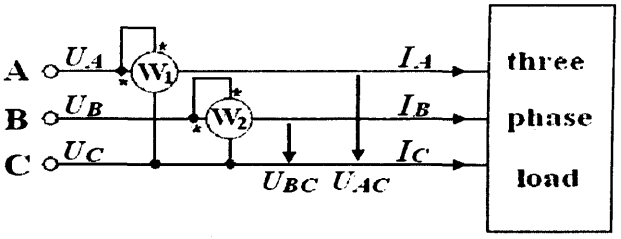

Fig. 1-7 Two-wattmeter method

according to the principle of wattmeter

$$P_1 = U_{AC} I_A \tag{1.28}$$

$$P_2 = U_{BC} I_B \tag{1.29}$$

$$P_1 + P_2 = U_{AC} I_A + U_{BC} I_B \tag{1.30}$$

because

$$U_{AC} = U_A - U_C \tag{1.31}$$

$$U_{BC} = U_B - U_C \tag{1.32}$$

$$I_A + I_B = -I_C \tag{1.33}$$

by introducing (1.31), (1.32) and (1.33) into (1.30)

$$P_1 + P_2 = U_A I_A + U_B I_B + U_C I_C \tag{1.34}$$

hence

$$P_{total} = P_1 + P_2 \tag{1.35}$$

In this investigation, the total iron losses of a model three-phase three-limb laminated transformer core has been measured under sinusoidal and PWM voltage excitation, following two-wattmeter method, as described in chapter 4.

1.3.4 Theory of estimating iron losses

Predicting iron losses in magnetic materials when a non-sinusoidal voltage supply is applied (in particular for PWM inverter supply), is still an open research field. Several approaches have been proposed.

1.3.4.1 Predicting the iron losses using loss separation criteria

A widely adopted approach uses the Bertotti-Fiorillo model [*1.23*], where the total iron losses can be analysed into three components, namely, static hysteresis loss, classical eddy-current loss and excess loss as [*1.24*]

$$P_{total} = K_a B_{peak}^{x} f + K_b B_{peak}^{2} f^2 + K_c B_{peak}^{1.5} f^{1.5} \quad \text{[W/kg]} \tag{1.36}$$

where x is the Steinmetz coefficient; K_a, K_b and K_c are coefficients of static hysteresis loss, classical eddy-current loss and excess loss, respectively [*1.24*].

When a magnetic core is energised by PWM voltage excitation additional power losses occur in the core due to the distorted PWM flux waveforms. Some investigators have used the loss

separation method in order to predict iron losses under PWM voltage excitation [*1.24*]-[*1.26*]. The total iron loss for a PWM flux waveform can be expressed by [*1.27*]

$$P_{total} = P_h + \frac{2}{3}\frac{\sigma d^2}{m}\frac{B_{peak}^2}{\sum \tau_i} + \frac{4\sqrt{2\sigma G V_0 A}}{m}\frac{B_{peak}^{1.5}}{\left(\sum \tau_i\right)^{0.5}} \quad \text{[W/kg]} \tag{1.37}$$

where P_h is the static hysteresis loss, σ is conductivity of the magnetic material, d is the thickness of the lamination, A is the cross-sectional area, m is density of the material, G and V_0 are parameters dependent on the material structure, which were determined from the previous experiments carried out by Bertotti and were found to be 0.1356 and 0.15 A/m of grain-oriented 3% silicon lamination, and 0.1356 and 0.12 A/m for no-oriented 3% silicon lamination [*1.23*].

In order to show the difference between frequency dependent total losses under sinusoidal and PWM voltage excitation, the total iron losses under sinusoidal voltage excitation can be expressed as [*1.28*]

$$P_{total} = P_h + \frac{\sigma \pi^2 d^2}{6m} B_{peak}^2 f^2 + \frac{\sqrt{2\sigma G V_0 A}}{m} B_{peak}^{1.5} f^{1.5} \quad \text{[W/kg]} \tag{1.38}$$

The form factor coefficient of PWM voltage excitation is the ratio between the form factor of the PWM voltage excitation and that of the sinusoidal voltage excitation, $F_c = 2/\left(\pi\sqrt{f\sum \tau_i}\right)$. If dynamic loss components in (1.38) are multiplied by this term under the condition of the PWM voltage excitation with respect to the sinusoidal voltage excitation, where F_c is 1, the total iron losses under PWM voltage excitation can be rewritten as [*1.28*]

$$P(f)_{total} = P_h + \frac{\frac{4}{\pi^2}\frac{1}{\sum \tau_i} P_e^{\sin}(f)}{f} + \frac{2}{\pi}\frac{P_{ex}^{\sin}(f)}{\sqrt{\sum \tau_i}\sqrt{f}} \quad \text{[W/kg]} \tag{1.39}$$

where $P_e^{\sin}(f)$ and $P_{ex}^{\sin}(f)$ are eddy-current loss and excess loss respectively under sinusoidal magnetisation. From equations (1.37) and (1.38), if the magnetising frequency, core parameters, such as resistivity, density and thickness of the core laminations as well as

the parameters of the PWM voltage are known, the classical eddy-current loss can be approximately calculated at a given peak flux density under sinusoidal and PWM voltage excitation. The form factor K_f of a periodic waveform $v(t)$ of complete period T is defined by

$$K_f = \frac{v_{rms}}{v_{rectmean}} = \frac{\sqrt{(1/T)\int_0^T v^2(t)dt}}{(1/T)\int_0^T |v(t)|dt} \tag{1.40}$$

where v_{rms} and $v_{rectmean}$ are root-mean-square and rectified mean values of the secondary induced voltage. Also, it can be seen from (1.37), that the total number of pulses $\sum \tau_i$ per half cycle is an important parameter of the PWM voltage excitation that influence the classical eddy-current loss, that is, as they increase the loss decreases. This parameter is determined by the control voltage frequency and the carrier frequency. If the ratio of these frequencies is large the number of pulses will be high, therefore, the eddy-current loss is expected to decrease.

Moreover, the loss separation method has been used successfully by several investigators such as Boglietti, Fiorillo, Novikov, Amar, Kaczmarek and Barbisio [*1.24*]-[*1.26*] [*1.28*]-[*1.30*] and they have found results confirming prediction of iron loss compared to measured iron loss results under PWM voltage excitation. The classical eddy-current loss is calculated from [*1.30*]

$$P_e = \frac{4}{3}\sigma d^2 B_{peak}^2 \, g_M(m_a, m_f)^2 \, f \qquad \text{[mJ/kg]} \tag{1.41}$$

where $g_M(m_a, m_f)$ is approximately obtained from [*1.30*]

$$g_M(m_a, m_f) \cong \frac{m_f}{1 + 2m_a \times \sum_{i=1}^{(m_f-1)/2} \sin[\,2\pi(3/4 + i - 1)/m_f\,]} \tag{1.42}$$

1.3.4.2 Viscosity approach of iron losses

Unlike the approach of Bertotti model, Zirka [*1.31*]-[*1.34*] has separated all three components of the total iron losses by a proposed dynamic Preisach model (DPM), which uses a finite-

element (FE) and finite-difference (FD) solvers of the diffusion equation for a thin ferromagnetic lamination.

The magnetisation process in a thin ferromagnetic sheet is based on the solution of the diffusion equation that links the magnetic field strength H and the magnetic induction B in a homogeneous material with electrical conductivity σ. If the x - axis is directed into the sheet of thickness d, the z - axis is taken along the rolling direction, the plane yz is coincident with the sheet surface, this equation has a form expressed by [*1.34*]

$$\sigma \frac{\partial B}{\partial t} = \frac{\partial^2 H}{\partial x^2} \qquad [1.34] \qquad (1.43)$$

where $H = H_z(x,t)$ and $B = B_z(x,t)$.

The excess loss is simulated by using the notion of "fast" magnetic viscosity, i.e. the lag of B behind H, to enable accurate reproduction of the frequency dependence of the excess losses. Equation (1.43) is applied to each point inside the sheet (to node i of the grid) and can be solved with a finite-difference scheme expressed by [*1.34*]

$$\frac{dB_1}{dt} = \frac{8H_2 - 7H_1 - H_3}{2\sigma l^2} + \frac{3(N-1)}{N_1 A} e(t),$$

$$\frac{dB_i}{dt} = \frac{H_{i-1} - 2H_i + H_{i+1}}{\sigma l^2}, \ (i = 2,...., N-1),$$

$$\frac{dB_N}{dt} = \frac{2(H_{N-1} - H_N)}{\sigma l^2} \qquad [1.34] \qquad (1.44)$$

where B_i and H_i are nodal induction and field linked by a dynamic Preisach model, A is cross-sectional area of the core, $l = d/[2(N-1)]$ is the step of a finite-difference grid with N nodes on the half sheet thickness $d/2$, and $e(t)$ is the voltage across the magnetising windings with N_1 turns [*1.34*]. I.e., the whole sheet is subdivided into N "layers" (normally, $N \doteq$ 15-25) and the process is analysed in every layer simultaneously. In order to know the total iron loss in the sheet, the loss in every sheet layer (finite-difference node) is calculated and then summed.

This approach can be used to accurately predict total losses in materials magnetised under sinusoidal or non-sinusoidal flux waveforms, in non-oriented and grain-oriented materials to within 2% of measured values [*1.27*]. Conceptually, the techniques are used by many other scientific researchers such as Dupre, Keer, Bottauscio, Chiampi and Melkebeek [*1.35*]-[*1.37*].

1.3.5 Analysis of localised flux density measurement using search coil techniques

High localised losses in three-phase transformer cores not only increase the overall power loss, but also can generate hot spots within the core. The power loss is generally higher where harmonics occur or where the flux deviates from the rolling direction. Since the localised power loss distribution is dependent on the localised flux density, a better appreciation and understanding of the localised flux density distribution in specific regions such as T-joints and corners within individual laminations is needed.

An investigation carried out by Moses and Thomas [*1.38*] [*1.39*] clarified the flux behaviour in individual laminations in T-joints and corners regions where the flux flows three dimensionally within the laminations.

In order to measure the local flux density at T-joints and corners regions, it is necessary to wind arrays of search coils on individual laminations. This technique was originally developed by Brailsford and Mazza [*1.40*], and then used by other researchers [*1.41*] - [*1.43*] to study the local flux distribution in transformer cores. By measuring the magnitude and relative phase in time of the voltage induced in the search coils, it is possible to calculate the magnitude and direction of the flux density at individual points. Moreover, localised loss produced by distorted flux waveforms is difficult to calculate but reasonable estimates can be made. The simple method is just to add the components of loss that would be produced if the harmonics were individually present in the steel, which is found to give reasonable accuracy.

Considering that the flux density is generally a vector, which has two components, one is in-plane and parallel to the surface of the lamination, which can be analysed into orthogonal components, the other is normal (interlaminar) and perpendicular to the lamination plane. The magnitude and direction of the instantaneous localised flux density can be calculated and analysed by measuring the induced voltages from corresponding search coils. Consider a point **m** on a lamination located in the middle of two orthogonal search coils **X** (rolling direction) and **Y** (transverse direction) as shown in fig. 1-8 (a).

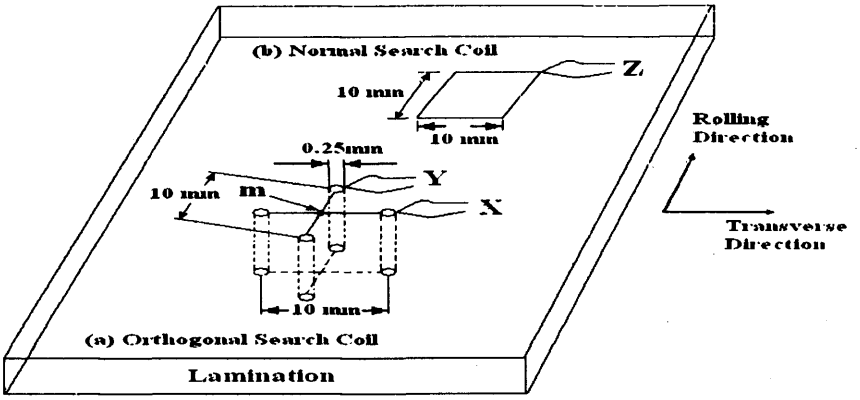

Fig. 1-8 Dimension of the search coils and search holes for: (a) orthogonal search coil; (b) normal search coil [*1.20*]

The instantaneous components of flux density in the rolling ($B_{ro}(t)$), transverse ($B_{tr}(t)$) and normal ($B_{no}(t)$) directions can be obtained using (1.10) giving

$$B_{ro}(t) = \frac{1}{N_{to} A_{ro}} \int e_{ro}(t) dt \tag{1.45}$$

$$B_{tr}(t) = \frac{1}{N_{tr} A_{tr}} \int e_{tr}(t) dt \tag{1.46}$$

$$B_{no}(t) = \frac{1}{N_{no} A_{no}} \int e_{no}(t) dt \tag{1.47}$$

where $e_{ro}(t)$, $e_{tr}(t)$ and $e_{no}(t)$ are instantaneous voltages induced in search coils in the rolling, transverse and normal directions respectively; A_{ro}, A_{tr} and A_{no} are cross-sectional areas in rolling, transverse and normal direction respectively; N_{ro}, N_{tr} and N_{no} are the corresponding number of turns of the search coils.

Moreover, in order to determine the phase difference between the *e.m.f* induced in the search coils, a reference search coil is used. The secondary winding of any phase of a three-phase transformer could be chosen as the reference. Each localised search coil *e.m.f* is compared with the voltage induced in the reference search coil. Therefore, each detected signal (fig. 1-8) can be represented by a vector having a magnitude and an angle with respect to the reference direction, which can be used to evaluate the resultant flux density at the specific point **m** (fig. 1-8).

The magnitude of the resultant in-plane instantaneous flux density $|B_{in-plane}(t)|$, and the vector sum of $|B_{ro}(t)|$ and $|B_{tr}(t)|$ that can be found from equations (1.45) and (1.46) by

$$|B_{in-plane}(t)| = \sqrt{B_{ro}(t)^2 + B_{tr}(t)^2} \tag{1.48}$$

and

$$\alpha_{in-plane} = \tan^{-1}\left(\frac{B_{tr}(t)}{B_{ro}(t)}\right) \tag{1.49}$$

where $\alpha_{in-plane}$ is the angle of the in-plane resultant flux density. These equations are valid for non-sinusoidal voltage waveforms provided that the flux waveform can be expressed analytically or replaced by its Fourier expansion.

The angle of the instantaneous normal flux density $B_{no}(t)$ is either + 90^0 or - 90^0. Ideally, flux does not flow normal to the sheet plane. However, normal or interlamina flux occurs in laminated and wound cores and causes planar eddy-current loss. This occurs not only in the corner joints of stacked transformer cores, but also between the turns of wound cores and even within limbs of simple stacked cores due to small differences between the in-plane permeability of individual laminations. Although $B_{no}(t)$ might be less than 0.1% of the in-plane flux density, localised losses can be much higher than those caused by the in-plane flux [*1.27*].

1.3.6 Vibration and acoustic noise of transformer cores

Transformer noise is especially annoying because of its character: a continuous "humming" consisting of pure a tone. In noise control legislation, this is often considered by setting the limits for pure tone noise 5 *dB* or even 10 *dB* lower than for normal broadband noise as, e.g., resulting from traffic [*1.44*]. British Standard BS EN 60551: 1993 [*1.45*] states that the maximum allowable acoustic noise level emitted by a transformer should be around 60 – 70 decibels and at this point, the acoustic noise level is equivalent to a car travelling at 60 km/h at 7 m distance. In a considerable fraction of transformers built today, the noise is equally, or even more, important than the power loss [*1.44*].

Under no-load condition, the "hum" developed by energised transformers originates in the core, where magnetic forces tend to make the laminations vibrate. The essential factors in noise production of a transformer core are consequently magnetostriction and mechanical vibration developed by the laminations.

1.3.6.1 Magnetostiction

The first observation of magnetostriction was made by Joule [*1.46*]. The essential nature of the effect is illustrated in fig. 1-9 (a), in which a rod of a magnetic material of length L is shown surrounded by a coil. When an electric current is passed through the wire (fig. 1-9 (*b*)) to produce a magnetic field, H along the rod, the length of the rod increases by a small amount, δL. The strain ($\delta L/L$) in the rod is the magnetostriction, λ. The variation of λ with field H is illustrated in fig. 1-10, which shows two important features of magnetostriction: firstly, with increasing H, λ eventually reaches a saturation value λ_{sat}, and secondly the sign of λ does not reverse when the direction of H is reversed [*1.47*].

Magnetostriction can be either positive or negative depending on material properties and magnetisation level. In fig. 1-9 and fig. 1-10, the length of the rod increases with increasing magnetic field, which is termed positive magnetostriction. It is therefore evident that the fundamental frequency of magnetostriction is twice that of the magnetisation frequency. The magnitude of λ is extremely small and often expressed as ppm (parts per million), $10^{-6}\varepsilon$ or simply $\mu\varepsilon$, microstrain. In this investigation, λ is expressed in terms of $\mu\varepsilon$.

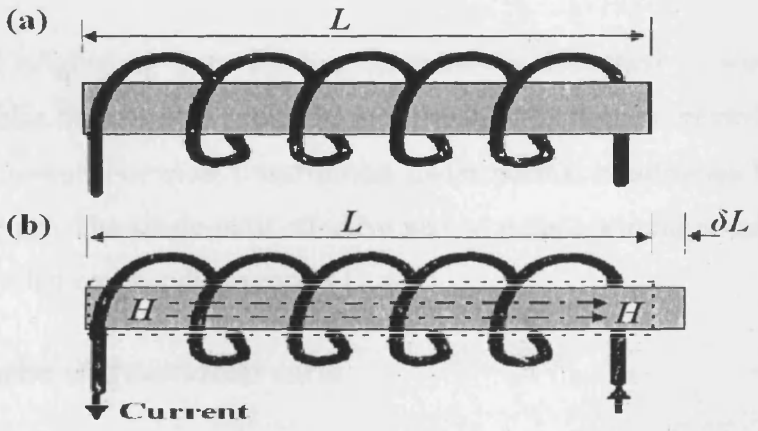

Fig. 1-9 Illustration of the effect of magnetostriction in a rod (a) in zero fields; (b) in field H [*1.48*]

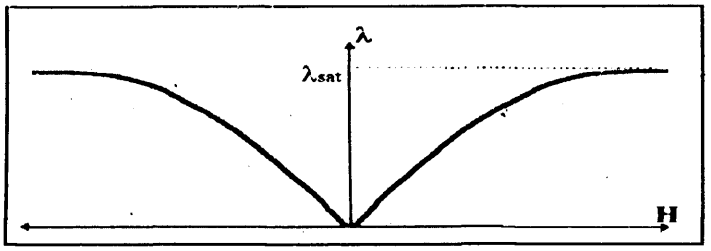

Fig. 1-10 Variation of magnetostriction with magnetic field [*1.47*]

1.3.6.2 Vibration phenomenon in transformer cores

1). *Core vibration*

Core vibration, the most important cause of transformer noise, is referred to as no-load noise or voltage noise because it is caused by the magnetisation of the core and is independent of the winding currents. If a core consisted of homogeneous steel, magnetostriction would cause vibration only in a plane parallel to that of the core. But as the laminations are not homogeneous, differential movements take place within the core, exciting vibrations in a direction perpendicular to the plane of the core. A core structure, having distributed mass and stiffness, possesses an infinite number of natural frequencies each associated with a particular mode. A few of these may lie in the range of magnetostrictive or magnetic force harmonics, but the questionable rigidity of mitred corner joints makes the mechanical problem difficult to analyse. Henshell and others [*1.48*] computed and measured some of the results and showed three modes of in-plane vibration and a typical out-of-plane mode, which could contribute considerably to the total transformer noise output.

2). *Winding vibration*

Transformer noise originating from winding vibrations is described as winding noise, load noise or current noise because it is caused by electromagnetic forces created by the magnetic field of the load current. For most transformers under normal continuous load, this type of noise is less important. The single most effective way to reduce windings noise is by having a good quality controlled coil winding process [*1.44*].

1.3.6.3 Acoustic noise of transformer cores

A transformer core is assembled by many laminations of electrical steel. The extensions and contractions take place erratically all over a lamination, and each lamination behaves

erratically with respect to its neighbour. Although these extensions and contractions are dimensionally small, they are sufficient to cause a vibration, and as a result, noise. Fig. 1-11 gives a schematic view of the noise generation and transmission in a transformer [*1.49*].

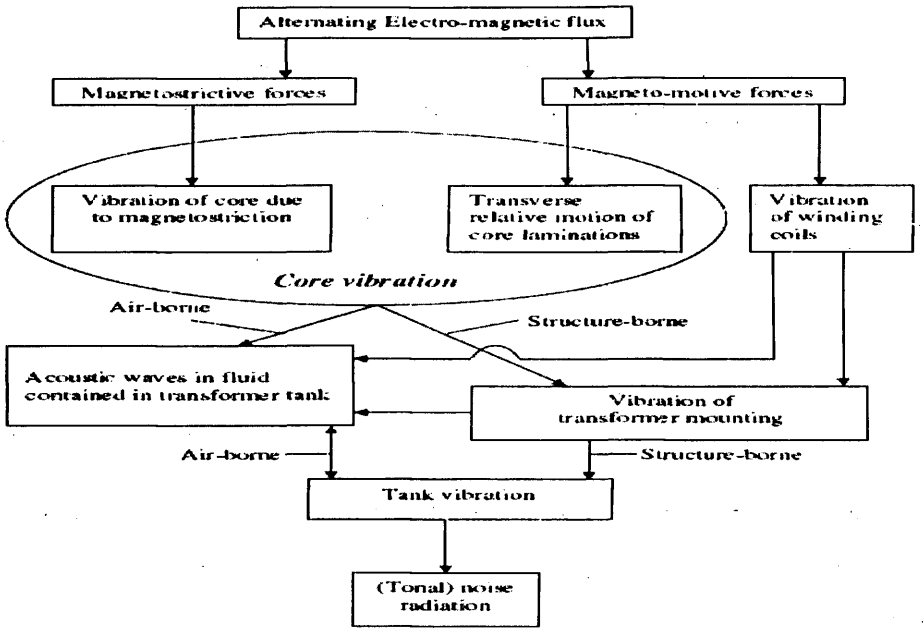

Fig. 1-11 A schematic view of noise generation and transmission in a power transformer [*1.49*]

The structural components of a transformer such as the core, windings, transformer mounting, tank, etc., are continuous systems with an infinite number of natural frequencies of vibration. But the core has been identified as a major source of noise [*1.49*].

1.3.6.4 Sound pressure level (*SPL*)

Sound is defined as any pressure variation that the human ear can detect, which is created when objects vibrate, resulting in a minute variation in surrounding atmospheric pressure. The range of magnitude from the faintest to the loudest sound the ear can hear is so large that sound pressure is expressed on a logarithmic scale in units called decibels (*dB*). The decibel as used in acoustics is a measurement comparing the pressure generated by a noise against some standard level [*1.50*].

Compared to the static air pressure (10^5 Pa), the audible sound pressure variations are very small ranging from about 20 μPa (20×10^{-6} Pa) to 100 Pa. 20 μPa corresponds to the average person's threshold of hearing. It is therefore called the threshold of hearing. A sound pressure of approximately 100 Pa is so loud that it causes pain and is therefore called the threshold of

pain. So, the linear scale with its large numbers is converted into a manageable scale from 0 *dB* at the threshold of hearing (20 μPa) to 130 *dB* at the threshold of pain (~100 Pa) [*1.50*].

Modern measuring instruments process sound signals through electronic networks the sensitivity of which varies with frequency in a manner similar to the human ear. This has resulted in a number of internationally standardised weightings, of which the A-weighted network is the most common [*1.45*].

In making measurements of acoustic noise at a particular point in space using a microphone, the quantity measured is the sound pressure level. When the decibel is used to give the sound level for a single sound rather than a ratio, then a reference level must be chosen. Therefore, the sound pressure level (*SPL*) (acoustic noise) is given by [*1.50*]

$$SPL = 20\log_{10}(\frac{p_{mea}}{p_{ref}}) \quad [dBA] \quad [1.50] \qquad (1.50)$$

where p_{mea} is the measured A-weighted sound pressure level, and the reference sound pressure level p_{ref} is 20 μPa. Standard measurements use the A-weighted sound pressure level as a measured variable and measurements on transformers are made under no-load condition [*1.45*]. The sound pressure level is measured by a pick-up microphone, which is placed at specified heights and locations around the transformer core and the results averaged [*1.51*]. It is necessary to provide a low level of background sound and avoid reflective surfaces to achieve accurate results [*1.52*].

Nowadays, the acoustic noise generated by a 15 MVA grain-oriented steel core is around 72 *dBA* having a 4 $\mu\varepsilon$ magnetostriction measured on a core limb [*1.51*]. Moreover, for a 40 MVA rated 132/33 kV transformer with tank-mounted radiators, two pumps and eight fans, by careful attention to core design and use of modern HiB steel, the acoustic noise has been achieved around 66 *dBA* at the rating. However, the acoustic noise is increased to around 82 *dBA* with all pumps and fans running [*1.53*]. Normally, typical average surface acoustic noise of a range of transformers is given by: 200 kVA – 1000 kVA (11 kV), the acoustic noise varied around in the range of 45 *dBA* - 55 *dBA* ; 2 MVA – 100 MVA (33 – 132 kV), the noise varied around 58 *dBA* - 80 *dBA* ; 200 MVA – 1000 MVA (275-400 kV), the noise varied around 80 *dBA* - 90 *dBA* [*1.53*].

References to Chapter 1:

[*1.1*] S. J. Chapman, "Electric machinery fundamentals", *Third Edition*, 1998.

[*1.2*] Z. C. Papazacharopoulos, A. G. Kladas and S. N. Manias, "Investigation of the switching frequency harmonics impact on PWM induction motor drive efficiency", *IEEE Power Electronics Specialist Conference*, vol. 2, pp. 1203-1208, June 17-21, 2001.

[*1.3*] E. N. Hildebrand and H. Roehrdanz, "Losses in three-phase induction machines fed by PWM converter", *IEEE Trans. on Energy Conversion*, vol. 16, no. 3, pp. 228-233, September 2001.

[*1.4*] J. J. Lee, Y. K. Kim and H. Nam, "Loss distribution of three-phase induction motor fed by pulsewidth-modulated inverter", *IEEE Trans. on Mag.*, vol. 40, no. 2, pp. 762-765, March 2004.

[*1.5*] A. J. Moses and N. Tutkun, "Localised losses in stator laminations of an induction motor under PWM excitation", *Journal of Materials Processing Technology*, vol. 161, pp. 79-82, 2005.

[*1.6*] K. Yamazaki and Y. Seto, "Iron loss analysis of interior permanent-magnet sysnchronous motors-variation of main loss factors due to driving condition", *IEEE Trans. on Industry Applications*, vol. 42, no. 4, pp. 1045-1052, July/August 2006.

[*1.7*] F. Barrero, S. Martinez, F. Yeves, F. Mur and P. M. Martinez, "Universal and reconfigurable to UPS active power filter for line conditioning", *IEEE Trans. on Power Delivery*, vol. 18, no. 1, pp. 283-290, January 2003.

[*1.8*] T. W. Kim, J. H. Choi and B. H. Kwon, "High performance line conditioner with output voltage regulation and power factor correction", *IEE Proceedings Power Applications*, vol. 151, no. 1, pp. 91-97, January 2004.

[*1.9*] C. A. Petry, J. C. Fagundes and I. Barbi, "Study of an AC-AC indirect converter for application as line conditioner", *IEEE International Symposium on Industrial Electronics*, pp. 757-762, June 20-23, 2005.

[*1.10*] Z. Chen and F. Blaabjerg, "Wind energy-the world's fastest growing energy source", *IEEE Power Electronics Society Newsletter*, vol. 18, no. 3, pp. 15-18, Third Quarter 2006.

[*1.11*] T. L. Mthombeni and P. Pillay, "Lamination core losses in motors with nonsinusoidal excitation with particular reference to PWM and SRM excitation waveforms", *IEEE Trans. on Energy Conversion*, vol. 20, no. 4, pp. 836-843, December 2005.

[*1.12*] R. F. Liu, C. C. T. Mi and D. W. Z. Gao, "Modeling of eddy-current loss of electrical machines and transformers operated by Pulsewidth-Modulated inverters", *IEEE Trans. on Mag.*, vol. 44, no. 8, pp. 2021-2028, August 2008.

[*1.13*] R. Valentine, "Motor control electronics handbook", *Mc Graw-Hill Handbooks*, 1998.

[*1.14*] A. Boglietti, P. Ferraris, M. Lazzari and F. Profumo, "Effects of different modulation index on iron losses in soft magnetic materials supplied by PWM inverter", *IEEE Trans., on Mag.*, vol. 29, no. 6, pp. 3234-3236, November 1993.

[*1.15*] N. Mohan, T. M. Undeland and W. P. Robbins, "Power Electronics: converters, applications and design", 1989.

[*1.16*] A. Boglietti, P. Ferraris, M. Lazzari and M. Pastorelli, "Change of the iron losses with the switching supply frequency in soft magnetic material supplied by PWM inverter", *IEEE Trans., on Mag.*, vol. 31, no. 6, pp. 4250-4252, November 1995.

[*1.17*] N. Tutkun, "Investigation of power loss under PWM voltage excitation in wound toroidal and stator cores", *PhD Thesis*, Cardiff University, December 1998.

[*1.18*] S. S. Mulukutla, "Electric machines-steady-state theory and dynamic performance", 1986.

[*1.19*] C. P. Steinmetz, *Trans. Amer. Inst. Engers.*, 9, pp. 642, 1892.

[*1.20*] Y. G. Kayhanian, "Novel concepts in transformer core design and minimisation of power loss", *PhD Thesis*, Cardiff University, June 1999.

[*1.21*] B. Walden, "A discussion on why the two-wattmeter method works on a three-phase, three-wire load regardless of how the load is internally connected", *Appendix E*, December 2004.

[*1.22*] W. R. Herron III, "Discussion on transformer testing in the factory", *paper No.: 7, HV Testing, Monitoring and Diagnostics Workshop, Workshop 2000*, Alexandria, Virginia, 13 & 14 September 2000.

[*1.23*] G. Bertotti, "General properties of power losses in soft ferromagnetic materials", *IEEE Trans. on Mag.*, vol. 24, no. 1, pp. 621-630, January 1988.

[*1.24*] A. Boglietti, A. Cavagnino, M. Lazzari and M. Pastorelli, "Predicting iron losses in soft magnetic materials with arbitrary voltage supply: an engineering approach", *IEEE Trans. on Mag.*, vol. 39, no. 2, pp. 981-989, March 2003.

[*1.25*] A. Boglietti, M. Chiampi, M. Repetto, O. Bottauscio and D. Chiarabaglio, "Loss separation analysis in ferromagnetic sheets under PWM inverter supply", *IEEE Trans., on Mag.*, vol. 34, no. 4, pp. 1240-1242, July 1998.

[*1.26*] F. Fiorillo and A. Novikov, "An improved approach to power losses in magnetic laminations under non-sinusoidal induction waveform", *IEEE Trans. on Mag.*, vol. 26, no. 5, pp. 2904-2910, September 1990.

[*1.27*] A. J. Moses, "Loss prediction in electrical steel laminations and motor cores", *Steel Research International Journal*, 76 (6), 455-460, 2005.

[*1.28*] M. Amar, R. Kacmarek and F. Protat, "Prediction of power losses in silicon iron sheets under PWM voltage supply", *JMMM*, vol. 133, pp. 140-143, 1994.

[*1.29*] R. Kacmarek, M. Amar and F. Protat, "Iron loss under PWM voltage supply on Epstein frame and in an induction motor core", *IEEE Trans. on Mag.*, vol. 31, no. 6, pp. 189-194, January 1996.

[*1.30*] E. Barbisio, F. Fiorillo and C. Ragusa, "Predicting loss in magnetic steels under arbitrary induction waveform and with minor hysteresis loops", *IEEE Trans. on Mag.*, vol. 40, no. 4, pp. 1810-1819, July 2004.

[*1.31*] S. E. Zirka, Y. I. Moroz, P. Marketos and A. J. Moses, "A novel approach to modelling losses in electrical steel laminations", *Printed and published by the IEE*, Savoy Place, London, WC2R 0BL, © 2002 The Institution of Electrical Engineers.

[*1.32*] S. E. Zirka, Y. I. Moroz, P. Marketos and A. J. Moses, "Modelling losses in electrical steel laminations", *IEE Proc. – Sci. Meas. Technol.*, vol. 149, no. 5, pp. 218-221, September 2002.

[*1.33*] S. E. Zirka, Y. I. Moroz, P. Marketos and A. J. Moses, "A viscous-type dynamic hysteresis model as a tool for loss separation in conducting ferromagnetic laminations", *IEEE Trans. on Mag.*, vol. 41, no. 3, pp. 1109-1111, March 2005.

[*1.34*] S. E. Zirka, Y. I. Moroz, P. Marketos and A. J. Moses, "Viscosity-based magnetodynamic model of soft magnetic materials", *IEEE Trans. on Mag.*, vol. 42, no. 9, pp. 2121-2132, September 2006.

[*1.35*] L. R. Dupre, R. V. Keer and J. A. A. Melkebeek, "Modelling and identification of iron losses in non-oriented steel laminations using Preisach theory", *IEE Proc. – Electr. Power Appl.*, vol. 144, no. 4, pp. 227-234, 1997.

[*1.36*] L. R. Dupre, G. Bertotti and J. A. A. Melkebeek, "Dynamic Preisach model and energy dissipation in soft magnetic materials", *IEEE Trans. on Mag.*, vol. 34, no. 4, pp. 1168-1170, July 1998.

[*1.37*] L. R. Dupre, O. Bottauscio, M. Chiampi and F. Fiorillo, "Dynamic Preisach modeling of ferromagnetic laminations under distorted flux excitations", *IEEE Trans. on Mag.*,

vol. 34, no. 4, pp. 1231-1233, July 1998.

[*1.38*] A. J. Moses and B. Thomas, "The spatial variation of localised power loss in two practical transformer T- joints", *IEEE Trans. on Mag.*, vol. MAG-9, no.4, pp. 655-659, December 1973.

[*1.39*] M. A. Jones and A. J. Moses, "Comparison of the localised power loss and flux distribution in the butt and lap and mitred overlap corner configurations", *IEEE Trans. on Mag.*, vol. MAG-10, no. 2, pp. 321-326, June 1974.

[*1.40*] F. Brailsford and V. R. Mazza, "The alternating magnetic flux distribution in right-angled corners of transformer laminations", *Proc. IEE*, V. 109A, no. 44, pp. 173-180, 1962.

[*1.41*] A. J. Moses, B. Thomas and J. E. Thompson, "Power loss and flux density distributions in the T-joint of a three phase transformer core", *IEEE Trans. on Mag.*, vol. MAG-8, no. 4, pp. 785-790, December 1972.

[*1.42*] A. J. Moses and B. Thomas, "Measurement of rotating flux in silicon iron laminations", *IEEE Trans. Mag.*, vol. MAG-9, no. 4, pp. 651-654, December 1973.

[*1.43*] A. J. Moses and B. Thomas, "Problems in the design of power transformers", *IEEE Trans. on Mag.*, vol. MAG-10, no.2, pp. 148-150, June 1974.

[*1.44*] B. Weiser, H. Pfützner and J. Anger, "Relevance of magnetostriction and forces for the generation of audible noise of transformer cores", *IEEE Trans. on Mag.*, vol. 36, no. 5, pp. 3759-3777, September 2000.

[*1.45*] BS EN 60551: 1993, "Determination of transformer and reactor sound levels", *British Standard Institution, Issue 2*, May 1998.

[*1.46*] J. P. Joule, "On the effects of magnetism upon the dimensions of iron and steel bars", *Philosophical Magazine*, vol. 30, part 4, pp. 76 -87, 1847.

[*1.47*] A. R. Piercy, "The changing shape of magnetostriction", *New Materials*, University of Brighton, UK.

[*1.48*] R. D. Henshell, P. J. Bennett, H. McCallion and M. Milner, "Natural frequencies and mode shapes of vibration of transformer cores", *Proc. IEE*, vol. 112, no. 11, pp. 2133-2139, November 1965.

[*1.49*] R. S. Masti, W. Desmet and W. Heylen, "On the influence of core laminations upon power transformer noise", *Proceedings of ISMA*, pp. 3851-3862, 2004.

[*1.50*] B. Truax, "Handbook for acoustic ecology", *Second Edition, Cambridge Street Publishing*, 1999.

[*1.51*] P. Beckley, "Electrical steels", European Electrical Steels, Orb Works, 2000

[*1.52*] M. van der Veen and F. de Leon, "Measuring acoustic noise emitted by power transformers", *AES 109th Convention*, Los Angeles, September 22-25, 2000.

[*1.53*] M. J. Heathcote, "The J & P transformer book", *Twelfth Edition*, 1998.

Chapter 2 Research on Electrical Steel and Transformer Cores

2.1 Introduction

Power transformers are the most efficient and reliable apparatus in power systems. Their efficiency is extremely high, typical values being close to 98% [*2.1*]. Modern highly grain-oriented 3% silicon electrical steel, which is commonly used in power transformers, has been the main beneficial factor in increasing transformer efficiency, has low core losses and its only major disadvantage being that it has high stress sensitivity [*2.2*]. Although cores losses are low in modern transformers, there is room for considerable improvement, much of which can be brought about by obtaining a better understanding of localised flux and loss distributions in cores. Transformer designers have a range of grain-oriented electrical steels and geometry options available which have a large influence on the power loss and acoustic noise.

2.2 Development of transformer cores

The development of transformers as very efficient machines is closely linked with the development of soft magnetic materials. In 1885, when the first practical modern transformer core was built by Stanley [*2.3*] and until 1907, cores were assembled from non-silicon steel which was susceptible to aging and their iron loss could increase by 10-30% after about a year of operation [*2.4*]. As a guide, the iron loss of a single-phase, 25 kVA rating transformer cores, operating at 50 Hz was about 270 W up to 1907 [*2.4*]. With the introduction of silicon into the iron, the losses of the same size cores dropped to 185 W. Nowadays, the iron loss of a similar size core built out of conventional grain-oriented electrical steel is approximately 60-70 W [*2.4*]. The difference in iron loss becomes even larger, considering that modern transformer cores operate at significantly higher magnetic inductions than the early ones. Even at these higher inductions, 1.8 T-1.9 T, compared to about 1.1 T-1.2 T of the early transformers, recent cores exhibit significantly lower power loss per unit mass and because they are operated at such high flux densities, their size is significantly reduced. The large reduction of transformer power loss through the years has resulted from a combination of improved, transformer core design and build, the development of superior magnetic materials and an improvement in the design of copper windings [*2.4*]. Today, almost all laminated cores have mitered corners, the overlap regions exhibiting either the so-called "conventional" SSL

(single-step lap joint assembling) technique or MSL (multi-step lap joint assembling) technique [*1.44*].

Advances made in transformer core materials and their resultant products have had considerable impact on worldwide energy-savings efforts and on environmental improvement. Considering the fact that newly developing countries with huge populations are consuming electrical power at ever-increasing rates, the role of transformers in energy efficiency and reduction of worldwide CO_2 emission is becoming significant. Table 2.1 summarizes the potential energy savings and reduction of CO_2 emissions in the major regions of the world [*2.5*]. Since the original table was prepared in 2005, the numbers for some of the developing countries should be considerably higher now than those given. In the table a conversion factor of 0.6 - 0.7 kg CO_2 / kWh was used for developed countries; in developing countries where fossil fuel is the dominant energy-generating source, this factor approaches 1 kg CO_2 / kWh. Thus, CO_2 emission associated with worldwide electricity consumption is becoming increasingly problematic, which can be mitigated by installing energy-efficient transformers [*2.5*].

Country	Annual transformer loss (TWh)	Annual potential savings (TWh)	Annual CO_2 reduction (M tonne)
USA	141	84	60
EU-25	55	22	15
Japan	44	31	17
China	33	18	13
India	6	3	3
Australia	6	3	3
Total	285	161	111

Table 2.1 Potential energy savings and reduction of CO_2 emissions in different regions of the world [*2.5*]

The estimates in table 2.1 for annual transformer loss are based on the assumption that electricity is distributed with sinusoidal current / voltage, which is no longer the case as a number of non-linear loads such as variable speed motors in manufacturing plants, personal computers, telecommunication devices, etc., are being added to electricity distribution systems. These non-linear loads introduce higher harmonics into the systems, which result in increased transformer losses. Therefore, under harmonic conditions, the numbers in table 2.1 become larger than those given if conventional silicon steel-based transformers are used [*2.5*].

2.3 Grain-oriented electrical steel

Grain-oriented, 3% silicon iron is used in large quantities in transformer cores. It is produced in different grades with their qualities assessed by iron losses. By a process of rolling and

annealing, alloys of suitable composition can be produced with a metallic crystal structure in which the grains are aligned so that magnetic properties are vastly superior in the direction of rolling. The discovery by Goss, of the grain-oriented electrical steel offered a huge reduction in the transformer core losses [*2.6*]. Goss discovered that certain chemical combinations can, after undergoing rolling and heat treatment, produce a magnetic material with highly directional magnetic properties. The first commercial grain-oriented silicon iron strip was produced in 1939 by Armco Electrical Steel Pennsylvania, USA. It was 0.32 mm thick, with a specific loss around 1.5 W/kg, at 1.5 T, 50 Hz. This material utilises the fact that the iron crystal has easy directions of magnetisation along its cube edges which means that it is possible, as long as the material is magnetised along its rolling, easy direction, to achieve high levels of magnetisation at relatively low power loss and low magnetic field intensity. A disadvantage is that the superior performance when magnetised along the rolling direction is compromised when magnetised along any other direction. Since in transformers the material is magnetised mostly along its rolling direction, grain-oriented electrical steel offered an important contribution to the reduction of the iron losses.

Hadfield produced the first electrical steel in 1903 [*2.7*]. He discovered that by alloying iron with other elements such as silicon and aluminium as well as phosphorus, permeability and electrical resistance increased thereby reducing eddy-current losses and giving low hysteresis qualities. He also found that satisfactory results could be achieved by combining two or three of above elements. Adding silicon content also reduces the anisotropy and magnetostriction [*2.8*], iron containing 3% silicon has four times the resistivity of pure iron [*2.9*]. On the other hand, when the silicon content exceeds 4%, the material has the disadvantages of reduced saturation magnetisation, increased hardness and increased brittleness.

Low eddy-current loss is obtained by reducing the thickness of electrical sheets. However, in grain-oriented electrical steel a metallurgical limit is approached in terms of the stabilisation of secondary recrystallisation [*2.10*]. This condition as well as other manufacturing difficulties, such as handling tends to cause steel production costs to rise. The hysteresis loss gradually increases with reduced thickness. This effect was explained by the higher coercivity of the thin sheet and the fact that the surface layer is disturbed; with falling thickness this occupies a greater proportion of the whole steel volume [*2.11*]. Normally, grain-oriented laminations are supplied fully processed, in widths typically from 20 mm to over 900 mm, in thicknesses of about 0.23 mm, 0.27 mm, 0.30 mm and 0.35 mm [*2.12*]. Fig. 2-1 shows the

typical specific total losses of grain-oriented electrical steel, M080-23N, M089-27N, M097-30N and M111-35N, at $f = 50$ Hz [*2.13*].

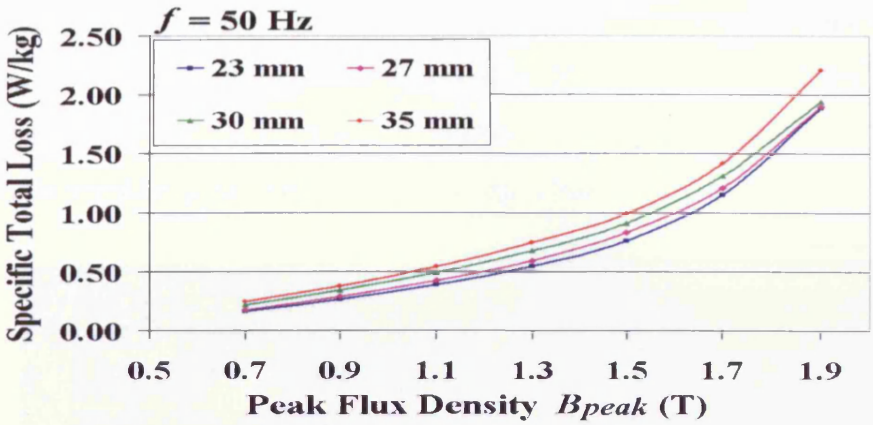

Fig. 2-1 Typical specific total losses of grain-oriented electrical steels [*2.13*]

Also, grain-oriented steels are used to build various types of strip wound toroidal cores which are largely used for applications such as audio, saturable reactors and high frequency transformers etc. Wound toroidal cores from grain-oriented steels have also been used as transformer cores in transmission lines using static converters for AC/DC links [*2.14*].

2.4 Methods of measuring magnetostriction

Several techniques have been successfully used for the measurement of magnetostriction in silicon-iron laminations. Probably the simplest method is a technique used by Neurath [*2.15*] to measure it in localised areas using displacement transducers. In 1966, the sensitivity and accuracy of the technique were improved by Brownsey [*2.16*] who measured the fundamental component of magnetostriction using a ceramic displacement transducer capable of measuring *ac* displacements in the range 10^{-4} to 10^{-8} cm. In 1968, Simmons [*2.17*] made a systematic study of the use of ceramic transducers and showed ways of avoiding errors produced by transverse or vertical vibrations. Moses [*2.18*] used displacement transducers technique to measure the dynamic fundamental and harmonic component of magnetostriction in silicon-iron lamination. Also, resistance foil and semiconductor strain gauges [*2.19*] are widely used and magnetostriction as low as 10^{-7} strain to be accurately detected [*2.20*], but this method has the disadvantages of requiring contact with the sample and high operator skill.

Piezoelectric transducers have a similar sensitivity approaching 10^{-8} strain and operate accurately over a wide frequency range. Once assembled and calibrated, piezoelectric

transducers can be used for localised or bulk measurements very quickly and conveniently. Calibration of this method is more tedious than strain gauge methods but no attachment to the surface is required [*2.20*].

A newly developed piezoelectric accelerometer measurement system has been established at Wolfson Centre for Magnetics, Cardiff University. The photograph of the measurement system is shown in fig. 2-2. Also, a typical tension/compression curve for peak magnetostriction versus applied stress is given in fig. 2-3 [*2.21*].

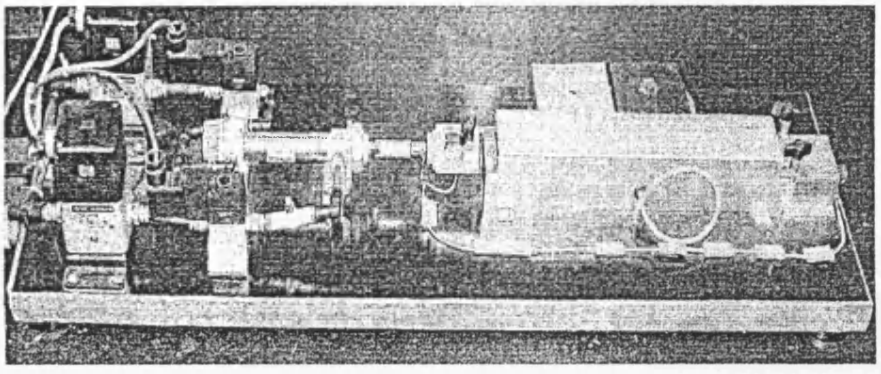

Fig. 2-2 Photograph of magnetostriction test frame stressing rig [*2.21*]

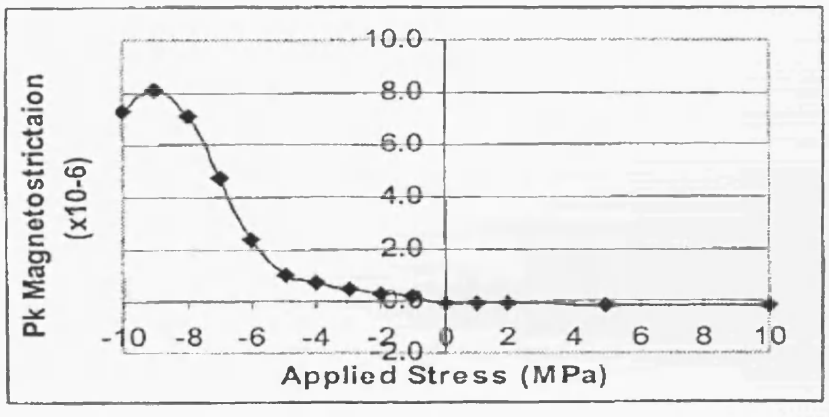

Fig. 2-3 Typical peak magnetostriction versus applied stress [*2.21*]

It is noted in fig. 2-3 that the magnetostriction is very low in non-stressed grain-oriented electrical steel. By using this measurement method, Anderson [*2.22*] found that the peak-to-peak magnetostriction λ_{pp} of the grain-oriented electrical steel in the form of Epstein strips cut at 0^0 to the rolling direction, was 0.40 $\mu\varepsilon$ under sinusoidal voltage excitation in unstressed condition, at B_{peak} = 1.5 T.

Optical method such as the laser displacement meter, laser Doppler vibrometer and laser velocimeter are used to measure magnetostriction. A non-contacting type, measurement of

wide range with high resolution and high accuracy becomes possible and little operator skill is required [*2.23*]-[*2.27*]. Fig. 2-4 shows the principle of the laser Doppler velocimeter measurement system [*2.23*].

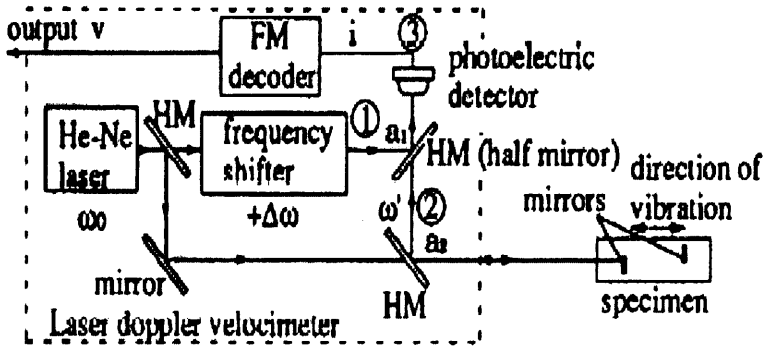

Fig. 2-4 Principle of laser Doppler velocimeter measurement system [*2.23*]

Nakata and Takahashi [*2.23*] used a laser Doppler velocimeter to measure the magnetostriction of grain-oriented silicon steel sheet with sensitivity of better than 4×10^{-8} m). Hirano et al. [*2.25*] compared a laser displacement meter and a laser vibrometer for measuring magnetostriction of grain-oriented silicon steel sheets. It was found that the overall tendencies of the magnetostriction characteristics measured by both methods have almost agreed. These optical techniques open the possibility of measuring magnetostriction in instances where it is not practical to attach strain gauges.

2.5 Magnetostriction of electrical steels

So far, extensive research about magnetostriction of grain-oriented electrical steel has been carried out over the years [*1.44*] [*2.28*]-[*2.30*]. In general, the value of magnetostriction is taken to be the peak value under *ac* conditions. Whilst this is reasonable, in many cases both the way in which the magnetostriction varies with the flux density (the well-known 'butterfly loop') and the magnitude of the 100 Hz (when magnetised at 50 Hz) fundamental component of magnetostriction is important. However, more importance in producing noise is the harmonics of magnetostriction which are far smaller in magnitude than the 100 Hz fundamental component, but very significant in the production of noise. The higher harmonics are also radiated far more efficiently than the fundamental component [*2.31*].

It has been known for many years that the magnetostriction of electrical steels is very dependent on mechanical stress and much research work has been carried out in assessing the

stress sensitivity of various materials [*2.18*] [*2.32*] [*2.33*]. Moses [*2.18*] found that the harmonics like the fundamental component of magnetostriction are stress-sensitive.

Mogi and Yabumoto [*2.24*] measured the magnetostriction of 0.35 mm thick grain-oriented silicon steel excited at 50 Hz under sinusoidal voltage excitation. Analysis of the measured magnetostriction result using FFT (Fast Fourier Transform), showed that the amplitude of the 100 Hz component gradually increased with increasing flux density up to 1.8 T and then decreased while the amplitude of the 200 Hz and 300 Hz harmonic components increased abruptly above 1.8 T. At 1.9 T, the amplitude of 200 Hz harmonic component was comparable with the fundamental 100 Hz component.

It is well known, T-joints regions of three-phase transformer cores tend to show rotational magnetisation (RM) patterns which yield distinct increases of magnetostriction. Krell and Baumgartinger [*2.30*] found for the yoke's horizontal direction, RM causing about 80% increase of total strain in the T-joints regions and 40% for the total yoke.

2.6 Magnetostrictive induced resonance of electrical steel

Phway and Moses [*2.34*], measured the magnetostriction of grain-oriented 3% silicon steel strips cut at 0^0 and 90^0 to rolling direction with dimensions 303 mm × 30 mm × 0.27 mm over a frequency range of 0.5 kHz to 8 kHz under sinusoidal voltage excitation. They inferred that a transformer core assembled from laminations of grain-oriented electrical steel about 0.30 m long of 0^0 would resonate at a magnetising frequency around 1.5 kHz .

When a sample strip is clamped at one end and magnetised, resonance occurs as a function of magnetising frequency f and velocity of magnetostrictively-induced velocity v of sound wave in the material as given in (2.1). The resonant condition occurs when the length of the sample is one quarter of the wavelength λ_{ws} of the sound [*2.34*]. Higher harmonics arise when the frequency is high enough to cause the waves to traverse the length an integer number of times. Therefore, the n^{th} harmonic of resonant frequency f_n can be obtained as a function of sample length as in (2.2) [*2.34*].

$$v = \lambda_{ws} f = \sqrt{\frac{E}{m}} \tag{2.1}$$

$$f_n = \frac{n}{4L}\sqrt{\frac{E}{m}} \tag{2.2}$$

The magnetostriction is independent of the direction of the flux density, so the fundamental component of magnetostriction caused by any flux density waveform will be double the value of the fundamental component of the frequency of the magnetizing waveform itself. Therefore, the magnetising frequency at resonance f_m is given by

$$f_m = \frac{n}{8L}\sqrt{\frac{E}{m}} \tag{2.3}$$

where E is Young's modulus measured along the longitudinal direction of the sample, m is its density, L is the sample length and n is the n^{th} harmonic order [*2.34*]. Table 2.2 shows a comparison between calculated and measured f_m of both 0^0 and 90^0 grain-oriented material. In each case, the first resonant point and its harmonics correspond with the calculated theoretical value [*2.34*]. Fig. 2-5 and fig. 2-6 show the variation in magnitude of peak-to-peak magnetostriction with magnetising frequency for 0^0 and 90^0 samples, respectively [*2.34*].

Sample	E (GPa)	m (kg/m³)	L (m)	N (harmonic number)	f_m (kHz)	
					Calculated	Measured
0° (Fig.2-5)	110	7650	0.303	1	1.56	1.70
				3	4.69	5.00
				5	7.82	7.50
90° (Fig.2-6)	193			1	2.07	2.00
				3	6.20	6.50

Table 2.2 Test sample parameters and comparison of calculated and measured resonance frequencies [*2.34*]

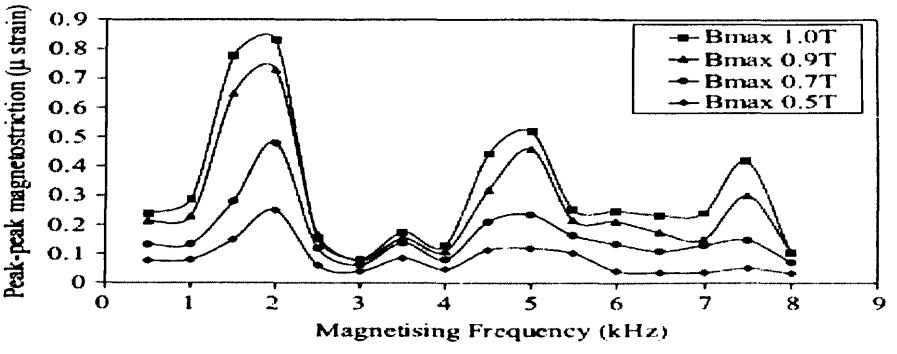

Fig. 2-5 Magnetostriction as a function of magnetising frequency of 3% Si-Fe grain-oriented 0^0 sample at B_{max} = 0.5, 0.7, 0.9 and 1.0 T [*2.34*]

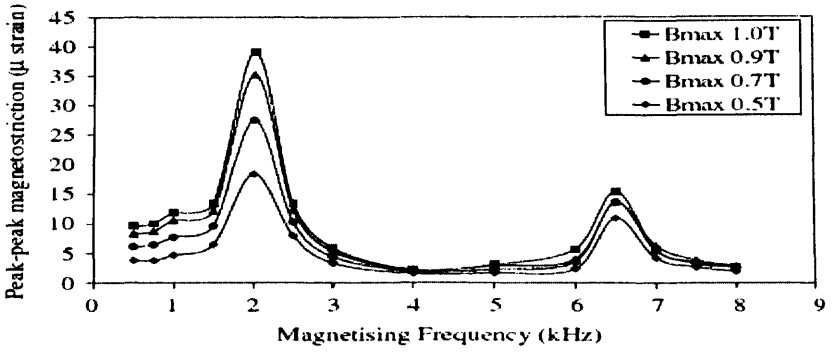

Fig. 2-6 Magnetostriction as a function of magnetising frequency of 3% Si-Fe grain-oriented 90⁰ sample at B_{max} = 0.5, 0.7, 0.9 and 1.0 T [2.34]

It was shown in fig. 2-5 that, at around 1.56 kHz, the vibration increased by a factor of around 320% due to resonance followed by an increase of 200% and 160% at 4.5 kHz and 7.5 kHz, respectively. These correspond to the mechanical resonance modes of the 0^0 grain-oriented steel under test [*2.34*]. Also, similar resonance characteristics were found in the 90^0 material where at around 2.0 kHz resonant point occurred, vibration caused by magnetostriction increased 400% and 150% at 6.5 kHz (fig. 2-6).

Fig. 2-7 shows the variation of calculated f_m in the fundamental mode of vibration with corresponding core length for 3% Si-Fe grain-oriented steel cut at 0^0 to the rolling direction. The existence of such resonance in single strips implies that similar resonance could exist in laminations of practical transformer cores. Extrapolation of the results predicts possible resonance effects in larger cores. This implies that the phenomenon can cause excessive noise in transformers operating under distorted flux conditions. Hence, it is important to understand the vibration modes of laminations in order to avoid this situation particularly in high frequency cores.

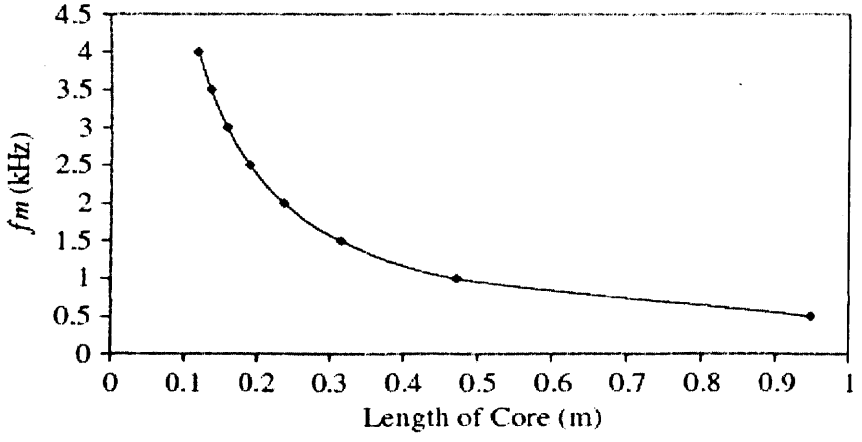

Fig. 2-7 f_m as a function of core length, l for a single-phase core assembled from 3% Si-Fe grain-oriented cut at 0^0 to its rolling direction [2.34]

2.7 Power losses of the transformer cores

It is known that the core loss is an important factor in the design of large power transformers, which depends on many factors, including quality of the material and joint designs. The basic design of transformer cores has not been changed significantly during for several decades. However, attempts to decrease losses have led to specific designs of corners and T-joint regions [*1.44*]. In these regions, the flux may deviate from the rolling direction of the steel or become distorted so that local areas of high losses are produced [*1.39*]. Almost all cores have mitred corners, the overlap regions exhibiting either the so called "conventional" SSL (fig. 2-8 (a)) or MSL (fig. 2-8 (b)) technique, where **a,** is the overlap length; **GB**, is the gap bridge and **g**, is the air gap length.

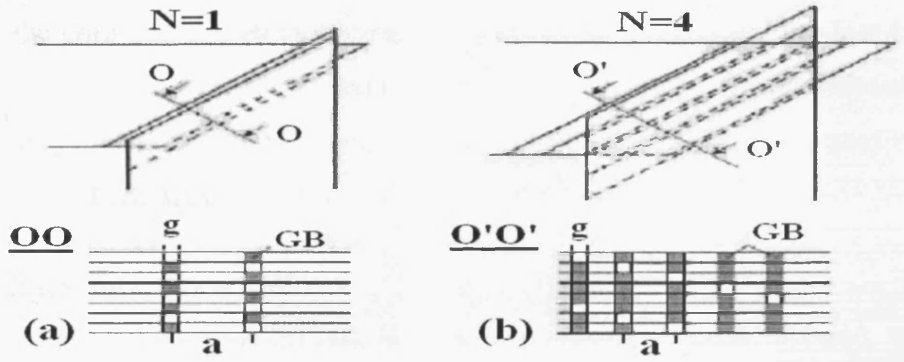

Fig. 2-8 Overlap designs in joint regions: (a) Conventional single-step lap assembling (SSL; N=1); (b) Multi-step lap assembling (MSL; N=4) [*2.1*]

Jones and Moses [*1.39*] found that the maximum localised loss was 26% higher than the mean limb loss in the butt-lap joint and 7% higher than the mean limb loss in the 45^0 mitred overlap joints. The author concluded that the reason for the higher loss in the butt-lap joints was due to a greater volume of saturated material and rotational flux [*1.39*].

Jones and Moses [*2.35*] measured total power loss of two experimental transformer cores which had been constructed with 45^0 mitred overlap joints under sinusoidal excitation. These two cores had been built such that the joint overlap lengths could be varied from 0 to 2.0 cm. The larger core was a single-phase configuration, which accommodated ten laminations per limb each of 92 cm × 15 cm × 0.033 cm; the smaller core was built from a total of 400 laminations, each of 57 cm × 11.5 cm × 0.033 cm. They found that the power loss of the larger core was minimal when the overlap was 0.5 cm, and also a minimum loss was found in the smaller core when its overlap length was 1.0 cm. In both cases, the optimum overlap length was independent of core size or flux density over the range from 1.0 T to 1.8 T. It was

found that the increase in loss for overlaps greater than the optimum was due mainly to an increase in the longitudinal flux density, whereas, for smaller overlaps, the eddy-current loss associated with the normal flux predominated, causing the overall loss to increase.

Moses reported on problems in the design of power transformers [*1.43*]. In this investigation, arrays of search coils were placed at the T-joints of a 45^0 mitred three-phase transformer core to capture and analyse the flux density distribution. The research was concentrated on the circulating flux in the core and the rotational flux present in such joints and their effects on the total core loss. It was found that the T-joints of a transformer core contain both alternating flux and rotational flux that made large contributions to the total power loss. The rotational loss was dependent on the T-joints design and was only present in that region causing localised areas of high power loss. Circulating flux on the other hand was present in the limbs and yokes of the core and causes an increase in loss of up to 20% of total loss in the cores investigated. This investigation concluded that a better design of the T-joints can significantly improve the core losses of a three-phase transformer core by eliminating part of both the circulating and rotational flux.

Basak and Moses investigated harmonic losses in a three-phase transformer core under sinusoidal voltage excitation [*2.36*]. Harmonics occur mostly in the T-joints where local regions are saturated and the flux deviates from the rolling direction [*1.38*]. The losses in the yokes and limbs of the core were calculated by adding all the components of loss, which would be produced if each harmonic was individually present in the steel. They found that in the joints themselves the flux distortion was much higher. The maximum 3^{rd} harmonic flux density component was about 0.3 T or 50% greater than the maximum in the centre limb when the core was magnetised at 1.5 T, 50 Hz. The peak values of the 5^{th} and 7^{th} harmonic components in the joints were about 0.06 T and 0.03 T respectively which were greater than those in the limbs. The experimental results showed that the loss associated with the harmonics in the yokes and limbs was 15% of the total loss, and corner loss accounted for 17% of the total [*2.36*].

Löffler and Booth investigated the relevance of step-lap joints for magnetic characteristics of transformer cores [*2.37*]. They looked at the differences between SSL and MSL core designs as well as the difference between model and full size cores. A reduction of core losses up to 5% or even 10% was reported in the case of full size MSL cores compared to the same size SSL transformer cores. The same authors having investigated SSL model cores [*2.38*] showed

that due to non-random distributions of air-gap lengths (**g**) shown in fig. 2-8 at the corner overlap regions, the flux tended to be inhomogeneous, concentrating in regions of low (**g**) thus causing localised saturation in parts of the core and at the same time high normal components of flux were generated causing in turn high localised eddy-current losses. If a high number of adjacent layers showed a distinctly decreased (**g**) in an ordered way, flux globally streamed to this region. Interlaminar flux passed through many layers and caused high planar eddy-current losses. In MSL cores this effect was less pronounced since local variations of (**g**) would not disturb the flux homogeneity of the core as much. Therefore, it was concluded in [*2.37*] that cores with MSL joints tend to have a more homogeneous flux distribution, a distinctly weaker dependence of power losses and excitation on air-gap length, as well as distinctly lower interlaminar flux, lower harmonics of induction.

Transformer iron losses can be reduced either by improving the quality of the steel or by using better building and design techniques. Today, almost all cores have mitred corners, the overlap regions exhibiting either SSL or MSL techniques. However, only limited research has been reported on non-sinusoidal excitation [*1.30*] [*2.39*] [*2.40*]

2.8 Flux density distribution in the joints of the transformer cores

Particular transformer core joint configurations might produce rotational flux, normal flux between layers of laminations, or alternating flux directed away from the rolling direction of the laminations, all of which tend to increase the core loss [*1.38*]. The flux distribution in the T-joints and corners regions of three-phase transformer cores was complicated [*1.38*]. Early evaluations of flux distribution were based on the work of Brailsford and Mazza [*1.40*] who experimentally investigated the flux distribution in a single lamination corner joint with the aid of search coils wound through small holes drilled through the material. This method was extended to stacks of laminations [*1.41*] in which harmonic components of flux were measured in three orthogonal directions in T-joints of transformer cores. This traditional technique is still successfully and extensively used even though it is time consuming and laborious and much valuable information, particularly on the distribution of harmonic flux in cores has been gathered [*1.38*] [*1.39*] [*1.41*] [*1.43*].

Search coils are placed at points of interest on various laminations in a model core, so that induced voltages proportional to orthogonal components of flux density at each point can be measured and analysed. In order to construct the search coils, care is necessary to minimise

the disturbance of the core by insertion of the search coil winding and presence of the holes, but extensive tests [*1.38*] [*1.39*] [*1.41*] [*1.42*] [*2.35*] have verified that the method gives a good indication of the flux distribution which would occur in a full size core.

Moses investigated the flux distribution in the T-joints of a transformer core with simple double overlap joints [*1.41*]. The flux density distribution was measured by an array of single turn search coils wound on individual laminations. The highest loss areas were the inner edges of the yoke and limb laminations at T-joints due to a high third harmonic flux density component. The fundamental component of flux density tended to follow the rolling direction of both yoke and limb laminations. However, some deviation of other harmonics from the rolling direction occurred [*1.41*].

Moses and Thomas [*1.38*] compared the flux distribution in the simple 45^0-90^0 T-joints (Fig. 2-9 (a)) and the slightly more complex 45^0 offset T-joint (Fig. 2-9 (b)). An array of search coils was used to measure the longitudinal, transverse and normal flux density variations in the laminations forming the T-joints. It was concluded that for the 15-cm-wide laminations used, the 45^0 offset T-joints was 10% more efficient than the 45^0-90^0 T-joints at 1.6 T. It was also found that a high third harmonic flux component circulates in the centre limb of the transformer core when either T-joints is used; this circulating third harmonic flux component is a probable reason for the centre limbs of some transformers having a higher loss than the outside limbs.

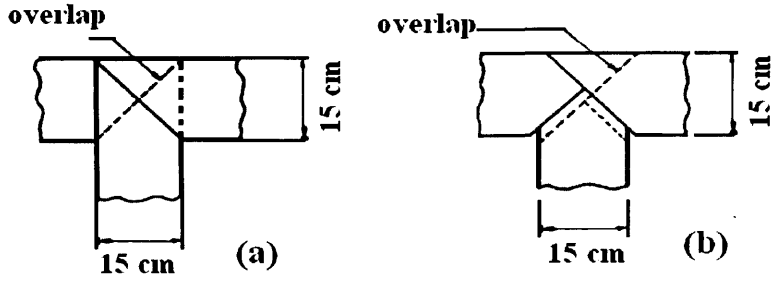

Fig. 2-9 Plan view of one layer of (a) the 45^0-90^0 T-joints and (b) the 45^0 offset T-joints [*1.38*]

Jones and Moses [*1.39*] measured localised flux distribution in two types of joints built from the same size and type of grain-oriented silicon-iron laminations, which one type was the simpler butt and lap joints (fig. 2-10 (a)) and the other one was 45^0 mitred overlap joints (fig. 2-10 (b)). It was found that there was a high normal flux in the mitred overlap joints, close to the butt gap but it dropped to 0.025 T in the overlap regions and to the interlaminar value of 0.001 T in the limbs when the overall core flux density was 1.5 T, 50 Hz. A small amount of

flux deviation from the rolling direction occurred at the overlaps, but no rotational flux was present in the joints. Some flux harmonics were found in the joints, however, nowhere were they greater than 5% of the fundamental component. It was concluded that the reason for the higher loss in the butt and lap joints was due to the presence of a greater volume of saturated material and rotational flux [*1.39*].

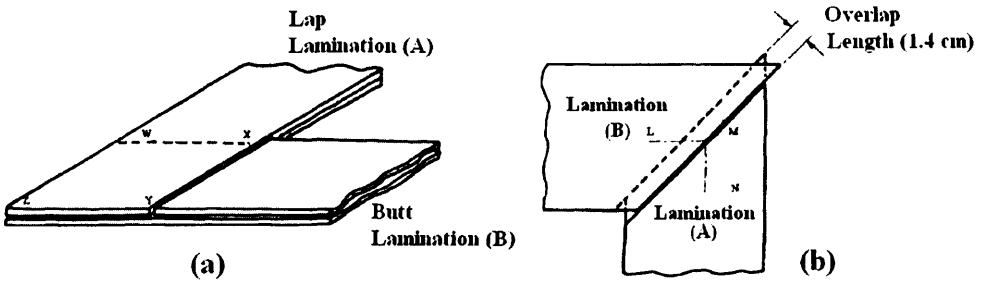

Fig. 2-10 Schematic layout of corner configuration (a) the butt and lap joints and (b) the mitred overlap joints [*1.39*]

Moses and Thomas [*1.42*] measured the rotating flux at a point in the T-joints of a three-phase, three-limb transformer core where the flux density varied both in angular velocity and magnitude. Fig. 2-11 shows the magnitude and direction of flux density at the measurement point in the T-joints of the core, where **RD** is the rolling direction. The main conclusion was that the high localised loss generated in transformer T-joints could be due to rotating fundamental and harmonics flux. An estimate of the localised loss could be made from the flux density at the measurement points [*1.42*].

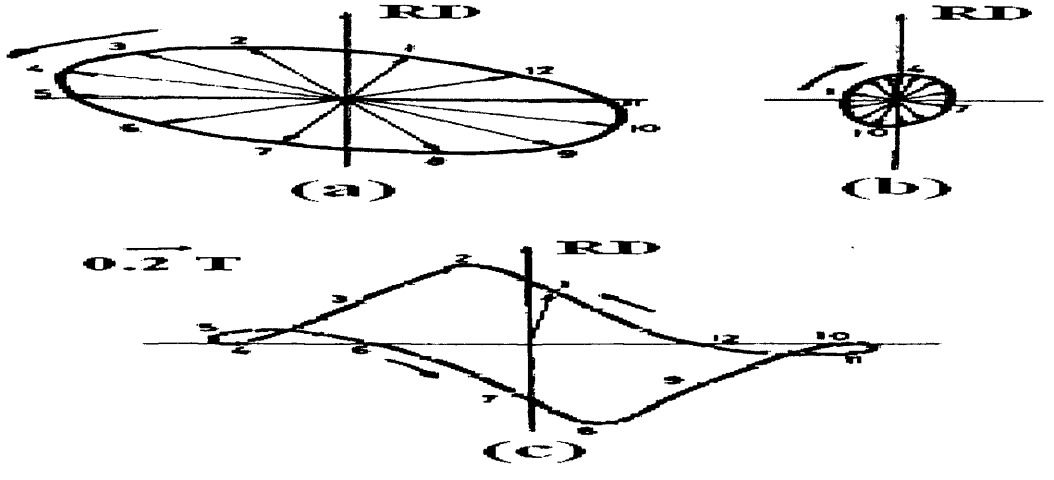

Fig. 2-11 Magnitude and direction of flux density at the measurement point in the T-joints of a three-phase transformer core. (a) 50 Hz component at 30^0 intervals relative to the flux in the right hand limb being zero. (b) 150 Hz component at 10^0 intervals relative to the flux in the right hand limb being zero. (c) Total flux magnitude at 30^0 intervals in time [*1.42*]

Megherbi and Basak [*2.41*] measured the in-plane and normal flux density of a stacked core built from amorphous magnetic material using the butt and lap joints and compared with those

obtained from a grain-oriented Si-Fe stacked core of the same dimensions. The anisotropy of amorphous material is lower than that of grain-oriented Si-Fe material so the local flux distribution was more uniform in the amorphous core. The normal flux was approximately three times larger in the amorphous core than in the grain-oriented Si-Fe core near the butt and lap joints at the corners and T-joints. This might be mainly due to the interlaminar short circuits caused by the uncoated laminations which allow flux to flow easily in the normal direction as it approaches the air gaps [*2.41*].

2.9 Acoustic noise and vibration of transformer cores

Many transformer users build special rooms to house their transformers in order to damp the noise. A high number of transformers operate below ground for the same reason. Transformer cores vibrate in a complex manner and it is difficult to relate core vibration to the longitudinal magnetostriction in any quantitative fashion. Due to inhomogenuities in the steel, the core vibrated not only in the plane of the laminations, but also perpendicular to them [*2.42*]. Core vibration can be simply measured using accelerometers placed against the core surface and the outputs analysed into their harmonic components and compared in phase with the magnetising waveform [*1.44*].

Moses and Pegler [*2.43*] found that the cores which were built in identical ways with the same grade of grain-oriented silicon steel either bolted together or bonded with the flexible adhesive, the mean vibration of the limb faces and edges is drastically reduced in the bonded core; in all cases, the higher harmonics of vibration fall more than the lower ones. They found that bonded core vibration was reduced by a factor between five and ten for a 20 kVA transformer core. The total noise output of bonded core at the same magnetising frequency was reduced by 3 *dBA* below that of a bolted core.

Weiser and Hasenzagl investigated the mechanisms of noise generation in two model transformer cores [*2.44*]. They found that in the overlap regions, which was shown an attractive interlaminar force P_z and normal displacements δ_z that were due to the normal components B_z of induction arising at overlap regions, and also, this attractive interlaminar force might yield a slight 100 Hz oscillation of the interlaminar gap length, and due to interlaminar friction, a possible source of vibration and noise [*2.44*].

Weiser and Pfützner reported on the relevance of magnetostriction and other magnetic forces on the generation of audible noise of transformer core [*1.44*]. They found that excess noise is due to both magnetostriction out of the rolling direction and magnetostatic forces acting between the sheets of the core. The magnetostatic forces include interlaminar repulsive forces between sheets due to in-plane flux, in-plane attractive forces between sheet ends and thus between limbs and yokes and interlaminar attractive forces between sheet ends in joints regions. All the above mechanism, the authors concluded, were enhanced by in-plane air-gaps which increase the transformer core noise.

Snell and Jenkins measured the acoustic noise associated with model step overlap (2, 4, 6 mm) transformer cores and found that 5 or 7 step lap cores with 4 mm or 6 mm step overlap tend to give a better noise performance than 3 step lap cores. Fig. 2-12 shows the measurement points of the noise for the model core and table 2.3 presents the noise results at investigated points, where the background noise during measurements was 30.4 ± 3 *dBA* [*2.21*].

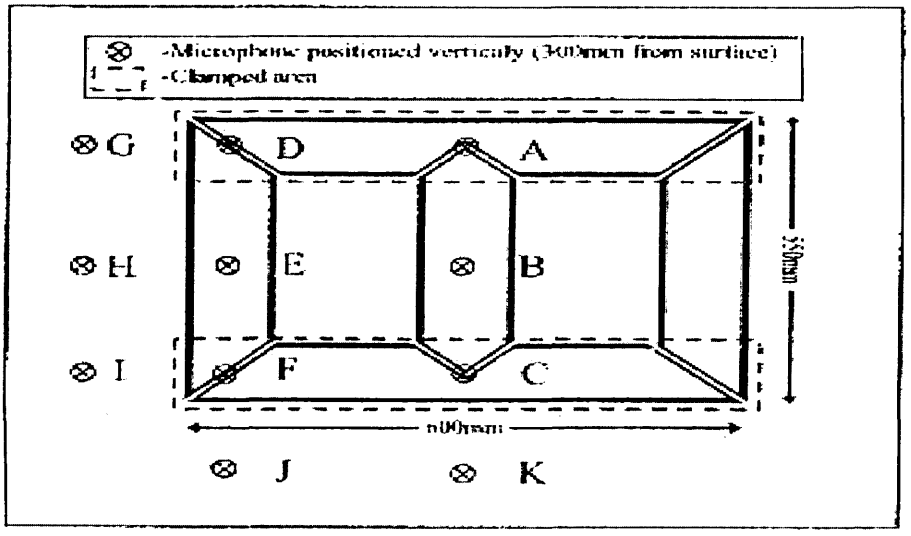

Fig. 2-12 Dimension and measurement points of model transformer core [*2.21*]

Reference		LAeq (dBA) at Various Core Locations (5 Steps, 6mm Overlap)					
		A	B	C	D	E	F
1.5T	B1	49.5	49.6	47.6	46.7	48.3	49.1
	B2	50.9	48.8	49.4	47.3	45.4	46.0
	B3	49.3	48.2	47.1	49.5	48.4	47.2
1.7T	B1	55.0	59.6	55.8	55.1	56.0	55.0
	B2	57.5	58.1	59.1	55.1	55.2	52.4
	B3	59.0	59.1	58.8	57.3	55.8	53.8
1.75T	B1	57.0	63.2	59.8	58.2	59.1	57.7
	B2	60.0	62.0	62.6	58.1	58.4	56.3
	B3	62.6	64.1	63.4	59.9	58.5	56.1

Table 2.3 Noise at investigated points of the model transformer core [*2.21*]

References to Chapter 2:

[2.1] A. Ilo, "Behaviour of transformer cores with multistep-lap joints", *IEEE Power Engineering Review*, pp. 43-47, March 2002.

[2.2] J. E. Thompson, "A review of some interdisciplinary work on grain oriented silicon iron and its use in larger power transformer", *J. Matl. Sci.*, vol. 2, pp. 395, 1967.

[2.3] W. Stanley, "Induction coil", United States Patent Office, Patent No. 349,611, September 21, 1886.

[2.4] P. Marketos, "Construction of transformer cores using consolidated stacks of electrical steel", Ph.D. Thesis, Cardiff University, April 2002.

[2.5] R. Hasegawa and D. Azuma, "Impacts of amorphous metal-based transformers on energy efficiency and environment", *JMMM*, 320 (2008) 2451-2456.

[2.6] N. P. Goss, "Electrical sheet and method and apparatus for its manufacture and test", United States Patent Office, Patent No. 1,965,559, July 1934.

[2.7] R. A. Hadfield, "Magnetic composition and method of making same", United States Patent Office, Robert, Patent No. 745,829, December 1, 1903.

[2.8] R. H. Pry and C. P. Bean, "Calculation of the energy loss in magnetic sheet materials using a domain model", *Journal of Applied Physics*, 29, 532, 1958.

[2.9] D. Jiles, "Introduction to magnetism and magnetic materials", Chapman and Hall, London, 1996.

[2.10] H. Matsuoka and O. Honjo, "Current status and future prospects for electrical steels", ASM Soft and Hard Magn. Mat. with Apps. Symp., Lake Buena Vista, Florida, 1986.

[2.11] C. Heck, "Magnetic materials and their applications", Butterworths, London, pp. 335-336, 1974.

[2.12] Hamdi, "Design of small electrical machine", Wiley, New York, 1994.

[2.13] Cogent Power, "Grain-oriented fully-processed steel", November 2002.

[2.14] M. Namikawa, H. Ninomiya and Y. Tanaka, "Magnetic properties of 6.5% silicon steel sheets under PWM voltage excitation", *IEEE Trans. on Mag.*, vol. 34, no. 4, pp. 1183-1185, July 1998.

[2.15] P. W. Neurath, "Magnetostriction and domain structure of materials for use in low noise equipment", *Electrical Engineering*, pp. 991-994, November 1954.

[2.16] C. M. Brownsey and G. C. Maples, "Magnetostriction characteristics of 3.1% grain-oriented silicon-iron transformer steel", *Proc. IEEE*, 113 (11), pp. 1859-1862, 1966.

[2.17] G. H. Simmons and J. E. Thompson, "Magnetic properties of grain-oriented silicon-iron. Part 1 – use of ceramic displacement transducers for the measurement of magnetostriction", *Proc. IEEE*, 115 (12), pp. 1835-1839, 1968.

[2.18] A. J. Moses, "Measurement of magnetostriction and vibration with regard to transformer noise", *IEEE Trans. on Mag.*, vol. MAG-10, no. 2, pp. 154-156, June 1974.

[2.19] M. Enokizono, S. Kanao and G. Shirakawa, "Measurement of arbitrary dynamic magnetostriction under alternating and rotating field", *IEEE Trans. on Mag.*, vol. 31, no. 6, pp. 3409-3411, November 1995.

[2.20] A. J. Moses, "Recent advances in experimental methods for the investigation of silicon iron", Physica Scripta, vol. T24, pp. 49-53, 1988.

[2.21] D. Snell and M. K. Jenkins, "Aspects of noise associated with GO electrical steels in transformer applications", one day seminar, 4 February 2009, Wolfson Centre for Magnetics, Cardiff University.

[2.22] P. Anderson, "A novel method of measurement and characterization of magnetostriction in electrical steels", *PhD Thesis*, Cardiff University, 2000.

[2.23] T. Nakata, N. Takahashi, M. Nakano, K. Muramatsu and M. Miyake, "Magnetostriction measurements with a laser Doppler velocimeter", *IEEE Trans. on Mag.*, vol. 30, no. 6, pp. 4563-4565, November 1994.

[2.24] H. Mogi, M. Yabumoto, M. Mizokami and Y. Okazaki, "Harmonic analysis of ac magnetostriction measurements under non-sinusoidal excitation", *IEEE Trans. on Mag.*, vol. 32, no. 5, pp. 4911-4913, September 1996.

[2.25] M. Hirano, Y. Ishihara, K. Harada and T. Todaka, "A study on measurement of magnetostriction of silicon steel sheet by laser displacement meter", *JMMM*, 254-255 (2003) 43-46.

[2.26] T. Nakase, M. Nakano and K. Fujiwara, "Measuring system for magnetostriction of silicon steel sheet under ac excitation using optical methods", *IEEE Trans. on Mag.*, vol. 34, no. 4, pp. 2072-2074, July 1998.

[2.27] T. P. P. Phway, A. J. Moses and D. C. Jiles, "Frequency dependence of magnetostriction for magnetic actuators", *Journal of Electrical Engineering*, vol. 55, no. 10/S, pp. 7-10, 2004.

[2.28] T. Sasaki, S. Takada, F. Ishibashi, I. Suzuki, S. Noda and M. Imamura, "Magnetostrictive vibration of electrical steel sheets under a non-sinusoidal

magnetising condition", *IEEE Trans. on Mag.*, vol. MAG-23, no. 5, pp. 3077-3079, September 1987.

[*2.29*] A. Hasenzagl, B. Weiser and H. Pfützner, "Magnetostriction of 3% SiFe for 2-D magnetization patterns", *JMMM*, 160 (1996) 55-56.

[*2.30*] C. Krell, N. Baumgartinger, G. Krismanic, E. Leiss and H. Pfützner, "Relevance of multidirectional magnetostriction for the noise generation of transformer cores", *JMMM*, 215-216 (2000) 634-636.

[*2.31*] J. E. Thompson and J. T. Wilkins, "Harmonics in transformer noise", *Electrical Times*, pp. 725-727, November 1963.

[*2.32*] C. Holt and J. A. Robey, "The ac magnetostriction of 3.25-percent grain oriented silicon-iron under combined longitudinal and normal compressive stress", *IEEE Trans. on Mag.*, vol. MAG-5, no. 3, pp. 384-388, September 1969.

[*2.33*] A. J. Moses, "Effects of applied stress on the magnetic properties of high permeability silicon-iron", *IEEE Trans. on Mag.*, vol. MAG-15, no. 6, pp. 1575-1579, November 1979.

[*2.34*] T. P. P. Phway and A. J. Moses, "Magnetisation-induced mechanical resonance in electrical steels", *JMMM*, 316 (2007) 468-471.

[*2.35*] M. A. Jones, A. J. Moses and J. E. Thompson, "Flux distribution and power loss in the mitred overlap joint in power transformer cores", *IEEE Trans. on Mag.*, vol. MAG-9, no. 2, pp. 114-122, June 1973.

[*2.36*] A. Basak and A. J. Moses, "Harmonic losses in a three phase transformer core", *IEEE Trans. on Mag.*, vol. MAG-14, no. 5, pp. 990-992, September 1978.

[*2.37*] F. Löffler, T. Booth, H. Pfützner, C. Bengtsson and K. Gramm, "Relevance of step-lap joints for magnetic characteristics of transformer cores", *IEE Proc. Electr. Power Appl.*, vol. 142, no. 6, pp. 371-378, November 1995.

[*2.38*] F. Löffler, H. Pfützner and T. Booth, "Influence of air gaps in stacked transformer cores consisting of several packages", *IEEE Trans. on Mag.*, vol. 30, no. 2, pp. 913-915, March 1994.

[*2.39*] G. F. Mechler and R. S. Girgis, "Magnetic flux distributions in transformer core joints", *IEEE Transactions on Power Delivery*, vol. 15, no.1, pp. 198-203, January 2000.

[*2.40*] H. Akcay and D. G. Ece, "Modeling of hysteresis and power losses in transformer laminations", *IEEE Transactions on Power Delivery*, vol. 18, no.2, pp. 487-492, April 2003.

[2.41] M. L. Megherbi and A. Basak, "Magnetic characteristics of sandwich-transformer cores built with Si-Fe and amorphous materials", *IEEE Trans. on Mag.*, vol. 25, no. 5, pp. 3336-3338, September 1989.

[2.42] A. T. Thoeng, "The lamination of transformer noise annoyance", Holectechnik 1 (1971), pp. 20-29.

[2.43] A. J. Moses and S. M. Pegler, "The effects of flexible bonding of laminations in a transformer core", *Journal of Sound and Vibration*, vol. 29 (1), pp. 103-112, 1973.

[2.44] B. Weiser, A. Hasenzagl, T. Booth and H. Pfützner, "Mechanisms of noise generation of model transformer cores", *JMMM*, 160 (1996) 207-209.

Chapter 3 Measurement and Analysis of Magnetostriction and Mechanical Resonance in Grain-Oriented Electrical Steel Induced by Magnetostriction under Sinusoidal and PWM Voltage Excitation

3.1 Introduction

Apart from magnetic forces [*3.1*], transformer core noise is due to magnetostrictive core vibration [*2.18*] [*2.25*]. The magnetostriction of grain-oriented electrical steel measured under non-sinusoidal voltage excitation is limited [*2.24*] [*2.28*]. Moreover, magnetostriction-induced mechanical resonance of grain-oriented and non-oriented electrical steel in the form of Epstein strips under sinusoidal and PWM voltage excitation at different magnetising frequency, different modulation index and different switching frequency has been recently studied [*2.34*] [*3.2*]. At resonance, displacement due to magnetostriction is maximal and this contributes towards the acoustic noise emission of transformer cores. In the case of PWM inverter-fed transformer cores, the distorted flux density waveform contains high-frequency harmonic components that might cause magnetostrictive resonance.

In this chapter, the measurement of magnetostriction of grain-oriented electrical steel in the form of Epstein strips under sinusoidal and PWM voltage excitation for assigned values of modulation index m_a with different switching frequency f_s, using single-point laser vibrometer (SPLV) has been carried out. The comparison of magnetostriction between sinusoidal and PWM voltage excitation, and analysis of the correlations between switching frequency f_s and the frequency spectrum of the sample vibration due to magnetostriction are included.

3.2 Experimental setup

The measurement system comprises a SPLV and a single strip tester [*3.3*], where the laser head and measured object were placed in the 3.3 m × 2.1 m × 2.1 m anechoic chamber (fig. 3-1), and the magnetising system was placed outside the chamber to ensure that interference from the equipment did not affect the measurement results (fig. 3-2). Also, safety is one of the reasons to do experiment in that room because of using laser beam.

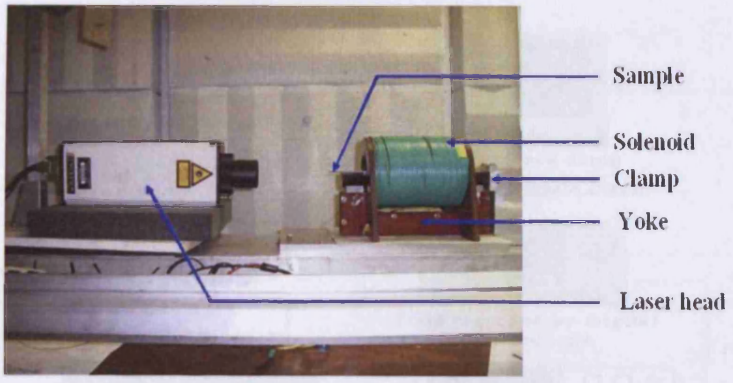

Fig. 3-1 Laser head, single strip tester with sample located in the anechoic chamber [*3.3*]

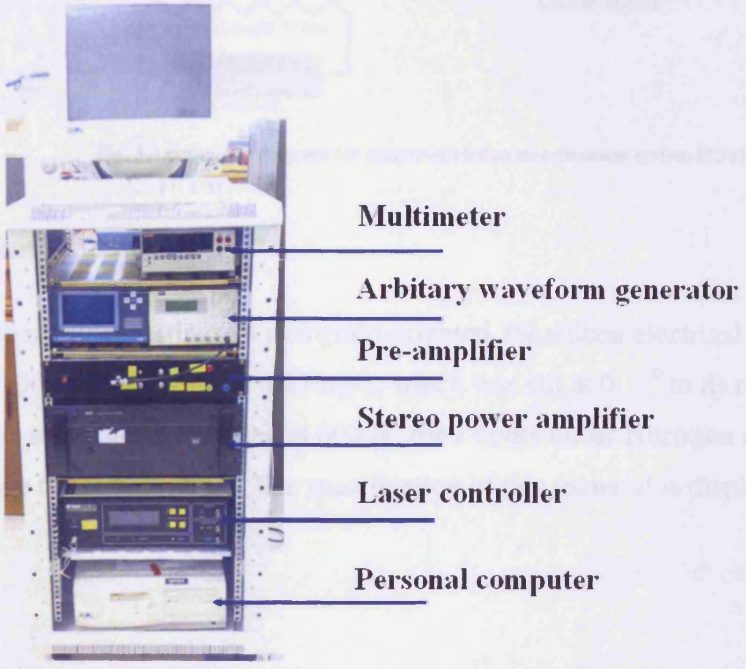

Fig. 3-2 Magnetising system and laser controller located outside the anechoic chamber [*3.3*]

The schematic connection of the magnetostriction measurement system is shown in fig. 3-3. It comprises discrete instruments that ma kes it very flexible, g iving a wide mag netising frequency range and access to arbitrary excitation waveforms [*3.4*].

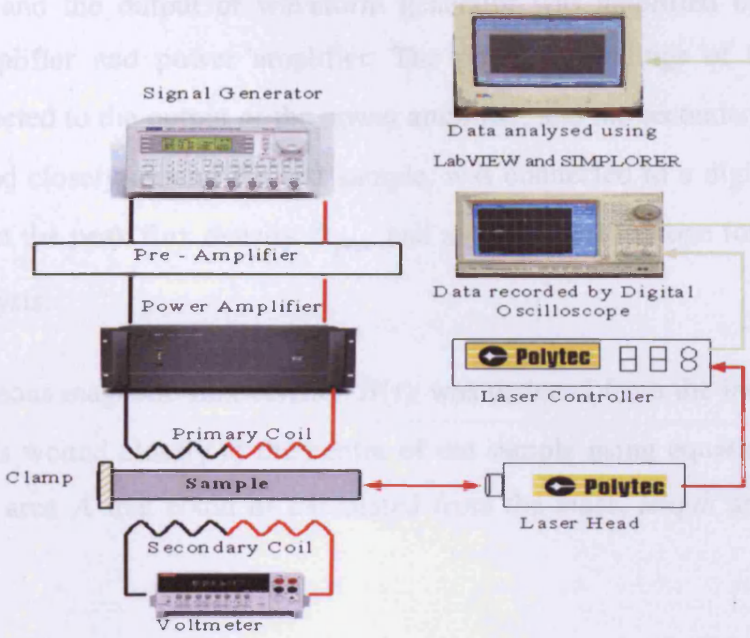

Fig. 3-3 Schematic diagram for magnetostriction measurement system [*2.34*]

3.3 Measurement procedure

The sample used in this investigation was grain-oriented 3% silicon electrical steel in the form of Epstein strip (303 mm × 30 mm × 0.27 mm), which was cut at 0 ^{0} to its rolling direction. After cutting, the sample was annealed at 800 [℃ for 2 hours under Nitrogen atmosphere [*3.5*] in order to relieve the cutting stress. The specification of this material is displayed in table 3.1 [*2.13*].

Steel type	Thickness d (mm)	Resistivity (m)	Conductivity ($^{-1}$m^{-1})	Conventional density (kg/m^3)
Grain-oriented 3% silicon electrical steel	0.27	0.46	2.17×10^6	7650

Table 3.1 Specification of the material [*2.13*]

It is shown in fig. 3-3, a 30 MHz arbitrary waveform generator (TGA1230) was used for *ac* signal generation, and the output of waveform generator was amplified by two cascaded amplifiers, pre-amplifier and power amplifier. The primary windings of the magnetising solenoid was connected to the output of the power amplifier, and the secondary windings (N_2 = 10), which wound closely around the test sample, was connected to a digital voltmeter, to use its $e.m.f$ to set the peak flux density B_{peak} and a digital oscilloscope for waveform data collection and analysis.

Also, the instantaneous magnetic flux density $B(t)$ was deduced from the induced voltage of secondary windings wound closely at the centre of the sample using equation (1.10), where the cross sectional area A that could be calculated from the *mass*, *length* and *density* of the test sample from

$$A = \frac{mass}{length \times density} \tag{3.1}$$

One end of the test strip was clamped and the instantaneous longitudinal displacement of the other end was measured using the SPLV. Then the instantaneous magnetostriction λ was calculated as the ratio of the instantaneous displacement to the magnetic path length L_p by:

$$\lambda = \frac{\delta L}{L} = \frac{displacement \times displacement.range}{L_p} \tag{3.2}$$

where L_p is 0.21 m [*3.3*], and the *displacement.range* is the output ratio from the laser controller (fig. 3-2), which is 0.5 um/V [*3.6*]. Fig. 3-4 shows the output signal of magnetostriction.

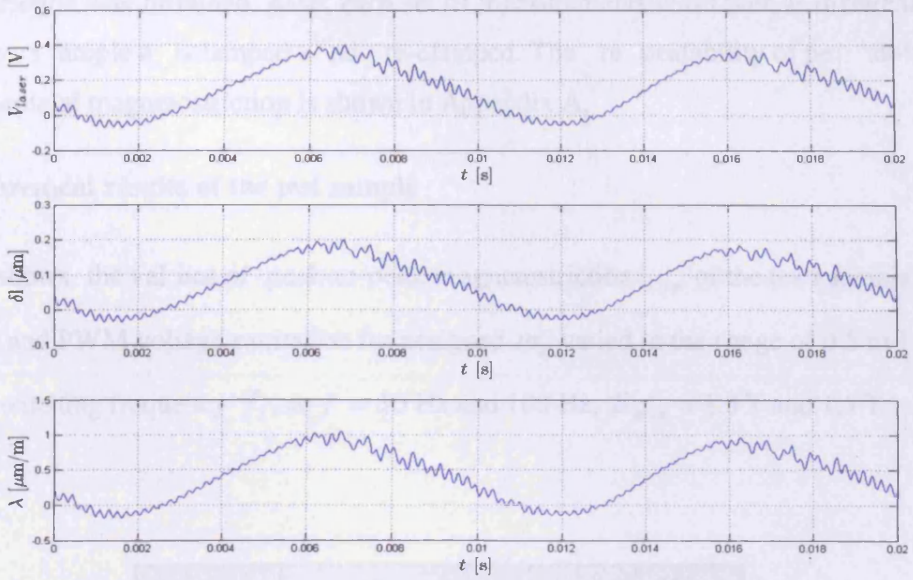

Fig. 3-4 Output signal of magnetostriction measurement

The SPLV (Polytec OFV-3001/303) is a wide range, high resolution, non-contact vibration measurement vibrometer, which directly measure velocity or displacement to a resolution of ± 0.002 μm within the frequency range of 0 – 20 kHz [*3.6*], and also, the resolution of magnetostriction measurement could be access to as low as around ± 0.01 μ . Also, the reliability of this system (fig. 3-3) and the accuracy of the measurement results were already confirmed, which the peak-to-peak magnetostriction values have uncertainty of 3.5% for five repeated measurements [*2.34*].

The test strip was magnetised under sinusoidal and PWM voltage excitation for assigned values of m_a in the range 0.5 to 1.2 with f_s varied in the range of 0.75 kHz to 2.75 kHz, at f = 50 Hz and 100 Hz, B_{peak} = 1.3 T and 1.5 T. The displacement output signal from the SPLV and the value of secondary induced voltage were recorded using a high resolution digital oscilloscope (YOKOGAWA DL716 - 16CH Digital Scope), which has plug-in high voltage isolation modules that display and save data in 16 - bit resolution at 16 MS/s (sampling rate) [*3.7*]. Algorithms embedded in "National Instrument LabVIEW" and "Ansoft Simplorer Simulation Centre 7.0" PC based support software were used for data processing and analysis.

Each measurement was carried out five times and then the average peak-to-peak value of magnetostriction was obtained. Also, each set of measurements was taken at different times having the sample unclamped and re-clamped. The repeatability of peak-to-peak measurements of magnetostriction is shown in Appendix A.

3.4 Measurement results of the test sample

Table 3.2 shows the values of peak-to-peak magnetostriction $_{pp}$ of the test sample under sinusoidal and PWM voltage excitation for assigned m_a varied in the range of 0.5 to 1.2 with different switching frequency f_s, at f = 50 Hz and 100 Hz, B_{peak} = 1.3 T and 1.5 T.

Magnetisation frequency (f)	Modulation index (m_a)	Switching frequency (f_s) (kHz)	Peak-to-peak magnetostriction $_{pp}$ (□□)	
			1.3 T	1.5 T
sine 50 Hz	--	--	0.21	0.45
PWM 50 Hz	0.5	0.75	0.36	0.64
	0.8	0.75	0.32	0.61
	0.8	2.75	0.27	0.56
	1.0	0.75	0.29	0.58
	1.2	0.75	0.26	0.55
PWM 100 Hz	0.8	1.50	0.61	0.88

Table 3.2 Peak-to-peak $_{pp}$ under sinusoidal and PWM voltage excitation for assigned m_a with f_s, at f = 50 Hz and 100 Hz, B_{peak} = 1.3 T and 1.5 T

Fig. 3-5 to 3-11 show the butterfly loops of magnetostriction of test sample under sinusoidal and PWM voltage excitation for assigned values of m_a varied in the range of 0.5 to 1.2 with different f_s, at f = 50 Hz and 100 Hz, B_{peak} = 1.3 T. Also, in each butterfly loop graph, 1000 data points were recorded.

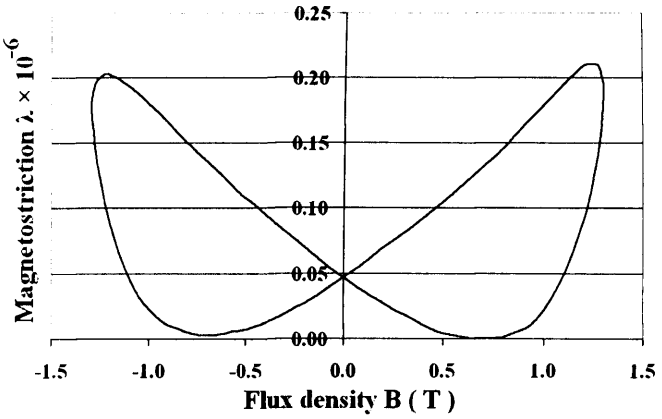

Fig. 3-5 Butterfly loops of magnetostriction λ under sinusoidal voltage excitation, f = 50 Hz, B_{peak} = 1.3 T

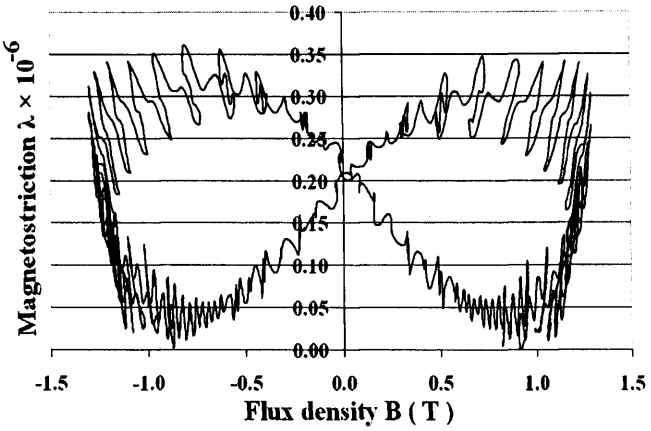

Fig. 3-6 Butterfly loops of magnetostriction λ under PWM voltage excitation, m_a = 0.5, f = 50 Hz, f_s = 0.75 kHz, B_{peak} = 1.3 T

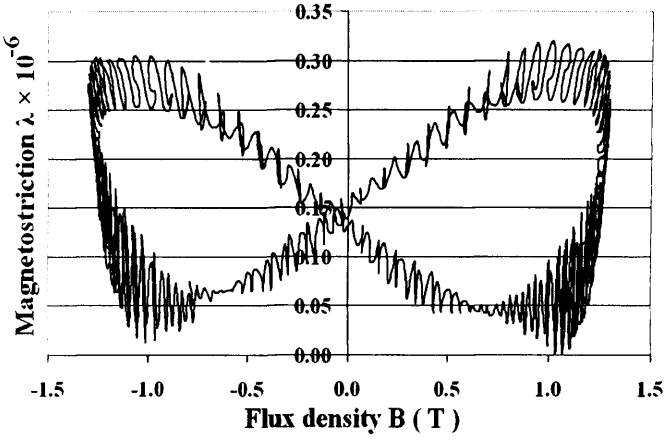

Fig. 3-7 Butterfly loops of magnetostriction λ under PWM voltage excitation, m_a = 0.8, f = 50 Hz, f_s = 0.75 kHz, B_{peak} = 1.3 T

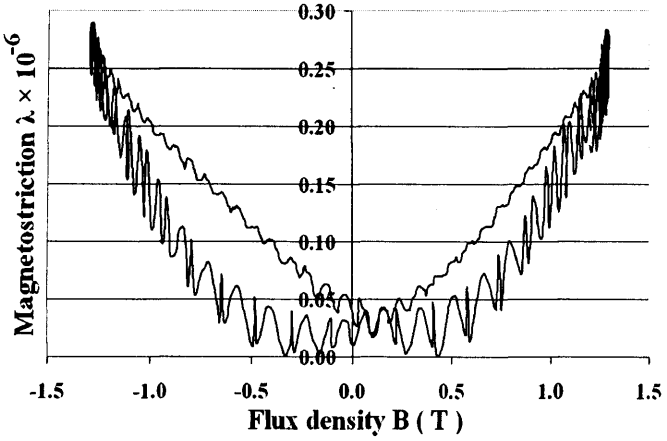

Fig. 3-8 Butterfly loops of magnetostriction λ under PWM voltage excitation, m_a = 1.0, f = 50 Hz, f_s = 0.75 kHz, B_{peak} = 1.3 T

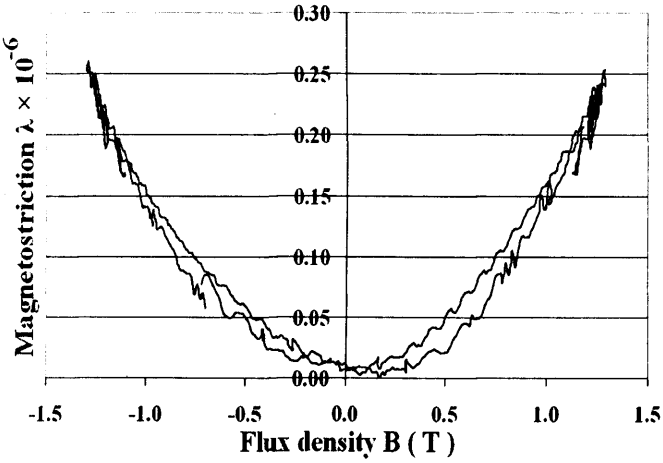

Fig. 3-9 Butterfly loops of magnetostriction λ under PWM voltage excitation, m_a = 1.2, f = 50 Hz, f_s = 0.75 kHz, B_{peak} = 1.3 T

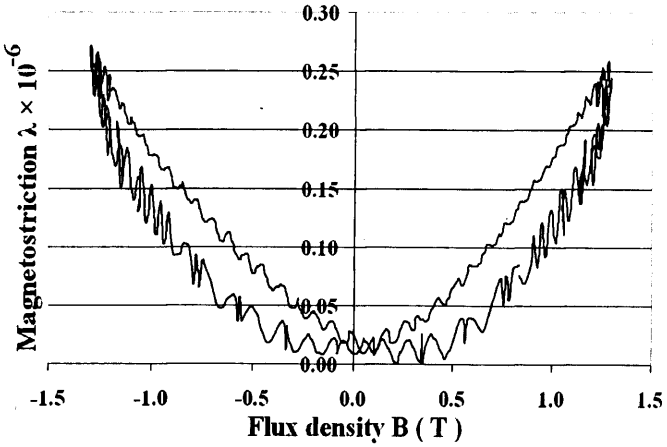

Fig. 3-10 Butterfly loops of magnetostriction λ under PWM voltage excitation, m_a = 0.8, f = 50 Hz, f_s = 2.75 kHz, B_{peak} = 1.3 T

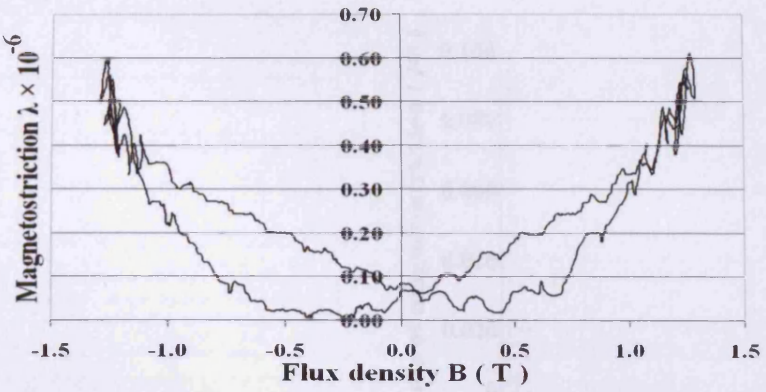

Fig. 3-11 Butterfly loops of magnetostriction under PWM voltage excitation, m_a = 0.8, f = 100 Hz, f_s = 1.5 kHz, B_{peak} = 1.3 T

The Total Harmonic Distortion (THD [%]), which is defined by (3.3), of under sinusoidal and PWM voltage excitation for assigned m_a varied with different f_s that were calculated using Fast Fourier Transform (FFT) analysis, performed with "Day Post Processor" in the "Ansoft Simplorer Simulation" environment, are shown in table 3.3.

$$THD[\%] = \frac{\sqrt{v_2^2 + v_3^2 + v_4^2 + \quad + v_n^2}}{v_1} \times 100 \tag{3.3}$$

where v_1 is the amplitude of the fundamental component; v_2 , v_3 ... v_n are the amplitude of the harmonic component of order 2, 3... n, respectively.

Magnetisation Frequency (f)	Modulation Index (m_a)	Switching frequency (f_s) (kHz)	THD [%] of	
			1.3 T	1.5 T
sine 50 Hz	--	--	7.5	11.4
PWM 50 Hz	0.5	0.75	20.7	23.6
	0.8	0.75	19.4	21.7
	0.8	2.75	15.6	17.9
	1.0	0.75	17.4	19.8
	1.2	0.75	16.2	18.7
PWM 100 Hz	0.8	1.50	17.7	21.3

Table 3.3 Variation THD [%] of magnetostriction under sinusoidal and PWM voltage excitation for assigned m_a varied with f_s, B_{peak} = 1.3 T and 1.5 T, f = 50 Hz and 100 Hz

Figs. 3-12 to 3-31 show corresponding frequency spectra of applied flux density $B(t)$ and , which were also obtained by using FFT.

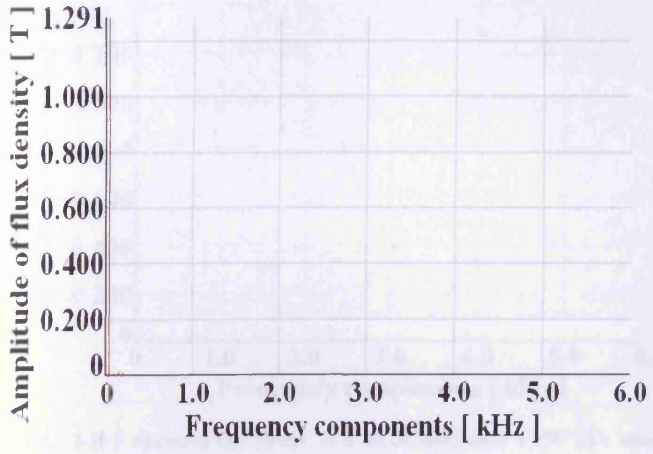

Fig. 3-12 Frequency spectrum of flux density under sinusoidal voltage excitation, f = 50 Hz, B_{peak} = 1.3 T

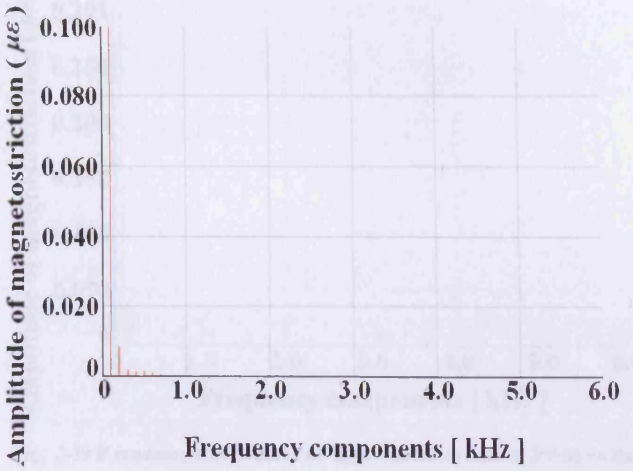

Fig. 3-13 Frequency spectrum of magnetostriction under sinusoidal voltage excitation, f = 50 Hz, B_{peak} = 1.3 T

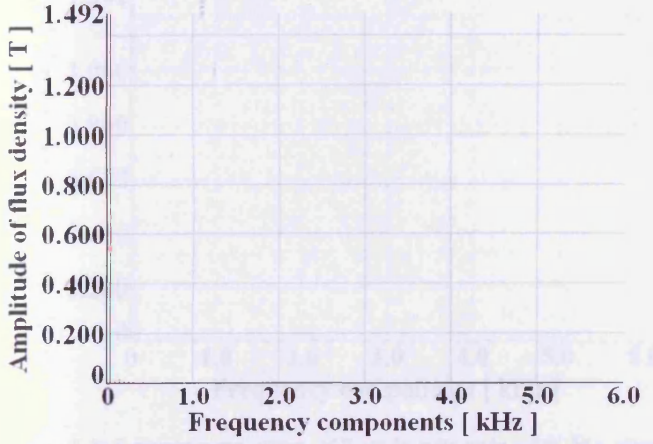

Fig. 3-14 Frequency spectrum of flux density under sinusoidal voltage excitation, f = 50 Hz, B_{peak} = 1.5 T

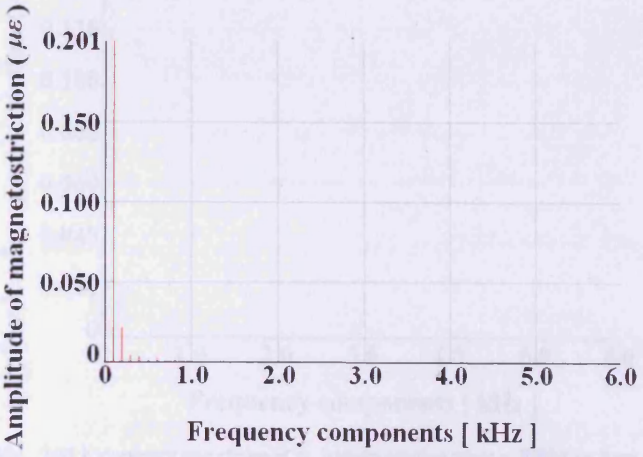

Fig. 3-15 Frequency spectrum of magnetostriction under sinusoidal voltage excitation, f = 50 Hz, B_{peak} = 1.5 T

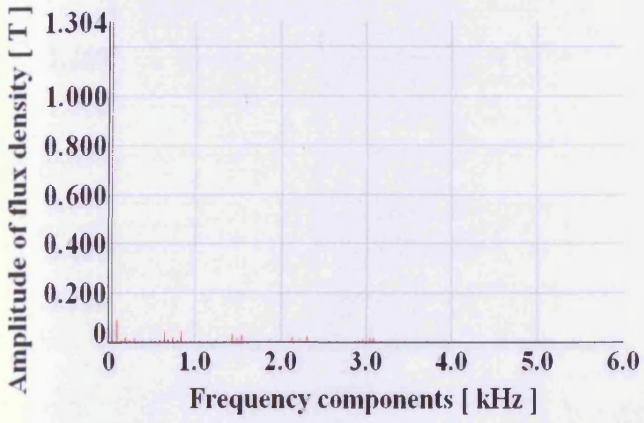

Fig. 3-16 Frequency spectrum of flux density under PWM voltage excitation, f = 50 Hz, m_a = 0.5, f_s = 0.75 kHz, B_{peak} = 1.3 T

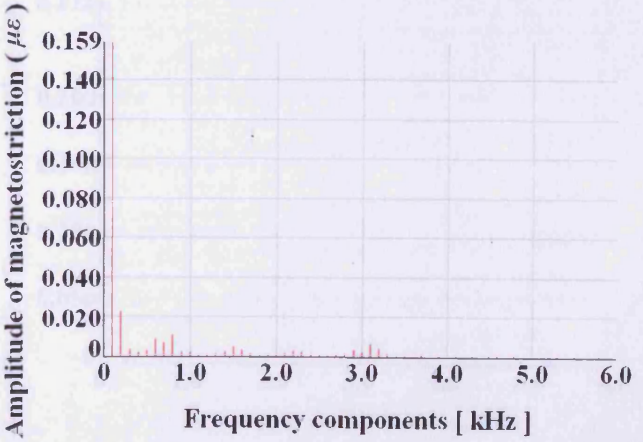

Fig. 3-17 Frequency spectrum of magnetostriction under PWM voltage excitation, f = 50 Hz, m_a = 0.5, f_s = 0.75 kHz, B_{peak} = 1.3 T

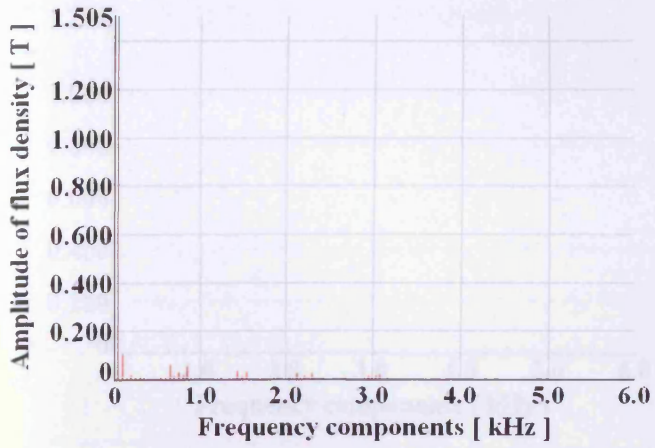

Fig. 3-18 Frequency spectrum of flux density under PWM voltage excitation, f = 50 Hz, m_a = 0.5, f_s = 0.75 kHz, B_{peak} = 1.5 T

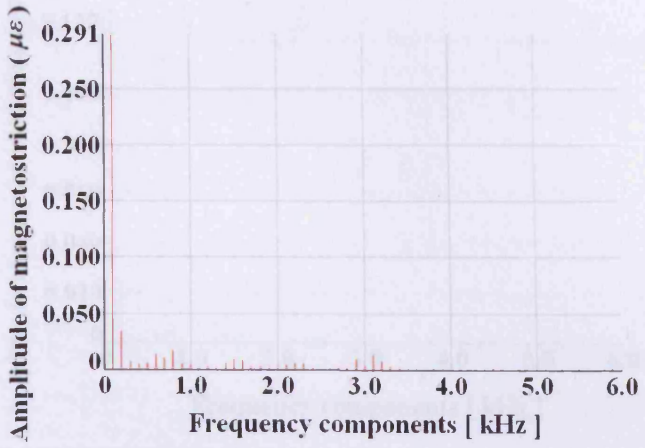

Fig. 3-19 Frequency spectrum of magnetostriction under PWM voltage excitation, f = 50 Hz, m_a = 0.5, f_s = 0.75 kHz, B_{peak} = 1.5 T

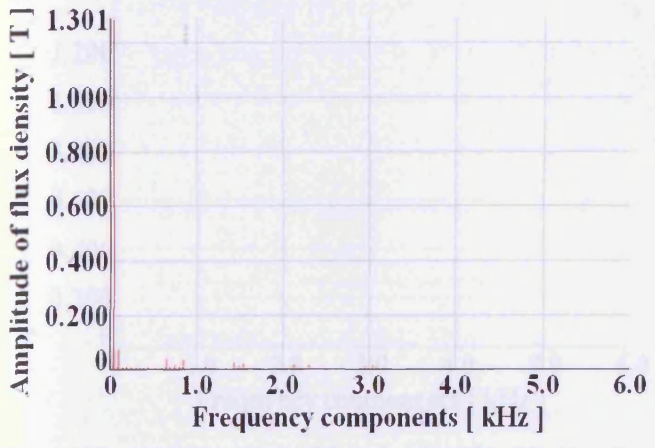

Fig. 3-20 Frequency spectrum of flux density under PWM voltage excitation, f = 50 Hz, m_a = 0.8, f_s = 0.75 kHz, B_{peak} = 1.3 T

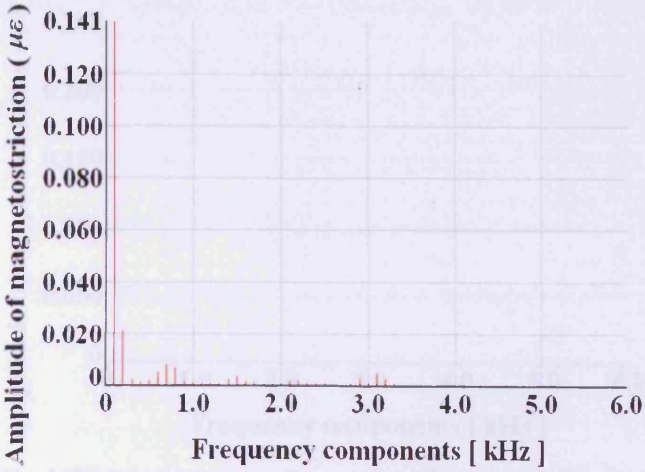

Fig. 3-21 Frequency spectrum of magnetostriction under PWM voltage excitation, f = 50 Hz, m_a = 0.8, f_s = 0.75 kHz, B_{peak} = 1.3 T

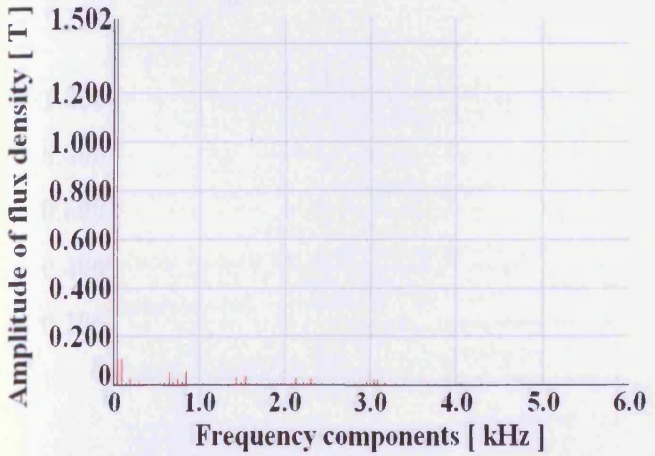

Fig. 3-22 Frequency spectrum of flux density under PWM voltage excitation, f = 50 Hz, m_a = 0.8, f_s = 0.75 kHz, B_{peak} = 1.5 T

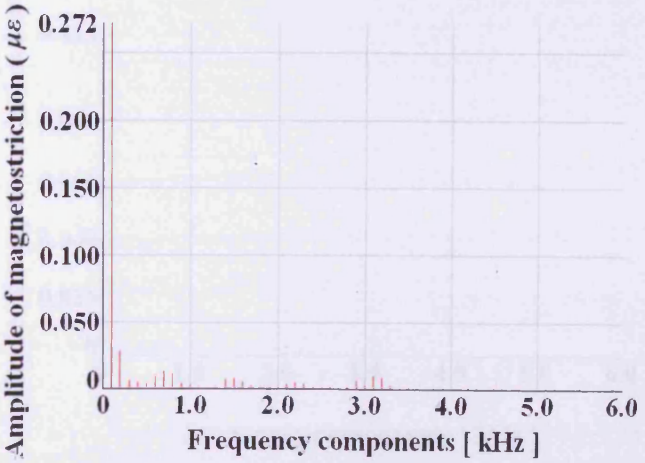

Fig. 3-23 Frequency spectrum of magnetostriction under PWM voltage excitation, f = 50 Hz, m_a = 0.8, f_s = 0.75 kHz, B_{peak} = 1.5 T

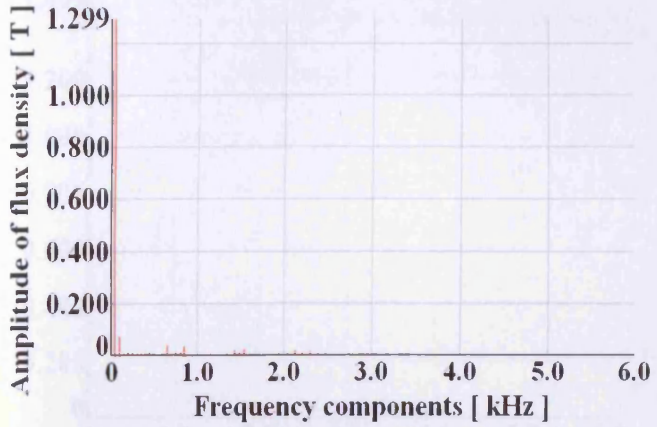

Fig. 3-24 Frequency spectrum of flux density under PWM voltage excitation, f = 50 Hz, m_a = 1.0, f_s = 0.75 kHz, B_{peak} = 1.3 T

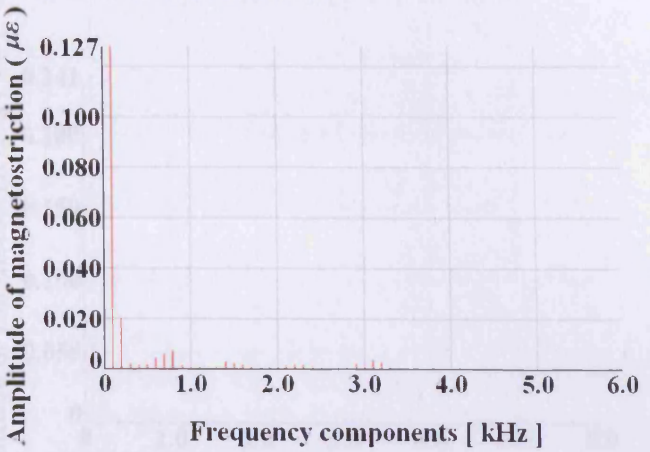

Fig. 3-25 Frequency spectrum of magnetostriction under PWM voltage excitation, f = 50 Hz, m_a = 1.0, f_s = 0.75 kHz, B_{peak} = 1.3 T

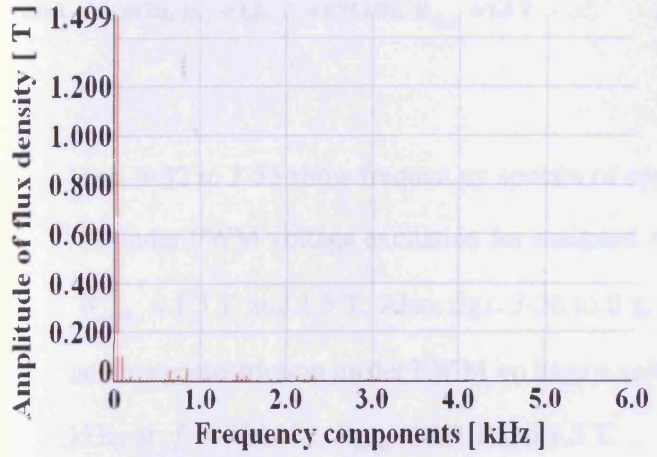

Fig. 3-26 Frequency spectrum of flux density under PWM voltage excitation, f = 50 Hz, m_a = 1.0, f_s = 0.75 kHz, B_{peak} = 1.5 T

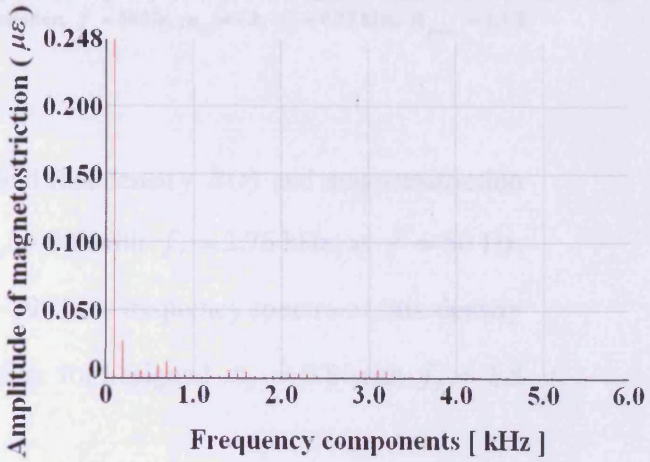

Fig. 3-27 Frequency spectrum of magnetostriction under PWM voltage excitation, f = 50 Hz, m_a = 1.0, f_s = 0.75 kHz, B_{peak} = 1.5 T

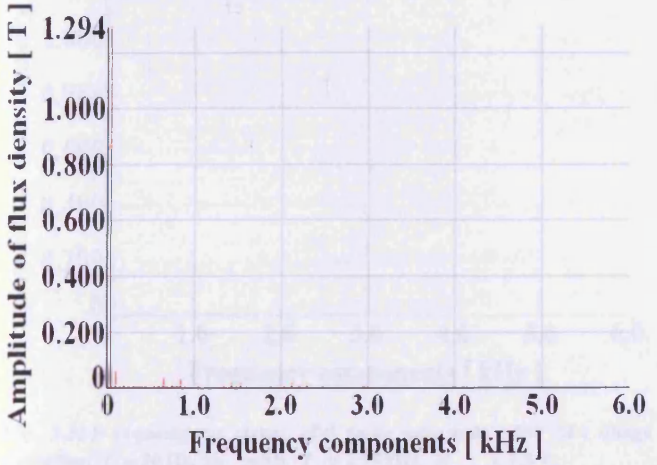

Fig. 3-28 Frequency spectrum of flux density under PWM voltage excitation, f = 50 Hz, m_a = 1.2, f_s = 0.75 kHz, B_{peak} = 1.3 T

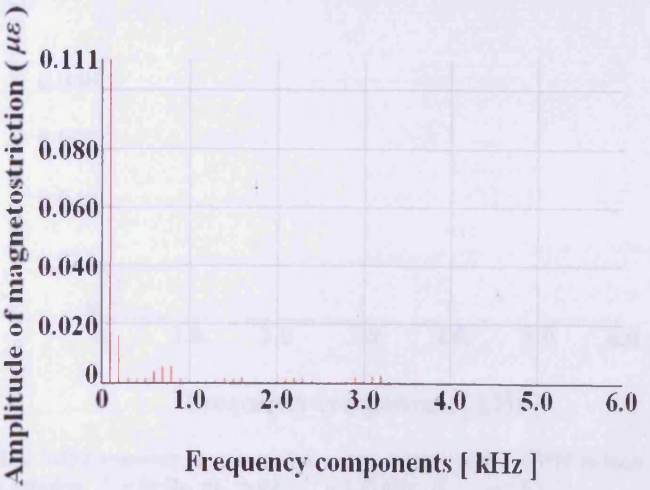

Fig. 3-29 Frequency spectrum of magnetostriction under PWM voltage excitation, f = 50 Hz, m_a = 1.2, f_s = 0.75 kHz, B_{peak} = 1.3 T

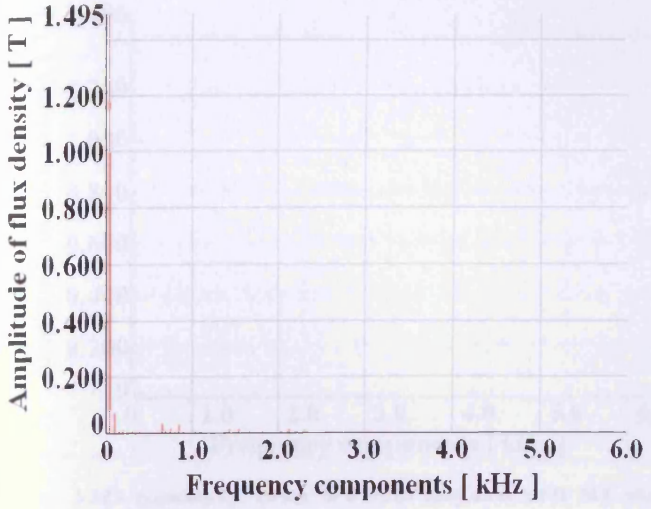

Fig. 3-30 Frequency spectrum of flux density under PWM voltage excitation, f = 50 Hz, m_a = 1.2, f_s = 0.75 kHz, B_{peak} = 1.5 T

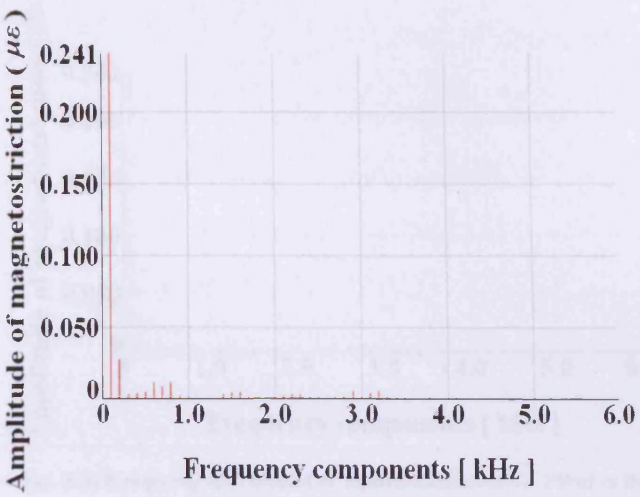

Fig. 3-31 Frequency spectrum of magnetostriction under PWM voltage excitation, f = 50 Hz, m_a = 1.2, f_s = 0.75 kHz, B_{peak} = 1.5 T

Figs. 3-32 to 3-35 show frequency spectra of applied flux density $B(t)$ and magnetostriction under PWM voltage excitation for assigned m_a = 0.8 with f_s = 2.75 kHz, at f = 50 Hz, B_{peak} = 1.3 T and 1.5 T. Also, figs. 3-36 to fig. 3-39 show frequency spectra of flux density and magnetostriction under PWM voltage excitation for assigned m_a = 0.8 with f_s = 1.5 kHz, at f = 100 Hz, B_{peak} = 1.3 T and 1.5 T.

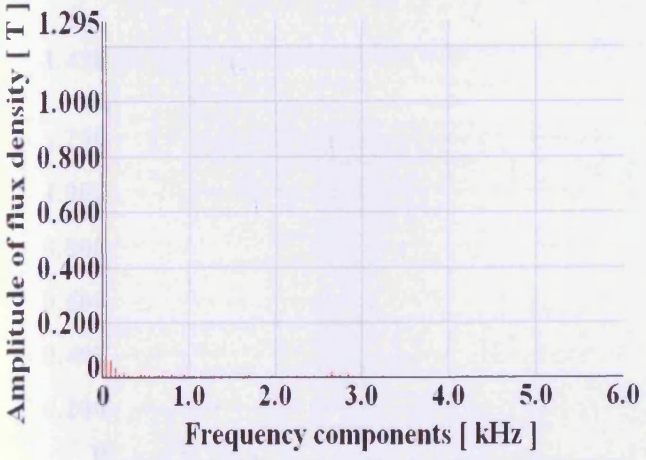

Fig. 3-32 Frequency spectrum of flux density under PWM voltage excitation, f = 50 Hz, m_a = 0.8, f_s = 2.75 kHz, B_{peak} = 1.3 T

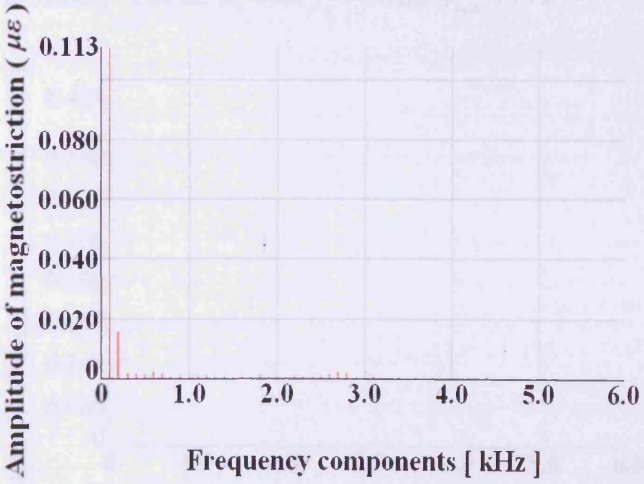

Fig. 3-33 Frequency spectrum of magnetostriction under PWM voltage excitation, f = 50 Hz, m_a = 0.8, f_s = 2.75 kHz, B_{peak} = 1.3 T

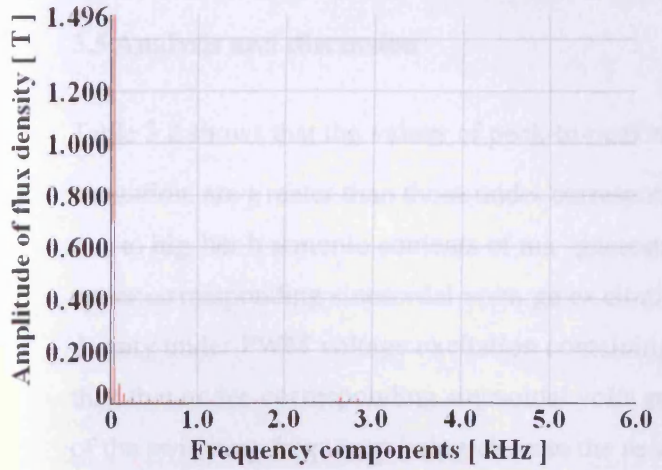

Fig. 3-34 Frequency spectrum of flux density under PWM voltage excitation, f = 50 Hz, m_a = 0.8, f_s = 2.75 kHz, B_{peak} = 1.5 T

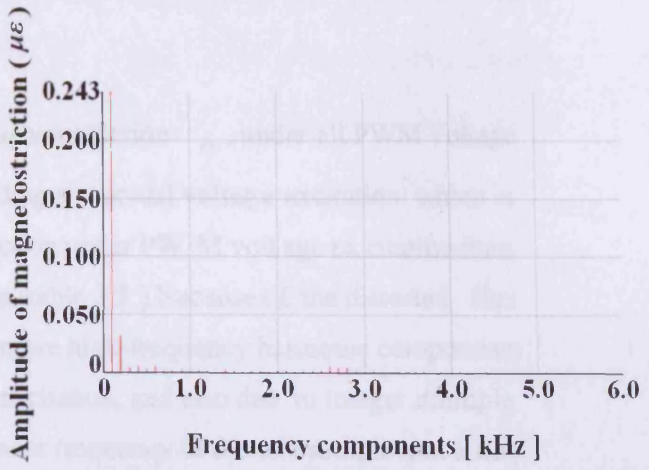

Fig. 3-35 Frequency spectrum of magnetostriction under PWM voltage excitation, f = 50 Hz, m_a = 0.8, f_s = 2.75 kHz, B_{peak} = 1.5 T

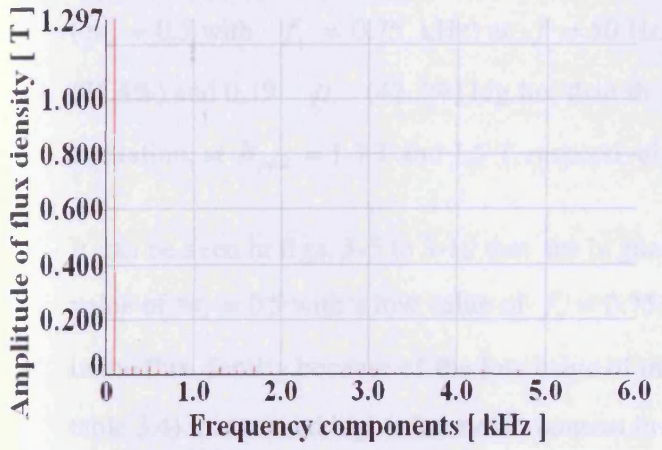

Fig. 3-36 Frequency spectrum of flux density under PWM voltage excitation, f = 100 Hz, m_a = 0.8, f_s = 1.5 kHz, B_{peak} = 1.3 T

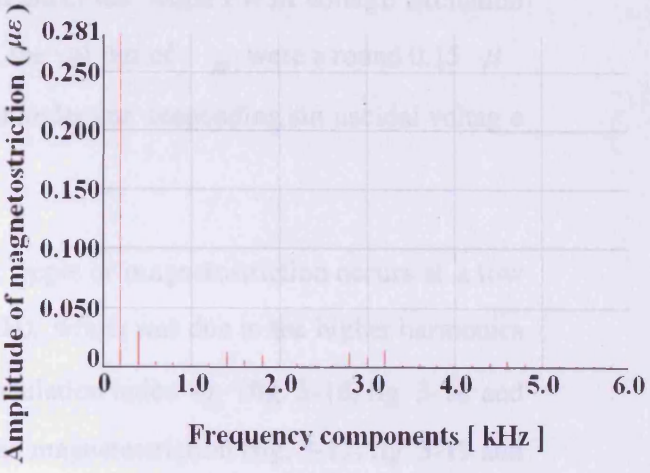

Fig. 3-37 Frequency spectrum of magnetostriction under PWM voltage excitation, f = 100 Hz, m_a = 0.8, f_s = 1.5 kHz, B_{peak} = 1.3 T

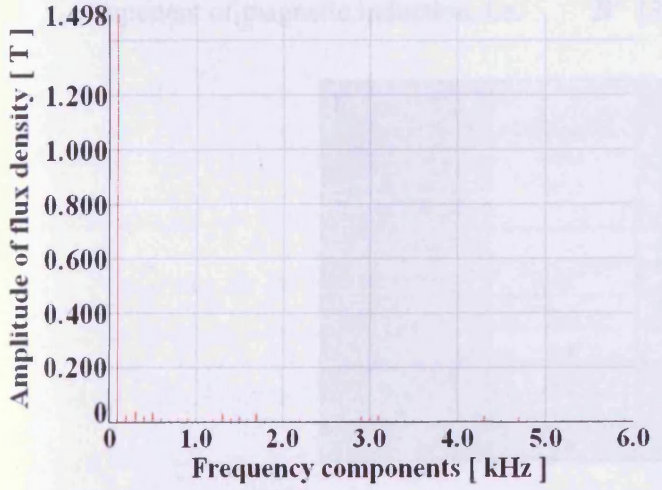

Fig. 3-38 Frequency spectrum of flux density under PWM voltage excitation, f = 100 Hz, m_a = 0.8, f_s = 1.5 kHz, B_{peak} = 1.5 T

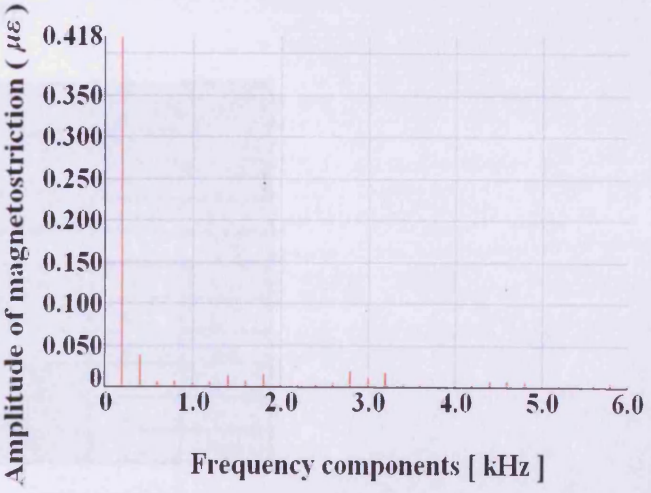

Fig. 3-39 Frequency spectrum of magnetostriction under PWM voltage excitation, f = 100 Hz, m_a = 0.8, f_s = 1.5 kHz, B_{peak} = 1.5 T

3.5 Analysis and discussion

Table 3.2 shows that the values of peak-to-peak magnetostriction $_{pp}$, under all PWM voltage excitation, are greater than those under correspon ding sinusoidal voltag e excitation, which is due to hig her h armonic contents of ma gnetostriction under PW M volt age ex citation than under co rresponding sinusoidal volta ge ex citation (table 3.3) b ecause of the distorted flux density under PWM voltage excitation containing more high-frequency harmonic components than that under corresponding sinusoidal volta ge excitation, and also due to integer multiple of the switching frequency being close to the re sonant frequency of the test sample that a tiny amplitude value of flux density can cause high magnetostriction when resonance occurs (fig. 3-12 to fig . 3-31 and ta ble 3.4). It was found th at under the worst PWM voltage excitation ($m_a = 0.5$ with $f_s = 0.75$ kHz) at $f = 50$ Hz , the val ues of $_{pp}$ were a round 0.15 μ (71.4%) and 0.19 μ (42.2%) hig her than th at under cor responding sin usoidal voltag e excitation, at $B_{peak} = 1.3$ T and 1.5 T, respectively.

It can be seen in fi gs. 3-5 to 3-10 that the hi ghest ripple of magnetostriction occurs at a low value of $m_a = 0.5$ with a low value of $f_s = 0.75$ kHz, which was due to the higher harmonics in the flux density because of the low value of m odulation index m_a (fig. 3-16, fig. 3-18 and table 3.4) that caused higher harmonic content in the magnetostriction (fig. 3-17, fig. 3-19 and table 3.3), where the ma gnetostriction is related t o the square of magnetic induction, and the components of mag netostriction harmonics ar e g iven as the square of each ha rmonic component of magnetic induction, i.e. B^2 [3.8].

Magnetisation Frequency (f)	Modulation index (m_a)	Switching frequency (f_s) (kHz)	THD [%] of flux density $B(t)$	
			1.3 T	1.5 T
sine 50 Hz	--	--	1.3	1.7
PWM 50 Hz	0.5	0.75	11.6	14.4
	0.8	0.75	10.2	13.1
	0.8	2.75	4.9	6.2
	1.0	0.75	7.9	9.4
	1.2	0.75	4.5	5.7
PWM 100 Hz	0.8	1.50	5.8	7.6

Table 3.4 Variation THD [%] of flux density $B(t)$ under sinusoidal and PWM voltage excitation for assigned m_a varied with f_s, f = 50 Hz and 100 Hz, B_{peak} = 1.3 T and 1.5 T

Fig. 3-12 to fig. 3-39 display the frequency spectra of the flux density and magnetostriction under sinusoidal and PWM voltage excitation for assigned values of m_a varied with different f_s. From figs. 3-16 to 3-39, it is observed evidently that the higher frequency components of the magnetostriction were the same as those of flux density because the ripples in the flux density could not change the sign of the *ac* components of the magnetostriction. Also, it was known that grain-oriented 3% silicon electrical steel in the form of Epstein strips would resonate when it was magnetised at approximately 1.56 kHz corresponding to its natural frequency, which was around 3.12 kHz (2×1.56 kHz) (section 2.6).

It is known that the higher harmonic components of the PWM waveform are clustered around multiple integers of switching frequency f_s (fig. 1-3). Therefore, it was shown in fig. 3-16, fig. 3-18, fig. 3-20, fig. 3-22, fig. 3-24, fig. 3-26, fig. 3-28 and fig. 3-30 that at f_s = 0.75 kHz, the second cluster harmonics of flux density were at around 1.5 kHz, which was close to the resonant magnetising frequency at about 1.56 kHz. From fig. 3-36 and fig. 3-38, it was clearly observed that at f_s = 1.5 kHz, the first cluster harmonics of flux density were close to the magnetising frequency at resonance. Also, it was noticed in fig. 3-32 and fig. 3-34 that at f_s = 2.75 kHz, there were no harmonic components of flux density coinciding with the magnetising frequency at resonance.

From fig. 3-16 to fig. 3-31, it can be seen that at the first cluster harmonics of flux density and magnetostriction, which was around 0.75 kHz, the trend for the ratio of the amplitude of magnetostriction to that of flux density under PWM voltage excitation for assigned values of m_a with f_s = 0.75 kHz was similar. Nevertheless, it was also shown in fig. 3-16 to fig. 3-31 that the low amplitude of flux density at around 3 kHz could cause high amplitude of magnetostriction at around 3 kHz, which was close to resonance frequency 3.12 kHz; particularly at f_s = 1.5 kHz (f = 100 Hz), where the second cluster harmonics of flux density at around 3 kHz corresponding to magnetostriction at around 3 kHz, which was closely coincided with the resonance frequency that was shown in fig. 3-36 to fig. 3-39. Therefore, there would be a high ripple of magnetostriction if the switching frequency f_s = 3 kHz, where the first harmonics cluster of the flux density occurs close to the resonance frequency.

From figs. 3-16 to 3-31, it can be seen that the reduction of high frequency harmonic components and harmonic content of the flux density (table 3.4) was due to a high value of modulation index at m_a = 1.2. However, even small amplitude of high frequency component of flux density (fig. 3-28 and fig. 3-30) at around 3 kHz could cause an amount of magnetostriction at frequency closely coinciding with resonant frequency (fig. 3-29 and fig. 3-31). In this study, although the high frequency components of the flux density at around 3 kHz were too small to detect because of a high value of m_a = 1.2 (fig. 3-28 and fig. 3-30), in reality, the applied voltage such as from the PWM inverter contains many high frequency components and some of these components grow at the resonance frequency of the specimen.

In table 3.2, it is noticed that the values of λ_{pp}, at a low f_s = 0.75 kHz, are greater than that at a high f_s = 2.75 kHz (f = 50 Hz, m_a = 0.8), which was due to reduction of harmonic content (table 3.4) and amplitude reduction of harmonic components of flux density (fig. 3-20, fig. 3-22, fig. 3-32 and fig. 3-34) at a high f_s = 2.75 kHz that caused the reduction of harmonic content (table 3.3) and amplitude reduction of harmonic components of magnetostriction (fig. 3-21, fig. 3-23, fig. 3-33 and fig. 3-35). Also, the low value of λ_{pp} occurred at f_s = 2.75 kHz since there was no high frequency components of flux density present at around the resonant frequency (fig. 3-32 and fig. 3-34). Therefore, the benefit performance of magnetostriction is at a high value of f_s. However, the value of f_s would have to avoid the resonance frequency of the specimen.

Also, it was observed in table 3.2 and table 3.3 that the values of λ_{pp} and THD [%] of magnetostriction at m_a = 1.2 (f_s = 0.75 kHz) were almost the same as those at m_a = 0.8 (f_s = 2.75 kHz), which was due to the unobservable high frequency magnetisations (fig. 3-28 and fig. 3-30) at m_a = 1.2 (f_s = 0.75 kHz) could cause an amount of magnetostrictive vibrations at frequencies closely coincided with mechanical resonant modes of the test sample (fig. 3-29 and fig. 3-31), even though the harmonic contents and amplitude of harmonic components of flux density were lower than that at m_a = 0.8 (f_s = 2.75 kHz). This was due to at a high value of m_a = 1.2 but with the f_s = 0.75 kHz, which has high frequency component of flux density that was close to the resonant frequency of the specimen.

According to equation (2.2), this magnetostriction induced mechanical resonance phenomenon would be similar in other materials if a natural frequency of the sample coincides with one of the magnetostrictive harmonics, since thickness, texture, grain size have no effect whereas density, length or modulus of elasticity variable with composition would have some influence. Although this experiment has been conducted on the single strips, similar effects would be expected in the transformer cores but with different resonant frequencies. High acoustic noise and vibration could be generated if the switching frequency f_s of the PWM inverter coincided with a resonant frequency of the transformer core.

References to Chapter 3:

[*3.1*] M. Enokizono, "Measurement of arbitrary dynamic magnetostriction", *Report on magnetics IEE Japan*, MAG-95-181 (1995).

[3.2] S. Somkun, A. J. Moses and P.Anderson, "Mechanical resonance in nonoriented electrical steels induced by magnetostriction under PWM voltage excitation", *IEEE Trans. Mag.*, vol. 44, no. 11, pp. 4062-4065, November 2008.

[*3.3*] T. P. P. Phway, "Magnetostrictively induced mechanical resonance of electrical steel strips", *PhD Thesis*, Cardiff University, 2008.

[*3.4*] P. Anderson, J. Leicht and A. J. Moses, "Non-standard magnetic measurement under controlled conditions", *UK Magnetic Society Seminar*, Warwick, 2000.

[*3.5*] S. Zurek, "Two-dimensional magnetisation problems in electrical steels", *PhD Thesis*, Cardiff University, 2005.

[*3.6*] Polytec laser Doppler vibrometer user manual – Controller: OFV – 3001; Sensor Heads: OFV – 303/- 353, OFV – 511/- 512.

[*3.7*] Yokogawa DL 716 Digital Scope User's Manual, *Yokogawa Electric Corporation.*

[*3.8*] C. G. Kim, H. C. Kim, S. J. Ahn, S. Y. Cha and S. K. Chang, "Magnetizing angle dependence of harmonics of magnetic induction and magnetostriction in electrical steel", *JMMM*, 215-216 (2000) 159-161.

Chapter 4 Measurement and Analysis of Total Power Losses, Localised Flux Density and Estimation of Localised Losses in the Joints of a Model Three-phase Three-limb Laminated Transformer Core under Sinusoidal and PWM Voltage Excitation

4.1 Introduction

In this chapter, the measurement results of total power losses, localised flux density in individual laminations at joint regions of a model three-phase transformer core under sinusoidal and PWM voltage excitation for assigned values of modulation index m_a with different switching frequency f_s at no-load condition have been presented. The analysis of specific total loss and its eddy-current loss component, localised flux density with its harmonic components behaviour and localised loss has been carried out.

4.2 Experimental setup

The basic apparatus consisted of a model three-phase three-limb laminated transformer core with associated equipment used to magnetise the core, measure the total power loss of the core. Also, laminations complete with single-turn search coils were placed at appropriate positions within the core for localised flux density measurement.

4.2.1 Transformer core construction

The laminations of model transformer core specified in table 3.1, were assembled horizontally on a flat "tufnol" base, where its surface was made smooth to prevent any stress being induced into the core. It was held in position by non-magnetic long plastic screws, which were fixed on the "tufnol" base and used to protect the core laminations from any side movement together with three non-magnetic clamping bars, which were clamped to the same torsion with bolts and brass stress-distributing washers at each end (fig. 4-1). The primary and

secondary windings were all connected in delta-delta (□-□) configurations, which had 50 turns of insulated copper wire each. The core laminations were weighed using an "Avery Berkel HL 206-31" balance and the core mass, m_{core} was 96.1 ± 0.01 kg. The layout of the core with dimensions is shown in fig. 4-2.

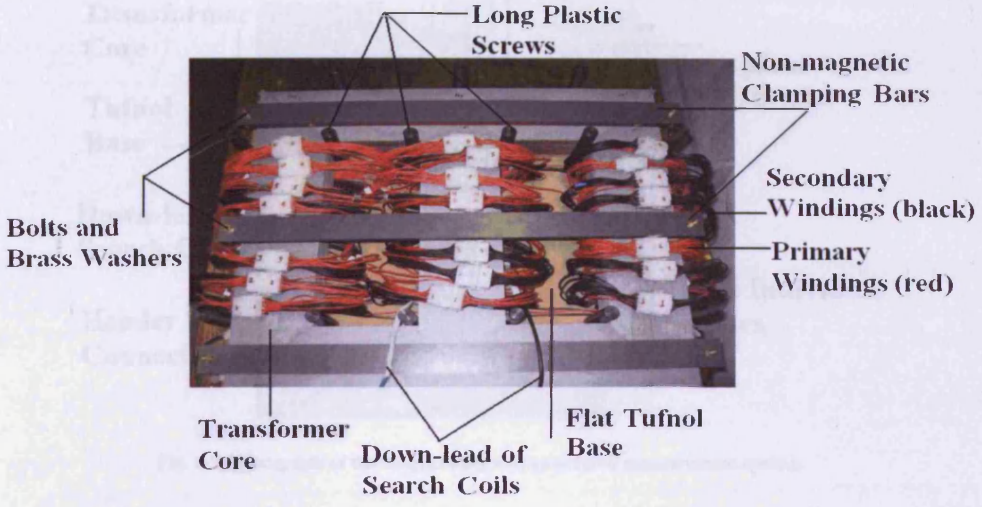

Fig. 4-1 Photograph of the model three-phase three-limb transformer core

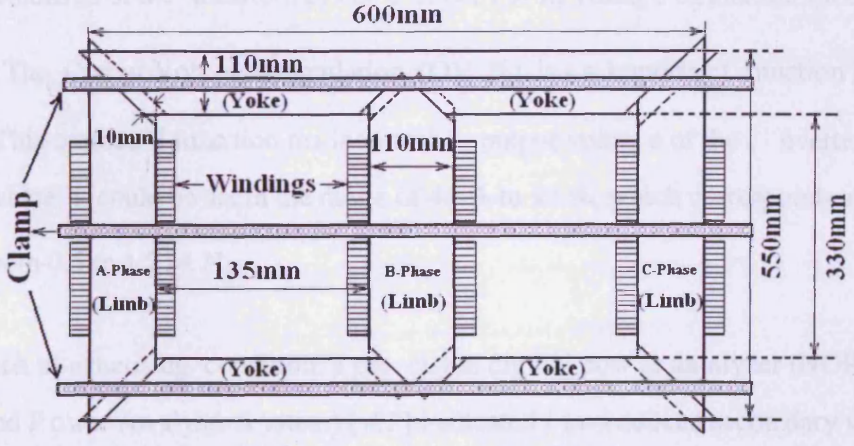

Fig. 4-2 Layout of the model three-phase three-limb transformer core

4.2.2 Total power loss measurement system

A photograph of the magnetising system and associated total power losses measurement system using two-wattmeter method is shown in fig. 4-3.

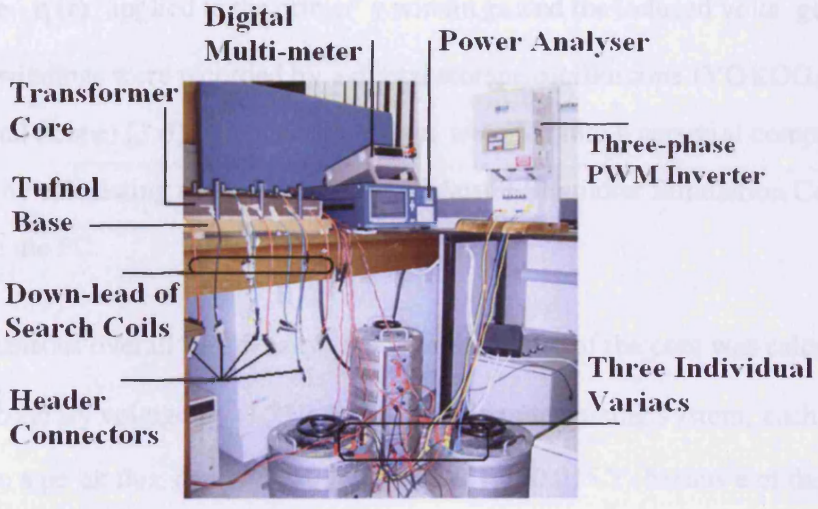

Fig. 4-3 Photograph of the magnetising and associated measurement system

It is shown in fig. 4-3, a three-phase PWM inverter (TOSHIBA - Transistor Inverter TOSVERT VF-A3) [*4.1*] was connected to three separate variacs, which supplied the three primary windings of the transformer core under PWM voltage excitation for assigned m_a with f_s. The Output Voltage Regulation (OV %) is an important function in the PWM inverter. This optional function maintains the output voltage of the inverter at a preset absolute value. It could be set in the range of 40 % to 90 %, which corresponds approximately to m_a from 0.5 to 1.2 [*4.1*].

Under each magnetising condition, a precision digital power analyzer (NORMA D6000 Wide-Band Power Analyser System) [*4.2*] indicated two induced secondary voltages, i.e., U_{AC} and U_{BC} to use in the two-wattmeter method, and a digital multi-meter (fig.4-3) [*4.3*] was used to monitor the third induced secondary voltage U_{AB} in order to ensure that the

three induced secondary voltages were balanced. Balance was achieved by adjusting the three variacs to produce the desired peak flux density B_{peak} in each limb with 120^0 out of phase in time.

The voltage $e_1(t)$ applied to the primary windings and the induced voltage $e_2(t)$ in the secondary windings were recorded by a digital storage oscilloscope (YOKOGAWA DL716 - 16CH Digital Scope) [*3.6*]. Then the saved data were fed into a personal computer for further processing by calculating and analysing using "Ansoft Simplorer Simulation Centre" software installed on the PC.

The instantaneous overall flux density $B(t)$ in each limb of the core was calculated from the induced secondary voltage by (1.21). By using this magnetising system, each limb could be energised to a peak flux density B_{peak} up to 1.5 T $\pm$0.015 T (because of the output range limit of variac).

Also, the power analyser was used to measure the total power loss P_{total} (W) of the core as given by equation (1.35). Therefore, the specific total power loss per kilogram P_{st} (W /kg) could be obtained from the ratio of the measured P_{total} (W) and the core mass m_{core} (kg) by:

$$P_{st} = \frac{P_{total}}{m_{core}} \quad \text{[W/kg]} \tag{4.1}$$

One important function of the "NORMA D6000" power analyser system is "transformer test", which is designed specially for testing transformers. It offers an even higher measuring accuracy at very low power factors. Accuracies of power measurements are better than 0.1% of power results for power factors of 0.1 to 1 and 0.4% for a power factor of 0.01, which allows exact analysis. Moreover, the no-load power losses are corrected automatically in

accordance with the form factor. The specification of components of the whole system is listed in table 4.1.

Instrument	Make and Model	Accuracy	Specifications etc.
TOSHIBA-TOSVERT Transistor Inverter	VFA3-4007PC (S/N: 92880027)	Permissible variations: (Voltage: ± 10%; Frequency: ± 5%) Frequency accuracy: ± 0.5% against the maximum frequency	Source: 3PH—380 ~ 415 V — 50/60 Hz Control method: Sinusoidal PWM control PWM carrier frequency switching: in the range 0.5 kHz to 3 kHz
Wide Band Power Analyzer System	Norma D6000 (S/N: ND58172RR)	Voltage accuracy: ± (0.1% of value + 0.08 % of range) Frequency accuracy: ± 0.025% of value	--
Digital Multi-Meter	Keithley 2001 (S/N: 0715176)	Accuracy: ± 0.015 % of Range (AC Volts) Resolution: 10 µV (RMS Range: 20 V) Resolution: 100 µV (RMS Range: 200 V	Input 1 M□ ± 2 % with < 140 pF
Digital Oscilloscope	YKOGAWA DL716 (Module 701857) (S/N: 12C702812)	Resolution: 16-bit A/D conversion Maximum sample rate: 16 MS/s	Input: 1 M□ ± 1 % Maximum isolated input voltage: 850 V (DC + AC peak)
Variac	V30 HM--G3 (S/N: BC)	Input: 415 V Output: 0 ~ 465 V	--

Table 4.1 Specification of measuring instrument [*3.6*] [*4.1*]-[[*4.3*]

4.2.3 Localised flux density measurement

4.2.3.1 Search coils construction

In order to measure the localised flux density within laminations of the core, an array of search coils was wound on individual laminations at appropriate positions using the technique similar to that described in chapter 1.

Components of in-plane flux densities in the rolling and transverse directions at measurement points in the joints of the core were found by measuring the induced voltages from 10 mm long single-turn orthogonal search coils threaded through 0.25 mm diameter holes (fig. 1-8 (a)). Solderable enamelled copper wire of 0. 15 mm diameter was used since it had already

been found thin enough for winding the single-turn search coils, without affecting the total power loss or flux distribution to any degree [*1.41*] [*2.41*]. Each pair of search coils leads was twisted tightly together to avoid any stray voltages. At each stage of search coils construction, a continuity test was carried out using a multi-meter to check for wire breakage or a short circuit between the lamination and the search coil.

Having determined the polarity of each search coil and marked on the search coil leads, and then they were soldered to 24 pin header connectors (fig. 4-3) and covered with epoxy resin. The reason for using header connectors was to link the induced voltage signals from search coils to the amplifier circuit, which was built to amplify induced voltage signals using precision "OPAMPS" and resistors. The positions of orthogonal search coils in the joints of the core are shown in fig. 4-4.

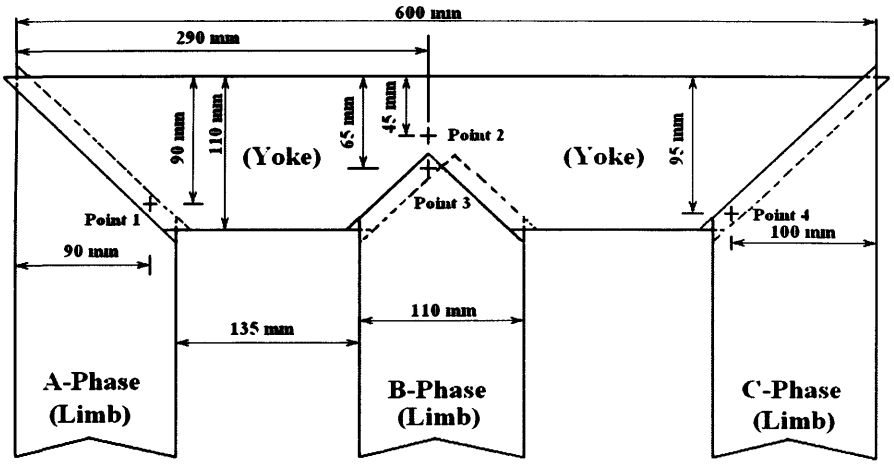

Fig. 4-4 Positions of orthogonal search coils within the laminations of the transformer core

Also, normal flux densities at measurement points within individual laminations of the core were measured by means of similar array of pre-shaped, 10 mm square, single-turn search coils, and the two ends were twisted tightly together to avoid picking up any stray voltages (fig. 1-8 (b)). These search coils were stuck on top of the individual laminations, using insulated varnish. Having determined the polarity of each search coil and marked on the search coil leads, and then the twisted leads were taken out in groups and soldered to 12 or 24

pin header connectors covered with epoxy resin after continuity testing. Fig. 4-5 shows the positions of normal search coils.

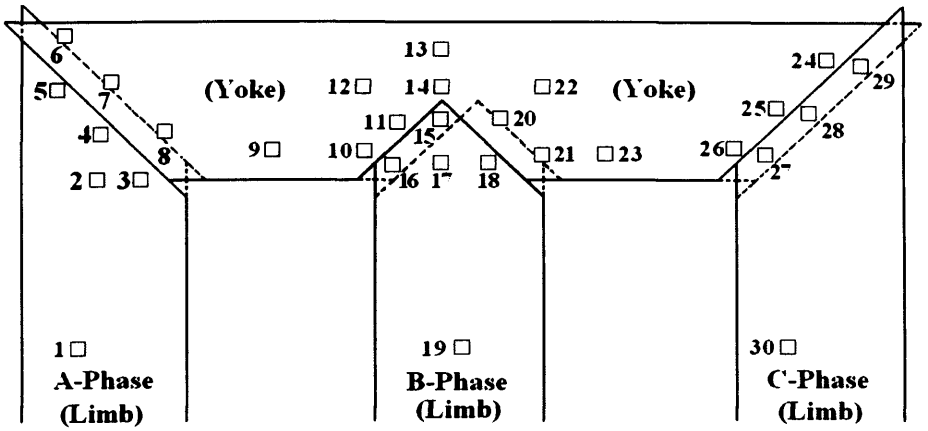

Fig. 4-5 Positions of search coils for measuring components of normal flux densities on the laminations of the core

Adhesive tape, 0.1 mm thick, was placed between the search coil leads and the edge of the laminations being used for localised flux density investigation in order to avoid any damage of the enamelled wire insulation.

4.2.3.2 Measurement process

Fig. 4-6 shows a schematic block diagram of the localised flux density measurement system, the reference signal was the B-Phase secondary induced voltage of the core.

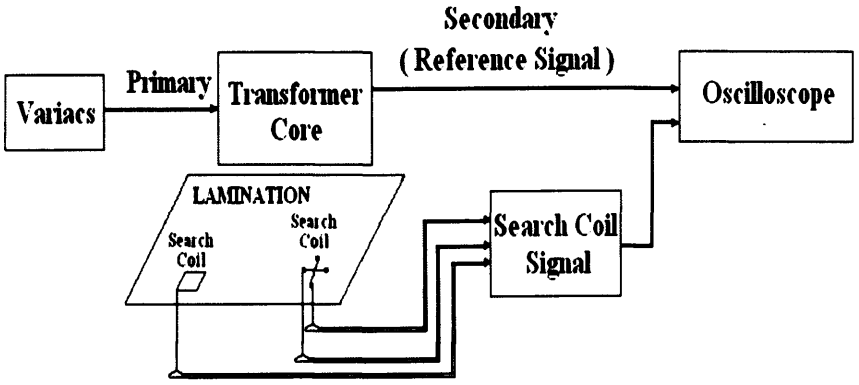

Fig. 4-6 Diagram of measuring system for the localised flux density

When the core was energised, the maximum amplitude of induced voltage in search coil was less than 1 mV. Therefore, the induced voltage signals from search coils were connected to an amplifier circuit by means of twisted search coils leads before being sent to a digital oscilloscope. The open-loop amplifier circuit which was used for this purpose is shown in fig. 4-7.

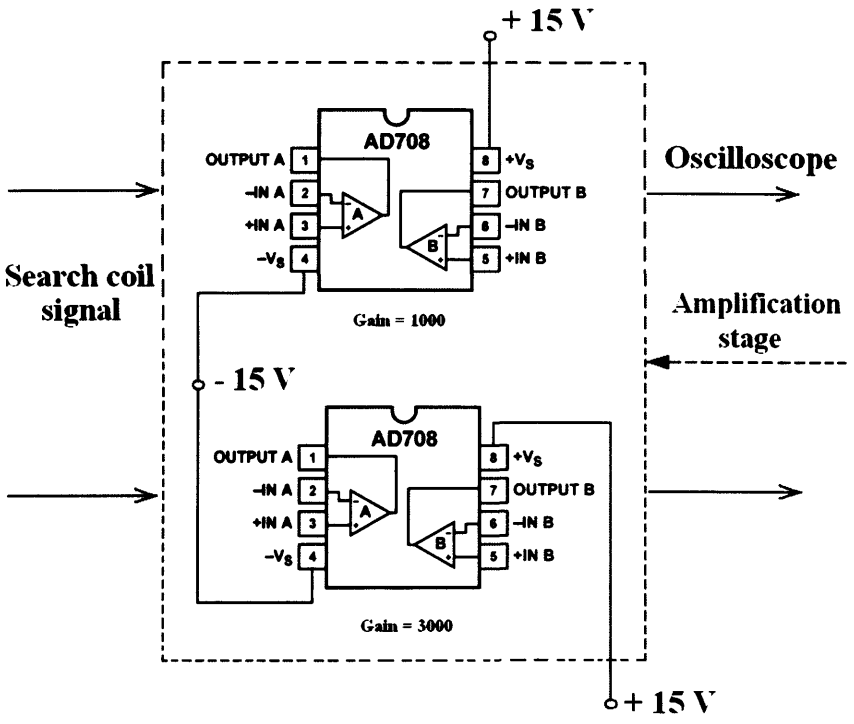

Fig. 4-7 Connection diagram of amplifier circuit

The amplifier circuit (AD708) could provide typical 10 V/□V open-loop gain and also could amplify very small signals with an accuracy better than 0.1% at voltage levels equivalent to the core flux densities without sacrificing overall system performance [*4.4*]. The amplifier circuit used in this investigation had gains of 1 000 for amplifying induced voltages from orthogonal search coils, and 3000 for amplifying induced voltages from normal search coils.

Then, the instantaneous induced voltages $e_{ro}(t)$, $e_{tr}(t)$ and $e_{no}(t)$ from search coils in rolling, transverse and normal direction, respectively (section 1.3.5), and the B-Phase secondary induced voltage $e_2(t)$ with respect to the reference voltage waveform were re

recorded using a digital storage oscilloscope (YOKOGAWA DL716 - 16CH Digital Scope). After this process, the saved data were fed into a personal computer for further processing by calculating and analysing using "Ansoft Simplorer Simulation Centre" and "Mat Lab 7.0" software installed on the PC.

After that, the instantaneous components of localised flux density flowing through the search coils in the rolling ($B_{ro}(t)$), transverse ($B_{tr}(t)$) and normal ($B_{no}(t)$) directions could be obtained by using equations (1.45), (1.46) and (1.47) respectively, where A_{ro} = 10 mm × 0.27 mm = 2.7×10^{-6} m^2, A_{tr} = 10 mm × 0.27 mm = 2.7×10^{-6} m^2 and A_{no} = 10 mm × 10 mm = 1.0×10^{-4} m^2.

Throughout the experiment, the model transformer core was excited under sinusoidal and PWM voltage excitation for assigned values of m_a in the range of 0.5 to 1.2, at f = 50 Hz and 100 Hz, and B_{peak} up to 1.5 T. Nevertheless, at f = 100 Hz, measurement results at B_{peak} = 1.5 T were only performed for m_a = 0.8, 1.0 and 1.2, because very high values of form factor K_f at low values of modulation index caused high magnetising voltages, which led to the protection circuits in the PWM inverter operating so that normal function was impeded. Also, no measurement at f = 100 Hz under sinusoidal voltage excitation taken because the magnetising voltage outranged the maximal limitation of the power amplifier, although 100 Hz three-phase sinusoidal voltage waveform could be provided by waveform generator. For the assigned values of m_a and f under PWM voltage excitation, the switching frequency f_s was varied in the range of 1 kHz to 3 kHz.

The model transformer core was carefully assembled and dismantled twice. The overlap length was set accurately by measuring the distance to ± 0.01 cm with a vernier gauge, and a minimum air gap at T-joints and corner joints of the core (less than 0.1 mm) was obtained. At each condition, the measurement was taken three times under each voltage excitation

condition. The repeatability of specific total power loss measurements was better than ± 1%, the repeatability of peak resultant in-plane flux density at measurement points was better than ± 2.0%, and the repeatability of peak normal flux density at limbs and yokes, T-joints and corners regions was better than ± 6.0%, which are shown in Appendix B.

During the experimental process, the variac had a filtering effect on the voltage waveform produced by the PWM inverter. It was believed that at low modulation indices, the narrowest pulses in the excitation were suppressed, which led to a reduction of *rms* and rectified mean values of the voltage. Therefore, a higher amount of energy was required to magnetise the core and even higher power losses were expected at low m_a, due to this shortcoming of the set-up.

4.3 Measurement results of the core under sinusoidal and PWM voltage excitation

4.3.1 Specific total power losses

Fig. 4-8 shows the mean P_{st} (W/kg) values of the core under sinusoidal and PWM voltage excitation for assigned values of m_a with f_s = 3 kHz, at f = 50 Hz. Fig. 4-9 and fig. 4-10 show the mean P_{st} (W/kg) values of the core under PWM voltage excitation for assigned values of m_a with f_s = 3 kHz, at f = 100 Hz.

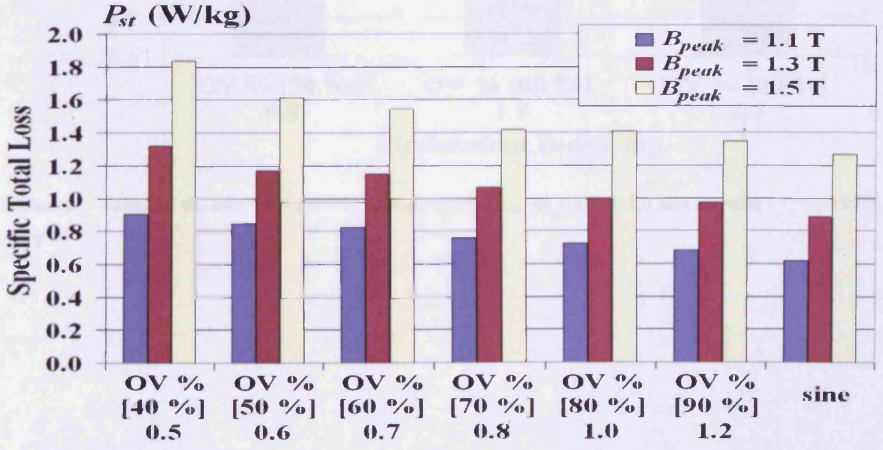

Fig. 4-8 Mean P_{st} values of the core under sinusoidal and PWM voltage excitation, m_a = 0.5 - 1.2 with f_s = 3 kHz, f = 50 Hz, B_{peak} = 1.1 T, 1.3 T and 1.5 T

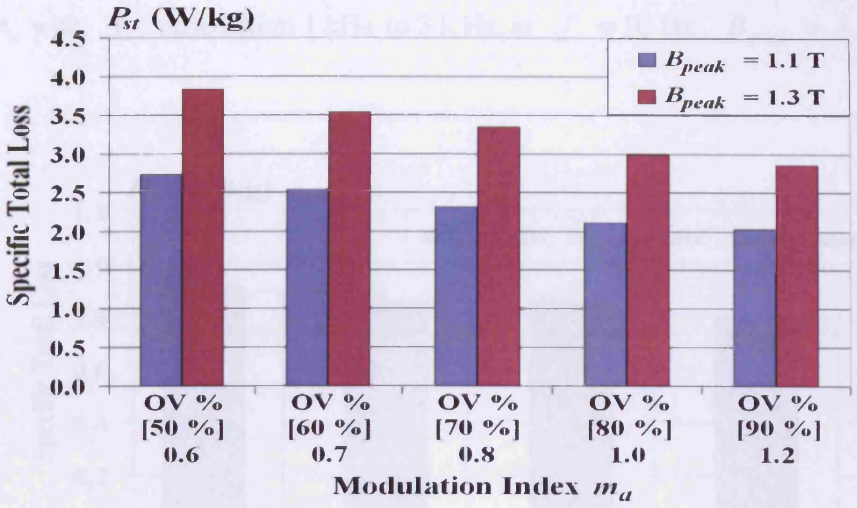

Fig. 4-9 Mean P_{st} values of the core under PWM voltage excitation, m_a = 0.6 - 1.2 with f_s = 3 kHz, f = 100 Hz, B_{peak} = 1.1 T and 1.3 T

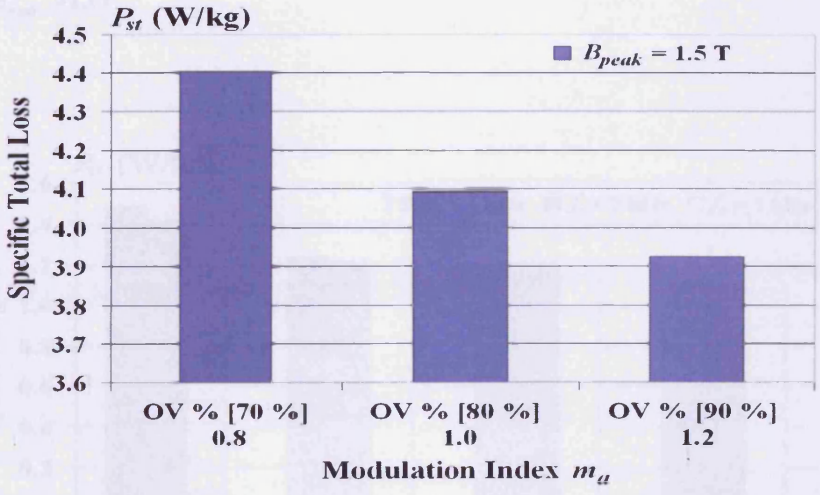

Fig. 4-10 Mean P_{st} values of the core under PWM voltage excitation, m_a = 0.8, 1.0 and 1.2 with f_s = 3 kHz, f = 100 Hz, B_{peak} = 1.5 T

Fig. 4-11 to fig. 4-13 show the mean P_{st} (W/kg) values under PWM voltage excitation for assigned m_a with f_s varied from 1 kHz to 3 kHz, at f = 50 Hz, B_{peak} = 1.1 T, 1.3 T and 1.5 T.

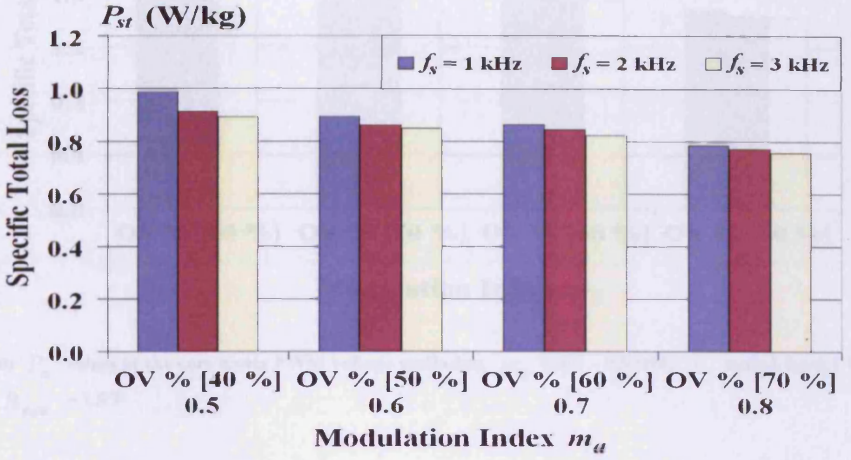

Fig. 4-11 Mean P_{st} values of the core under PWM voltage excitation, m_a = 0.5 - 0.8 with f_s varied from 1 kHz to 3 kHz, f = 50 Hz, B_{peak} = 1.1 T

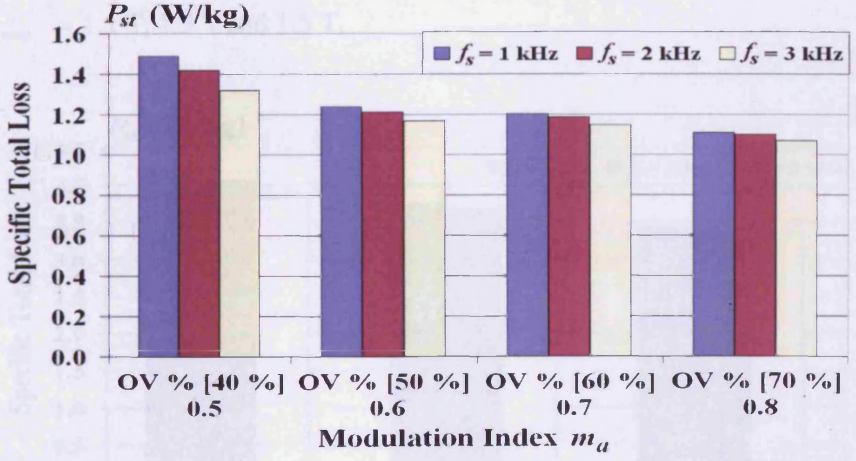

Fig. 4-12 Mean P_{st} values of the core under PWM voltage excitation, m_a = 0.5 - 0.8 with f_s varied from 1 kHz to 3 kHz, f = 50 Hz, B_{peak} = 1.3 T

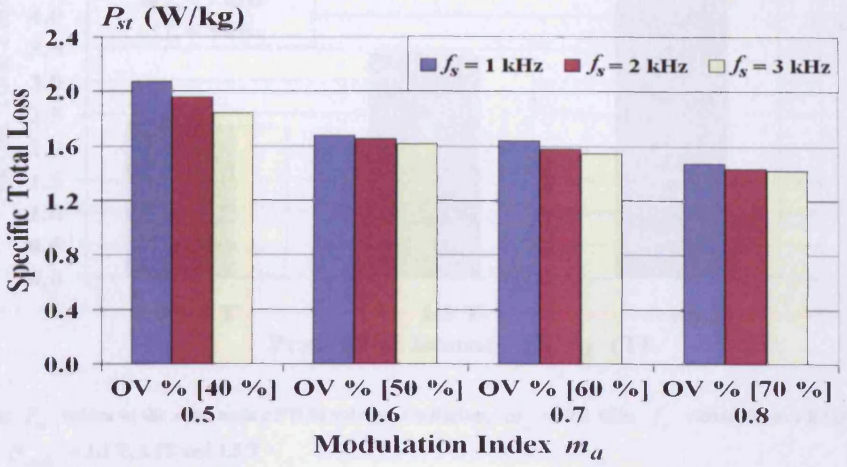

Fig. 4-13 Mean P_{st} values of the core under PWM voltage excitation, m_a = 0.5 - 0.8 with f_s varied from 1 kHz to 3 kHz, f = 50 Hz, B_{peak} = 1.5 T

Fig. 4-14 shows the mean P_{st} (W/kg) values under PWM voltage excitation for assigned m_a with f_s varied from 1 kHz to 3 kHz, at f = 100 Hz, B_{peak} = 1.3 T. Fig. 4-15 shows the mean P_{st} (W/kg) values for m_a = 0.8 with f_s varied from 1 kHz to 3 kHz, at f = 100 Hz, B_{peak} = 1.1 T, 1.3 T and 1.5 T.

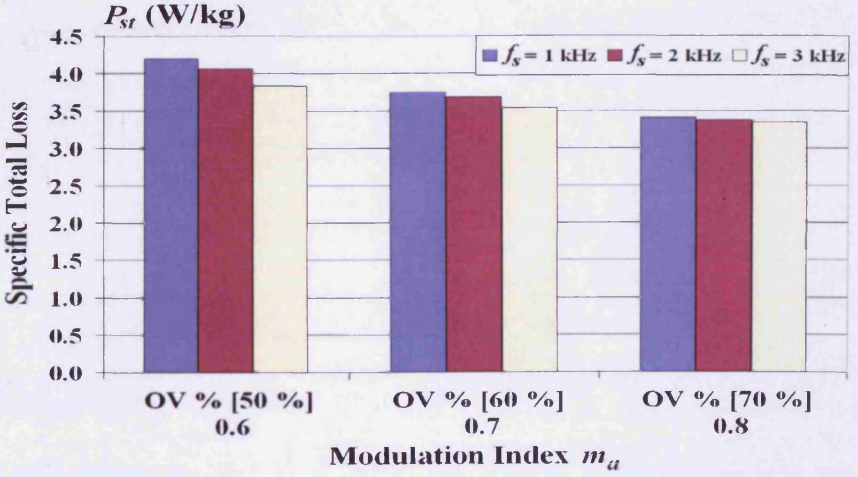

Fig. 4-14 Mean P_{st} values of the core under PWM voltage excitation, m_a = 0.6, 0.7 and 0.8 with f_s varied from 1 kHz to 3 kHz, f = 100 Hz, B_{peak} = 1.3T

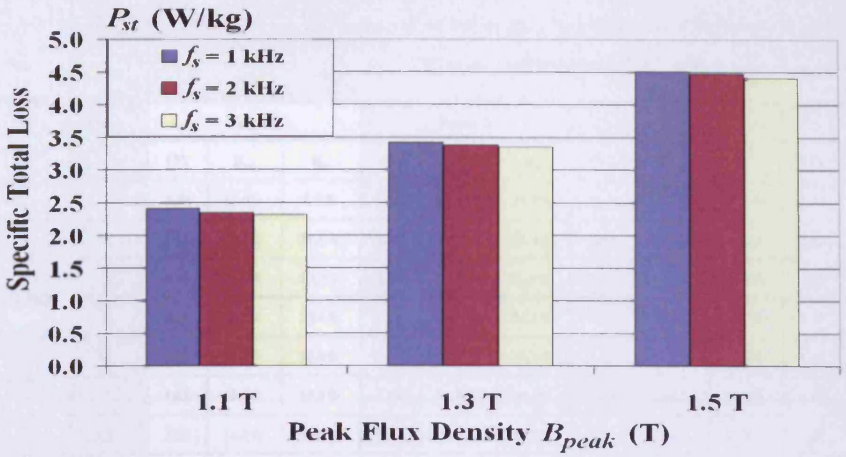

Fig. 4-15 Mean P_{st} values of the core under PWM voltage excitation, m_a = 0.8 with f_s varied from 1 kHz to 3 kHz, f = 100 Hz, B_{peak} = 1.1 T, 1.3T and 1.5 T

4.3.2 Results of the in-plane flux density at investigated points in the joints

Table 4.2 and table 4.3 display peak values of resultant in-plane flux density and THD [%] of components in rolling ($\mathbf{B_{ro}}$) and transverse ($\mathbf{B_{tr}}$) direction at four investigated points (fig. 4-4) in the joints under sinusoidal and PWM voltage excitation for assigned values of m_a with f_s varied in the range of 1 kHz to 3 kHz, at f = 50 Hz and 100 Hz, B_{peak} = 1.3 T and 1.5 T.

f	m_a [OV %]	f_s [kHz]	Peak resultant flux density [T] and *THD* [%] of flux density in rolling (B_{ro}) and transverse (B_{tr}) direction											
			Point 1			Point 2			Point 3			Point 4		
			[T]	B_{ro}	B_{tr}	[T]	B_{ro}	B_{tr}	[T]	B_{ro}	B_{tr}	[T]	B_{ro}	B_{tr}
sine 50 Hz	--	--	1.59	13.0%	8.8%	1.65	18.1%	21.7%	1.61	10.2%	19.2%	1.63	5.2%	20.6%
PWM 50 Hz	0.5 [40 %]	1	1.66	19.1%	36.5%	1.75	25.9%	37.4%	1.69	16.5%	36.2%	1.72	11.4%	36.3%
		2	1.65	17.8%	33.3%	1.73	24.3%	36.0%	1.68	16.0%	35.1%	1.71	10.9%	34.5%
		3	1.65	16.7%	32.6%	1.72	23.2%	34.2%	1.67	15.7%	33.7%	1.70	10.3%	33.4%
	0.8 [70 %]	1	1.63	15.9%	26.5%	1.70	21.3%	30.7%	1.65	14.5%	28.9%	1.68	8.9%	30.7%
		2	1.62	15.6%	25.9%	1.69	21.0%	30.2%	1.65	14.1%	28.2%	1.68	8.6%	30.2%
		3	1.62	15.1%	25.2%	1.69	20.6%	29.7%	1.64	13.8%	27.7%	1.67	8.2%	29.5%
	1.2 [90 %]	3	1.61	14.5%	24..6%	1.67	19.5%	28.9%	1.63	13.4%	26.8%	1.65	7.8%	28.2%
PWM 100 Hz	0.8 [70 %]	1	1.64	16.3%	30.6%	1.72	22.7%	32.8%	1.66	15.3%	32.5%	1.69	9.9%	32.1%
		2	1.63	16.0%	29.2%	1.71	22.1%	31.8%	1.66	15.0%	31.7%	1.69	9.6%	31.7%
		3	1.63	15.8%	27.3%	1.70	21.6%	31.3%	1.65	14.8%	30.8%	1.68	9.2%	31.1%

Table 4.2 Peak resultant flux density and variation *THD* [%] of components at measurement points under sinusoidal and PWM voltage excitation for assigned values of m_a with f_s, at f = 50 Hz and 100 Hz, B_{peak} = 1.5 T

f	m_a [OV %]	f_s [kHz]	Peak resultant flux density [T] and *THD* [%] of flux density in rolling (B_{ro}) and transverse (B_{tr}) direction											
			Point 1			Point 2			Point 3			Point 4		
			[T]	B_{ro}	B_{tr}	[T]	B_{ro}	B_{tr}	[T]	B_{ro}	B_{tr}	[T]	B_{ro}	B_{tr}
PWM 100 Hz	0.7 [60 %]	1	1.45	16.0%	25.4%	1.53	20.9%	27.7%	1.49	13.2%	25.6%	1.51	7.2%	27.4%
		2	1.45	15.5%	25.1%	1.52	20.6%	27.1%	1.48	12.7%	25.1%	1.51	6.9%	26.7%
		3	1.44	15.2%	24.8%	1.52	20.1%	26.6%	1.48	12.4%	24.7%	1.50	6.6%	26.1%
	0.8 [70 %]	1	1.44	15.7%	25.2%	1.51	20.7%	27.4%	1.47	12.9%	25.3%	1.49	7.0%	27.0%
		2	1.43	15.4%	24.5%	1.50	20.2%	26.8%	1.47	12.5%	24.5%	1.48	6.7%	26.4%
		3	1.43	14.9%	23.9%	1.49	19.7%	25.9%	1.46	12.1%	23.9%	1.48	6.4%	25.8%
	1.2 [90 %]	3	1.42	14.3%	22.7%	1.48	19.2%	24.5%	1.45	11.7%	22.7%	1.47	6.1%	24.7%

Table 4.3 Peak resultant flux density and variation *THD* [%] of components at measurement points under PWM voltage excitation for assigned values of m_a with f_s, at f = 100 Hz, B_{peak} = 1.3 T

The in-plane flux density is presented in vector form, which is drawn from the intersection of the orthogonal search coils, where the magnitude of the vector represents the magnitude of the flux density and its direction indicates the direction of the flow of flux at the selected instant of time. Therefore, the instantaneous vectors of harmonic components and total resultant in-plane flux density during one complete magnetising cycle at investigated points under sinusoidal and PWM voltage excitation could be obtained by using "MatLab 7.0" software.

Fig. 4-16 to fig. 4-21 and fig. 4-22 to fig. 4-26 show the corresponding vectors of harmonic components and total resultant in-plane flux density at point 3 (fig. 4-4) in the T-joints relative to the flux in the B-Phase limb being zero, under sinusoidal and PWM voltage excitation for assigned values of m_a with f_s varied from 1 kHz to 3 kHz, at f = 50 Hz and 100 Hz, B_{peak} = 1.3 T and 1.5 T.

In the following figures, $\mathbf{B_{rofund}}$, $\mathbf{B_{ro3}}$, $\mathbf{B_{ro5}}$, $\mathbf{B_{ro7}}$, $\mathbf{B_{ro9}}$ and $\mathbf{B_{ro}}$ represent fundamental, 3rd, 5th, 7th, 9th harmonic components of flux density and component of resultant flux density in the rolling direction, respectively, and $\mathbf{B_{trfund}}$, $\mathbf{B_{tr3}}$, $\mathbf{B_{tr5}}$, $\mathbf{B_{tr7}}$, $\mathbf{B_{tr9}}$ and $\mathbf{B_{tr}}$ represent fundamental, 3rd, 5th, 7th, 9th harmonic components of flux density and component of resultant flux density in the transverse direction, respectively. Moreover, number **1** in each graph represents vector of flux density at t = 0, and also the vector of flux density rotates in the direction of the arrows.

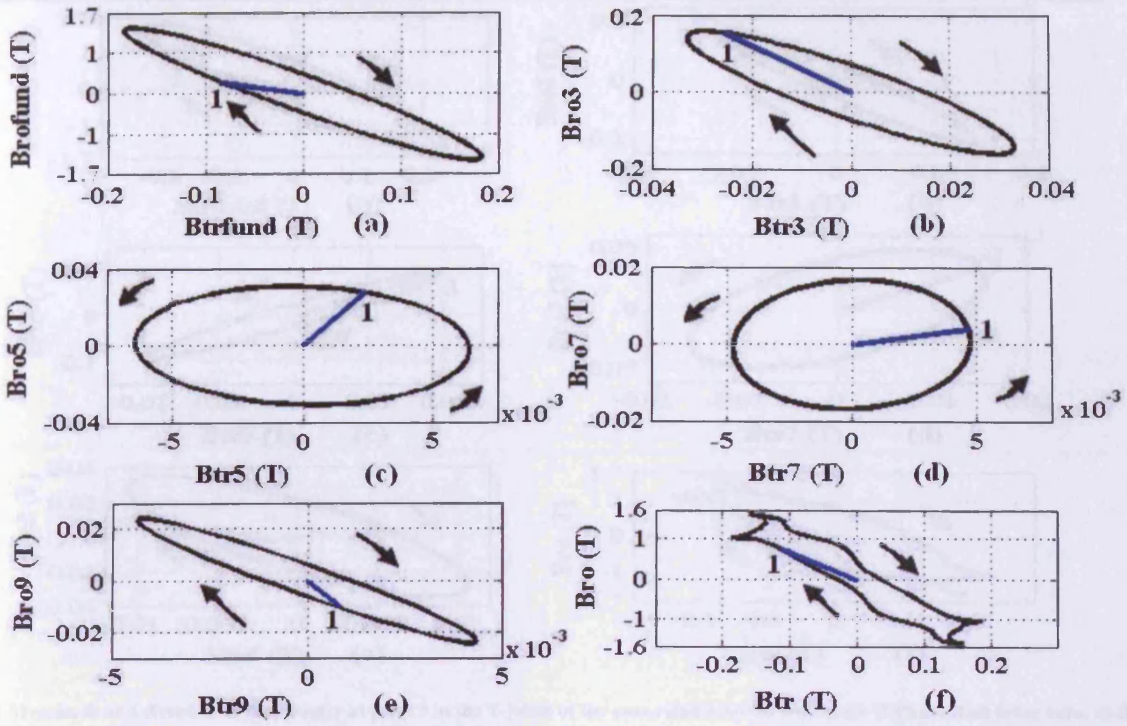

Fig. 4-16 Magnitude and direction of flux density at point 3 in the T-joints of the core relative to the flux in the B-Phase limb being zero, under sinusoidal voltage excitation, f = 50 Hz, B_{peak} = 1.5 T. (a) Fundamental component of the flux; (b) 3rd harmonic component of the flux; (c) 5th harmonic component of the flux; (d) 7th harmonic component of the flux; (e) 9th harmonic component of the flux; (f) Total resultant flux magnitude in time

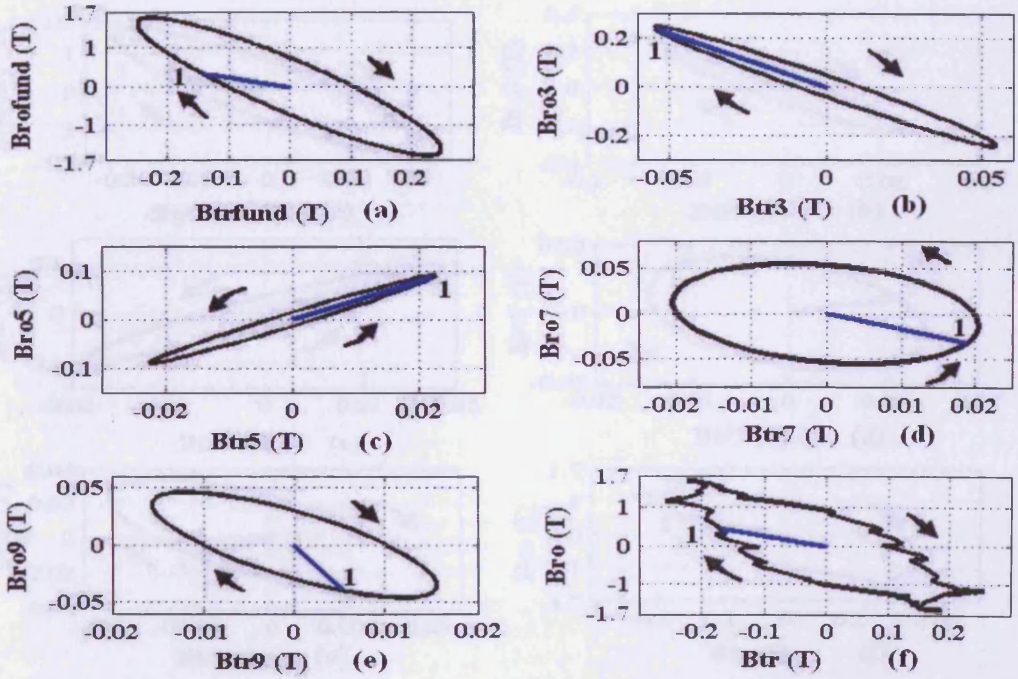

Fig. 4-17 Magnitude and direction of flux density at point 3 in the T-joints of the core relative to the flux in the B-Phase limb being zero, under PWM voltage excitation, m_a = 0.5, f_s = 1 kHz, f = 50 Hz, B_{peak} = 1.5 T. (a) Fundamental component of the flux; (b) 3rd harmonic component of the flux; (c) 5th harmonic component of the flux; (d) 7th harmonic component of the flux; (e) 9th harmonic component of the flux; (f) Total resultant flux magnitude in time

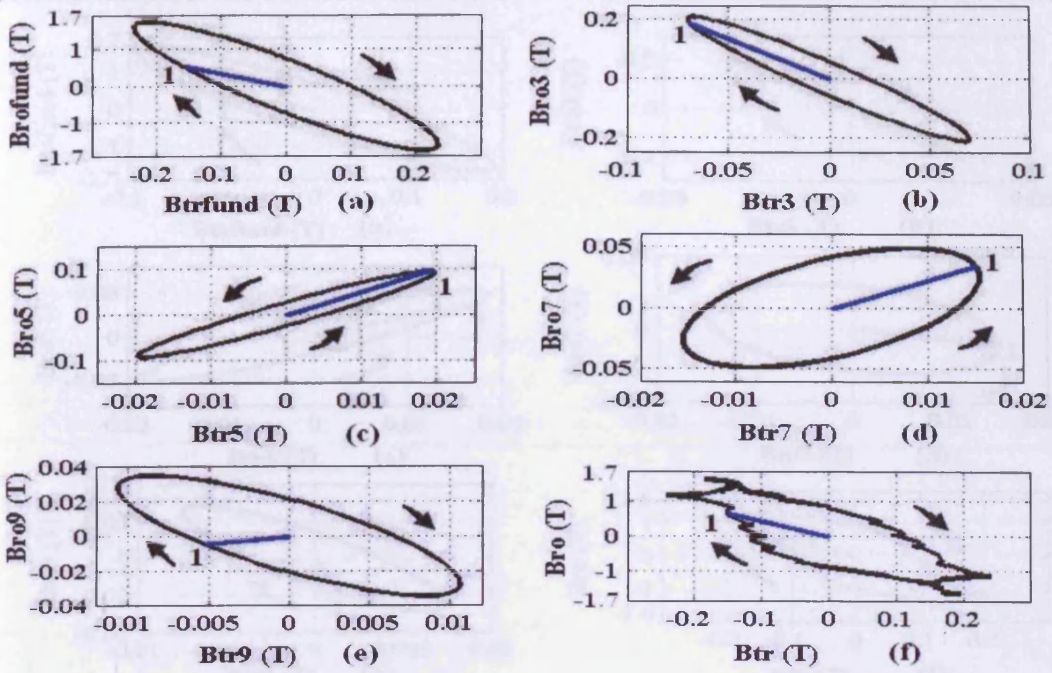

Fig. 4-18 Magnitude and direction of flux density at point 3 in the T-joints of the core relative to the flux in the B-Phase limb being zero, under PWM voltage excitation, m_a = 0.5, f_s = 2 kHz, f = 50 Hz, B_{peak} = 1.5 T. (a) Fundamental component of the flux; (b) 3rd harmonic component of the flux; (c) 5th harmonic component of the flux; (d) 7th harmonic component of the flux; (e) 9th harmonic component of the flux; (f) Total resultant flux magnitude in time

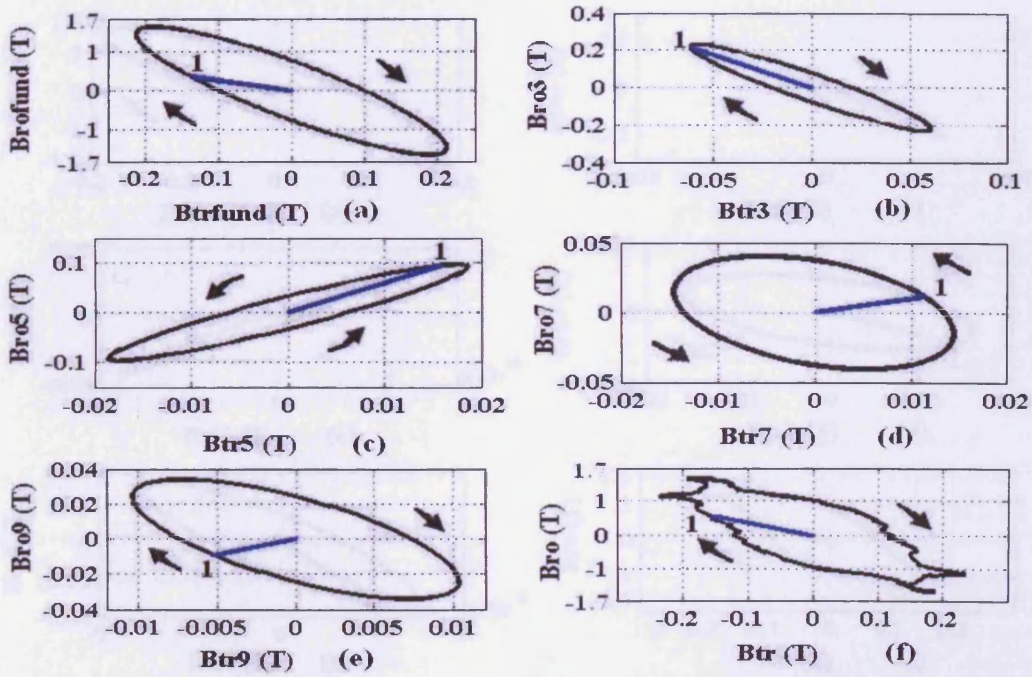

Fig. 4-19 Magnitude and direction of flux density at point 3 in the T-joints of the core relative to the flux in the B-Phase limb being zero, under PWM voltage excitation, m_a = 0.5, f_s = 3 kHz, f = 50 Hz, B_{peak} = 1.5 T. (a) Fundamental component of the flux; (b) 3rd harmonic component of the flux; (c) 5th harmonic component of the flux; (d) 7th harmonic component of the flux; (e) 9th harmonic component of the flux; (f) Total resultant flux magnitude in time

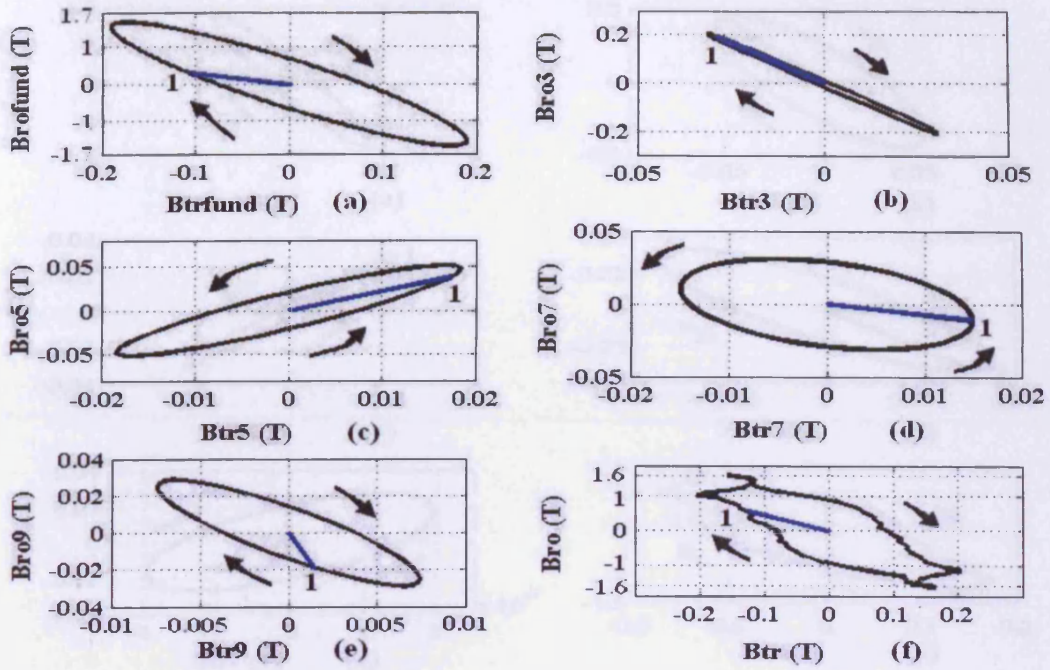

Fig. 4-20 Magnitude and direction of flux density at point 3 in the T-joints of the core relative to the flux in the B-Phase limb being zero, under PWM voltage excitation, m_a = 0.8, f_s = 3 kHz, f = 50 Hz, B_{peak} = 1.5 T. (a) Fundamental component of the flux; (b) 3rd harmonic component of the flux; (c) 5th harmonic component of the flux; (d) 7th harmonic component of the flux; (e) 9th harmonic component of the flux; (f) Total resultant flux magnitude in time

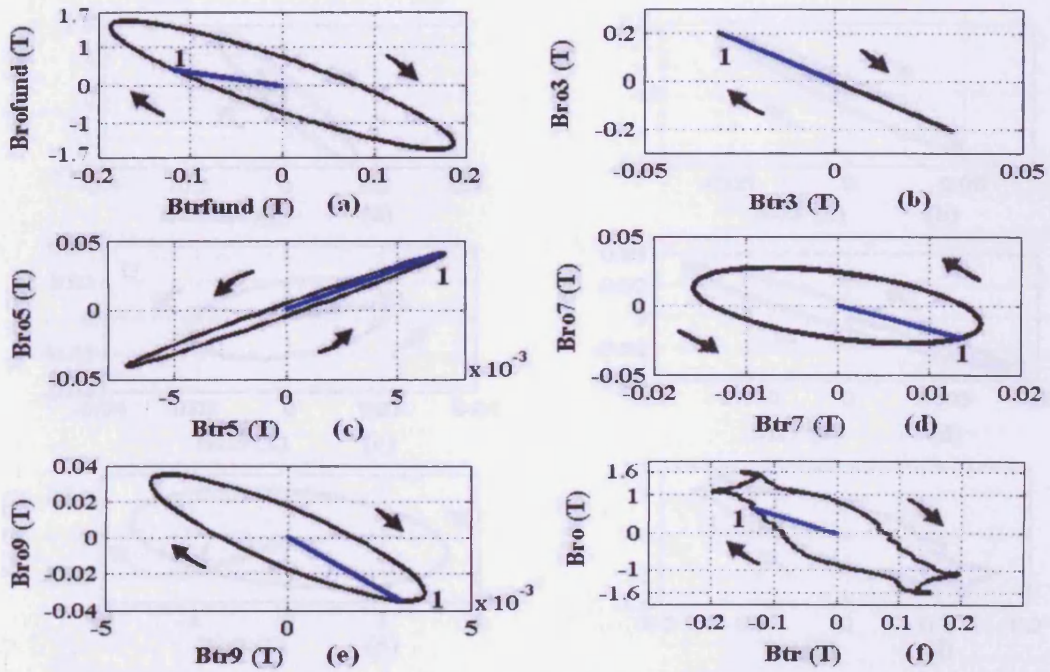

Fig. 4-21 Magnitude and direction of flux density at point 3 in the T-joints of the core relative to the flux in the B-Phase limb being zero, under PWM voltage excitation, m_a = 1.2, f = 50 Hz, f_s = 3 kHz, B_{peak} = 1.5 T. (a) Fundamental component of the flux; (b) 3rd harmonic component of the flux; (c) 5th harmonic component of the flux; (d) 7th harmonic component of the flux; (e) 9th harmonic component of the flux; (f) Total resultant flux magnitude in time

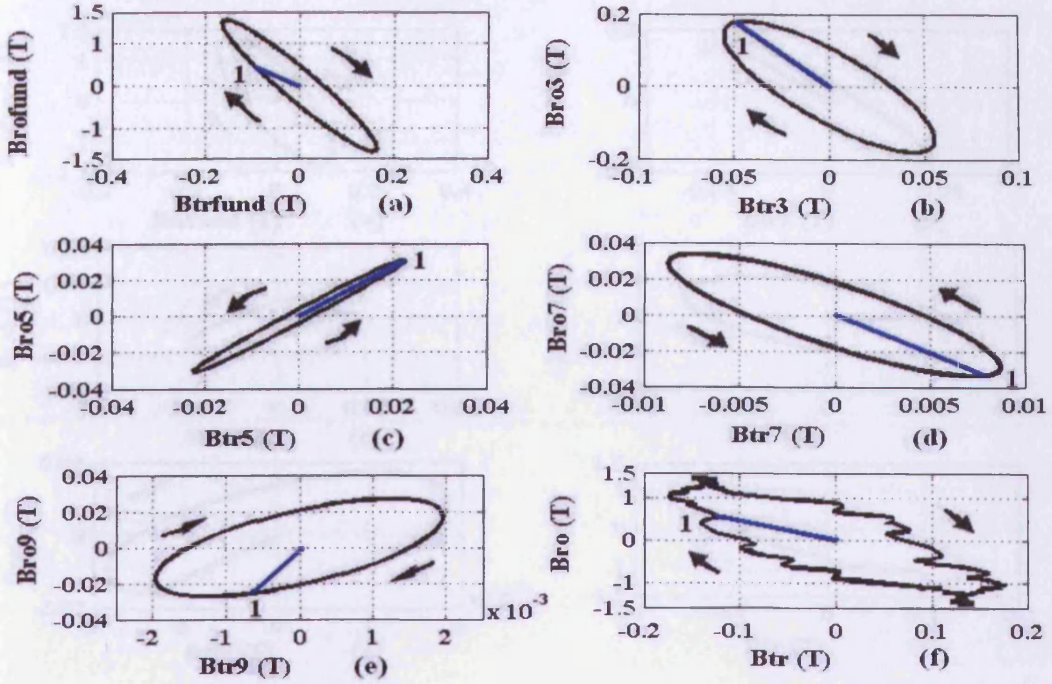

Fig. 4-22 Magnitude and direction of flux density at point 3 in the T-joints of the core relative to the flux in the B-Phase limb being zero, under PWM voltage excitation, m_a = 0.7, f_s = 1 kHz, f = 100 Hz, B_{peak} = 1.3 T. (a) Fundamental component of the flux; (b) 3rd harmonic component of the flux; (c) 5th harmonic component of the flux; (d) 7th harmonic component of the flux; (e) 9th harmonic component of the flux; (f) Total resultant flux magnitude in time

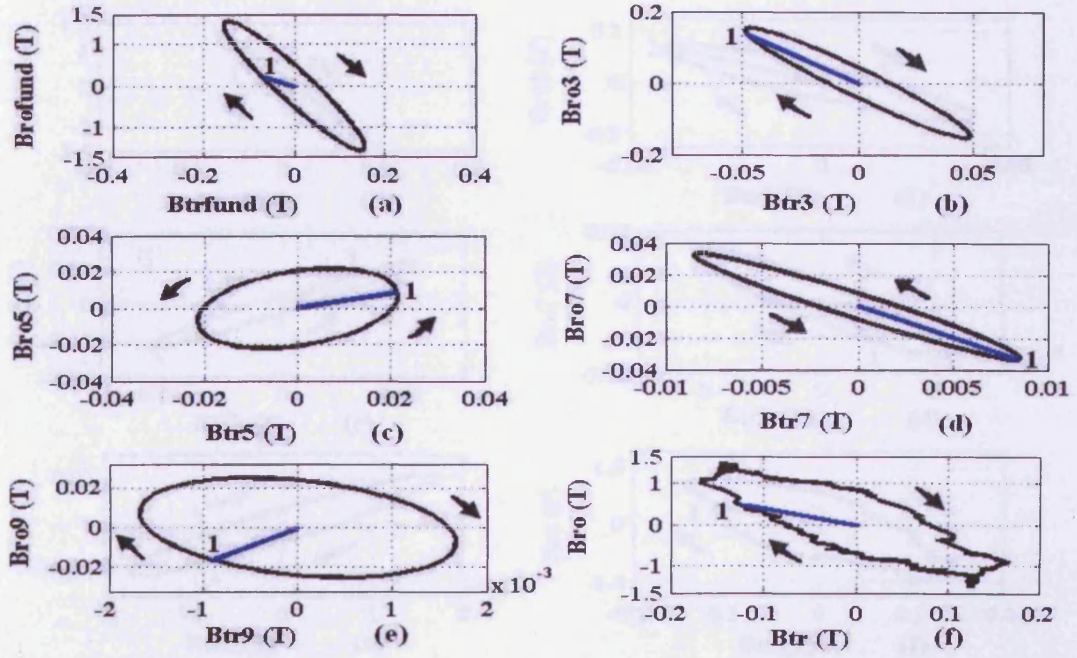

Fig. 4-23 Magnitude and direction of flux density at point 3 in the T-joints of the core relative to the flux in the B-Phase limb being zero, under PWM voltage excitation, m_a = 0.7, f_s = 2 kHz, f = 100 Hz, B_{peak} = 1.3 T. (a) Fundamental component of the flux; (b) 3rd harmonic component of the flux; (c) 5th harmonic component of the flux; (d) 7th harmonic component of the flux; (e) 9th harmonic component of the flux; (f) Total resultant flux magnitude in time

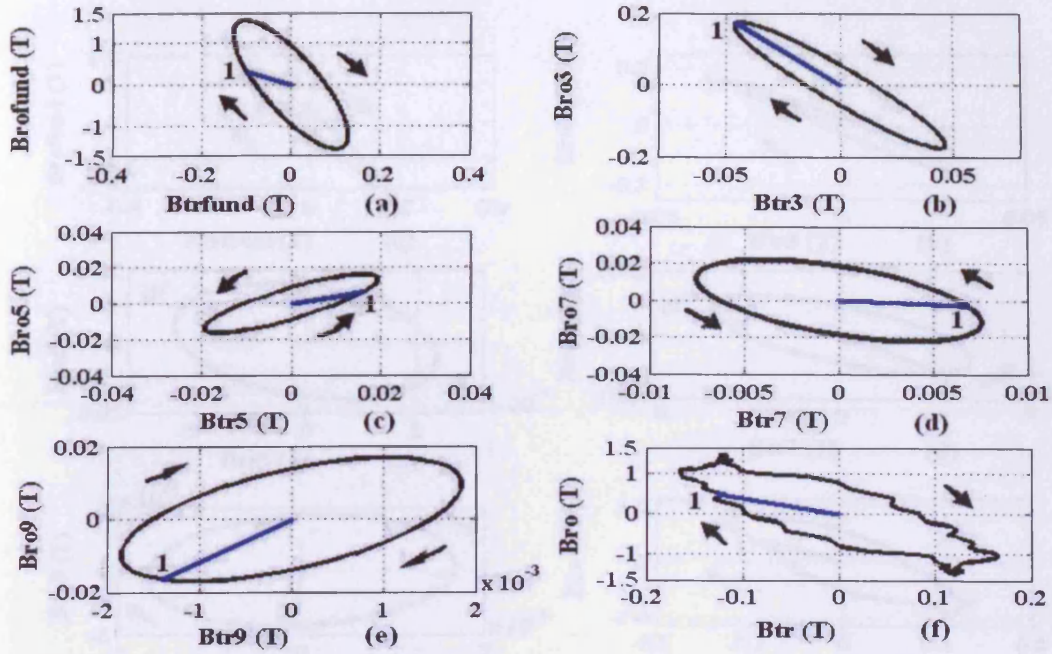

Fig. 4-24 Magnitude and direction of flux density at point 3 in the T-joints of the core relative to the flux in the B-Phase limb being zero, under PWM voltage excitation, m_a = 0.7, f_s = 3 kHz, f = 100 Hz, B_{peak} = 1.3 T. (a) Fundamental component of the flux; (b) 3rd harmonic component of the flux; (c) 5th harmonic component of the flux; (d) 7th harmonic component of the flux; (e) 9th harmonic component of the flux; (f) Total resultant flux magnitude in time

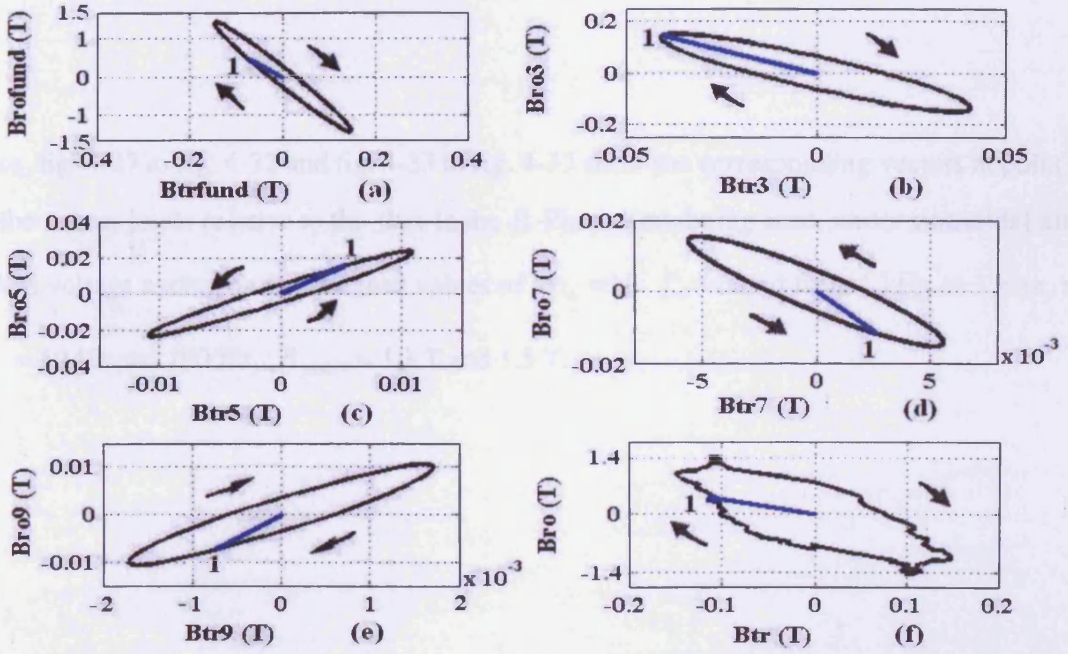

Fig. 4-25 Magnitude and direction of flux density at point 3 in the T-joints of the core relative to the flux in the B-Phase limb being zero, under PWM voltage excitation, m_a = 0.8, f_s = 3 kHz, f = 100 Hz, B_{peak} = 1.3 T. (a) Fundamental component of the flux; (b) 3rd harmonic component of the flux; (c) 5th harmonic component of the flux; (d) 7th harmonic component of the flux; (e) 9th harmonic component of the flux; (f) Total resultant flux magnitude in time

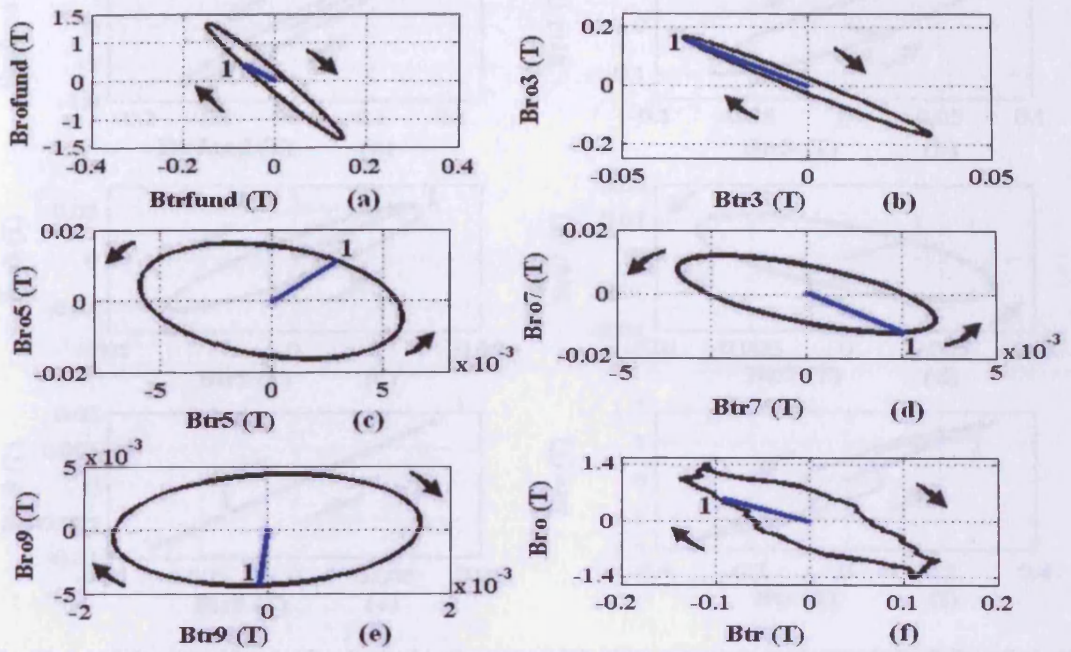

Fig. 4-26 Magnitude and direction of flux density at point 3 in the T-joints of the core relative to the flux in the B-Phase limb being zero, under PWM voltage excitation, m_a = 12, f_s = 3 kHz, f = 100 Hz, B_{peak} = 1.3 T. (a) Fundamental component of the flux; (b) 3rd harmonic component of the flux; (c) 5th harmonic component of the flux; (d) 7th harmonic component of the flux; (e) 9th harmonic component of the flux; (f) Total resultant flux magnitude in time

Also, fig. 4-27 to fig. 4-32 and fig. 4-33 to fig. 4-37 show the corresponding vectors at point 4 in the corner joints relative to the flux in the B-Phase limb being zero, under sinusoidal and PWM voltage excitation for assigned values of m_a with f_s varied from 1 kHz to 3 kHz, at f = 50 Hz and 100 Hz, B_{peak} = 1.3 T and 1.5 T.

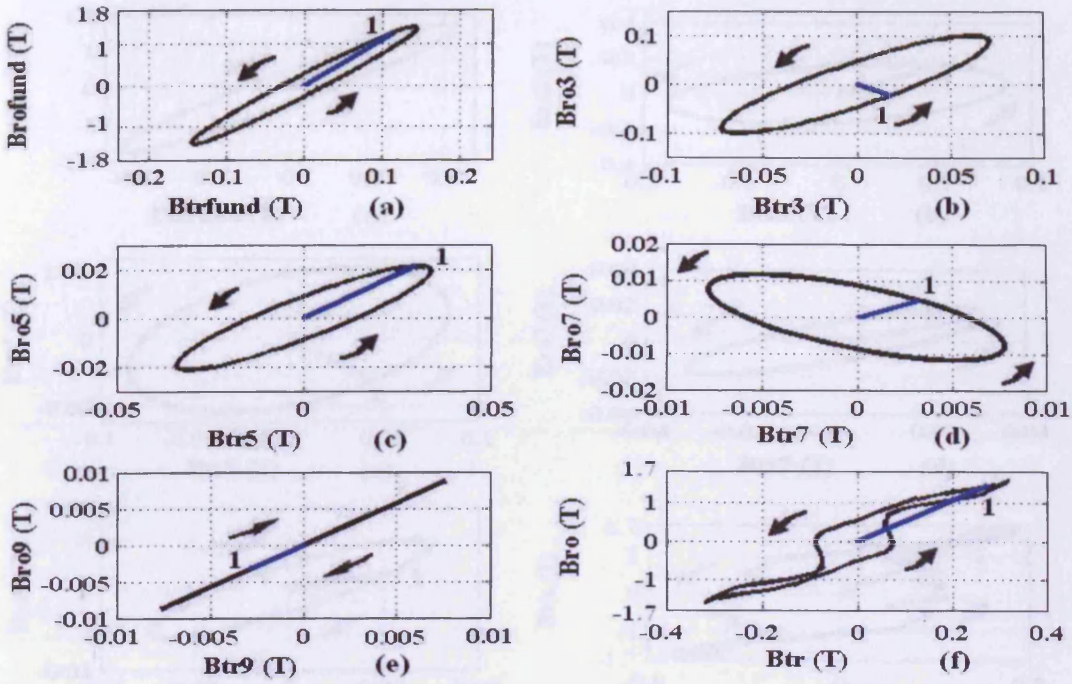

Fig. 4-27 Magnitude and direction of flux density at point 4 in the corner joints of the core relative to the flux in the B-Phase limb being zero, under sinusoidal voltage excitation, f = 50 Hz, B_{peak} = 1.5 T. (a) Fundamental component of the flux; (b) 3 rd harmonic component of the flux; (c) 5th harmonic component of the flux; (d) 7th harmonic component of the flux; (e) 9th harmonic component of the flux; (f) Total resultant flux magnitude in time

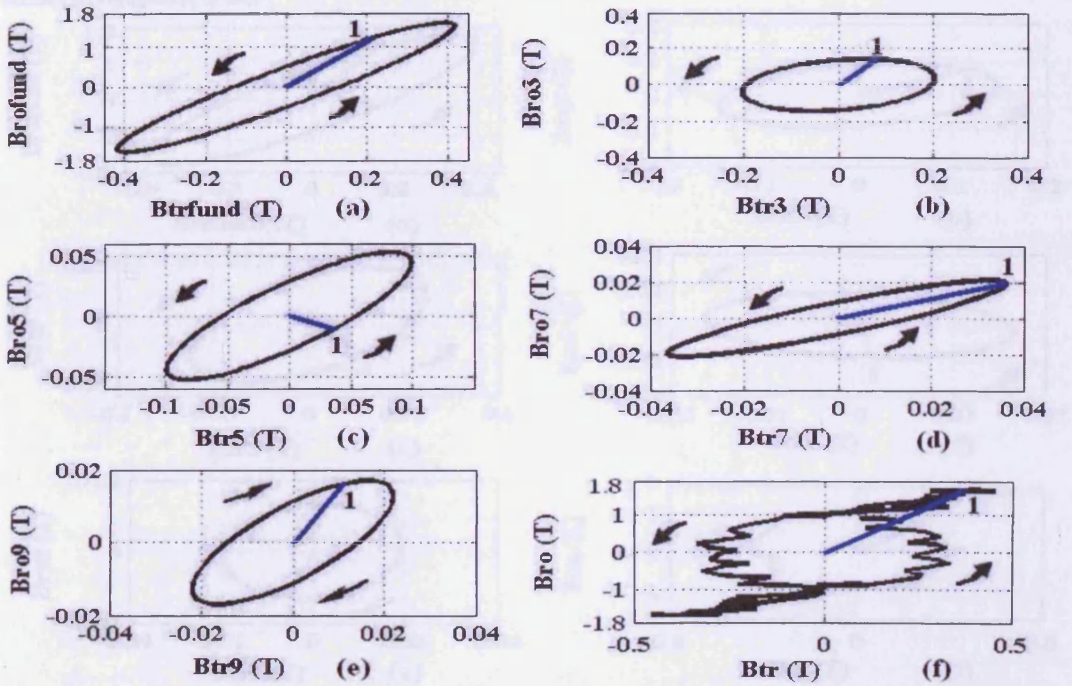

Fig. 4-28 Magnitude and direction of flux density at point 4 in the corner joints of the core relative to the flux in the B-Phase limb being zero, under PWM voltage excitation, m_a = 0.5, f_s = 1 kHz, f = 50 Hz, B_{peak} = 1.5 T. (a) Fundamental component of the flux; (b) 3rd harmonic component of the flux; (c) 5th harmonic component of the flux; (d) 7th harmonic component of the flux; (e) 9th harmonic component of the flux; (f) Total resultant flux magnitude in time

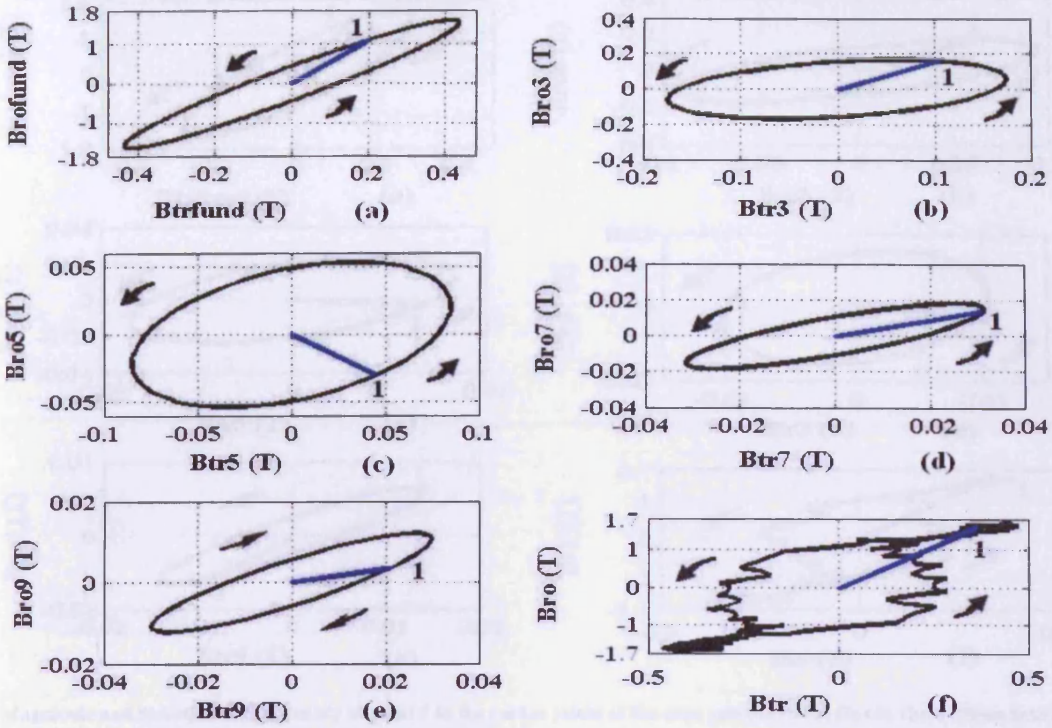

Fig. 4-29 Magnitude and direction of flux density at point 4 in the corner joints of the core relative to the flux in the B-Phase limb being zero, under PWM voltage excitation, m_a = 0.5, f_s = 2 kHz, f = 50 Hz, B_{peak} = 1.5 T. (a) Fundamental component of the flux; (b) 3rd harmonic component of the flux; (c) 5th harmonic component of the flux; (d) 7th harmonic component of the flux; (e) 9th harmonic component of the flux; (f) Total resultant flux magnitude in time

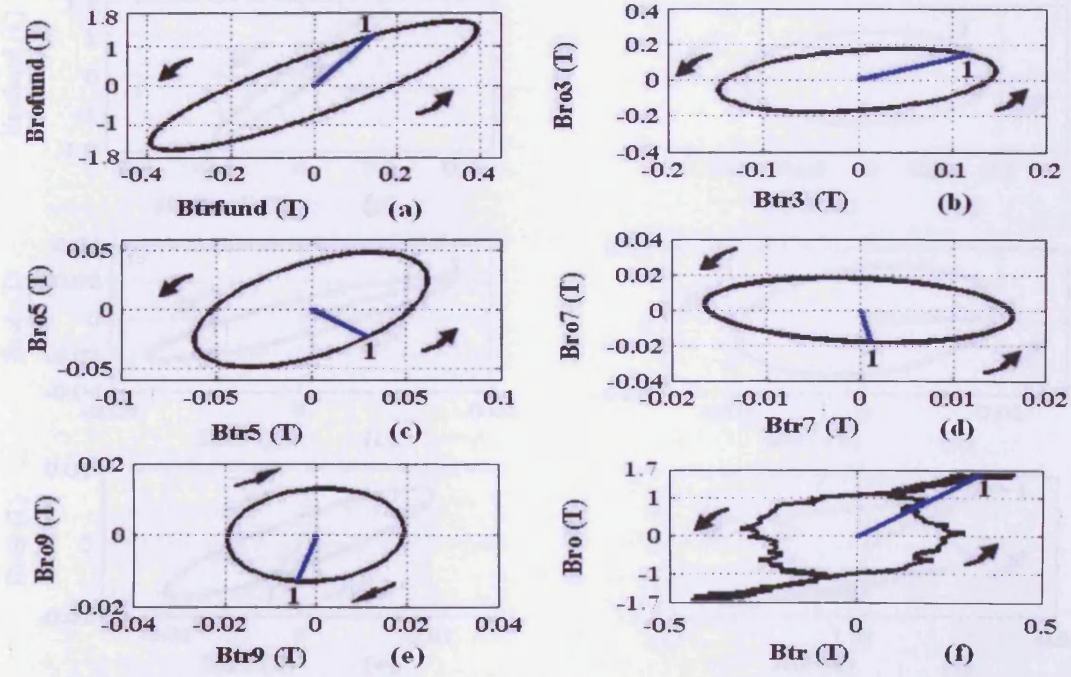

Fig. 4-30 Magnitude and direction of flux density at point 4 in the corner joints of the core relative to the flux in the B-Phase limb being zero, under PWM voltage excitation, m_a = 0.5, f_s = 3 kHz, f = 50 Hz, B_{peak} = 1.5 T. (a) Fundamental component of the flux; (b) 3rd harmonic component of the flux; (c) 5th harmonic component of the flux; (d) 7th harmonic component of the flux; (e) 9th harmonic component of the flux; (f) Total resultant flux magnitude in time

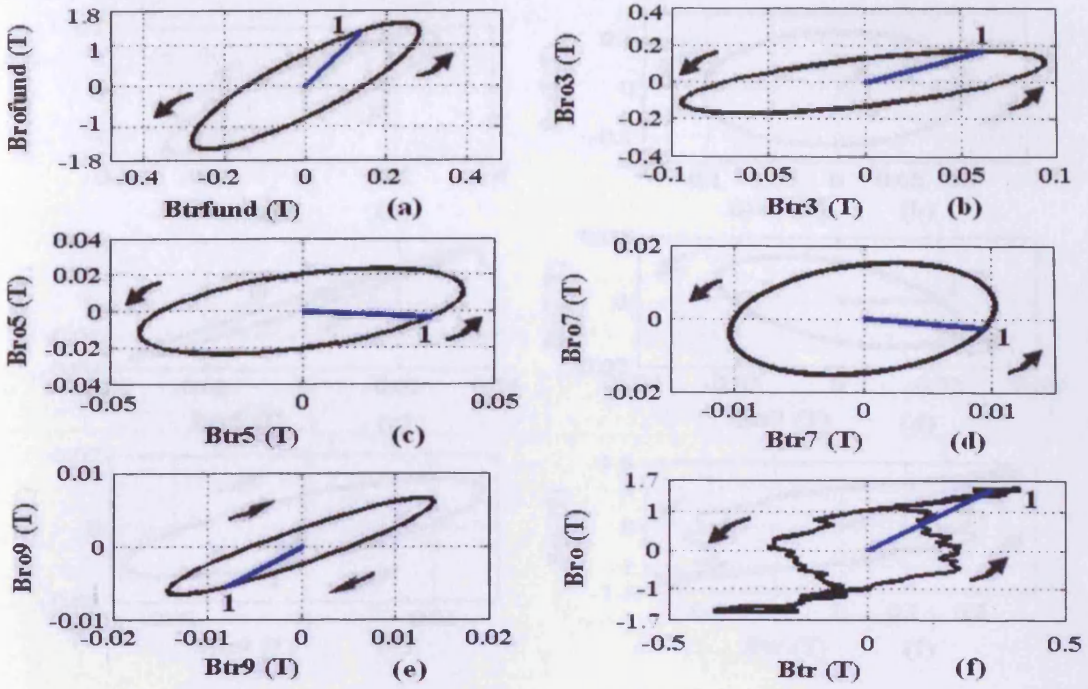

Fig. 4-31 Magnitude and direction of flux density at point 4 in the corner joints of the core relative to the flux in the B-Phase limb being zero under PWM voltage excitation, m_a = 0.8, f_s = 3 kHz, f = 50 Hz, B_{peak} = 1.5 T. (a) Fundamental component of the flux; (b) 3rd harmonic component of the flux; (c) 5th harmonic component of the flux; (d) 7th harmonic component of the flux; (e) 9th harmonic component of the flux; (f) Total resultant flux magnitude in time

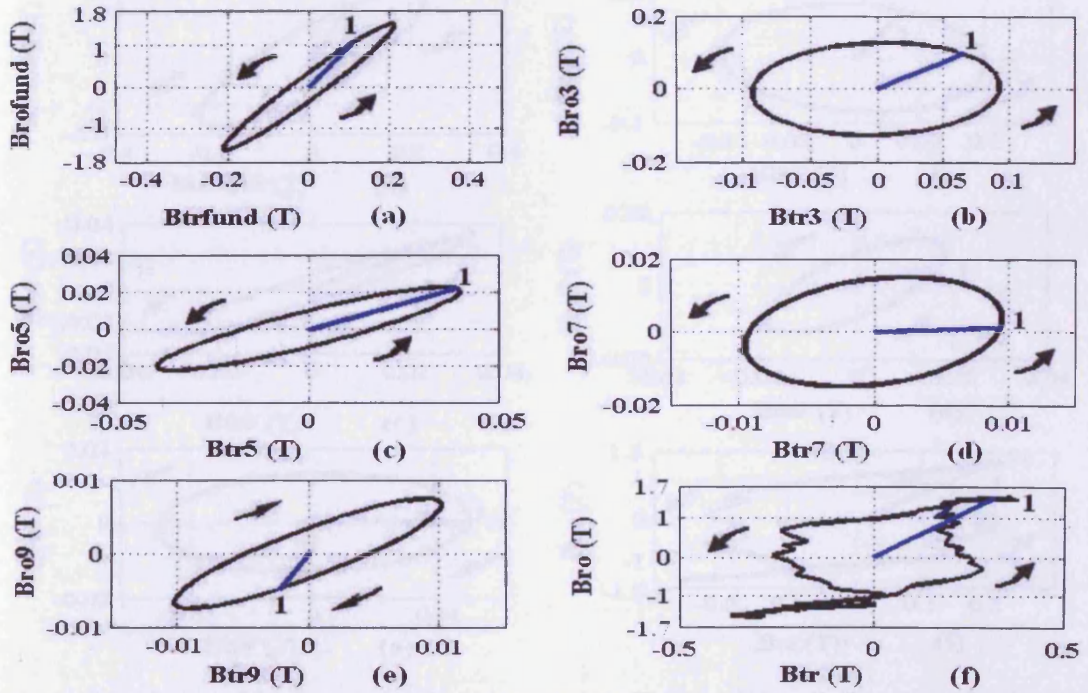

Fig. 4-32 Magnitude and direction of flux density at point 4 in the corner joints of the core relative to the flux in the B-Phase limb being zero under PWM voltage excitation, m_a = 1.2, f_s = 3 kHz, f = 50 Hz, B_{peak} = 1.5 T. (a) Fundamental component of the flux; (b) 3rd harmonic component of the flux; (c) 5th harmonic component of the flux; (d) 7th harmonic component of the flux; (e) 9th harmonic component of the flux; (f) Total resultant flux magnitude in time

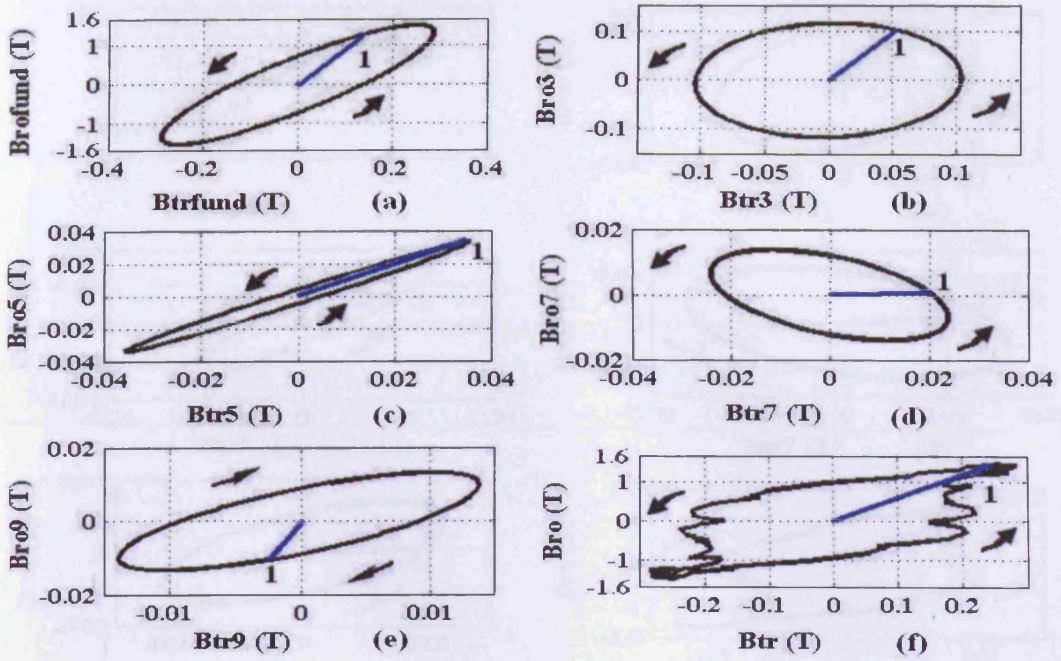

Fig. 4-33 Magnitude and direction of flux density at point 4 in the corner joints of the core relative to the flux in the B-Phase limb being zero, under PWM voltage excitation, m_a = 0.7, f_s = 1 kHz, f = 100 Hz, B_{peak} = 1.3 T. (a) Fundamental component of the flux; (b) 3rd harmonic component of the flux; (c) 5th harmonic component of the flux; (d) 7th harmonic component of the flux; (e) 9th harmonic component of the flux; (f) Total resultant flux magnitude in time

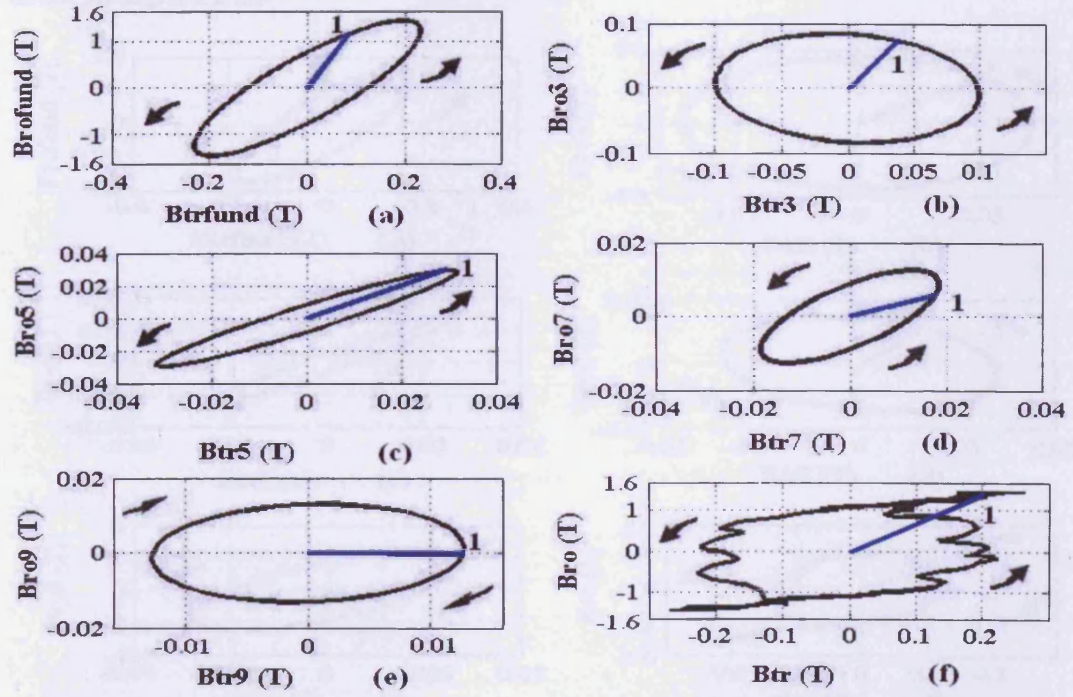

Fig. 4-34 Magnitude and direction of flux density at point 4 in the corner joints of the core relative to the flux in the B-Phase limb being zero, under PWM voltage excitation, m_a = 0.7, f_s = 2 kHz, f = 100 Hz, B_{peak} = 1.3 T. (a) Fundamental component of the flux; (b) 3rd harmonic component of the flux; (c) 5th harmonic component of the flux; (d) 7th harmonic component of the flux; (e) 9th harmonic component of the flux; (f) Total resultant flux magnitude in time

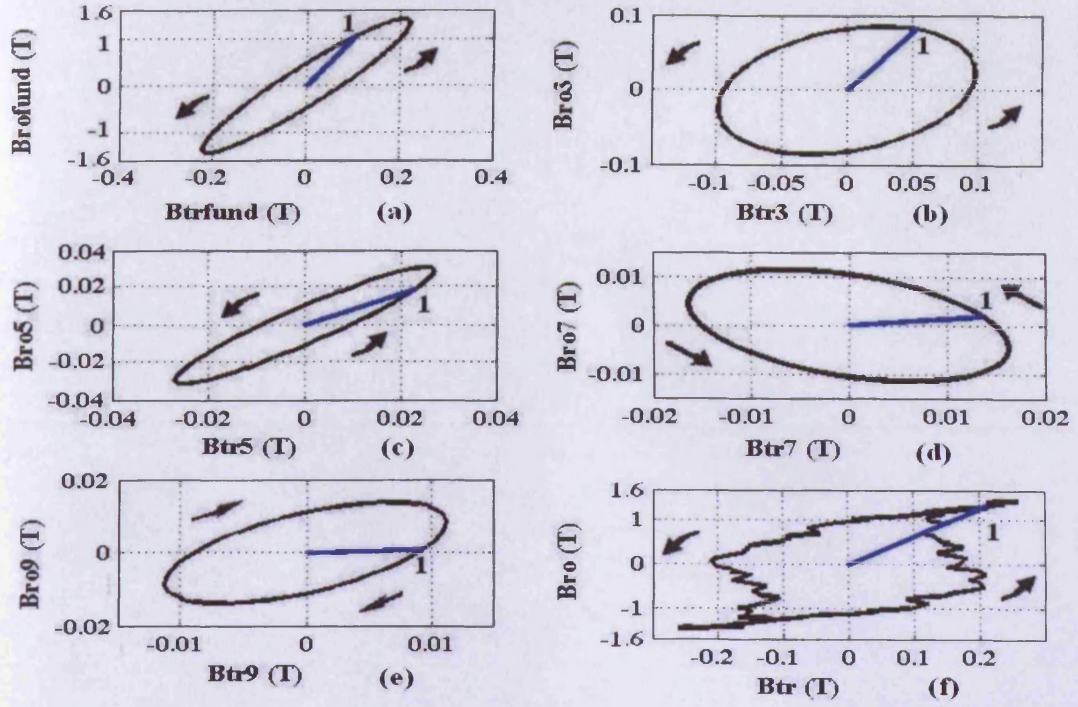

Fig. 4-35 Magnitude and direction of flux density at point 4 in the corner joints of the core relative to the flux in the B-Phase limb being zero, under PWM voltage excitation, m_a = 0.7, f_s = 3 kHz, f = 100 Hz, B_{peak} = 1.3 T. (a) Fundamental component of the flux; (b) 3rd harmonic component of the flux; (c) 5th harmonic component of the flux; (d) 7th harmonic component of the flux; (e) 9th harmonic component of the flux; (f) Total resultant flux magnitude in time

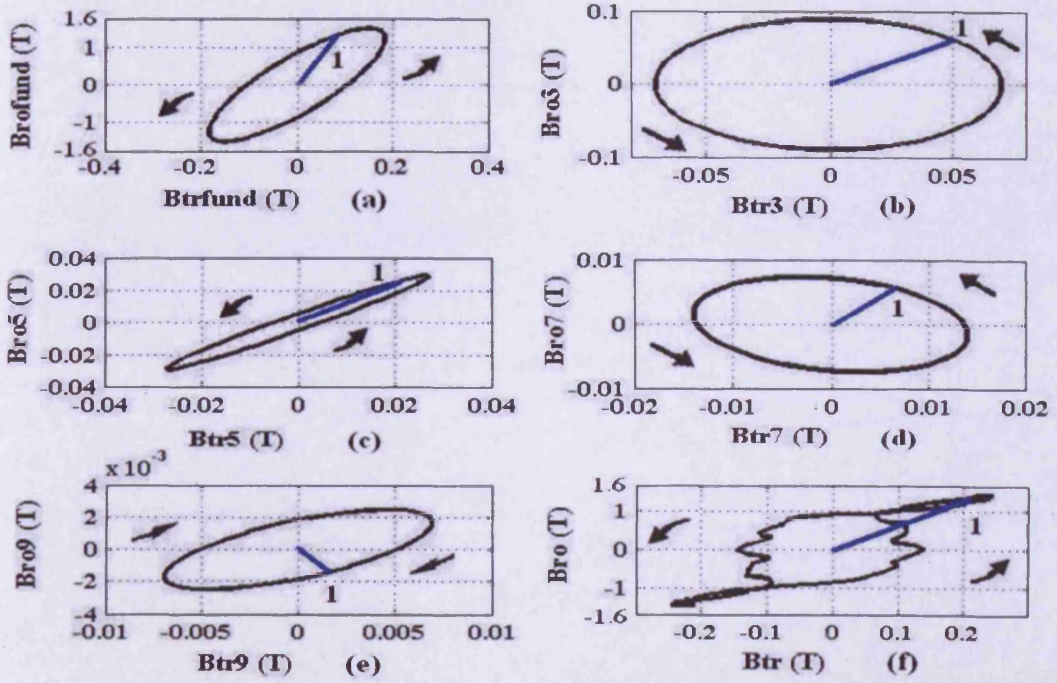

Fig. 4-36 Magnitude and direction of flux density at point 4 in the corner joints of the core relative to the flux in the B-Phase limb being zero, under PWM voltage excitation, m_a = 0.8, f_s = 3 kHz, f = 100 Hz, B_{peak} = 1.3 T. (a) Fundamental component of the flux; (b) 3rd harmonic component of the flux; (c) 5th harmonic component of the flux; (d) 7th harmonic component of the flux; (e) 9th harmonic component of the flux; (f) Total resultant flux magnitude in time

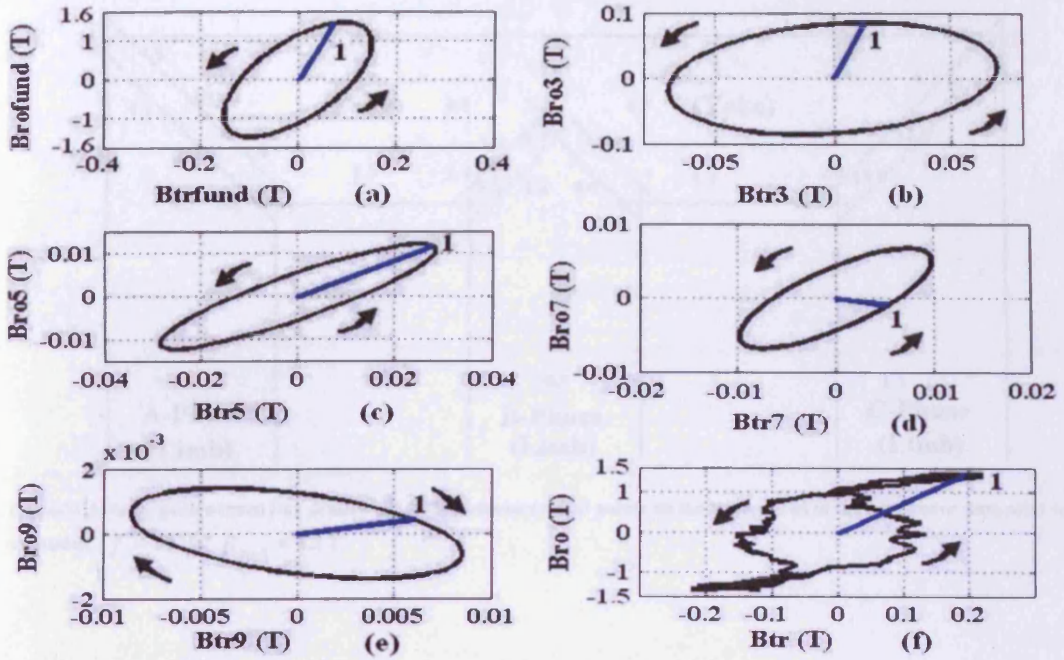

Fig. 4-37 Magnitude and direction of flux density at point 4 in the corner joints of the core relative to the flux in the B-Phase limb being zero, under PWM voltage excitation, m_a = 1.2, f_s = 3 kHz, f = 100 Hz, B_{peak} = 1.3 T. (a) Fundamental component of the flux; (b) 3rd harmonic component of the flux; (c) 5th harmonic component of the flux; (d) 7th harmonic component of the flux; (e) 9th harmonic component of the flux; (f) Total resultant flux magnitude in time

4.3.3 Measurement results of localised normal flux density

Fig. 4-38 to fig. 4-43 and fig. 4-44 to fig. 4-48 show the average peak values of normal flux density $\hat{B}_z$ (mT) at measurement points on the laminations of the core under sinusoidal and PWM voltage excitation for assigned values of m_a with f_s varied in the range of 1 kHz to 3 kHz, at f = 50 Hz and 100 Hz, B_{peak} = 1.3 T and 1.5 T.

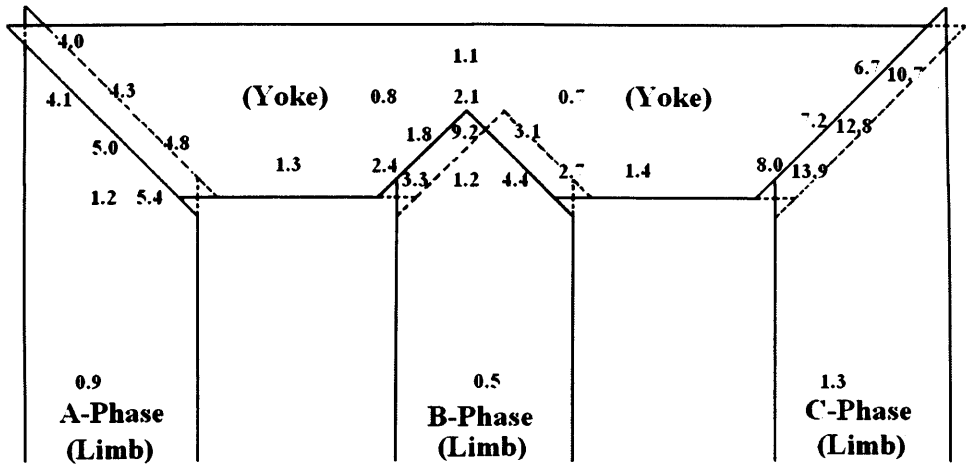

Fig. 4-38 Average peak normal flux density $\hat{B}_z$ (mT) at measurement points on the laminations of the core under sinusoidal voltage excitation, f = 50 Hz, B_{peak} = 1.5 T

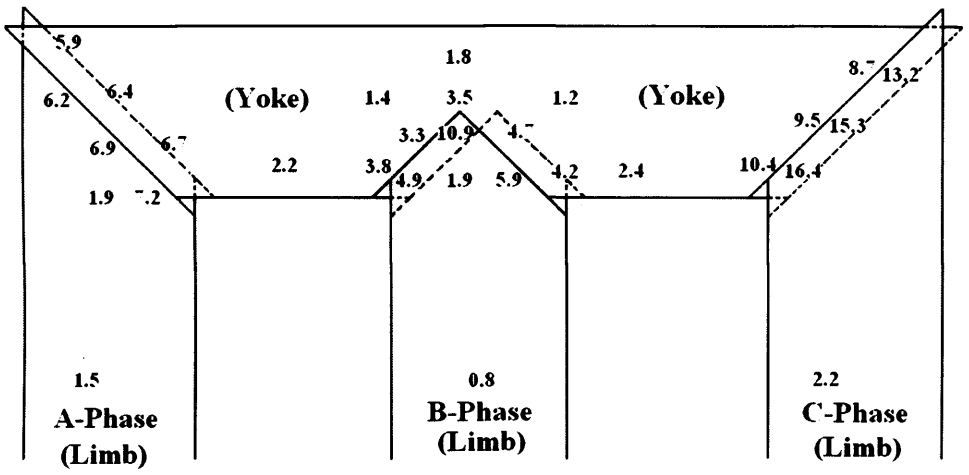

Fig. 4-39 Average peak normal flux density $\hat{B}_z$ (mT) at measurement points on the laminations of the core under PWM voltage excitation, m_a = 0.5, f_s = 1 kHz, f = 50 Hz, B_{peak} = 1.5 T

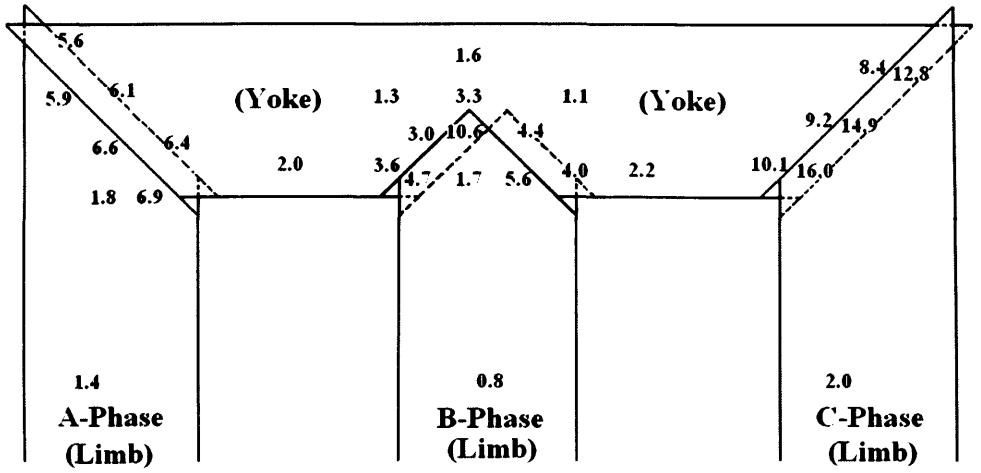

Fig. 4-40 Average peak normal flux density $\hat{B}_z$ (mT) at measurement points on the laminations of the core under PWM voltage excitation, m_a = 0.5, f_s = 2 kHz, f = 50 Hz, B_{peak} = 1.5 T

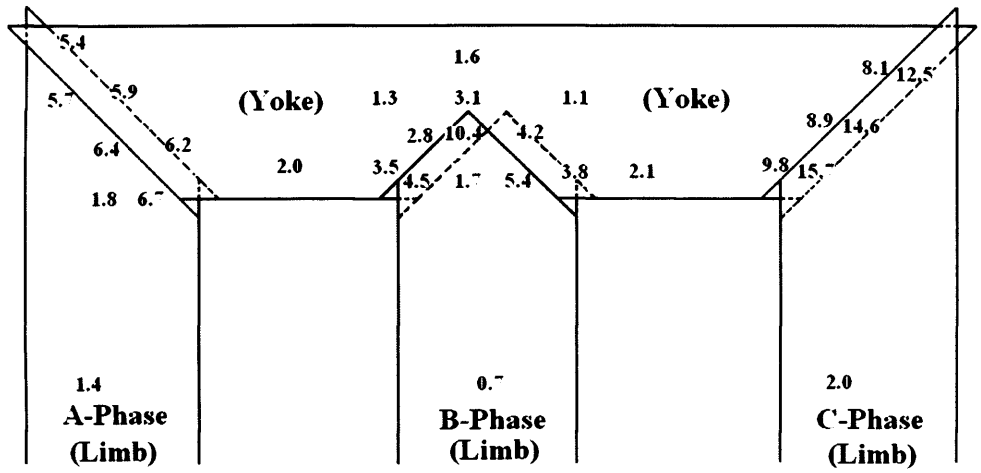

Fig. 4-41 Average peak normal flux density $\hat{B}_z$ (mT) at measurement points on the laminations of the core under PWM voltage excitation, m_a = 0.5, f_s = 3 kHz, f = 50 Hz, B_{peak} = 1.5 T

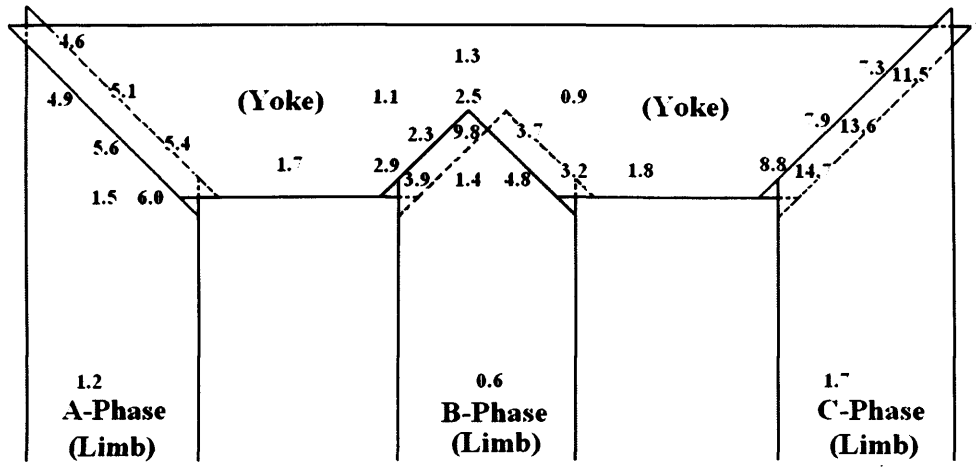

Fig. 4-42 Average peak normal flux density $\hat{B}_z$ (mT) at measurement points on the laminations of the core under PWM voltage excitation, m_a = 0.8, f_s = 3 kHz, f = 50 Hz, B_{peak} = 1.5 T

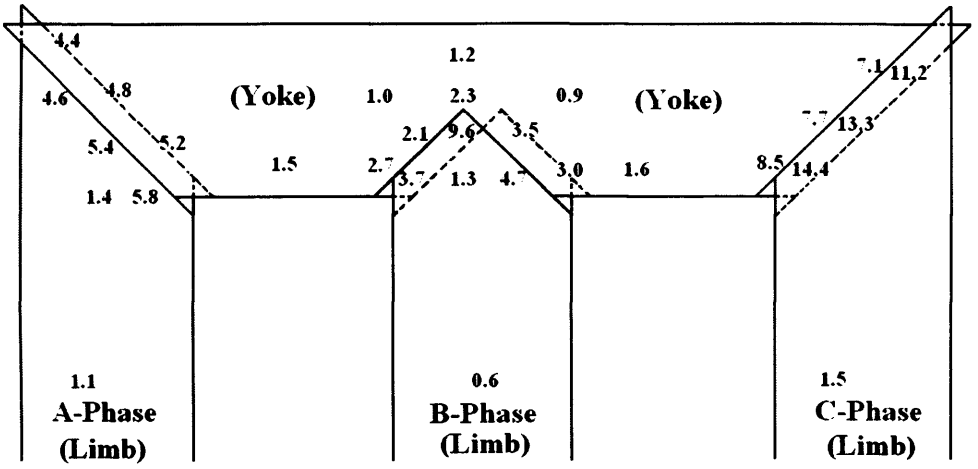

Fig. 4-43 Average peak normal flux density $\hat{B}_z$ (mT) at measurement points on the laminations of the core under PWM voltage excitation, m_a = 1.2, f_s = 3 kHz, f = 50 Hz, B_{peak} = 1.5 T

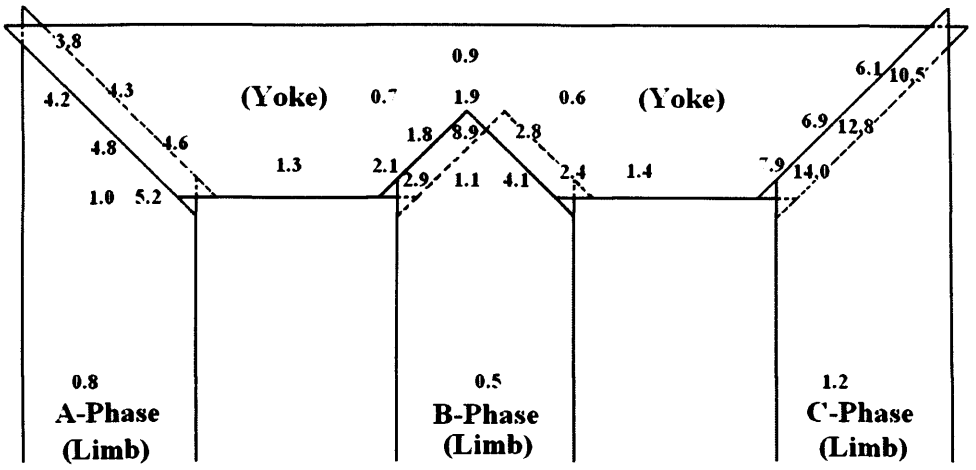

Fig. 4-44 Average peak normal flux density $\hat{B}_z$ (mT) at measurement points on the laminations of the core under PWM voltage excitation, m_a = 0.7, f_s = 1 kHz, f = 100 Hz, B_{peak} = 1.3 T

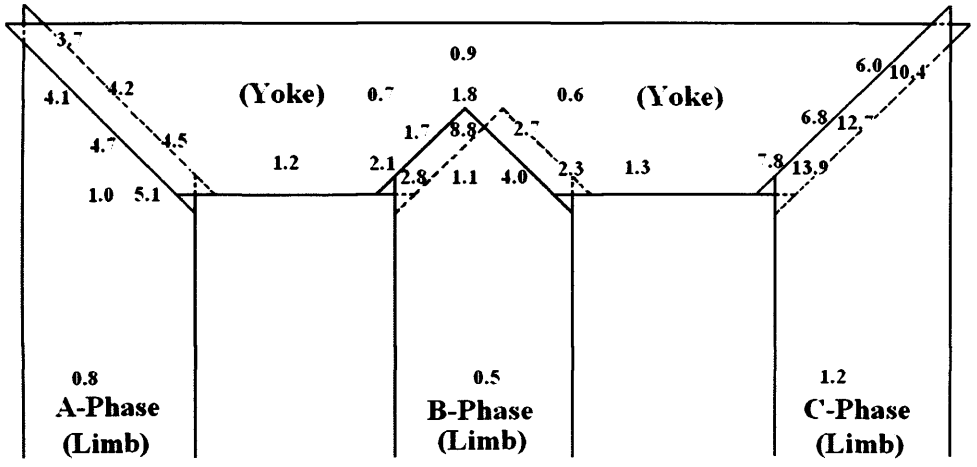

Fig. 4-45 Average peak normal flux density $\hat{B}_z$ (mT) at measurement points on the laminations of the core under PWM voltage excitation, m_a = 0.7, f_s = 2 kHz, f = 100 Hz, B_{peak} = 1.3 T

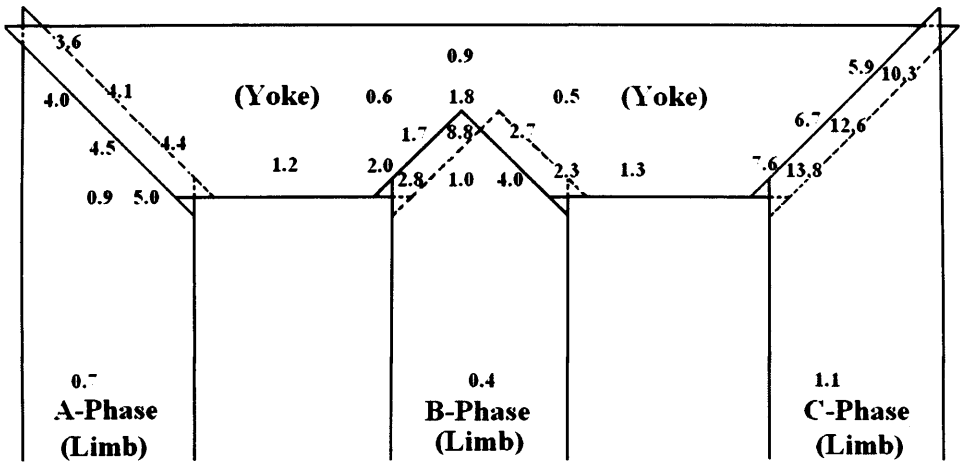

Fig. 4-46 Average peak normal flux density $\hat{B}_z$ (mT) at measurement points on the laminations of the core under PWM voltage excitation, m_a = 0.7, f_s = 3 kHz, f = 100 Hz, B_{peak} = 1.3 T

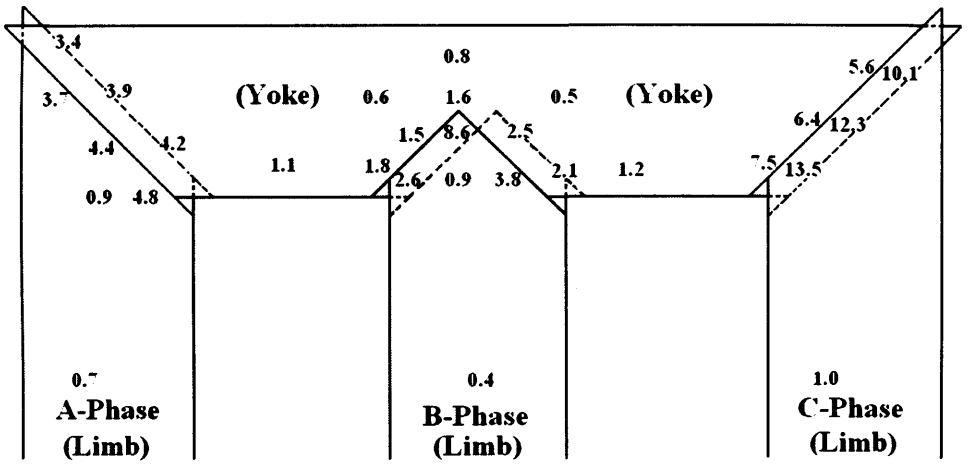

Fig. 4-47 Average peak normal flux density $\hat{B}_z$ (mT) at measurement points on the laminations of the core under PWM voltage excitation, m_a = 0.8, f_s = 3 kHz, f = 100 Hz, B_{peak} = 1.3 T

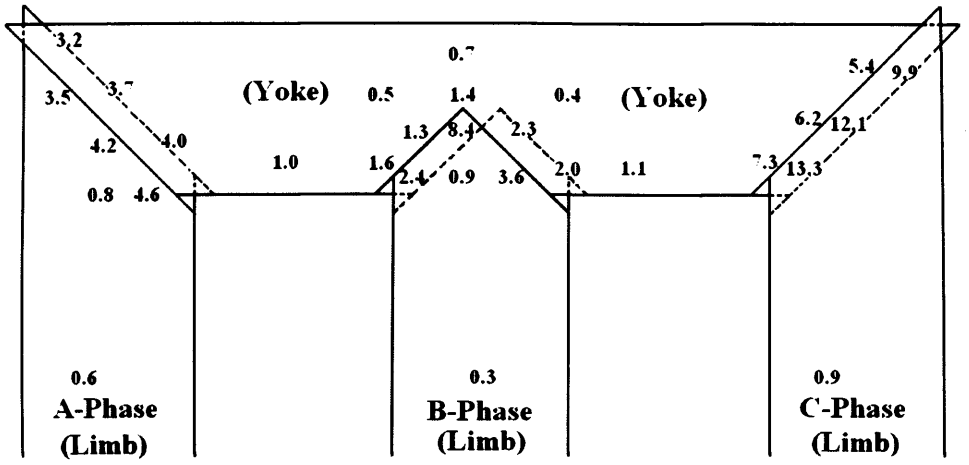

Fig. 4-48 Peak normal flux density $\hat{B}_z$ (mT) at measurement points on the laminations of the core under PWM voltage excitation, m_a = 1.2, f_s = 3 kHz, f = 100 Hz, B_{peak} = 1.3 T

Fig. 4-38 to fig. 4-48 show the mean peak values distribution of normal flux density $\hat{B}_z$ at measurement points on the laminations of the core (fig. 4-5) under sinusoidal and PWM voltage excitation. Therefore, the mean peak values of normal flux density at different regions of the core, i.e., limbs and yokes, T-joints and corner joints, could be inferred, which are shown in table 4.4.

Magnetisation frequency [f]	Modulation index m_a [OV %]	Switching frequency [f_s][kHz]	Limb, Yoke $\hat{B}_z$ [mT]		T-joints $\hat{B}_z$ [mT]		Corners $\hat{B}_z$ [mT]	
			1.3 T	1.5 T	1.3 T	1.5 T	1.3 T	1.5 T
sine 50 Hz	--	--	--	1.0	--	3.6	--	7.1
PWM 50 Hz	0.5 [40 %]	1	--	1.8	--	5.2	--	9.4
		2	--	1.6	--	4.9	--	9.1
		3	--	1.6	--	4.7	--	8.8
	0.8 [70 %]	1	--	1.4	--	4.2	--	8.2
		2	--	1.3	--	4.2	--	8.0
		3	--	1.3	--	4.1	--	7.9
	1.2 [90 %]	3	--	1.2	--	3.9	--	7.7
PWM 100 Hz	0.7 [60 %]	1	1.0	--	3.4	--	7.0	--
		2	0.9	--	3.3	--	6.9	--
		3	0.9	--	3.1	--	6.7	--
	0.8 [70 %]	1	0.9	1.5	3.1	4.4	6.7	8.4
		2	0.8	1.5	3.0	4.3	6.6	8.3
		3	0.8	1.4	3.0	4.3	6.6	8.3
	1.2 [90 %]	3	0.7	--	2.8	--	6.4	--

Table 4.4 Mean peak normal flux density at different regions of the core under sinusoidal and PWM voltage excitation for assigned values of m_a with f_s varied from 1 kHz to 3 kHz, at f = 50 Hz and 100 Hz, B_{peak} = 1.3 T and 1.5 T

4.4 Analysis and discussion

4.4.1 Influence of modulation index and switching frequency on specific total power losses and its eddy-current losses component of the core

The $THD[\%]$ of primary voltage $e_1(t)$ and the form factor K_f of secondary induced voltages $e_2(t)$, calculated after FFT analysis, are shown in table 4.5 and table 4.6 for assigned values of m_a in the range of 0.5 to 1.2 with f_s varied from 1 kHz to 3 kHz, at f = 50 Hz and 100 Hz, B_{peak} = 1.3 T.

Magnetisation frequency $[f]$	Modulation index m_a [OV %]	Switching frequency $[f_s]$[kHz]			
		1	2	3	--
sine 50 Hz	--	--	--	--	2.4
PWM 50 Hz	0.5 [40 %]	117	112	109	--
	0.7 [60 %]	90.1	86.7	83.5	--
	0.8 [70 %]	71.8	67.1	62.5	--
	1.0 [80 %]	--	--	55.4	--
	1.2 [90 %]	--	--	49.1	--
PWM 100 Hz	0.6 [50 %]	121	117	114	--
	0.7 [60 %]	95.9	92.1	88.6	--
	0.8 [70 %]	76.4	75.3	74.0	--
	1.0 [80 %]	--	--	63.1	--
	1.2 [90 %]	--	--	54.3	--

Table 4.5 $THD[\%]$ **of** $e_1(t)$ **under sinusoidal and PWM voltage excitation,** m_a **= 0.5 - 1.2 with** f_s **varied from 1 kHz to 3 kHz, at** f **= 50 Hz and 100 Hz,** B_{peak} **= 1.3 T**

Magnetisation frequency [f]	Modulation index m_a [OV %]	Form factor K_f			
		f_s = 1 kHz	f_s = 2 kHz	f_s = 3 kHz	--
sine 50 Hz	--	--	--	--	1.15
PWM 50 Hz	0.5 [40 %]	1.57	1.42	1.41	--
	0.7 [60 %]	1.38	1.34	1.28	--
	0.8 [70 %]	1.28	1.28	1.24	--
	1.0 [80 %]	--	--	1.21	--
	1.2 [90 %]	--	--	1.19	--
PWM 100 Hz	0.6 [50 %]	1.45	1.45	1.40	--
	0.7 [60 %]	1.38	1.38	1.35	--
	0.8 [70 %]	1.35	1.35	1.30	--
	1.0 [80 %]	--	--	1.26	--
	1.2 [90 %]	--	--	1.22	--

Table 4.6 K_f of $e_2(t)$ under sinusoidal and PWM voltage excitation, m_a = 0.5 - 1.2 with f_s varied from 1 kHz to 3 kHz, at f = 50 Hz and 100 Hz, B_{peak} = 1.3 T

From fig. 4-8 to fig. 4-10, the highest specific total losses of the core occurs at the lowest values of m_a = 0.5 and 0.6 (f_s = 3 kHz) as f was set to 50 Hz and 100 Hz respectively, and it was noticed that the specific total losses were decreased with the increase of modulation index m_a. It was observed that at m_a = 0.5 and 0.6, the losses were around 0.35 W/kg (36.0%) and 0.98 W/kg (34.3%) respectively, greater than those at m_a = 1.2 as f was set to 50 Hz and 100 Hz, at B_{peak} = 1.3 T. This was caused by higher harmonic contents in the voltage waveforms produced by the PWM inverter at the lower values of m_a (table 4.5), which resulted in the higher form factors of the secondary induced voltages (table 4.6).

It is shown in fig. 4-11 to fig. 4-14 that the highest specific total losses were seen to be at the lowest values of m_a = 0.5 and 0.6 and at the lowest value of switching frequency f_s = 1

kHz as f was set to 50 Hz and 100 Hz respectively. Also, from fig. 4-11 to fig. 4-15, it was noticed that an increase in the switching frequency f_s led, under all PWM voltage excitation, to a reduction in specific total losses. It was observed that, at m_a = 0.5 and 0.8 (f = 50 Hz), the reduction of specific total losses were around 0.17 W/kg (11.4%) and 0.03 W/kg (3.1%) respectively, with an increase in f_s from 1 kHz to 3 kHz, at B_{peak} = 1.3 T, and also the reduction of losses were around 0.23 W/kg (11.1%) and 0.05 W/kg (3.4%) respectively, at B_{peak} = 1.5 T. Moreover, at m_a = 0.6 and 0.8, the reduction of specific total losses were around 0.37 W/kg (8.8%) and 0.08 W/kg (2.3%) respectively, with an increase in f_s from 1 kHz to 3 kHz as f was set to 100 Hz, at B_{peak} = 1.3 T. Also, at m_a = 0.8, the reduction of loss was around 0.10 W/kg (2.2%) with an increase in f_s from 1 kHz to 3 kHz, at B_{peak} = 1.5 T. This was caused by higher harmonic contents in the primary voltage waveforms produced by the PWM inverter at lower value of f_s (table 4.5), which resulted in higher form factors of the secondary induced voltages (table 4.6). The beneficial effect observed was enhanced at low value of m_a and at f = 50 Hz. It can be seen in table 4.6 that at f = 50 Hz, the values of K_f were decreased around 10.2% and 3.1% at m_a = 0.5 and 0.8 respectively, when f_s was increased from 1 kHz to 3 kHz. Whereas, at f = 100 Hz, the values of K_f were decreased around 3.4% and 3.7% at m_a = 0.6 and 0.8 respectively, when f_s was increased from 1 kHz to 3 kHz.

It is known that the iron loss increases in the case of PWM supply is mainly attributed to the eddy-current component loss increment inside the iron core [*4.5*]. Also, Under PWM voltage excitation, there are many high-frequency harmonic flux density components; each harmonic component will contribute to the total eddy-current component loss. In transformer core with laminations of thickness d [m], resistivity [□m] and density m [kg/m^3], the eddy-current

component loss P_e (W/kg) is given by (4.2), so the eddy-current loss of each harmonic component can be calculated.

$$P_e = \frac{4d^2 K_f^2}{3\ m} \square B_n^2 f_n^2 \qquad [4.6] \qquad (4.2)$$

Analysis of the flux density $B(t)$ in the core under sinusoidal and PWM voltage excitation using FFT, performed with "Day Post Processor" in " Ansoft Simplorer Simulation Centre" environment, was carried out to obtain the harmonic components of amplitude B_n and frequency f_n, which were used to calculate the eddy-current loss by equation (4.2). Therefore, the eddy-current loss is mainly related to the amplitude of the fundamental and the amplitude of the harmonics at the switching frequency f_s (fig. 1-3).

Fig. 4-49 and fig. 4-50 show the specific total losses and its eddy-current components under sinusoidal and PWM voltage excitation for assigned values of m_a with f_s, at f = 50 Hz and 100 Hz, B_{peak} = 1.3 T.

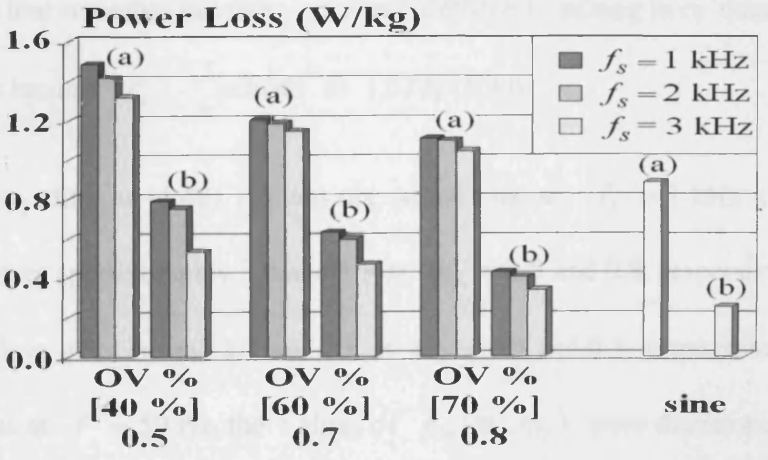

Fig. 4-49 Specific total losses (a) and its eddy-current component losses (b) under sinusoidal and PWM voltage excitation, m_a = 0.5, 0.7 and 0.8 with f_s varied from 1 kHz to 3 kHz, at f = 50 Hz, B_{peak} = 1.3 T

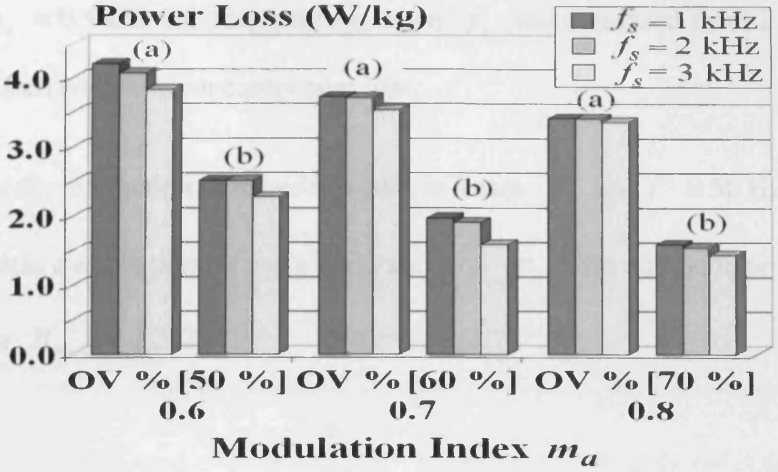

Fig. 4-50 Specific total losses (a) and its eddy-current component losses (b) under PWM voltage excitation, m_a = 0.6, 0.7 and 0.8 with f_s varied from 1 kHz to 3 kHz, at f = 100 Hz, B_{peak} = 1.3 T

It was expected in fig. 4-49 and fig. 4-50 that the specific total losses and its eddy-current component losses were reduced when the value of m_a and f_s were increased, which was due to higher harmonic contents in the flux density waveforms at low values of m_a and f_s that was caused by higher form factors of the secondary induced voltages (table 4.6); also, since the PWM harmonics appear as sidebands of the switching frequency f_s and their multiples (fig. 1-3), increasing the f_s shifts the harmonics even far away from the fundamental so that smoothes out flux steps (dB/dt), resulting in reduced eddy-current component loss because $P_e \propto \int_0^T |dB/dt|^2 dt$ [*1.11*] [*1.30*].

In addition, according to (1.42), it was obtained that at f_s = 1 kHz, the values of $g_M(m_a, m_f)$ were approximately 3.0 and 1.9 at m_a = 0.5 and 0.8, respectively; also, at f_s = 3 kHz, the values were around 2.7 and 1.8 at m_a = 0.5 and 0.8, respectively. Therefore, it was noticed that at f = 50 Hz, the values of $g_M(m_a, m_f)$ were decreased around 10.0%

and 5.3% at m_a = 0.5 and 0.8, respectively, when f_s was increased from 1 kHz to 3 kHz, resulting in reduced eddy-current component loss.

Table 4.7 shows the reduction of the eddy-current losses P_e, at f = 50 Hz and 100 Hz, under PWM voltage excitation for assigned values of m_a with an increase in f_s from 1 kHz to 3 kHz, at B_{peak} = 1.3 T.

Magnetisation frequency [f]	Modulation index m_a [OV %]	Reduction [%]
PWM 50 Hz	0.5 [40 %]	40.8
	0.8 [70 %]	20.8
PWM 100 Hz	0.6 [50 %]	9.4
	0.8 [70 %]	9.7

Table 4.7 Reduction of P_e under PWM voltage excitation for assigned values of m_a with an increase in f_s from 1 kHz to 3 kHz, at f = 50 Hz and 100 Hz, B_{peak} = 1.3 T

It was observed in table 4.7 that, at f = 50 Hz, the eddy-current losses were affected by variations in the f_s, especially at low value of m_a = 0.5. However, at f = 100 Hz, although higher value of f_s proved beneficial, their effect on eddy-current losses was not apparent.

Table 4.8 shows the variation of specific total losses P_{sl} (W/kg) and its eddy-current component losses P_e (W/kg) under sinusoidal and PWM voltage excitation for assigned values of m_a with f_s varied in the range of 1 kHz to 3 kHz, at f = 50 Hz and 100 Hz, B_{peak} = 1.5 T.

Magnetisation frequency [f]	Modulation index m_a [OV %]	Specific total losses and its eddy-current component losses (W/kg)							
		f_s = 1 kHz		f_s = 2 kHz		f_s = 3 kHz		--	
		P_{st}	P_e	P_{st}	P_e	P_{st}	P_e	P_{st}	P_e
sine 50 Hz	--	--	--	--	--	--	--	1.27	0.35
PWM 50 Hz	0.5 [40 %]	2.07	1.14	1.96	0.87	1.84	0.64	--	--
	0.7 [60 %]	1.64	0.79	1.58	0.64	1.54	0.60	--	--
	0.8 [70 %]	1.47	0.62	1.44	0.51	1.42	0.49	--	--
PWM 100 Hz	0.8 [70 %]	4.50	2.15	4.48	2.06	4.40	1.92	--	--

Table 4.8 Results of P_{st} and P_e under sinusoidal and PWM voltage excitation for assigned values of m_a with f_s varied from 1 kHz to 3 kHz, at f = 50 Hz and 100 Hz, B_{peak} = 1.5 T

It can be seen in table 4.8 that, at f = 50 Hz, B_{peak} = 1.5 T, the reduction of eddy-current losses was highest at m_a = 0.5, which was around 0.5 W/kg (43.9%), and was lowest at m_a = 0.8, which was around 0.13 W/kg (21.0%), when switching frequency f_s was increased from 1 kHz to 3 kHz. At f = 100 Hz, the reduction of eddy-current losses was around 0.23 W/kg (10.7%) at m_a = 0.8 with an increase in f_s from 1 kHz to 3 kHz. These results confirmed the validity of the analysis carried out for 1.3 T (table 4.7).

When the peak core flux density was set to 1.5 T, the increase in specific total loss P_{st} under PWM voltage excitation compared to sinusoidal voltage excitation was defined by the ratio I [%]

$$I[\%] = \frac{P_{PWM} - P_{\sin e}}{P_{\sin e}} \times 100 \tag{4.3}$$

where losses under sinusoidal and PWM voltage excitation are $P_{\sin e}$ and P_{PWM}, respectively. Fig. 4-51 shows the variation of I [%] under PWM voltage excitation for assigned values of m_a with f_s, at f = 50 Hz, B_{peak} = 1.5 T.

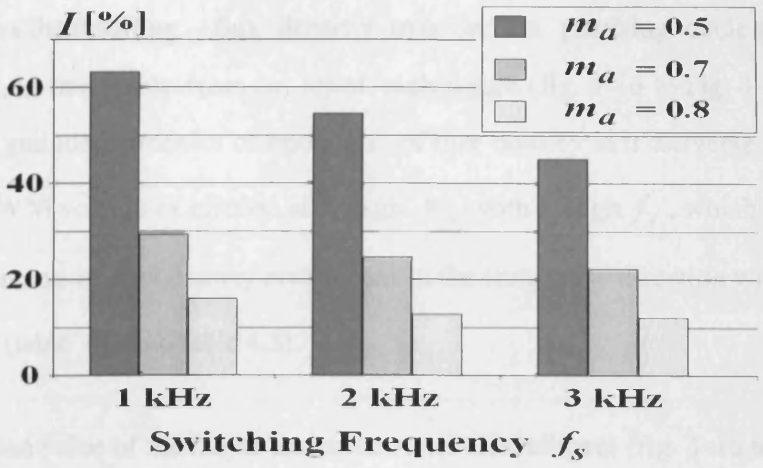

Fig. 4-51 Variation of I [%] under PWM voltage excitation, m_a = 0.5, 0.7 and 0.8 with f_s varied from 1 kHz to 3 kHz, at f = 50 Hz, B_{peak} = 1.5 T

It can be seen in fig. 4-51 that the ratio I [%] was the highest (63.0%) at the lowest value of m_a = 0.5 and at the lowest f_s = 1 kHz; and was the lowest (11.8%) at the highest value of m_a = 0.8 and at the highest f_s = 3 kHz. These results enhanced the benefit on the performance of the transformer core under PWM voltage excitation at a high value of f_s, especially at a low value of m_a.

The results analysed in this section was found to be in agreement with the previous research work [*1.12*] that the modulation index m_a played an important role in the specific total losses and its eddy-current component losses. However, at a high value of m_a, there was a small decrease in the specific total losses and its eddy-current component losses with an increase in f_s, but the decrease was not significant.

4.4.2 Localised rotational flux density and estimate rotational power losses

It can be clearly seen in fig. 4-16 to fig. 4-37 that the variation of the localised flux density in the corner and T-joints is complex under sinusoidal and PWM voltage excitation. Graph (**f**) in

each figure shows the resulting flux density over one magnetising cycle at the points considered. Also, in the graphs from (**a**)-(**e**) of each figure (fig. 4-16 to fig. 4-37), it can be seen that the magnitude harmonics components of flux density in transverse direction was reduced under PWM voltage excitation at a high m_a with a high f_s, which was due to a low harmonic contents of flux density component in the transverse direction with an increase in m_a and f_s (table 4.2 and table 4.3).

By taking the mean value of the major and minor axes flux ellipses (fig. 4-16 to fig. 4-37) of the fundamental component, the localised loss due to this flux density can be obtained. If the loss is assumed to be approximately proportional to the square both of flux density and frequency, then the other harmonic components of loss (3^{rd}, 5^{th}, 7^{th} and 9^{th}), which was due to harmonic components of flux density acting individually, can be inferred from the fundamental component figure.

Table 4.9 and table 4.10 display the mean flux density of harmonics at point 1 in the corner joints under sinusoidal and PWM voltage excitation for assigned values of m_a with f_s ranging from 1 kHz to 3 kHz, at f = 50 Hz and 100 Hz, B_{peak} = 1.3 T and 1.5 T.

Magnetisation frequency [f]	Modulation index m_a [OV %]	Switching frequency [f_s][kHz]	Resultant (mean) [T]	1st (mean) [T]	3rd (mean) [T]	5th (mean) [T]	7th (mean) [T]	9th (mean) [T]
sine 50 Hz	--	--	0.99	0.93	0.10	0.03	0.01	0.02
PWM 50 Hz	0.5 [40 %]	1	1.15	1.07	0.18	0.11	0.03	0.04
		2	1.13	1.05	0.17	0.10	0.03	0.04
		3	1.12	1.03	0.16	0.10	0.03	0.04
	0.8 [70 %]	1	1.07	0.98	0.14	0.08	0.02	0.03
		2	1.06	0.97	0.14	0.08	0.02	0.03
		3	1.06	0.97	0.13	0.07	0.02	0.03
	1.2 [90 %]	3	1.04	0.96	0.13	0.07	0.02	0.03

Table 4.9 Mean flux density of harmonics at point 1 under sinusoidal and PWM voltage excitation for assigned values of m_a with f_s varied from 1 kHz to 3 kHz, at f = 50 Hz, B_{peak} = 1.5 T

Magnetisation frequency [f]	Modulation index m_a [OV %]	Switching frequency [f_s][kHz]	Resultant (mean) [T]	1st (mean) [T]	3rd (mean) [T]	5th (mean) [T]	7th (mean) [T]	9th (mean) [T]
PWM 100 Hz	0.7 [60 %]	1	0.91	0.87	0.12	0.07	0.02	0.02
		2	0.91	0.87	0.12	0.07	0.01	0.02
		3	0.90	0.85	0.11	0.06	0.01	0.02
	0.8 [70 %]	1	0.90	0.86	0.12	0.06	0.02	0.02
		2	0.90	0.85	0.11	0.06	0.01	0.02
		3	0.89	0.84	0.11	0.05	0.01	0.01
	1.2 [90 %]	3	0.87	0.83	0.10	0.05	0.01	0.01

Table 4.10 Mean flux density of harmonics at point 1 under PWM voltage excitation for assigned values of m_a with f_s varied from 1 kHz to 3 kHz, at f = 100 Hz, B_{peak} = 1.3 T

Fig. 4-52 to fig. 4-57 show the approximate mean loss of harmonics due to mean flux density of harmonic components (table 4.9 and table 4.10) acting individually at point 1 under sinusoidal and PWM voltage excitation for assigned m_a with f_s varied from 1 kHz to 3 kHz, at f = 50 Hz and 100 Hz, B_{peak} = 1.3 T and 1.5 T.

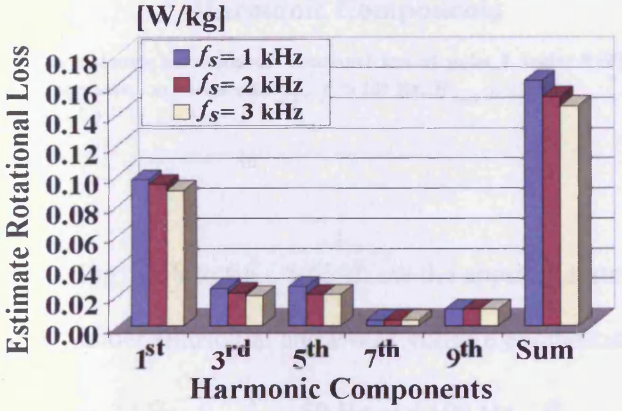

Fig. 4-52 Estimate harmonics of rotational loss at point 1 under PWM voltage excitation, m_a = 0.5 with f_s, f = 50 Hz, B_{peak} = 1.5 T

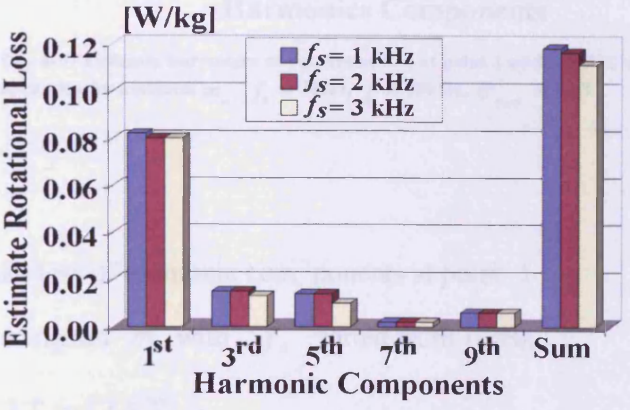

Fig. 4-53 Estimate harmonics of rotational loss at point 1 under PWM voltage excitation, m_a = 0.8 with f_s, f = 50 Hz, B_{peak} = 1.5 T

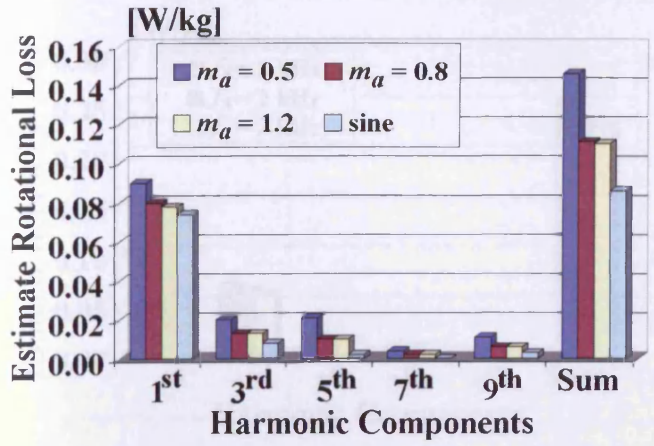

Fig. 4-54 Estimate harmonics of rotational loss at point 1 under sinusoidal and PWM voltage excitation for assigned m_a, f_s = 3 kHz, f = 50 Hz, B_{peak} = 1.5 T

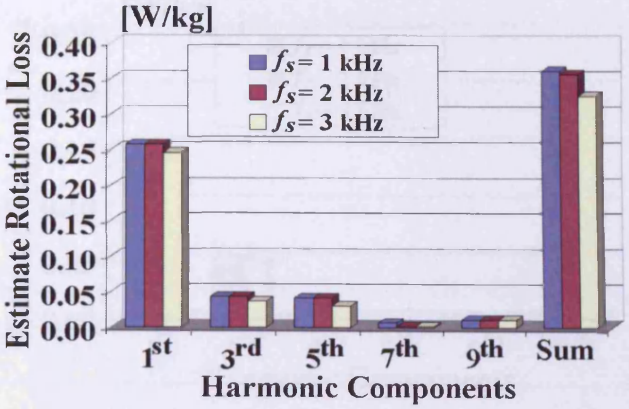

Fig. 4-55 Estimate harmonics of rotational loss at point 1 under PWM voltage excitation, m_a = 0.7 with f_s, f = 100 Hz, B_{peak} = 1.3 T

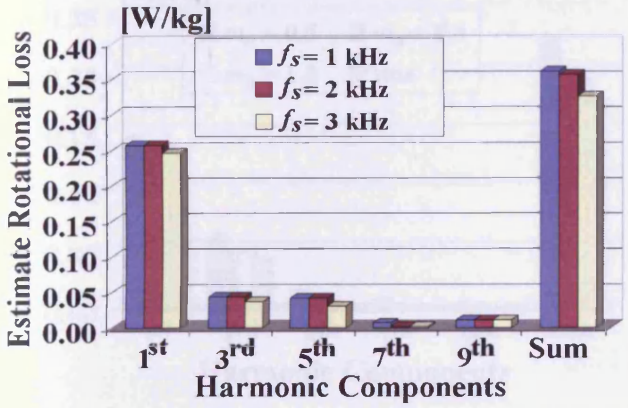

Fig. 4-56 Estimate harmonics of rotational loss at point 1 under PWM voltage excitation, m_a = 0.8 with f_s, f = 100 Hz, B_{peak} = 1.3 T

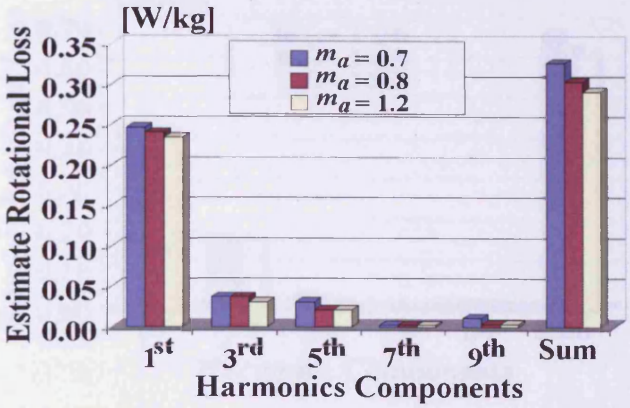

Fig. 4-57 Estimate harmonics of rotational loss at point 1 under PWM voltage excitation for assigned m_a, f_s = 3 kHz, f = 100 Hz, B_{peak} = 1.3 T

Fig. 4-58 to fig . 4-63 sh ow the approx imate mean loss of harmonic com ponents at point 2 under sinusoidal and PWM voltage excitation for assigned m_a with f_s varied from 1 kHz to 3 kHz, at f = 50 Hz and 100 Hz, B_{peak} = 1.3 T and 1.5 T.

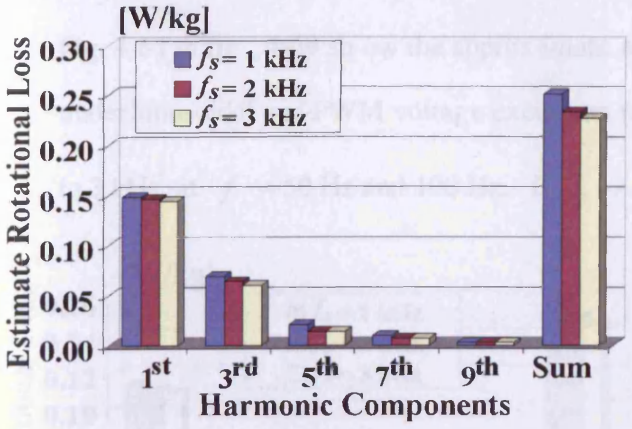

Fig. 4-58 Estimate harmonics of rotational loss at point 2 under PWM voltage excitation, m_a = 0.5 with f_s, f = 50 Hz, B_{peak} = 1.5 T

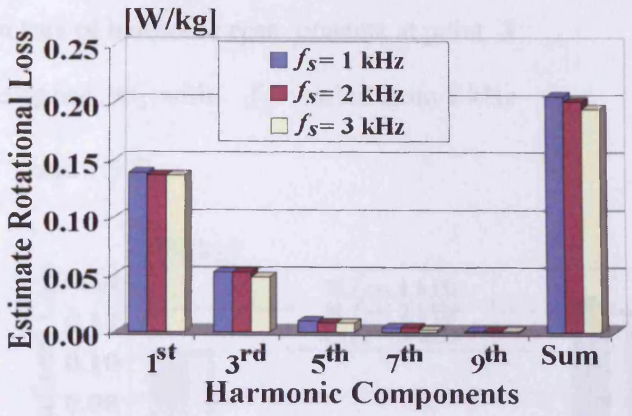

Fig. 4-59 Estimate harmonics of rotational loss at point 2 under PWM voltage excitation, m_a = 0.8 with f_s, f = 50 Hz, B_{peak} = 1.5 T

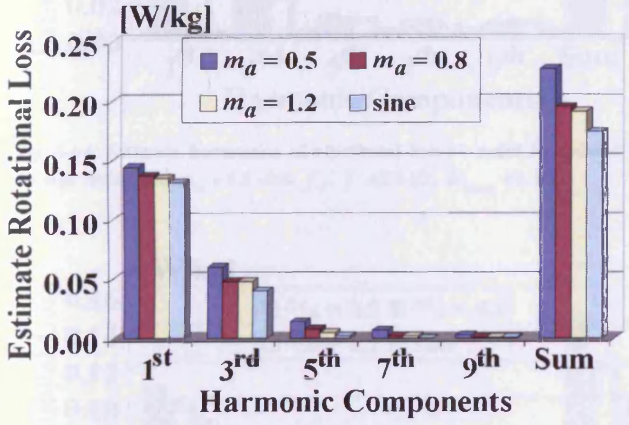

Fig. 4-60 Estimate harmonics of rotational loss at point 2 under sinusoida and PWM voltage excitation for assigned m_a, f_s = 3 kHz, f = 50 Hz B_{peak} = 1.5 T

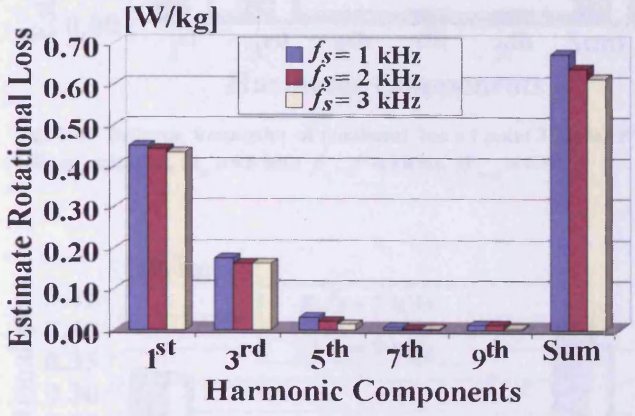

Fig. 4-61 Estimate harmonics of rotational loss at point 2 under PWM voltage excitation, m_a = 0.7 with f_s, f = 100 Hz, B_{peak} = 1.3 T

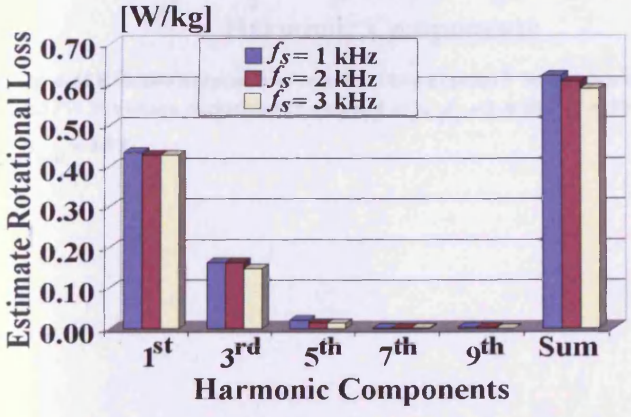

Fig. 4-62 Estimate harmonics of rotational loss at point 2 under PWM voltage excitation, m_a = 0.8 with f_s, f = 100 Hz, B_{peak} = 1.3 T

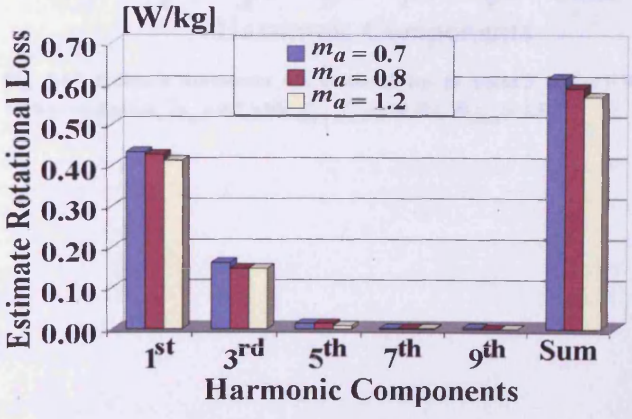

Fig. 4-63 Estimate harmonics of rotational loss at point 2 under PWM voltage excitation for assigned m_a, f_s = 3kHz, f = 100 Hz, B_{peak} = 1.3 T

Fig. 4-64 to fig . 4-69 sh ow the approx imate mean loss of harmonic com ponents at point 3 under sinusoidal and PWM voltag e excitation for assigned m_a with f_s varied from 1 kHz to 3 kHz, at f = 50 Hz and 100 Hz, B_{peak} = 1.3 T and 1.5 T.

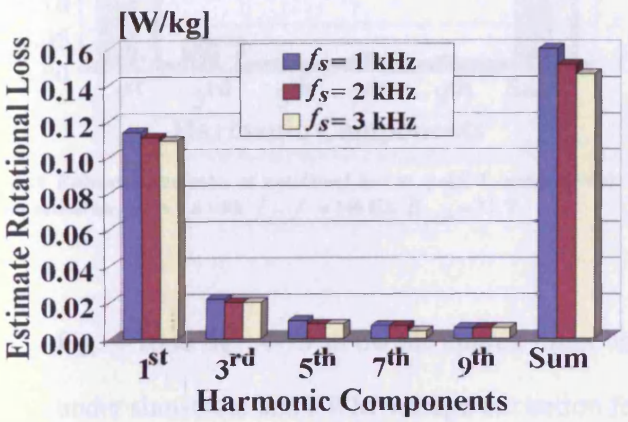

Fig. 4-64 Estimate harmonics of rotational loss at point 3 under PWM voltage excitation, m_a = 0.5 with f_s, f = 50 Hz, B_{peak} = 1.5 T

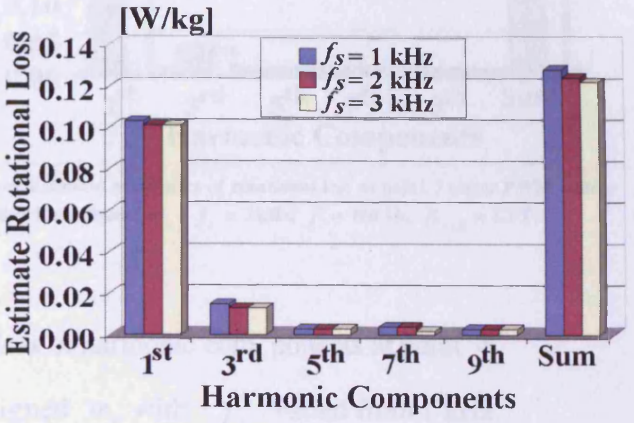

Fig. 4-65 Estimate harmonics of rotational loss at point 3 under PWM voltage excitation, m_a = 0.8 with f_s, f = 50 Hz, B_{peak} = 1.5 T

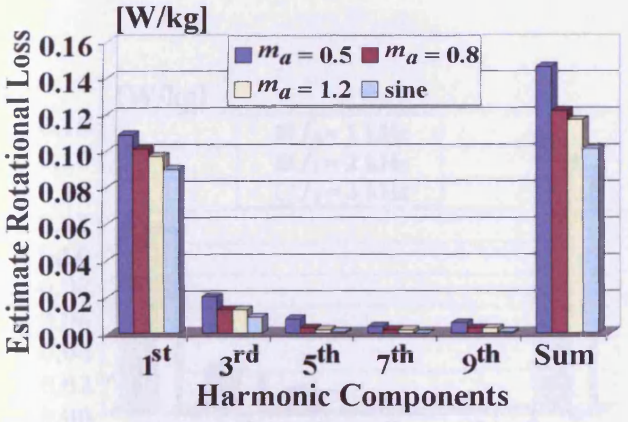

Fig. 4-66 Estimate harmonics of rotational loss at point 3 under sinusoidal and PWM voltage excitation for assigned m_a, f_s = 3 kHz, f = 50 Hz, B_{peak} = 1.5 T

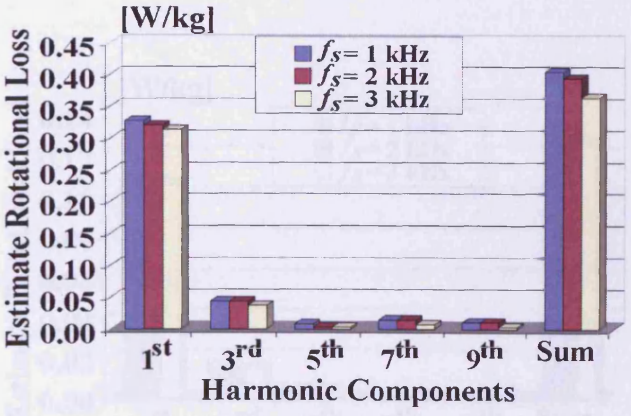

Fig. 4-67 Estimate harmonics of rotational loss at point 3 under PWM voltage excitation, m_a = 0.7 with f_s, f = 100 Hz, B_{peak} = 1.3 T

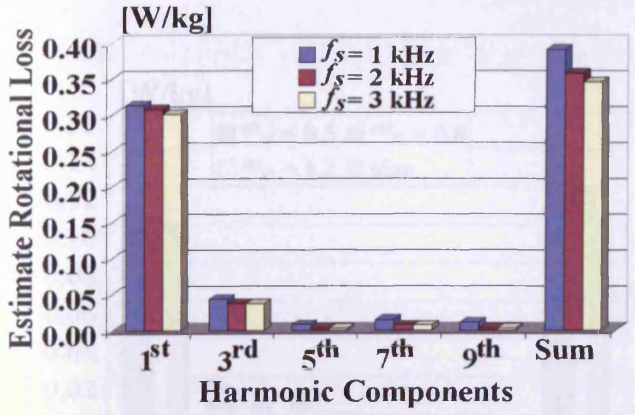

Fig. 4-68 Estimate harmonics of rotational loss at point 3 under PWM voltage excitation, m_a = 0.8 with f_s, f = 100 Hz, B_{peak} = 1.3 T

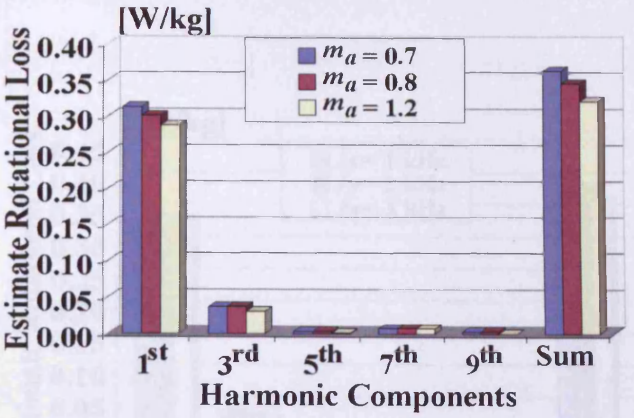

Fig. 4-69 Estimate harmonics of rotational loss at point 3 under PWM voltage excitation for assigned m_a, f_s = 3kHz, f = 100 Hz, B_{peak} = 1.3 T

Fig. 4-70 to fig . 4-75 sh ow the approx imate mean loss of harmonic com ponents at point 4 under sinusoidal and PWM voltage excitation for assigned m_a with f_s varied from 1 kHz to 3 kHz, at f = 50 Hz and 100 Hz, B_{peak} = 1.3 T and 1.5 T.

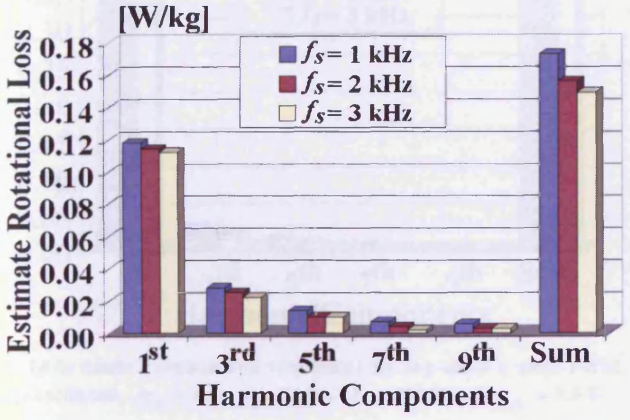

Fig. 4- 70 Es timate h armonics of rotational l oss at p oint 4 u nder PWM voltage excitation, m_a = 0.5 with f_s, f = 50 Hz, B_{peak} = 1.5 T

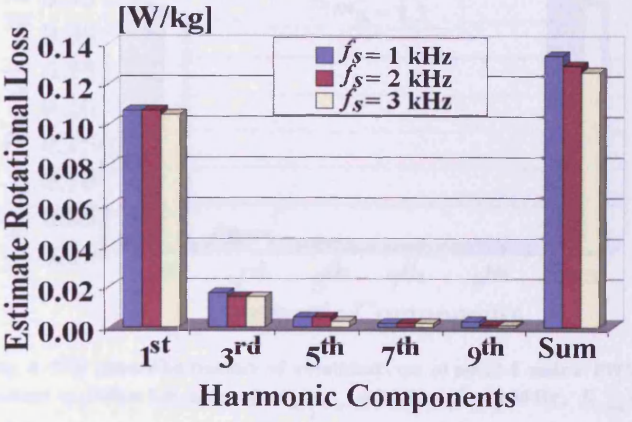

Fig. 4- 71 Es timate h armonics of rotational l oss at p oint 4 u nder PWM voltage excitation, m_a = 0.8 with f_s, f = 50 Hz, B_{peak} = 1.5 T

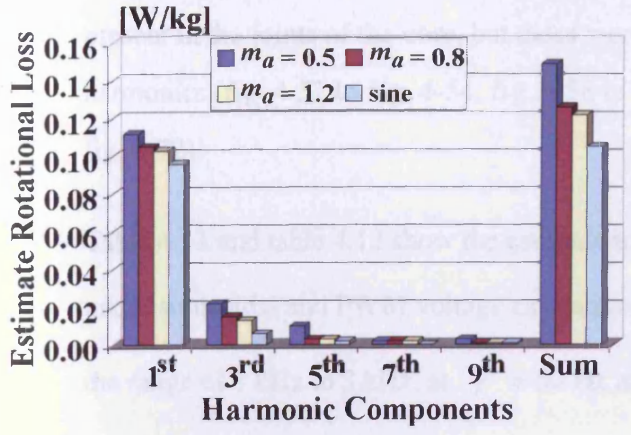

Fig. 4-72 Estimate harmonics of rotational loss at point 4 under sinusoidal and PWM voltage excitation for assigned m_a, $f_s = 3$ kHz, $f = 50$ Hz, $B_{peak} = 1.5$ T

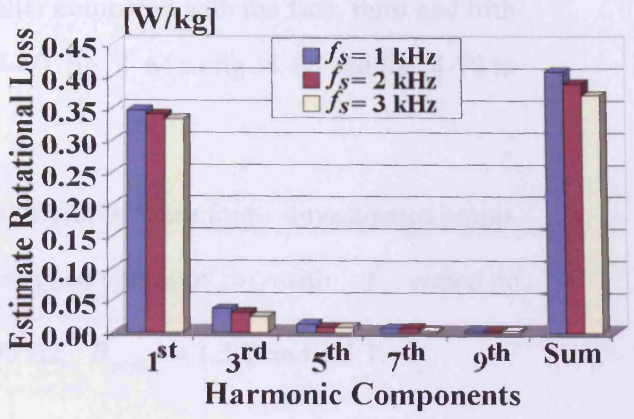

Fig. 4-73 Estimate harmonics of rotational loss at point 4 under PWM voltage excitation, $m_a = 0.7$ with f_s, $f = 100$ Hz, $B_{peak} = 1.3$ T

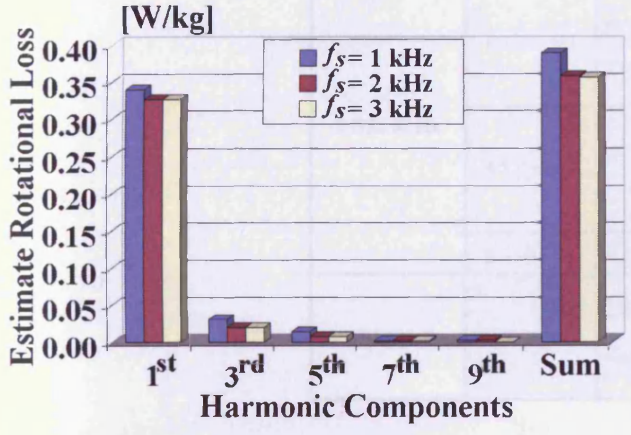

Fig. 4-74 Estimate harmonics of rotational loss at point 4 under PWM voltage excitation, $m_a = 0.8$, $f_s = 3$ kHz, $f = 100$ Hz, $B_{peak} = 1.3$ T

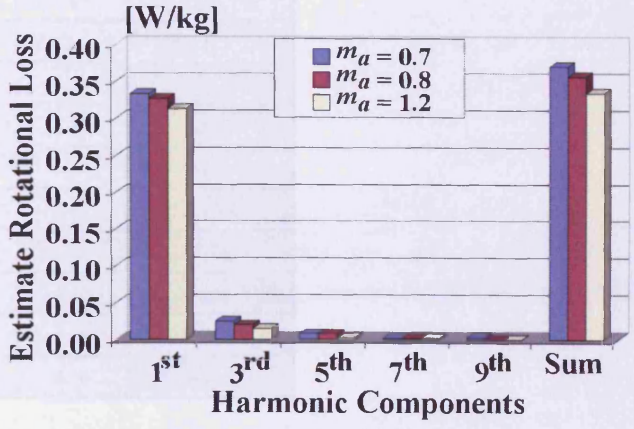

Fig. 4-75 Estimate harmonics of rotational loss at point 4 under PWM voltage excitation for assigned m_a, $f_s = 3$ kHz, $f = 100$ Hz, $B_{peak} = 1.3$ T

It was observed that the mean fundamental and third harmonics rotational losses contributed to the most of estimate localised rotational loss under sinusoidal voltage excitation (fig. 4-54, fig. 4-60, fig. 4-66 and fig. 4-72), which was primarily caused by a rotating fundamental and third harmonic flux (table 4.9). Nevertheless, under PWM voltage excitation, it was noticed

that the mean losses of the higher harmonics, i.e., the seventh and ninth harmonics, were also present in the joints of the core, but these were smaller compared with the first, third and fifth harmonics (fig. 4-52 to fig. 4-54, fig. 4-58 to fig. 4-60, fig. 4-64 to fig. 4-66 and fig. 4-70 to fig. 4-72).

Table 4.11 and table 4.12 show the estimate total losses of these four investigated points under sinusoidal and PWM voltage excitation for assigned values of m_a with f_s varied in the range of 1 kHz to 3 kHz, at f = 50 Hz and 100 Hz, B_{peak} = 1.3 T and 1.5 T.

Magnetisation frequency [f]	Modulation index m_a [OV %]	Switching frequency [f_s] [kHz]	Specific total loss [W/kg]	Average estimated loss [W/kg]
sine 50 Hz	--	--	1.27	0.117
PWM 50 Hz	0.5 [40 %]	1	2.07	0.187
		2	1.96	0.173
		3	1.84	0.167
	0.8 [70 %]	1	1.47	0.147
		2	1.44	0.143
		3	1.42	0.139
	1.2 [90 %]	3	1.35	0.135
PWM 100 Hz	0.8 [70 %]	1	4.50	0.625
		2	4.48	0.605
		3	4.40	0.591

Table 4.11 Average loss at investigated points under sinusoidal and PWM voltage excitation for assigned m_a with f_s varied from 1 kHz to 3 kHz, at f = 50 Hz and 100 Hz, B_{peak} = 1.5 T

Magnetisation frequency [f]	Modulation index m_a [OV %]	Switching frequency [f_s][kHz]	Specific total loss [W/kg]	Average estimated loss [W/kg]
PWM 100 Hz	0.7 [60 %]	1	3.74	0.462
		2	3.70	0.444
		3	3.54	0.418
	0.8 [70 %]	1	3.42	0.437
		2	3.39	0.412
		3	3.34	0.399
	1.2 [90 %]	3	2.85	0.379

Table 4.12 Average loss at investigated points under PWM voltage excitation for assigned m_a with f_s varied from 1 kHz to 3 kHz, at f = 100 Hz, B_{peak} = 1.3 T

Table 4.11 and table 4.12 show that the estimate rotational losses in the joints of the core was around 9%-10% of the specific total losses under sinusoidal and PWM voltage excitation, at f = 50 Hz, and was around 12%-13% under PWM voltage excitation, at f = 100 Hz, which was found that the amount of rotational losses occurring in the joints of the core was a small proportion of the total core loss.

Table 4.11 shows that at a low value of m_a = 0.5 (f_s = 3 kHz) the estimated rotational loss was around 0.03 W/kg (23.7%) higher than that at a high value of m_a = 1.2 (f_s = 3 kHz), at B_{peak} = 1.5 T, which was due to higher harmonic contents in flux density of components in rolling and transverse direction at a low m_a = 0.5 (table 4.2). Whilst, at f = 100 Hz, B_{peak} = 1.3 T, the average loss at a low m_a = 0.7 (f_s = 3 kHz) was around 0.04 W/kg (10.3%) greater than that at a high m_a = 1.2 (f_s = 3 kHz) (table 4.12). These results enhanced the benefit on the performance of the transformer core at a high value of m_a.

Also, it was observed in table 4.11 and table 4.12 that an increase in switching frequency f_s led, under all PWM voltage excitation, to a reduction of rotational loss in the core. At f =

50 Hz and B_{peak} = 1.5 T, the reduction of rotational loss at m_a = 0.5 was around 0.02 W/kg (10.7%) with an increase in f_s from 1 kHz to 3 kHz, which was due to higher harmonic contents in flux density of components in rolling and transverse direction at a low f_s = 1 kHz (table 4.2), and the reduction of loss at m_a = 0.8 was around 0.01 W/kg (5.4%) with f_s increasing from 1 kHz to 3 kHz.

At f = 100 Hz and B_{peak} = 1.3 T, the reduction of rotational loss was around 0.04 W/kg (9.5%) and 0.04 W/kg (8.7%) at m_a = 0.7 and 0.8 respectively, when f_s was increased from 1 kHz to 3 kHz (table 4.12), and also, the reduction of loss was around 0.03 W/kg (5.4%) at m_a = 0.8 with f_s increasing from 1 kHz to 3 kHz (table 4.11), at B_{peak} = 1.5 T, which was confirmed that the validity of the analysis carried out for 1.3 T.

These results analysed above enhanced the benefit on the performance of the transformer core under PWM voltage excitation at a high value of f_s, especially at a low value of m_a. However, at a high value of m_a, the results showed that switching frequency had a little effects on the rotational loss.

In this section, the mean flux density of harmonics at investigated points in the joints of the core has been analysed, and also the estimate mean loss of harmonics has been presented, which could help give a better understanding of the influence of modulation index m_a and switching frequency f_s.

4.4.3 Planar eddy-current losses of the core

Fig. 4-38 to fig. 4-48 show the mean peak values of normal flux density $\hat{B}_z$ at different measurement points (fig. 4-5), and table 4.4 presents mean values of peak normal flux density

at the limbs and yokes, T-joints and corners regions of the core under sinusoidal and PWM voltage excitation. It is shown in table 4.4 that at f = 50 Hz, B_{peak} = 1.5 T, the mean peak normal flux density at limbs and yokes of the core was around 1.0 mT under sinusoidal voltage excitation and it rose to around 1.8 mT under the worst distorted PWM voltage excitation, at m_a = 0.5 and f_s = 1 kHz ; and also, the highest mean peak normal flux density at T-joints and corner regions was around 5.2 mT and 9.4 mT, respectively. Moreover, the highest values of mean peak normal flux density at limbs and yokes, T-joints and corners were around 1.0 mT, 3.4 mT and 7.0 mT, respectively, when the core was subjected to PWM voltage excitation at m_a = 0.7, f_s = 1 kHz as f was set to 100 Hz, at B_{peak} = 1.3 T.

Theoretically, normal flux component $_z$ yields resulting planar eddy-current loss P_{pe} (W/kg), which is proved to be approximately proportional to ^2_z [*4.7*]. According to equation (1.8), it could be inferred that P_{pe} is approximately proportional to B_z^2.

It is known that single strips of grain-oriented, 3% silicon electrical steel indicated that planar eddy-current loss would be around 0.04 W /kg at 10 mT (50 Hz) [*4.8*]. Also, when magnetisation frequency was at f = 100 Hz, the planar eddy-current loss assumed to be approximately proportional to the square of both peak normal flux density and frequency, which could be inferred from the 50 Hz condition. Therefore, the planar eddy-current loss of the core can be inferred under sinusoidal and PWM voltage excitation.

Table 4.13 and table 4.14 show the variation of the specific total loss P_{st} (W/kg), the planar eddy-current loss P_{pe} (W/kg) at different regions and the estimate total planar eddy-current loss of the core under sinusoidal and PWM voltage excitation.

Magnetisation frequency [f]	Modulation index m_a [OV %]	Switching frequency [f_s] [kHz]	Total P_{st}	Limb, Yoke P_{pe}	T-joints P_{pe}	Corners P_{pe}	Total P_{pe}
sine 50Hz	--	--	1.27	0.004	0.014	0.028	0.046
PWM 50Hz	0.5 [40 %]	1	2.07	0.007	0.021	0.038	0.066
		2	1.96	0.006	0.020	0.036	0.062
		3	1.84	0.006	0.019	0.035	0.060
	0.8 [70 %]	1	1.47	0.006	0.017	0.033	0.056
		2	1.44	0.005	0.017	0.032	0.054
		3	1.42	0.005	0.016	0.032	0.053
	1.2 [90%]	3	1.35	0.005	0.016	0.031	0.052

Table 4.13 Variation of P_{st} and P_{pe} at different sections of the core under sinusoidal and PWM voltage excitation for assigned values of m_a with f_s varied from 1 kHz to 3 kHz, at f = 50 Hz, B_{peak} = 1.5 T

Magnetisation frequency [f]	Modulation index m_a [OV %]	Switching frequency [f_s] [kHz]	Total P_{st}	Limb, Yoke P_{pe}	T-joints P_{pe}	Corners P_{pe}	Total P_{pe}
PWM 100Hz	0.7 [60 %]	1	3.74	0.016	0.054	0.112	0.182
		2	3.70	0.014	0.053	0.110	0.177
		3	3.54	0.014	0.050	0.107	0.171
	0.8 [70 %]	1	3.42	0.014	0.050	0.107	0.171
		2	3.39	0.013	0.048	0.106	0.167
		3	3.34	0.013	0.048	0.106	0.167
	1.2 [90%]	3	2.85	0.011	0.045	0.102	0.158

Table 4.14 Variation of P_{st} and P_{pe} at different sections of the core under PWM voltage excitation for assigned values of m_a with f_s varied from 1 kHz to 3 kHz, at f = 100 Hz, B_{peak} = 1.3 T

Table 4.15 shows the variation of the P_{st} (W /kg), P_{pe} (W /kg) at different regions and estimate total P_{pe} (W/kg) of the core under PWM voltage excitation for assigned value of m_a = 0.8 with f_s varied from 1 kHz to 3 kHz, at f = 100 Hz, B_{peak} = 1.5 T.

Magnetisation frequency [f]	Modulation index m_a [OV %]	Switching frequency [f_s] [kHz]	Total P_{st}	Limb, Yoke P_{pe}	T-Joints P_{pe}	Corners P_{pe}	Total P_{pe}
PWM 100Hz	0.8 [70 %]	1	4.50	0.024	0.070	0.134	0.228
		2	4.48	0.024	0.069	0.133	0.226
		3	4.40	0.003	0.069	0.133	0.224

Table 4.15 Variation of P_{st} and P_{pe} at different sections of the core under PWM voltage excitation for m_a = 0.8 with f_s varied from 1 kHz to 3 kHz, at f = 100 Hz, B_{peak} = 1.5 T

It was shown in table 4. 13 that under sinusoidal voltage excitation, the planar eddy-current loss P_{pe} in the limbs and yokes was around 0.004 W/kg, and was around 0.014 W/kg and 0.028 W/kg in the T-joints and corners, respectively, which was found to be approximately in agreement with the previous research, where the planar eddy-current losses were around 0.01 W/kg in the joints and 0.001 W/kg in the limbs and yokes [*4.9*]. Also, it was observed that, at B_{peak} = 1.5 T, at a low m_a = 0.5 (f_s = 3 kHz), the total estimate planar eddy-current loss was around 0.01 W /kg (15.4%) higher than that at a high of m_a = 1.2 (f_s = 3 kHz) (table 4.13), which was due to a higher normal flux density at a low m_a = 0.5 (table 4.4). Whilst, at f = 100 Hz, B_{peak} = 1.3 T, the planar eddy-current loss at a low m_a = 0.7 (f_s = 3 kHz) was around 0.01 W /kg (8.2%) greater than that at a high m_a = 1.2 (f_s = 3 kHz) (table 4.14).

It was found in table 4.13 to table 4.15 that, an increase in switching frequency f_s led, under all PWM voltage excitation, to a reduction of planar eddy-current loss P_{pe}. It was observed in table 4.13 that, at f = 50 Hz and B_{peak} = 1.5 T, the reduction of planar eddy-current loss at m_a = 0.5 was around 0.01 W/kg (9.1%) with an increase in f_s from 1 kHz to 3 kHz, which was due to a higher normal flux density at a low f_s = 1 kHz (table 4.4), and also, the

loss reduction at m_a = 0.8 was around only 0.003 W/kg (5.4%) with f_s increasing from 1 kHz to 3 kHz.

From table 4.14 it can be seen that at f = 100 Hz, B_{peak} = 1.3 T, the reduction of planar eddy-current loss was around 0.01 W/kg (6.0%) and 0.004 W/kg (2.3%) at m_a = 0.7 and 0.8 respectively, when f_s was increased from 1 kHz to 3 kHz; and also, at B_{peak} = 1.5 T, the reduction of loss was around 0.004 W/kg (1.8%) at m_a = 0.8 with f_s increasing from 1 kHz to 3 kHz (table 4.15), which was confirmed that the validity of the analysis carried out for 1.3 T.

From table 4.13 to table 4.14, it could be inferred that, at f = 50 Hz and B_{peak} = 1.5 T, P_{pe} of the core accounted for around 3.2 % - 3.8 % under sinusoidal and PWM voltage excitation for assigned m_a with f_s varied in the range of 1 kHz to 3 kHz. Also, at f = 100 Hz and B_{peak} = 1.3 T, P_{pe} of the core accounted for around 4.8% - 5.5% under PWM voltage excitation for assigned m_a with varied f_s.

These results confirmed that the planar eddy-current loss of the core was reduced at a high value of f_s, especially at a low value of m_a. Nevertheless, at a high value of m_a, the results showed that the switching frequency had little effects on the planar eddy-current loss.

References to Chapter 4:

[4.1] "High performance inverter TOSVERT VF-A3 instruction manual", *Industrial Equipment Export Department*, TOSHIBA INTERNATIONAL COPORATION.

[4.2] "Norma D6000 wide band power analyser operating instructions", LEM NORMA Gmbh, AUSTRIA.

[4.3] Digital Multimeter User Manual, *Keithley Instrumens Inc.*, 28775 Aurora Roads, Cleveland, USA, 2001.

[4.4] "Ultra-low offset voltage dual Op Amp AD 708", ANALOG DEVICES, One Technology Way, P. O. Box 9106, Norwood, MA 02062-9106, U. S. A. (www.analog.com).

[4.5] A. Boglietti, P. Ferraris, M. Lazzari and F. Profumo, "Iron losses in magnetic materials with six-step and PWM inverter supply", *IEEE Trans. Mag.*, vol. 27, no. 6, pp. 5334-5336, November 1991.

[4.6] Lu C. B and Zhu Y. H, "Calculations in electrical transformers", *Hei Long Jiang Institute of Technology - Scientific Press*, pp. 46, 1990.

[4.7] H. Pfützner, C. Bengtsson, T. Booth, F. Löffler and K. Gramm, "Three-dimensional flux distributions in transformer cores as a function of package design", *IEEE Trans. on Mag.*, vol. 30, no. 5, pp. 2713-2727, September 1994.

[4.8] A. J. Moses, "Comparison of transformer loss prediction from computed and measured flux density distribution", *IEEE Trans. Mag.*, vol. 34, no. 4, pp. 1186-1188, July 1998.

[4.9] A. J. Moses, "Prediction of core losses of three phase transformers from estimation of the components contributing to the building factor", *JMMM*, 254-255, pp. 615-617, 2003.

Chapter 5 Measurement and Analysis of Acoustic Noise and Vibration of the Model Core under Sinusoidal and PWM Voltage Excitation

5.1 Experimental setup

The basic measurement apparatus consisted of a model three-phase transformer core, which was already introduced in chapter 4 (fig. 4-1), and associated system for measuring acoustic noise and core surface vibration, which would be introduced later. The positions at which acoustic noise and vibration of the core were measured are shown in fig. 5-1.

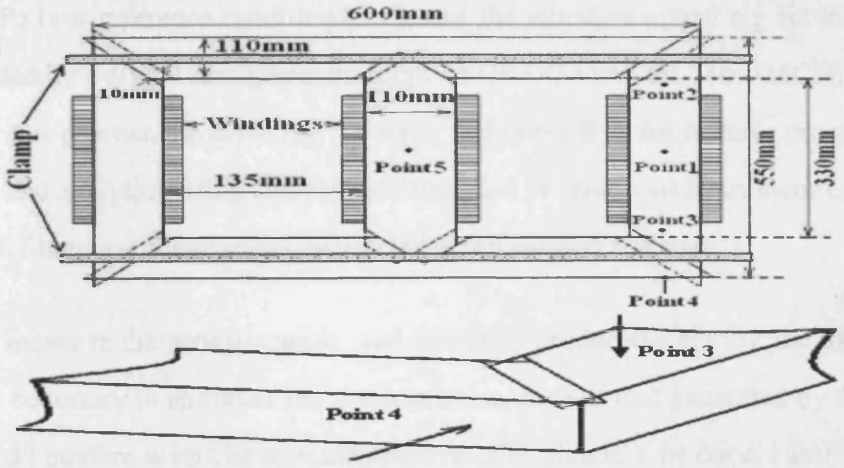

Fig. 5-1 Layout of the core showing measurement points; arrows indicate the measurement direction of vertical and horizontal vibration

Where the position of point 1 was located in the middle of the limb; the positions of point 2 and point 3 were located at corner regions of the core at same distance from point 1; point 4 was located on the side of the core and point 5 was located at the centre of the middle limb.

5.2 Measurement procedure

It is shown in fig. 5-2 that the A-weighted sound pressure level (*SPL*) was recorded using a "Brüel & Kjaer" type 4955 microphone, which has optimised frequency response in the range of 5 Hz up to 20 kHz [*5.1*]. It was fixed 0.5 m vertical above the measurement

points 1, 2 and 3 in turn. The corresponding vertical vibration of the core surface at each point was measured using a single-point laser vibrometer (SP LV) [*2.34*]. When the microphone was fixed 0.5 m directly vertical above the core centre, i.e., point 5, the corresponding horizontal displacement measurement was taken on the side of the core at point 4. The resultant acoustic noise of the core was presented as a mean value of the noise obtained from these four points under each test condition.

The sound pressure level signal from the microphone, passing through a conditioning amplifier (Brüel & Kjaer 2692C NEXUS Conditioning Amplifier) (fig. 5-2) [*5.2*], which the uncertainty of this sound pressure level measurement system $u(dBA)$ is ± 0.2 *dBA* when 20 μ Pa is at reference condition [*5.1*], and the vibration output signal from SP LV were recorded by a digital storage oscilloscope (YOKOGAWA DL716 - 16CH) (fig. 5-2) [*3.6*]. After this process, the saved data were fed into a PC for further processing by calculating and analysing using algorithms embedded in "National Instrument LabVIEW" and "Ansoft Simplorer Simulation Centre" PC based support software.

In order to measure the acoustic noise and vibration produced only by the transformer core, it was necessary to eliminate the ambient noise, such as that generated by the variacs, which could interfere with the measurement results. Hence, the core, laser head and microphone were located in the anechoic chamber (fig. 5-3), which was mentioned in chapter 4, while the other associated equipment were placed outside the chamber (fig. 5-4).

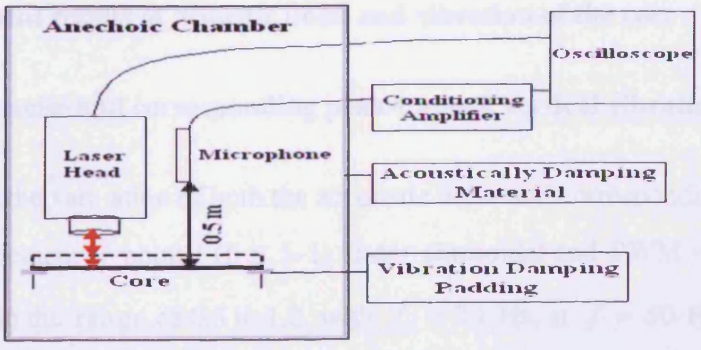

Fig. 5-2 Schematic of vibration and acoustic noise measurement setup

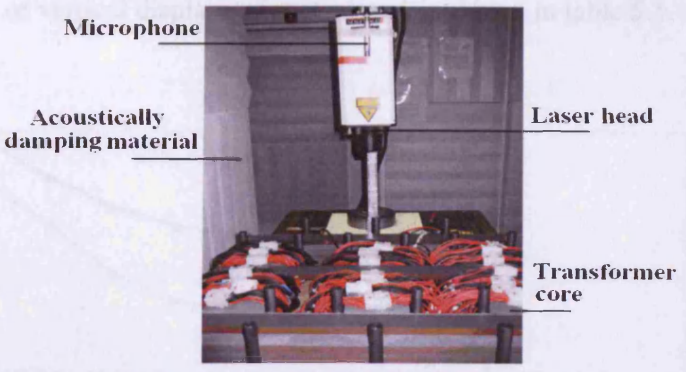

Fig. 5-3 Photograph of transformer core, laser head and microphone located in anechoic chamber

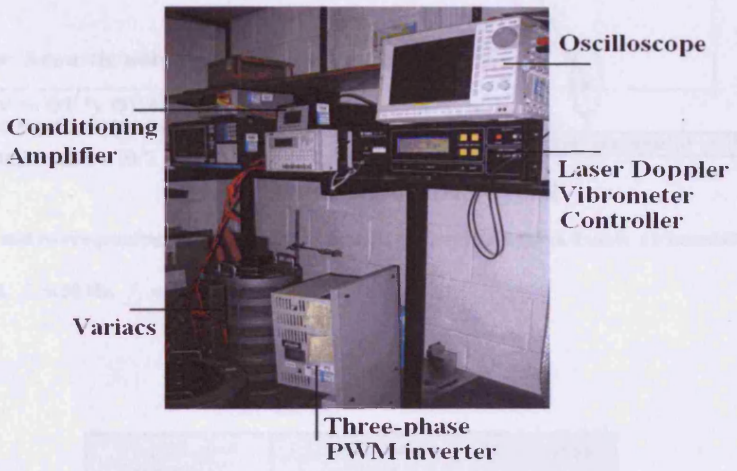

Fig. 5-4 Photograph of magnetising system and other associated equipment located outside the anechoic chamber

The transformer core was assembled and dismantled twice. Each measurement was taken three times at each measuring point under each voltage excitation condition. The repeatability of the mean values of sound pressure level was better than ± 1% and the core vibration results were repeatable to ± 3%, which is shown in Appendix C.

5.3 Measurement results of acoustic noise and vibration of the core

5.3.1 Acoustic noise and corresponding peak-to-peak vertical vibration at point 1

Fig. 5-5 shows the variation of both the acoustic noise and corresponding peak-to-peak vertical displacement at point 1 (fig. 5-1) under sinusoidal and PWM voltage excitation for m_a varied in the range of 0.5 to 1.2 with $f_s = 3$ k Hz, at $f = 50$ Hz, $B_{peak} = 1.3$ T,

and the $THD[\%]$ of vertical displacement at point 1 is shown in table 5.1.

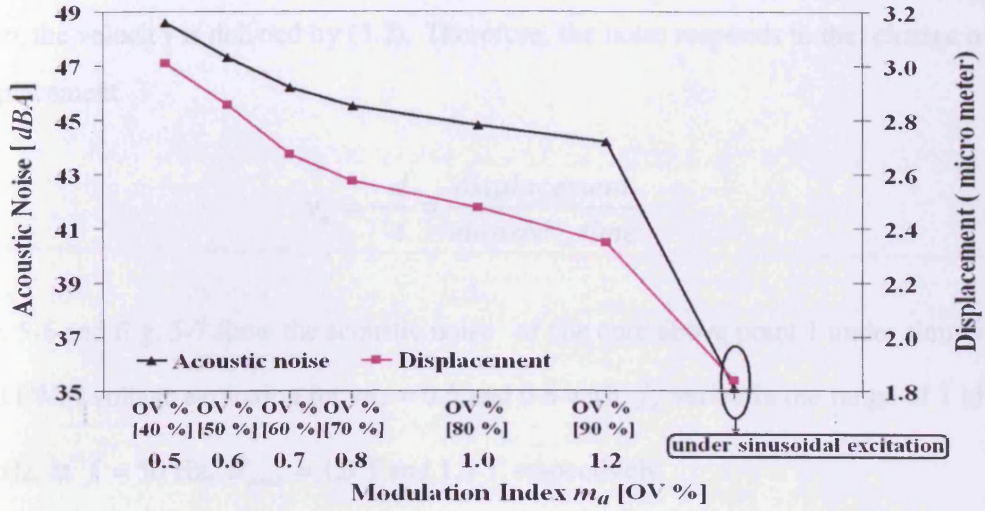

Fig. 5-5 A coustic n oise and co rresponding pea k-to-peak ve rtical dis placement a t poi nt 1 unde r s inusoidal a nd PWM vo ltage excitation, m_a = 0.5 - 1.2, f = 50 Hz, f_s = 3 kHz, B_{peak} = 1.3 T

Magnetisation frequency [f]	Modulation index m_a [OV %]	$THD[\%]$
sine 50 Hz	--	14.6
PWM 50 Hz	0.5 [40 %]	32.1
	0.6 [50 %]	30.2
	0.7 [60 %]	29.0
	0.8 [70 %]	27.8
	1.0 [80 %]	26.5
	1.2 [90 %]	25.3

Table 5.1 Variation $THD[\%]$ of vertical displacement at point 1 under sinusoidal and PWM voltage excitation, m_a = 0.5 - 1.2, f = 50 Hz, f_s = 3 kHz, B_{peak} = 1.3 T

It was known that the emitted sound pressure (noise) can be described as (5.1) [*1.44*]

$$p = F_i rc \int_S v_n^2 dS_c \qquad [1.44] \qquad (5.1)$$

where F_i is the irradiation factor that can be assumed to be constant of the core; r is the

density of the propagation medium (air); c is the corresponding sound velocity; v_n is the value of the surface velocity and the core surface elements represented by dS_c [*1.44*]. Also, the velocity is defined by (5.2). Therefore, the noise responds to the change of the displacement.

$$v_n = \frac{d}{t} = \frac{displacement}{elapsed\_time} \tag{5.2}$$

Fig. 5-6 and fig. 5-7 show the acoustic noise of the core above point 1 under sinusoidal and PWM voltage excitation for m_a = 0.5 and 0.6 with f_s varied in the range of 1 kHz to 3 kHz, at f = 50 Hz, B_{peak} = 1.3 T and 1.5 T, respectively.

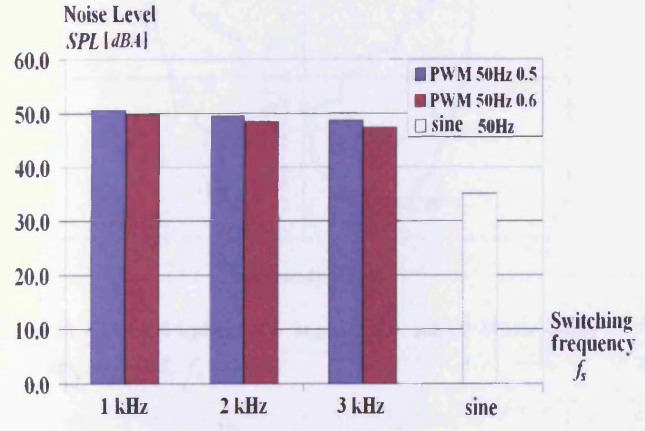

Fig. 5-6 Acoustic noise above point 1 under sinusoidal and PWM voltage excitation, m_a = 0.5 and 0.6 with f_s, at f = 50 Hz, B_{peak} = 1.3 T

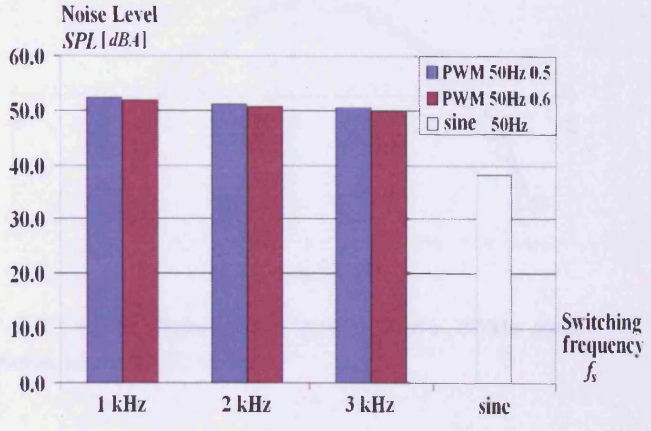

Fig. 5-7 Acoustic noise above point 1 under sinusoidal and PWM voltage excitation, m_a = 0.5 and 0.6 with f_s, at f = 50 Hz, B_{peak} = 1.5 T

Fig. 5-8 to fig. 5-11 show plots of vertical displacement with flux density, and table 5.2 displays the variation THD[%] of vertical displacement at point 1 under sinusoidal and PWM voltage excitation for m_a = 0.5 with f_s varied in the range of 1 kHz to 3 kHz, at f = 50 Hz, B_{peak} = 1.5 T.

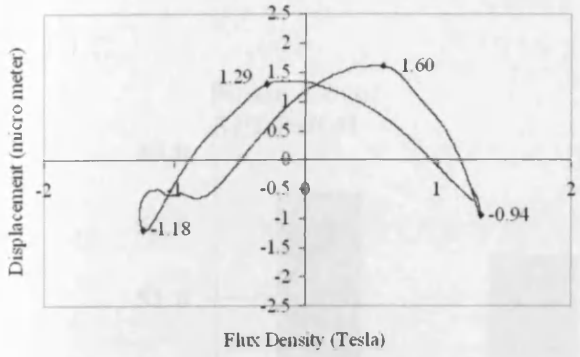

Fig. 5-8 Vertical displacement at point 1 under sinusoidal voltage excitation

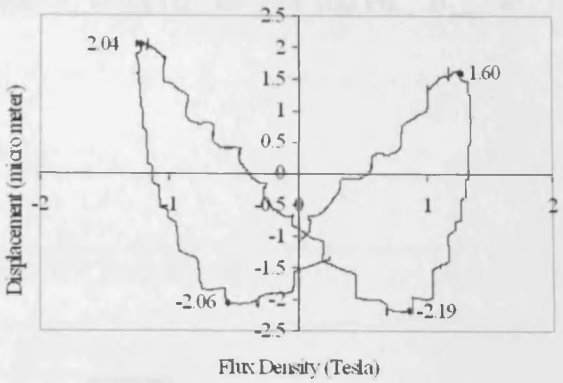

Fig. 5-9 Vertical displacement at point 1 under PWM voltage excitation, $m_a = 0.5$, $f_s = 1$ kHz

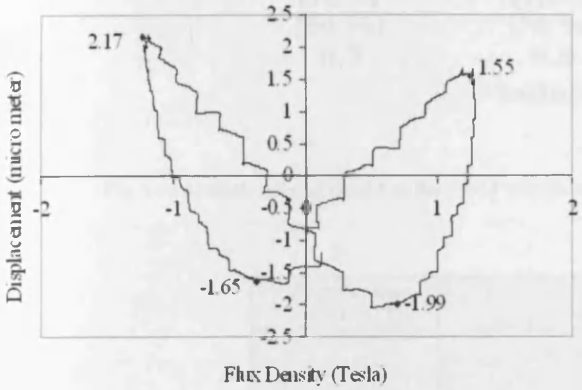

Fig. 5-10 Vertical displacement at point 1 under PWM voltage excitation, $m_a = 0.5$, $f_s = 2$ kHz

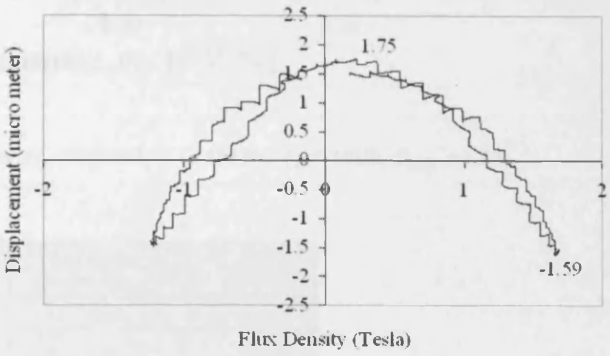

Fig. 5-11 Vertical displacement at point 1 under PWM voltage excitation, $m_a = 0.5$, $f_s = 3$ kHz

Magnetisation frequency [f]	Modulation index m_a [OV %]	Switching frequency [f_s] [kHz]	THD[%]
sine 50 Hz	--	--	23.4
PWM 50 Hz	0.5 [40 %]	1	42.3
		2	39.4
		3	36.5

Table 5.2 Variation THD[%] of vertical displacement at point 1 under sinusoidal and PWM voltage excitation for $m_a = 0.5$ with f_s varied from 1 kHz to 3 kHz, at $f = 50$ Hz, $B_{peak} = 1.5$ T

Fig. 5-12 shows the acoustic noise, and table 5.3 gives the corresponding peak-to-peak vertical displacement and the variation THD[%] of displacement at point 1 under PWM

voltage excitation for assigned values of m_a with $f_s = 3$ kHz, at $f = 100$ Hz, $B_{peak} = 1.3$ T.

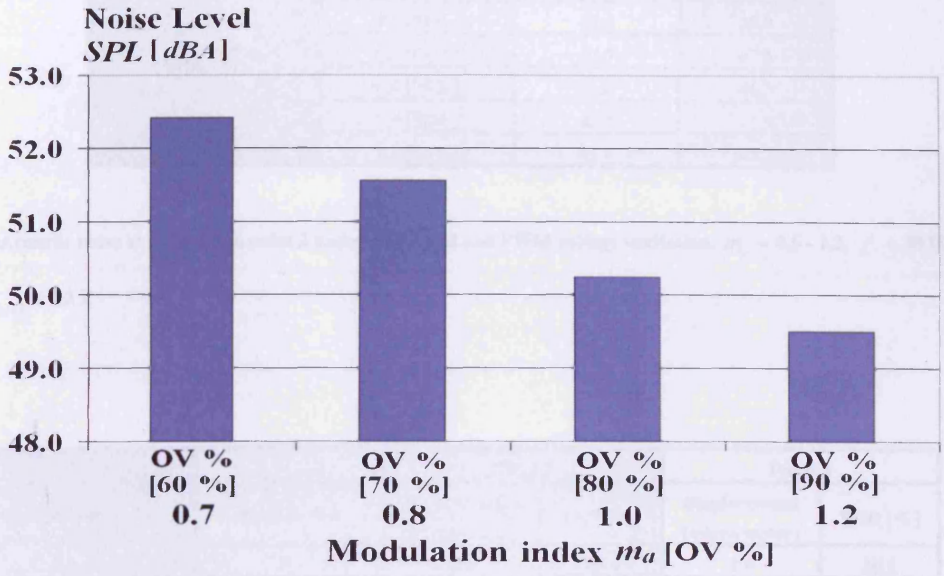

Fig. 5-12 Acoustic noise at point 1 under PWM voltage excitation, m_a = 0.7 - 1.2, f = 100 Hz, f_s = 3 kHz, B_{peak} = 1.3 T

Magnetisation frequency [f]	Modulation index m_a [OV %]	Displacement (micro meter)	THD[%]
PWM 100 Hz	0.7 [60 %]	4.4	40.2
	0.8 [70 %]	4.2	36.4
	1.0 [80 %]	4.0	34.2
	1.2 [90 %]	3.9	33.3

Table 5.3 Peak-to-peak vertical displacement and variation THD[%] of displacement at point 1 under PWM voltage excitation, m_a = 0.7 - 1.2, f = 100 Hz, f_s = 3 kHz, B_{peak} = 1.3 T

5.3.2 Acoustic noise and corresponding peak-to-peak vertical vibration at point 2 and point 3

Table 5.4 shows the acoustic noise, and table 5.5 gives the corresponding peak-to-peak vertical displacement and the variation THD[%] of displacement at point 2 and point 3, under sinusoidal and PWM voltage excitation for assigned values of m_a with $f_s = 3$ kHz, at $f = 50$ Hz, $B_{peak} = 1.3$ T.

Magnetisation frequency [f]	Modulation index m_a [OV %]	Acoustic noise *SPL* [*dBA*]	
		Point 2	Point 3
sine 50 Hz	--	36.8	37.0
PWM 50 Hz	0.5 [40%]	49.9	50.0
	0.6 [50%]	48.6	49.0
	0.7 [60%]	47.5	47.8
	0.8 [70%]	46.8	46.3
	1.0 [80%]	45.5	45.9
	1.2 [90%]	45.0	45.2

Table 5.4 Acoustic noise at point 2 and point 3 under sinusoidal and PWM voltage excitation, m_a = 0.5 - 1.2, f = 50 Hz, f_s = 3 kHz, B_{peak} = 1.3 T

Magnetisation frequency [f]	Modulation index m_a [OV %]	Point 2		Point 3	
		Displacement (micro meter)	*THD* [%]	Displacement (micro meter)	*THD* [%]
sine 50 Hz	--	2.0	19.4	2.0	20.1
PWM 50 Hz	0.5 [40 %]	3.2	36.8	3.3	37.4
	0.6 [50 %]	3.0	34.6	3.1	35.5
	0.7 [60 %]	2.9	33.5	2.9	34.1
	0.8 [70 %]	2.8	32.4	2.7	32.9
	1.0 [80 %]	2.7	30.6	2.6	31.3
	1.2 [90 %]	2.5	28.1	2.4	28.9

Table 5.5 Peak-to-peak vertical displacement and variation *THD*[%] of displacement at point 2 and point 3 under sinusoidal and PWM voltage excitation, m_a = 0.5 - 1.2, f = 50 Hz, f_s = 3 kHz, B_{peak} = 1.3 T

Fig. 5-13 to fig. 5-18 show plots of vertical displacement with flux density, and fig. 5-19 to fig. 5-24 show the harmonic components of vertical displacement at point 2, which were obtained by FFT, under PWM voltage excitation for assigned values of m_a with f_s = 3 kHz, at f = 50 Hz, B_{peak} = 1.3 T.

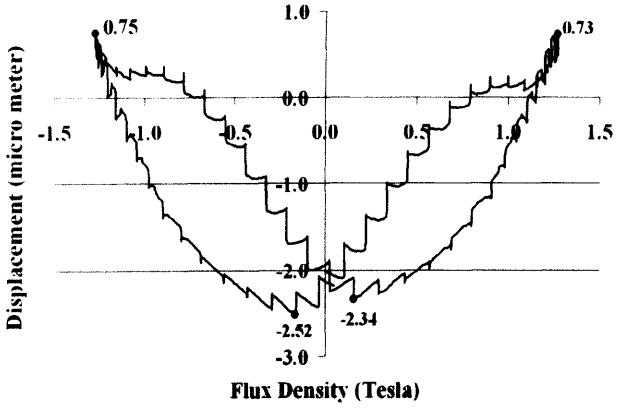

Fig. 5-13 Vertical displacement at point 2 under PWM voltage excitation, m_a = 0.5, f_s = 3 kHz, f = 50 Hz, B_{peak} = 1.3 T

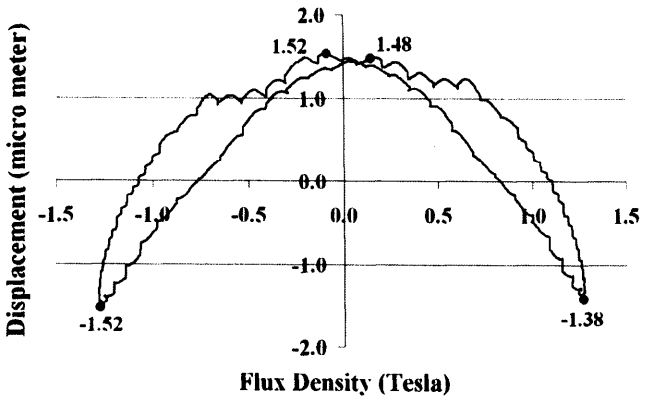

Fig. 5-14 Vertical displacement at point 2 under PWM voltage excitation, m_a = 0.6, f_s = 3 kHz, f = 50 Hz, B_{peak} = 1.3 T

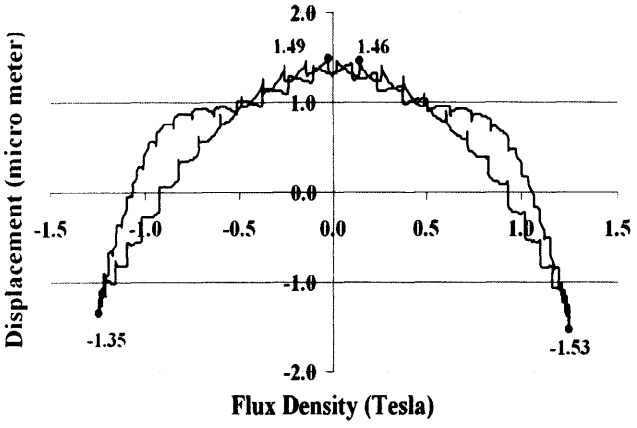

Fig. 5-15 Vertical displacement at point 2 under PWM voltage excitation, m_a = 0.7, f_s = 3 kHz, f = 50 Hz, B_{peak} = 1.3 T

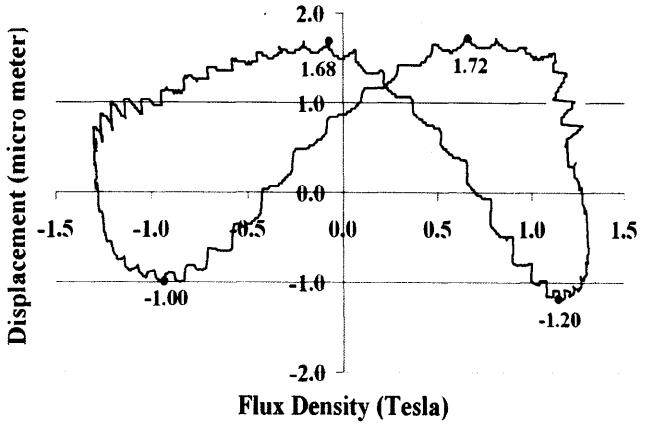

Fig. 5-16 Vertical displacement at point 2 under PWM voltage excitation, m_a = 0.8, f_s = 3 kHz, f = 50 Hz, B_{peak} = 1.3 T

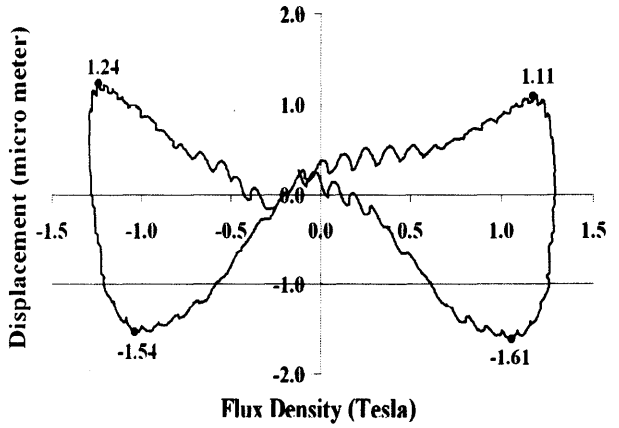

Fig. 5-17 Vertical displacement at point 2 under PWM voltage excitation, m_a = 1.0, f_s = 3 kHz, f = 50 Hz, B_{peak} = 1.3 T

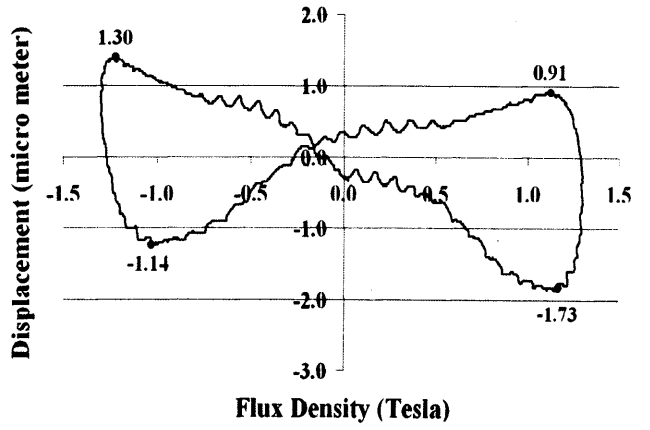

Fig. 5-18 Vertical displacement at point 2 under PWM voltage excitation, m_a = 1.2, f_s = 3 kHz, f = 50 Hz, B_{peak} = 1.3 T

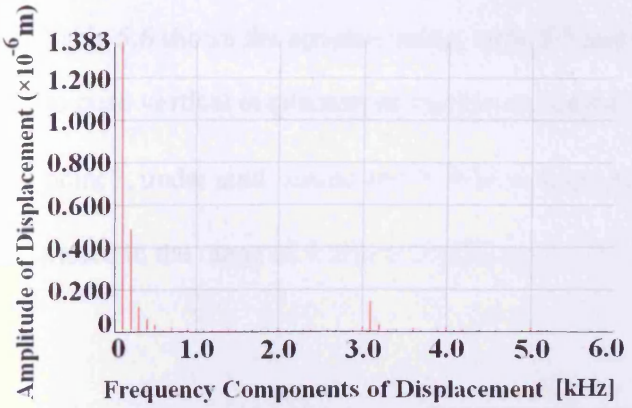

Fig. 5-19 Harmonic components of vertical displacement at point 2 under PWM voltage excitation, m_a = 0.5, f_s = 3 kHz, f = 50 Hz, B_{peak} = 1.3 T

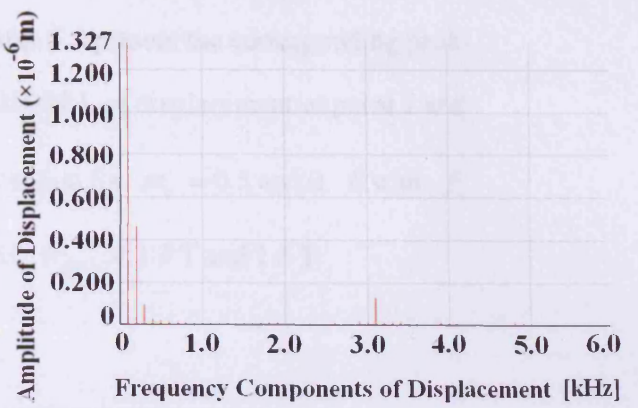

Fig. 5-20 Harmonic components of vertical displacement at point 2 under PWM voltage excitation, m_a = 0.6, f_s = 3 kHz, f = 50 Hz, B_{peak} = 1.3 T

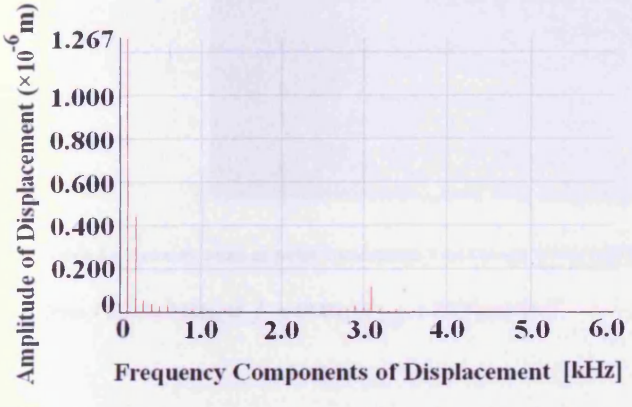

Fig. 5-21 Harmonic components of vertical displacement at point 2 under PWM voltage excitation, m_a = 0.7, f_s = 3 kHz, f = 50 Hz, B_{peak} = 1.3 T

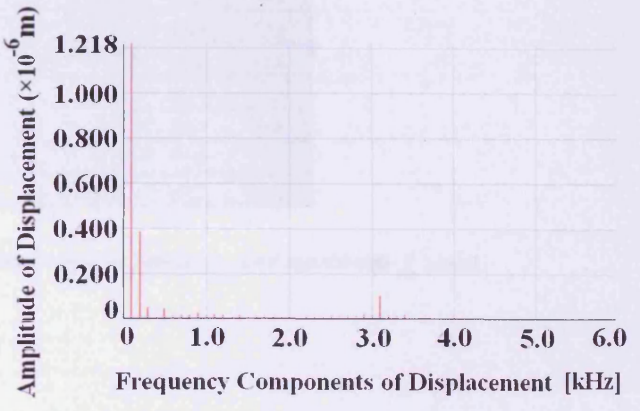

Fig. 5-22 Harmonic components of vertical displacement at point 2 under PWM voltage excitation, m_a = 0.8, f_s = 3 kHz, f = 50 Hz, B_{peak} = 1.3 T

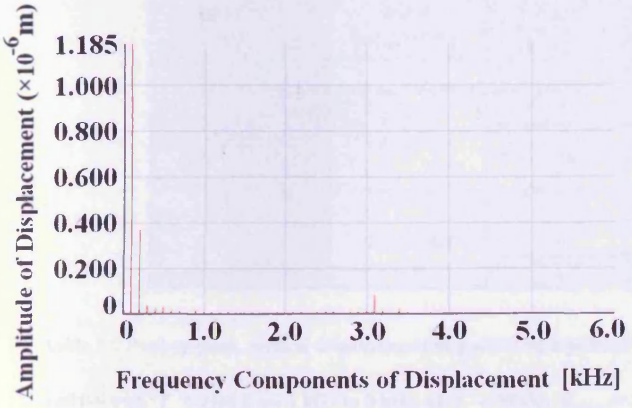

Fig. 5-23 Harmonic components of vertical displacement at point 2 under PWM voltage excitation, m_a = 1.0, f_s = 3 kHz, f = 50 Hz, B_{peak} = 1.3 T

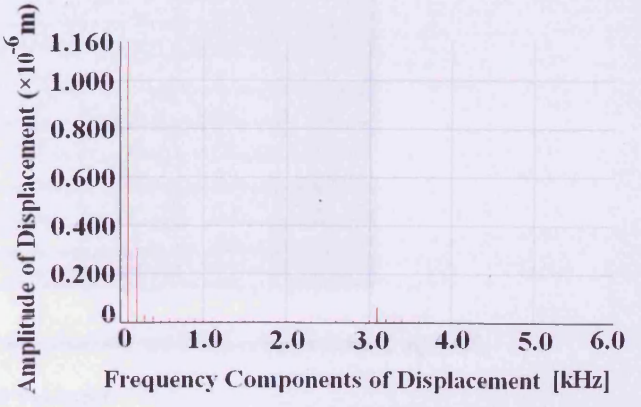

Fig. 5-24 Harmonic components of vertical displacement at point 2 under PWM voltage excitation, m_a = 1.2, f_s = 3 kHz, f = 50 Hz, B_{peak} = 1.3 T

Table 5.6 shows the acoustic noise, table 5.7 and table 5.8 present the corresponding peak-to-peak vertical displacement and the va riation $THD[\%]$ of displacement at poi nt 2 and point 3, under sinu soidal and P WM vo ltage ex citation for $m_a = 0.5$ and 0. 6 with f_s varied in the range of 1 kHz to 3 kHz, at $f = 50$ Hz, $B_{peak} = 1.3$ T and 1.5 T.

Magnetisation frequency [f]	Modulation index m_a [OV %]	Switching frequency [f_s] [kHz]	Acoustic noise SPL [dBA]			
			1.3 T		1.5 T	
			Point 2	Point 3	Point 2	Point 3
sine 50 Hz	--	--	36.8	37.0	39.6	39.7
PWM 50 Hz	0.5 [40 %]	1	51.9	51.9	54.0	53.6
		2	50.7	50.8	52.5	52.4
		3	49.9	50.0	51.7	51.5
	0.6 [50 %]	1	50.7	50.8	53.0	52.8
		2	49.3	49.9	51.8	51.7
		3	48.6	49.0	50.7	50.6

Table 5.6 Acoustic noise at point 2 and point 3 under sinusoidal and PWM voltage excitation, $m_a = 0.5$ and 0.6 with f_s varied from 1 kHz to 3 kHz, at $f = 50$ Hz, $B_{peak} = 1.3$ T and 1.5 T

Magnetisation frequency [f]	Modulation index m_a [OV %]	Switching frequency [f_s] [kHz]	Displacement (micro meter)			
			1.3 T		1.5 T	
			Point 2	Point 3	Point 2	Point 3
sine 50 Hz	--	--	2.0	2.0	2.7	2.6
PWM 50 Hz	0.5 [40 %]	1	3.6	3.8	4.1	4.2
		2	3.4	3.6	3.8	3.9
		3	3.2	3.3	3.6	3.6
	0.6 [50 %]	1	3.4	3.6	3.8	3.9
		2	3.2	3.3	3.5	3.6
		3	3.0	3.1	3.4	3.4

Table 5.7 Peak-to-peak vertical displacement at point 2 and point 3 under sinusoidal and PWM voltage excitation, $m_a = 0.5$ and 0.6 with f_s varied from 1 kHz to 3 kHz, at $f = 50$ Hz, $B_{peak} = 1.3$ T and 1.5 T

Magnetisation frequency [f]	Modulation index m_a [OV %]	Switching frequency [f_s] [kHz]	THD [%]			
			Point 2		Point 3	
			1.3 T	1.5 T	1.3 T	1.5 T
sine 50 Hz	--	--	19.4	27.5	20.1	28.3
PWM 50 Hz	0.5 [40 %]	1	40.7	45.2	41.3	45.7
		2	38.6	42.8	39.2	43.2
		3	36.8	40.3	37.4	40.8
	0.6 [50 %]	1	38.1	42.4	38.5	43.1
		2	36.2	39.7	36.9	40.3
		3	34.6	38.4	35.5	38.9

Table 5.8 THD [%] of vertical displacement at point 2 and point 3 under sinusoidal and PWM voltage excitation, m_a = 0.5 and 0.6 with f_s varied from 1 kHz to 3 kHz, at f = 50 Hz, B_{peak} = 1.3 T and 1.5 T

Fig. 5-25 to fig. 5-32 show plots of ve rtical displacement with flux density, and fig. 5-33 to fig. 5-40 sho w harmonic components o f displacement at point 2 under sinusoidal and PWM voltage excitation for m_a = 0.6 with f_s varied from 1 kHz to 3 kHz, at f = 50 Hz, B_{peak} = 1.3 T and 1.5 T.

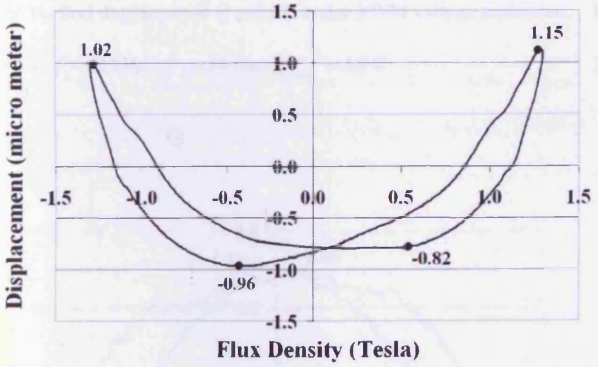

Fig. 5-25 V ertical di splacement at po int 2 under s inusoidal vo ltage excitation, f = 50 Hz, B_{peak} = 1.3 T

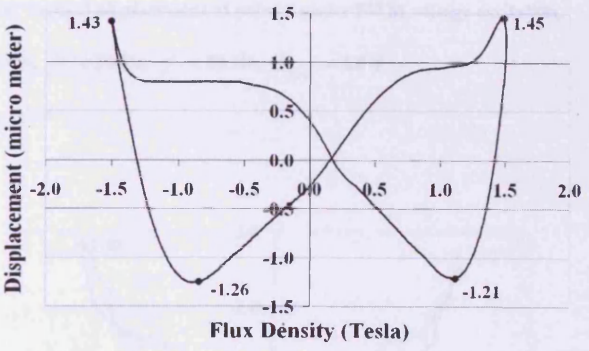

Fig. 5-26 V ertical di splacement at po int 2 under s inusoidal vo ltage excitation, f = 50 Hz, B_{peak} = 1.5 T

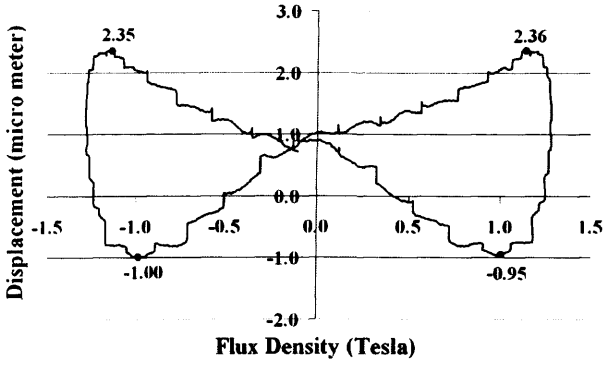

Fig. 5-27 Vertical displacement at point 2 under PWM voltage excitation, $m_a = 0.6$, $f_s = 1$ kHz, $f = 50$ Hz, $B_{peak} = 1.3$ T

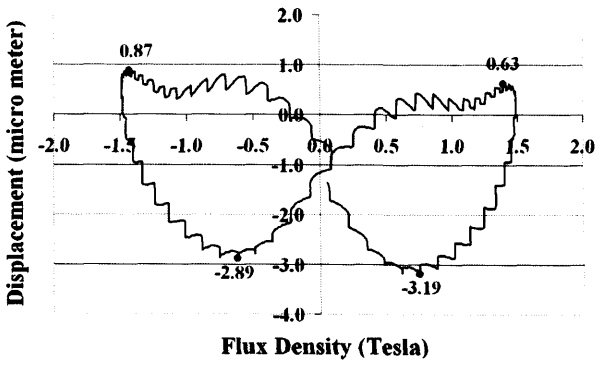

Fig. 5-28 Vertical displacement at point 2 under PWM voltage excitation, $m_a = 0.6$, $f_s = 1$ kHz, $f = 50$ Hz, $B_{peak} = 1.5$ T

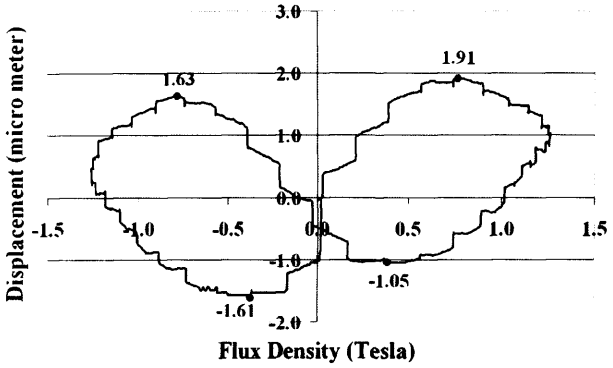

Fig. 5-29 Vertical displacement at point 2 under PWM voltage excitation, $m_a = 0.6$, $f_s = 2$ kHz, $f = 50$ Hz, $B_{peak} = 1.3$ T

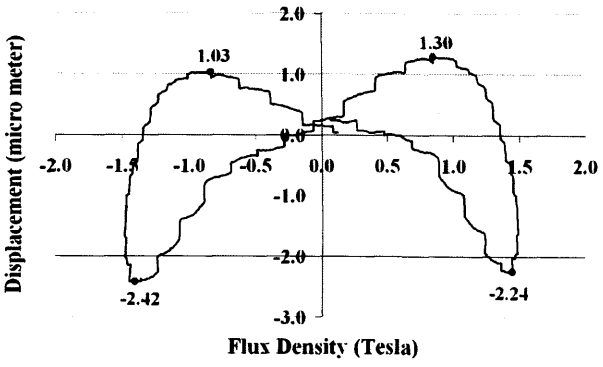

Fig. 5-30 Vertical displacement at point 2 under PWM voltage excitation, $m_a = 0.6$, $f_s = 2$ kHz, $f = 50$ Hz, $B_{peak} = 1.5$ T

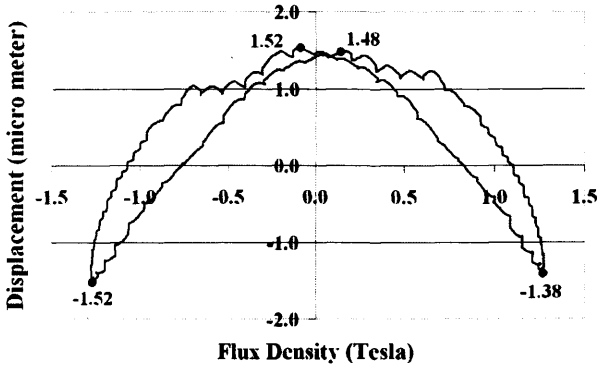

Fig. 5-31 Vertical displacement under at point 2 PWM voltage excitation, $m_a = 0.6$, $f_s = 3$ kHz, $f = 50$ Hz, $B_{peak} = 1.3$ T

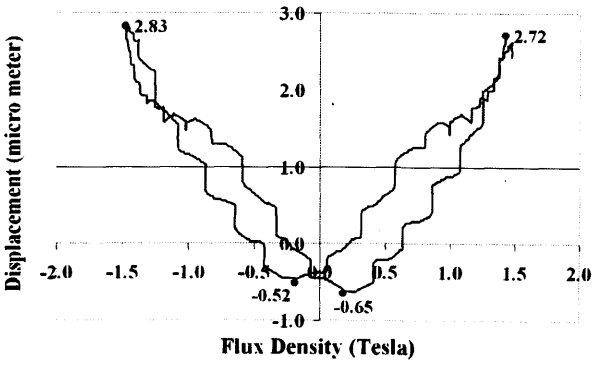

Fig. 5-32 Vertical displacement at point 2 under PWM voltage excitation, $m_a = 0.6$, $f_s = 3$ kHz, $f = 50$ Hz, $B_{peak} = 1.5$ T

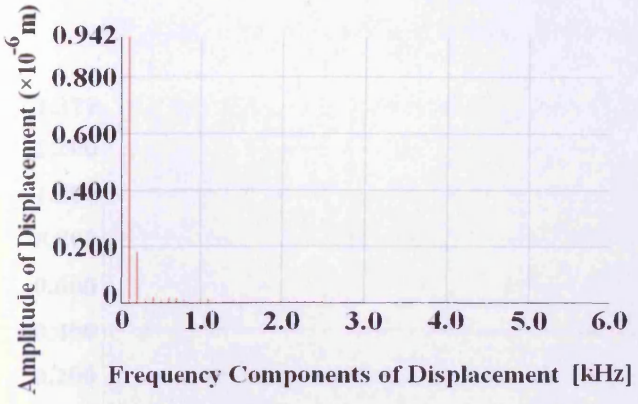

Fig. 5-33 Harmonic components of vertical displacement at point 2 under sinusoidal voltage excitation, f = 50 Hz, B_{peak} = 1.3 T

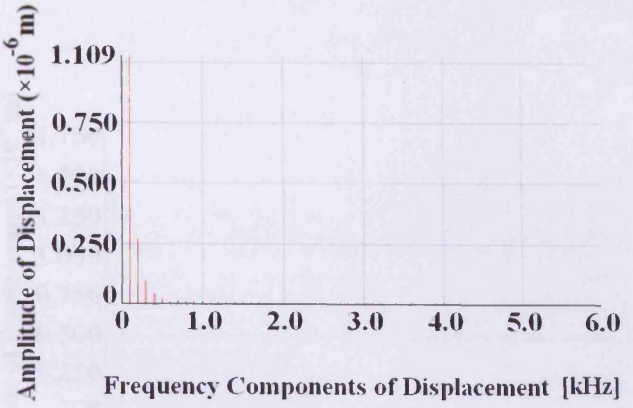

Fig. 5-34 Harmonic components of vertical displacement at point 2 under sinusoidal voltage excitation, f = 50 Hz, B_{peak} = 1.5 T

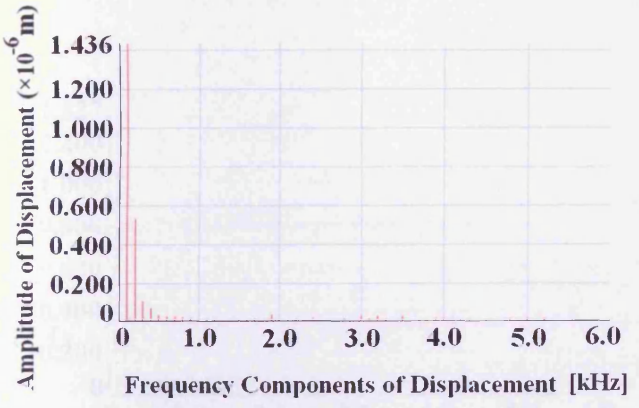

Fig. 5-35 Harmonic components of vertical displacement at point 2 under PWM voltage excitation, m_a = 0.6, f_s = 1 kHz, f = 50 Hz, B_{peak} = 1.3 T

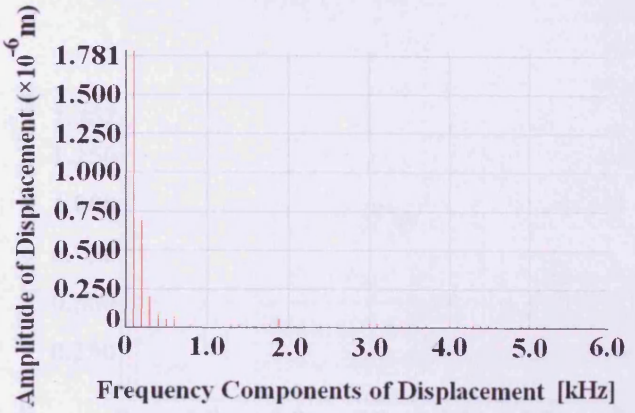

Fig. 5-36 Harmonic components of vertical displacement at point 2 under PWM voltage excitation, m_a = 0.6, f_s = 1 kHz, f = 50 Hz, B_{peak} = 1.5 T

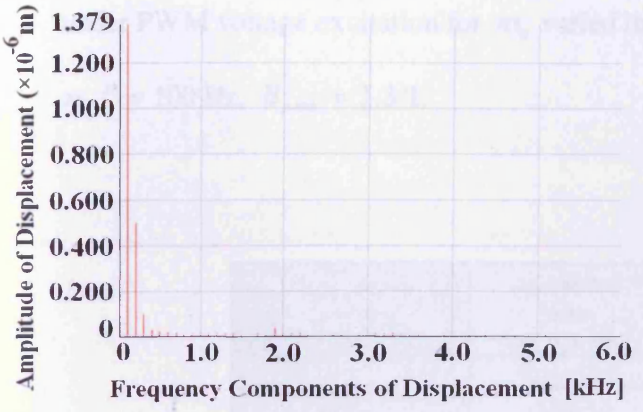

Fig. 5-37 Harmonic components of vertical displacement at point 2 under PWM voltage excitation, m_a = 0.6, f_s = 2 kHz, f = 50 Hz, B_{peak} = 1.3 T

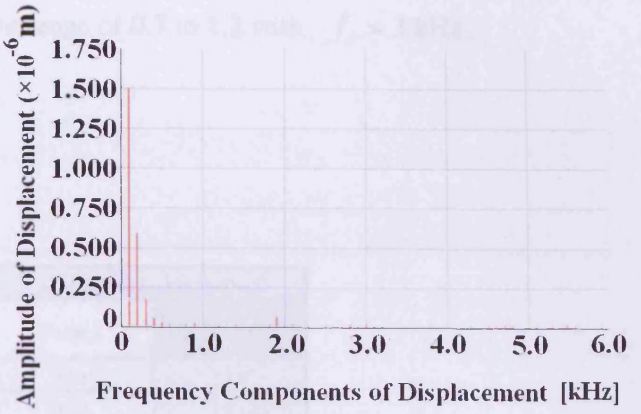

Fig. 5-38 Harmonic components of vertical displacement at point 2 under PWM voltage excitation, m_a = 0.6, f_s = 2 kHz, f = 50 Hz, B_{peak} = 1.5 T

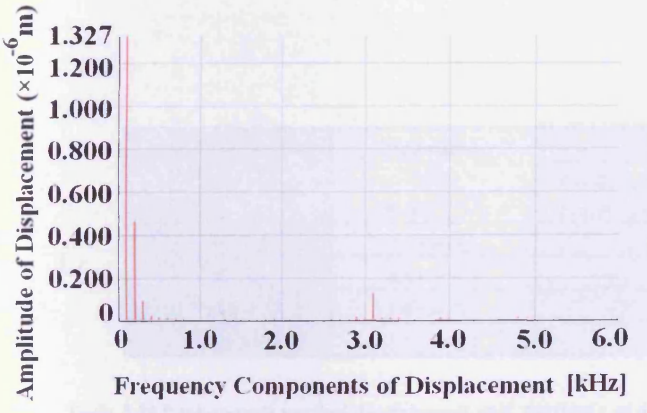

Fig. 5-39 Harmonic components of vertical displacement at point 2 under PWM voltage excitation, m_a = 0.6, f_s = 3 kHz, f = 50 Hz, B_{peak} = 1.3 T

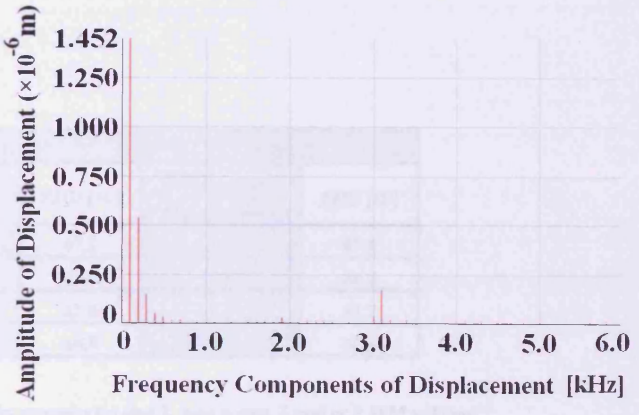

Fig. 5-40 Harmonic components of vertical displacement at point 2 under PWM voltage excitation, m_a = 0.6, f_s = 3 kHz, f = 50 Hz, B_{peak} = 1.5 T

Table 5.9 shows the acoustic noise, table 5. 10 indicates the corresponding peak-to-peak vertical displacement and the variation $THD[\%]$ of displacement at point 2 and point 3 under PWM voltage excitation for m_a varied in the range of 0.7 to 1.2 with $f_s = 3$ kHz, at $f = 100$ Hz, $B_{peak} = 1.3$ T.

Magnetisation frequency $[f]$	Modulation index m_a [OV %]	Acoustic noise *SPL [dBA]*	
		Point 2	Point 3
PWM 100 Hz	0.7 [60 %]	53.3	53.0
	0.8 [70 %]	52.5	52.1
	1.0 [80 %]	51.7	51.4
	1.2 [90 %]	50.2	50.8

Table 5.9 Acoustic noise at point 2 and point 3 under PWM voltage excitation, m_a = 0.7 - 1.2, f = 100 Hz, f_s = 3 kHz, B_{peak} = 1.3 T

Magnetisation Frequency $[f]$	Modulation index m_a [OV %]	Point 2		Point 3	
		Displacement (micro meter)	*THD* [%]	Displacement (micro meter)	*THD* [%]
PWM 100 Hz	0.7 [60 %]	4.6	47.1	4.8	47.8
	0.8 [70 %]	4.4	43.6	4.6	44.2
	1.0 [80 %]	4.2	41.4	4.3	41.7
	1.2 [90 %]	4.0	40.9	4.1	40.3

Table 5.10 Peak-to-peak vertical displacement and $THD[\%]$ of displacement at point 2 and point 3 under PWM voltage excitation, m_a = 0.7 - 1.2, f = 100 Hz, f_s = 3 kHz, B_{peak} = 1.3 T

Fig. 5-41 to fig. 5-44 show plots of vertical displacement with flux density, and fig. 5-45 to fig. 5-48 show harmonic components of displacement at point 2 under PWM voltage excitation for m_a varied in the range of 0.7 to 1.2 with $f_s = 3$ kHz, at $f = 100$ Hz, $B_{peak} = 1.3$ T.

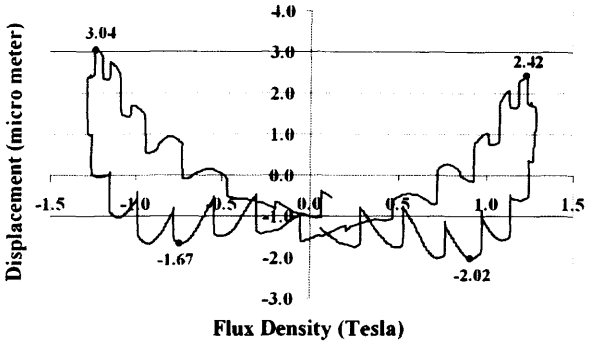

Fig. 5-41 V ertical di splacement a t po int 2 unde r PW M vo ltage excitation, m_a = 0.7, f_s = 3 kHz, f = 100 Hz, B_{peak} = 1.3 T

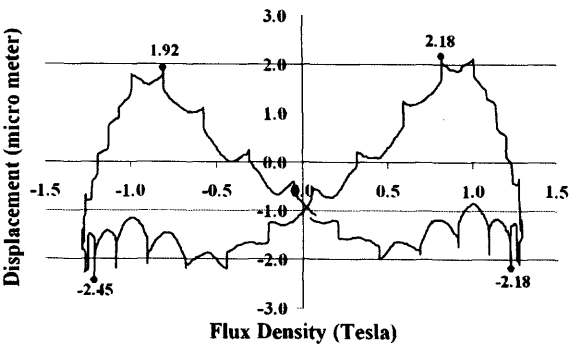

Fig. 5-42 V ertical di splacement a t po int 2 unde r PW M vo ltage excitation, m_a = 0.8, f_s = 3 kHz, f = 100 Hz, B_{peak} = 1.3 T

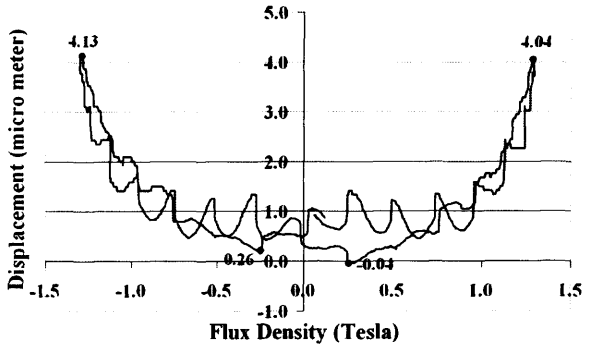

Fig. 5-43 V ertical di splacement a t po int 2 unde r PW M vo ltage excitation, m_a = 1.0, f_s = 3 kHz, f = 100 Hz, B_{peak} = 1.3 T

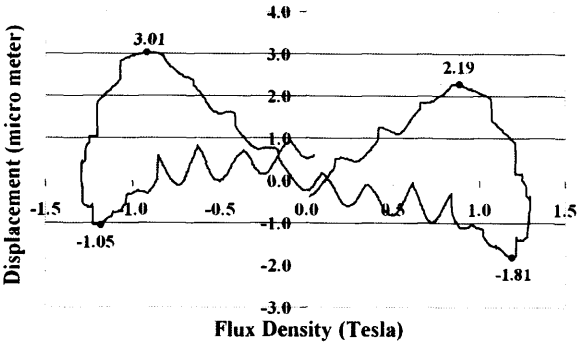

Fig. 5-44 V ertical di splacement a t po int 2 unde r P WM vo ltage excitation, m_a = 1.2, f_s = 3 kHz, f = 100 Hz, B_{peak} = 1.3 T

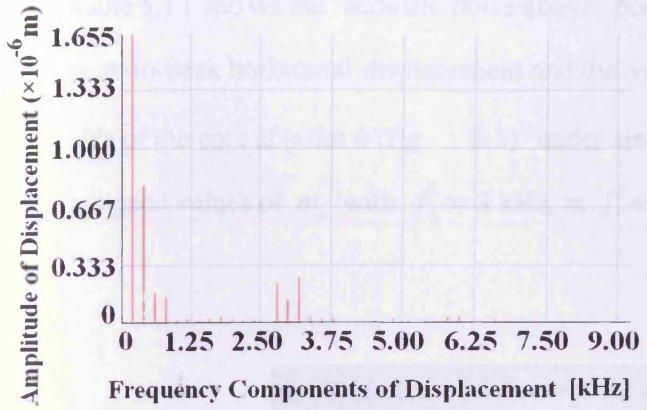

Fig. 5-45 Harmonic components of vertical displacement at point 2 under PWM voltage excitation, m_a = 0.7, f_s = 3 kHz, f = 100 Hz, B_{peak} = 1.3 T

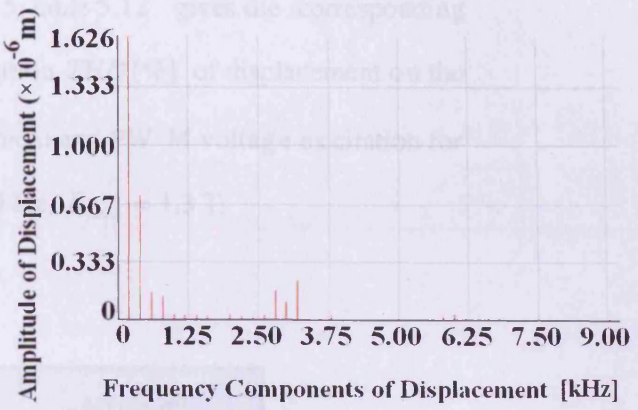

Fig. 5-46 Harmonic components of vertical displacement at point 2 under PWM voltage excitation, m_a = 0.8, f_s = 3 kHz, f = 100 Hz, B_{peak} = 1.3 T

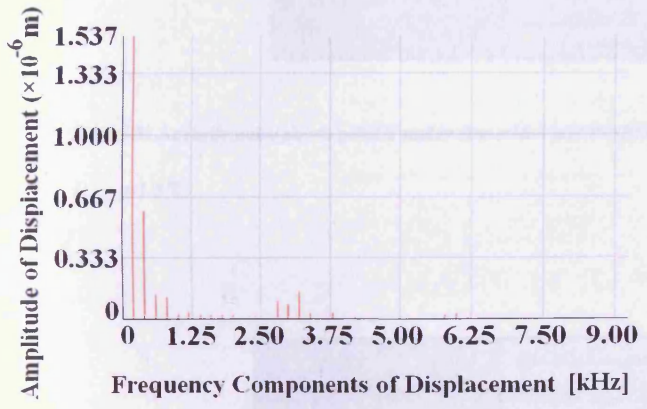

Fig. 5-47 Harmonic components of vertical displacement at point 2 under PWM voltage excitation, m_a = 1.0, f_s = 3 kHz, f = 100 Hz, B_{peak} = 1.3 T

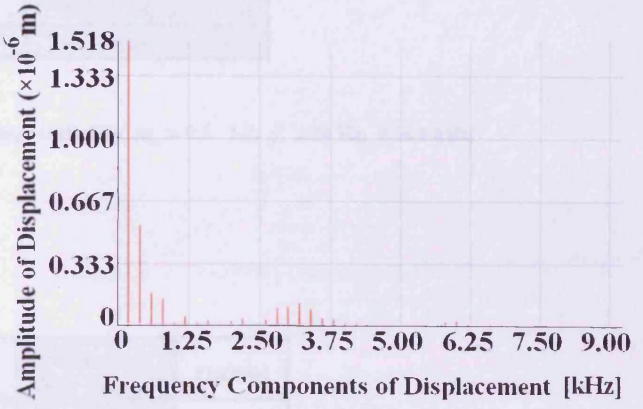

Fig. 5-48 Harmonic components of vertical displacement at point 2 under PWM voltage excitation, m_a = 1.2, f_s = 3 kHz, f = 100 Hz, B_{peak} = 1.3 T

5.3.3 Acoustic noise at point 5 and corresponding peak-to-peak horizontal vibration at point 4

Table 5.11 shows the acoustic noise above point 5, table 5.12 gives the corresponding peak-to-peak horizontal displacement and the variation THD [%] of displacement on the side of the core at point 4 (fig. 5-1) under sinusoidal and PWM voltage excitation for assigned values of m_a with f_s = 3 kHz, at f = 50 Hz, B_{peak} = 1.3 T.

Magnetisation frequency [f]	Modulation index m_a [OV %]	Acoustic noise SPL [dBA]
sine 50 Hz	--	37.7
PWM 50 Hz	0.5 [40 %]	50.8
	0.6 [50 %]	49.6
	0.7 [60 %]	48.3
	0.8 [70 %]	47.4
	1.0 [80 %]	46.6
	1.2 [90 %]	45.5

Table 5.11 Acoustic noise above point 5 under sinusoidal and PWM voltage excitation, m_a = 0.5 - 1.2, f = 50 Hz, f_s = 3 kHz, B_{peak} = 1.3 T

Magnetisation frequency [f]	Modulation index m_a [OV %]	Displacement (micro meter)	THD[%]
sine 50 Hz	--	0.21	12.2
PWM 50 Hz	0.5 [40 %]	0.33	38.2
	0.6 [50 %]	0.31	34.9
	0.7 [60 %]	0.29	31.8
	0.8 [70 %]	0.28	28.7
	1.0 [80 %]	0.26	26.5
	1.2 [90 %]	0.24	25.2

Table 5.12 Peak-to-peak horizontal displacement and variation THD [%] of displacement at point 4 under sinusoidal and PWM voltage excitation, m_a = 0.5 - 1.2, f = 50 Hz, f_s = 3 kHz, B_{peak} = 1.3 T

Fig. 5-49 to fig. 5-54 show plots of horizontal displacement with flux density, and fig. 5-55 to fig. 5-60 display harmonic components of displacement at point 4 under PWM voltage excitation for m_a of 0.5 to 1.2 with $f_s = 3$ kHz, at $f = 50$ Hz, $B_{peak} = 1.3$ T.

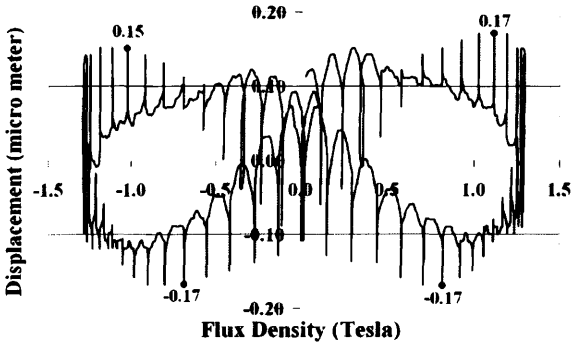

Fig. 5-49 Horizontal displacement at point 4 under PWM voltage excitation, $m_a = 0.5$, $f_s = 3$ kHz, $f = 50$ Hz, $B_{peak} = 1.3$ T

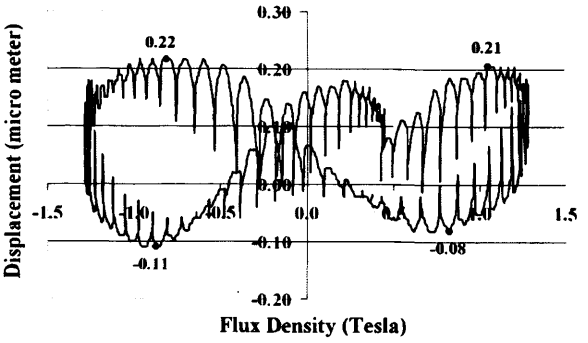

Fig. 5-50 Horizontal displacement at point 4 under PWM voltage excitation, $m_a = 0.6$, $f_s = 3$ kHz, $f = 50$ Hz, $B_{peak} = 1.3$ T

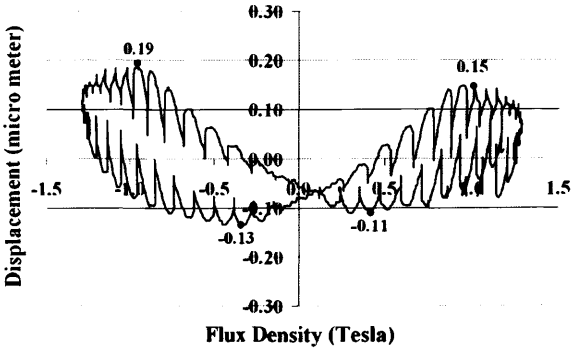

Fig. 5-51 Horizontal displacement at point 4 under PWM voltage excitation, $m_a = 0.7$, $f_s = 3$ kHz, $f = 50$ Hz, $B_{peak} = 1.3$ T

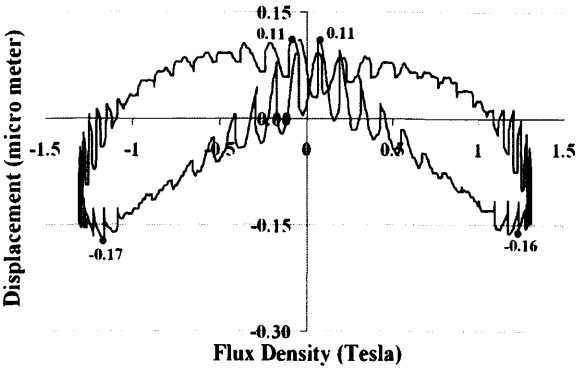

Fig. 5-52 Horizontal displacement at point 4 under PWM voltage excitation, $m_a = 0.8$, $f_s = 3$ kHz, $f = 50$ Hz, $B_{peak} = 1.3$ T

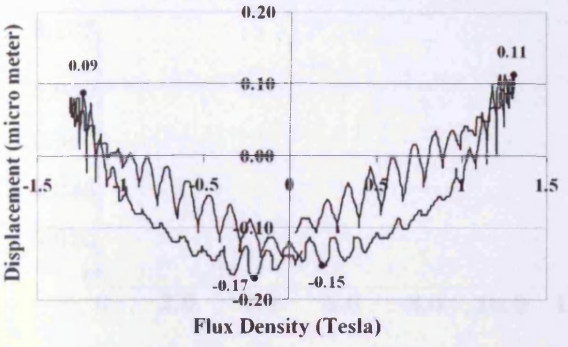

Fig. 5-53 Horizontal displacement at point 4 under PWM voltage excitation, m_a = 1.0, f_s = 3 kHz, f = 50 Hz, B_{peak} = 1.3 T

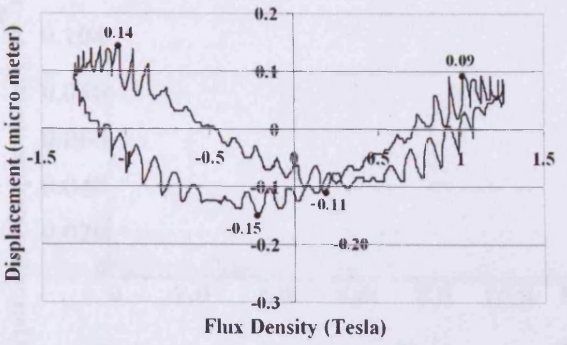

Fig. 5-54 Horizontal displacement at point 4 under PWM voltage excitation, m_a = 1.2, f_s = 3 kHz, f = 50 Hz, B_{peak} = 1.3 T

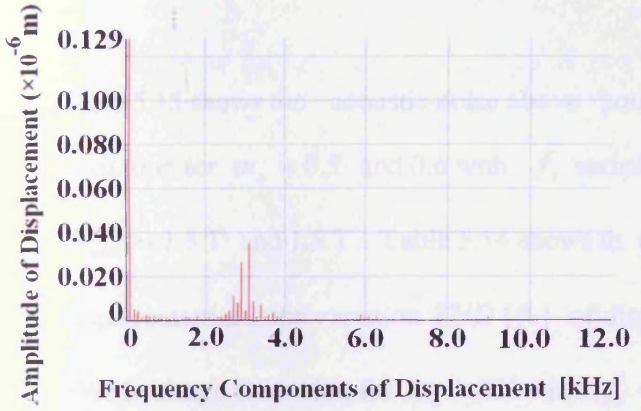

Fig. 5-55 Harmonic components of horizontal displacement at point 4 under PWM voltage excitation, m_a = 0.5, f_s = 3 kHz, f = 50 Hz, B_{peak} = 1.3 T

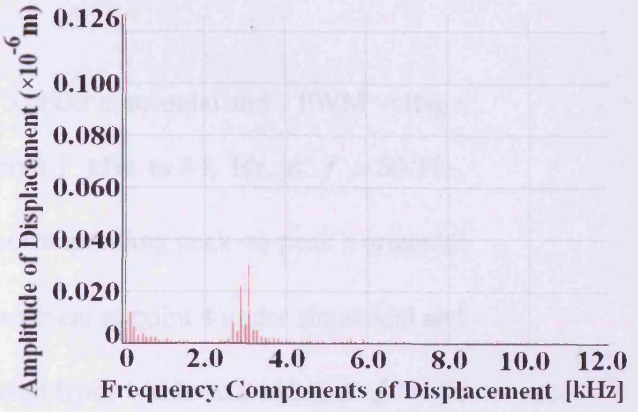

Fig. 5-56 Harmonic components of horizontal displacement at point 4 under PWM voltage excitation, m_a = 0.6, f_s = 3 kHz, f = 50 Hz, B_{peak} = 1.3 T

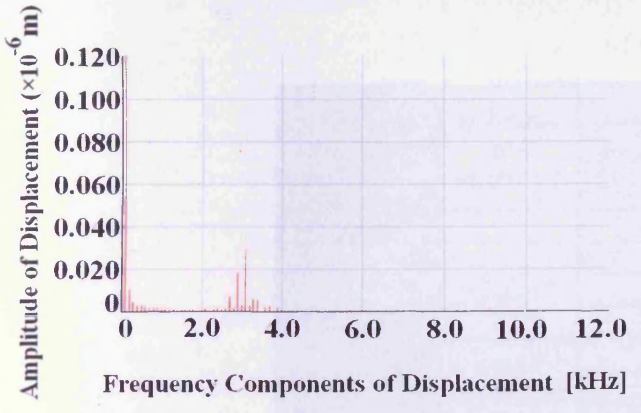

Fig. 5-57 Harmonic components of horizontal displacement at point 4 under PWM voltage excitation, m_a = 0.7, f_s = 3 kHz, f = 50 Hz, B_{peak} = 1.3 T

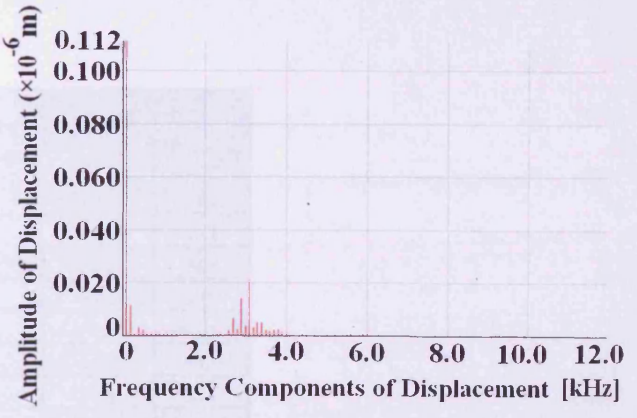

Fig. 5-58 Harmonic components of horizontal displacement at point 4 under PWM voltage excitation, m_a = 0.8, f_s = 3 kHz, f = 50 Hz, B_{peak} = 1.3 T

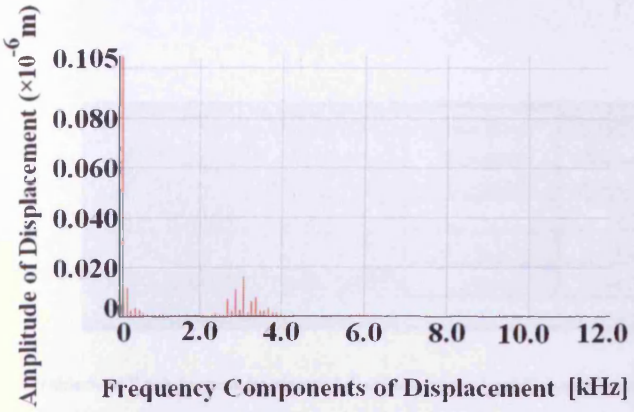

Fig. 5-59 Harmonic components of horizontal displacement at point 4 under PWM voltage excitation, m_a = 1.0, f_s = 3 kHz, f = 50 Hz, B_{peak} = 1.3 T

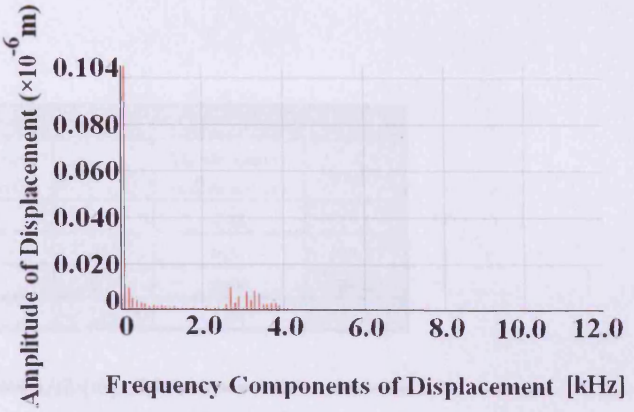

Fig. 5-60 Harmonic components of horizontal displacement at point 4 under PWM voltage excitation, m_a = 1.2, f_s = 3 kHz, f = 50 Hz, B_{peak} = 1.3 T

Table 5.13 shows the acoustic noise above point 5 under sinusoidal and PWM voltage excitation for m_a = 0.5 and 0.6 with f_s varied from 1 kHz to 3 k Hz, at f = 50 Hz, B_{peak} = 1.3 T and 1.5 T . Table 5.14 shows the corresponding peak-to-peak horizontal displacement and the variation THD [%] of displacement at point 4 under sinusoidal and PWM voltage excitation for m_a = 0.6 with f_s varied from 1 kHz to 3 kHz , at f = 50 Hz, B_{peak} = 1.3 T and 1.5 T.

Magnetisation frequency [f]	Modulation index m_a [OV %]	Switching frequency [f_s] [kHz]	Acoustic noise SPL [dBA]	
			1.3 T	1.5 T
sine 50 Hz	--	--	37.7	40.6
PWM 50 Hz	0.5 [40 %]	1	52.2	54.3
		2	51.4	53.1
		3	50.8	52.5
	0.6 [50 %]	1	51.6	53.3
		2	50.1	52.2
		3	49.6	51.8

Table 5. 13 Acoustic noise at point 5 under sinusoidal and PWM voltage excitation for assigned m_a = 0.5 and 0.6 with f_s varied from 1 kHz to 3 kHz, at f = 50 Hz, B_{peak} = 1.3 T and 1.5 T

Magnetisation frequency [f]	Modulation index m_a [OV %]	Switching frequency [f_s] [kHz]	1.3 T		1.5 T	
			Displacement (micro meter)	THD[%]	Displacement (micro meter)	THD[%]
sine 50Hz	--	--	0.21	12.2	0.48	19.1
PWM 50Hz	0.6 [50 %]	1	0.36	40.5	0.59	43.2
		2	0.33	37.7	0.56	40.4
		3	0.31	34.9	0.54	37.2

Table 5. 14 P eak-to-peak ho rizontal di splacement a t poi nt 4 and var iation THD [%] of d isplacement unde r s inusoidal a nd PWM voltage excitation for m_a = 0.6 with f_s varied from 1 kHz to 3 kHz, at f = 50 Hz, B_{peak} = 1.3 T and 1.5 T

Fig. 5-61 to fig. 5-68 show plots of horiz ontal displacement with flux density, and fig. 5-69 to fig. 5-76 displa y harmonic components of horizontal displacement at point 4 under sinusoidal and PWM voltage excitation for $m_a = 0.6$ with f_s varied from 1 kHz to 3 kHz, at f = 50 Hz, B_{peak} = 1.3 T and 1.5 T.

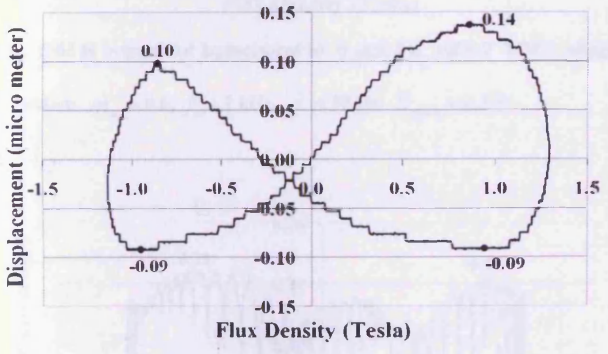

Fig. 5- 61 Horizontal d isplacement at p oint 4 u nder s inusoidal v oltage excitation, f = 50 Hz, B_{peak} = 1.3 T

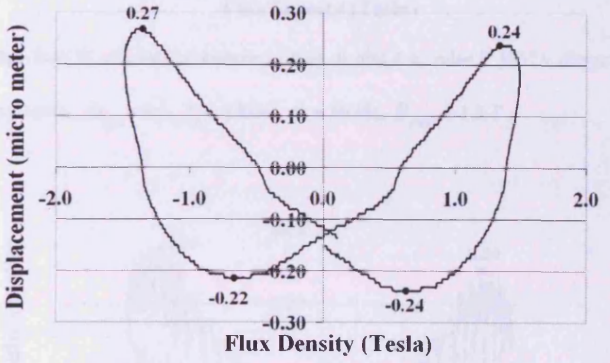

Fig. 5- 62 H orizontal d isplacement at p oint 4 u nder s inusoidal v oltage excitation, f = 50 Hz, B_{peak} = 1.5 T

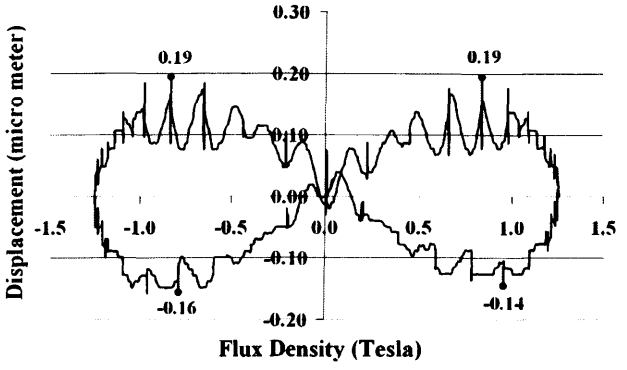

Fig. 5-63 H orizontal d isplacement at p oint 4 u nder P WM v oltage excitation, m_a = 0.6, f_s = 1 kHz, f = 50 Hz, B_{peak} = 1.3 T

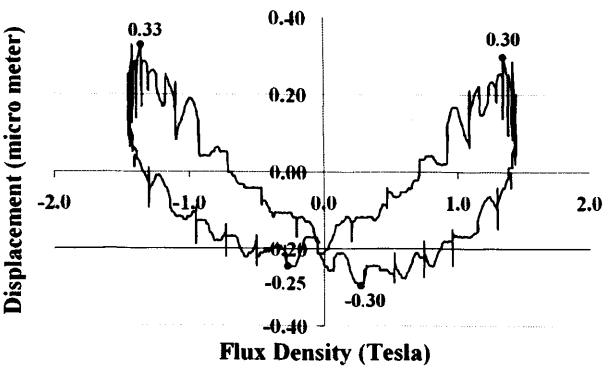

Fig. 5-64 H orizontal d isplacement at p oint 4 u nder P WM v oltage excitation, m_a = 0.6, f_s = 1 kHz, f = 50 Hz, B_{peak} = 1.5 T

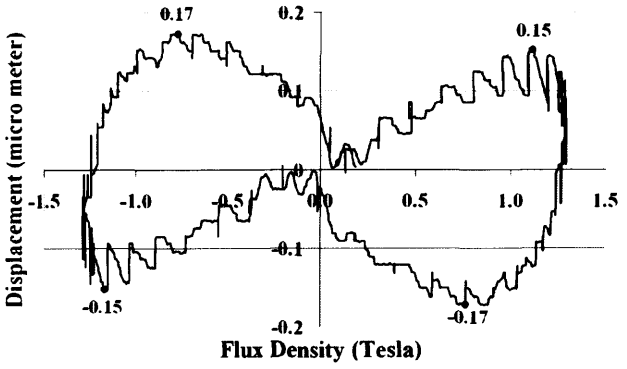

Fig. 5-65 H orizontal d isplacement at p oint 4 u nder P WM v oltage excitation, m_a = 0.6, f_s = 2 kHz, f = 50 Hz, B_{peak} = 1.3 T

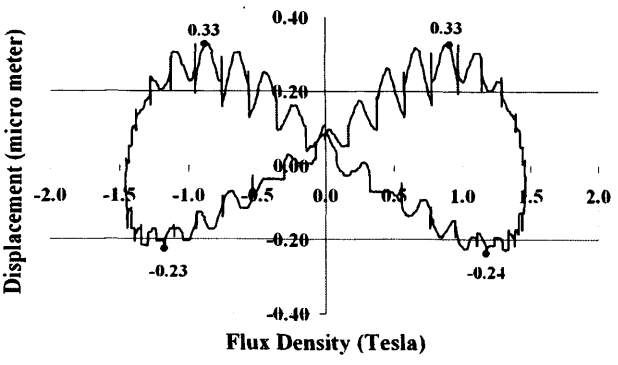

Fig. 5-66 H orizontal d isplacement at p oint 4 u nder P WM v oltage excitation, m_a = 0.6, f_s = 2 kHz, f = 50 Hz, B_{peak} = 1.5 T

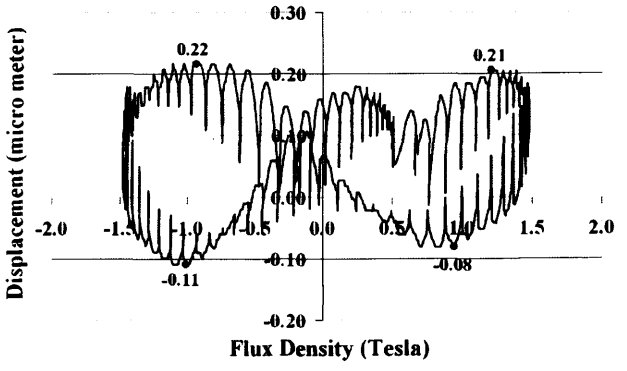

Fig. 5-67 H orizontal d isplacement at p oint 4 u nder P WM v oltage excitation, m_a = 0.6, f_s = 3 kHz, f = 50 Hz, B_{peak} = 1.3 T

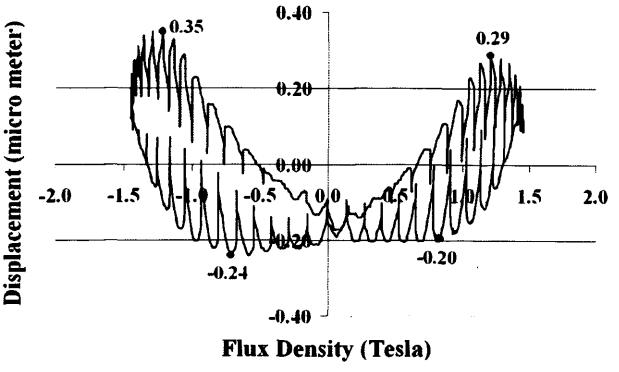

Fig. 5-68 H orizontal d isplacement at p oint 4 u nder P WM v oltage excitation, m_a = 0.6, f_s = 3 kHz, f = 50 Hz, B_{peak} = 1.5 T

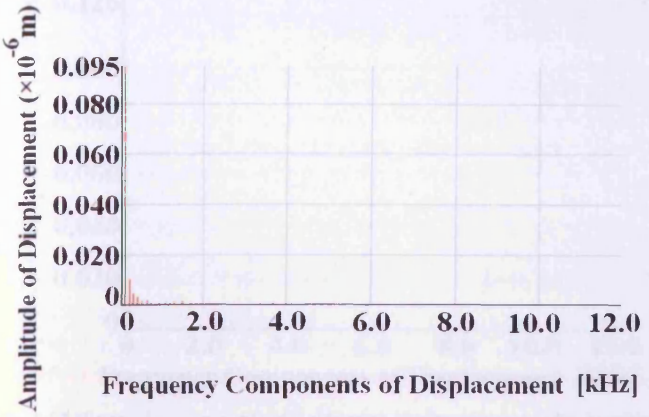

Fig. 5-69 Harmonic components of horizontal displacement at point 4 under sinusoidal voltage excitation, f = 50 Hz, B_{peak} = 1.3 T

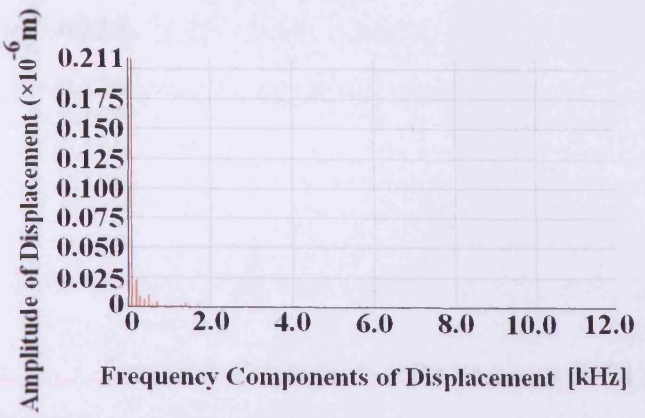

Fig. 5-70 Harmonic components of horizontal displacement at point 4 under sinusoidal voltage excitation, f = 50 Hz, B_{peak} = 1.5 T

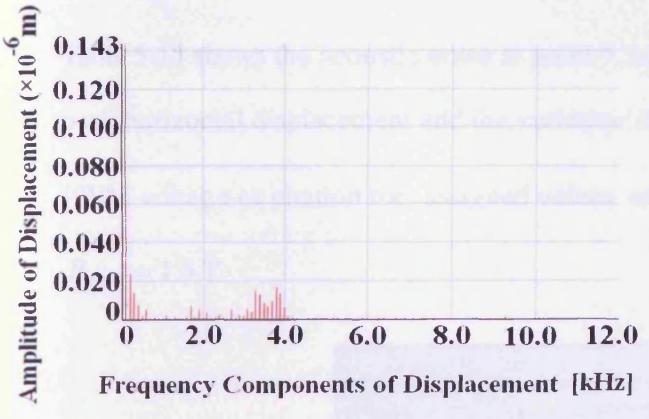

Fig. 5-71 Harmonic components of horizontal displacement at point 4 under PWM voltage excitation, m_a = 0.6, f_s = 1 kHz, f = 50 Hz, B_{peak} = 1.3 T

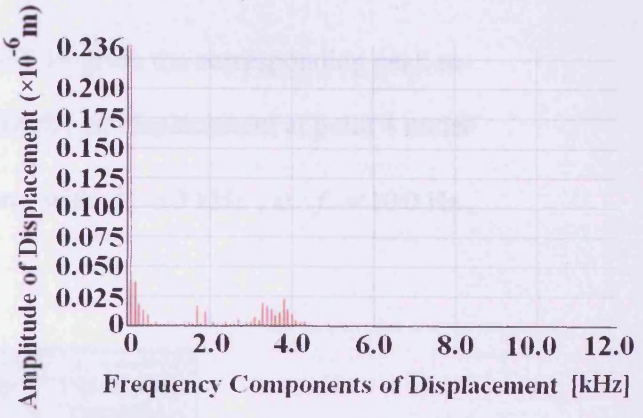

Fig. 5-72 Harmonic components of horizontal displacement at point 4 under PWM voltage excitation, m_a = 0.6, f_s = 1 kHz, f = 50 Hz, B_{peak} = 1.5 T

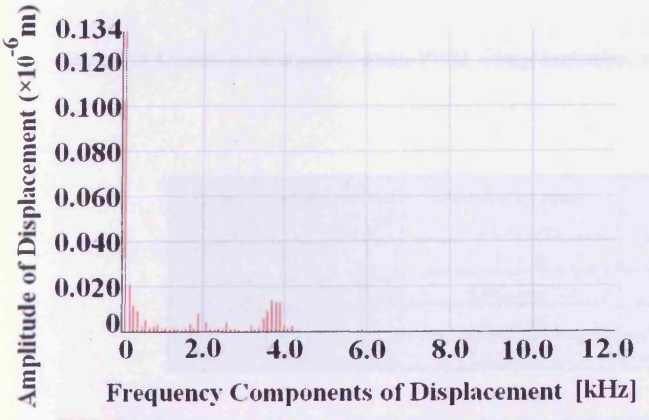

Fig. 5-73 Harmonic components of horizontal displacement at point 4 under PWM voltage excitation, m_a = 0.6, f_s = 2 kHz, f = 50 Hz, B_{peak} = 1.3 T

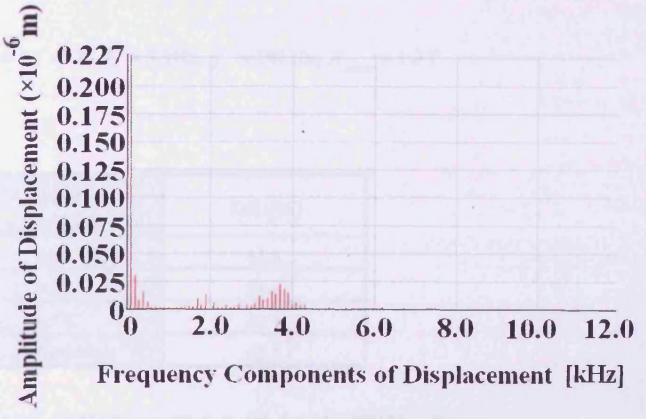

Fig. 5-74 Harmonic components of horizontal displacement at point 4 under PWM voltage excitation, m_a = 0.6, f_s = 2 kHz, f = 50 Hz, B_{peak} = 1.5 T

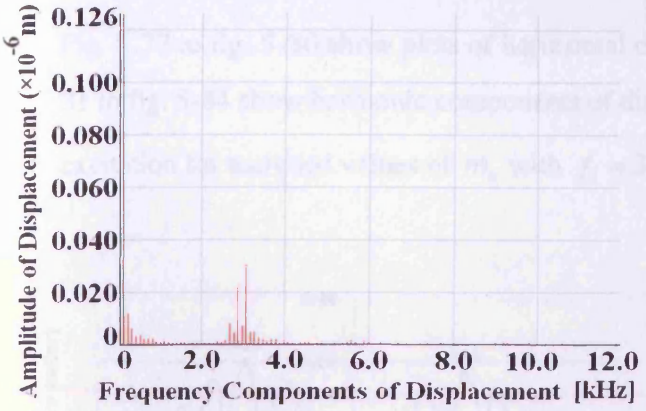

Fig. 5-75 Harmonic components of horizontal displacement at point 4 under PWM voltage excitation, m_a = 0.6, f_s = 3 kHz, f = 50 Hz, B_{peak} = 1.3 T

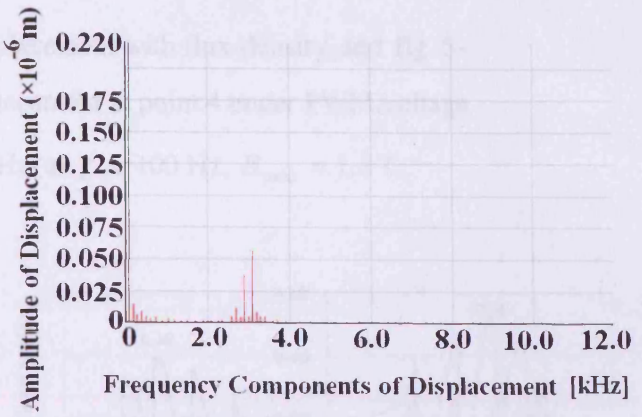

Fig. 5-76 Harmonic components of horizontal displacement at point 4 under PWM voltage excitation, m_a = 0.6, f_s = 3 kHz, f = 50 Hz, B_{peak} = 1.5 T

Table 5.15 shows the acoustic noise at point 5, table 5.16 gives the corresponding peak-to-peak horizontal displacement and the variation $THD[\%]$ of displacement at point 4 under PWM voltage excitation for assigned values of m_a with f_s = 3 kHz, at f = 100 Hz, B_{peak} = 1.3 T.

Magnetisation frequency [f]	Modulation index m_a [OV %]	Acoustic noise SPL [dBA]
PWM 100 Hz	0.7 [60 %]	54.3
	0.8 [70 %]	53.1
	1.0 [80 %]	52.2
	1.2 [90 %]	51.2

Table 5.15 Acoustic noise at point 5 under PWM voltage excitation, m_a = 0.7 - 1.2, f_s = 3 kHz, f = 100 Hz, B_{peak} = 1.3 T

Magnetisation frequency [f]	Modulation index m_a [OV %]	Displacement (micro meter)	THD[%]
PWM 100 Hz	0.7 [60 %]	0.59	81.8
	0.8 [70 %]	0.57	76.6
	1.0 [80 %]	0.55	68.7
	1.2 [90 %]	0.52	62.5

Table 5.16 Peak-to-peak horizontal displacement and variation THD [%] of displacement at point 4 under PWM voltage excitation, m_a = 0.7 - 1.2, f_s = 3 kHz, f = 100 Hz, B_{peak} = 1.3 T

Fig. 5-77 to fig. 5-80 show plots of horizontal displacement with flux density, and fig. 5-81 to fig. 5-84 show harmonic components of displacement at point 4 under PWM voltage excitation for assigned values of m_a with $f_s = 3$ kHz, at $f = 100$ Hz, $B_{peak} = 1.3$ T.

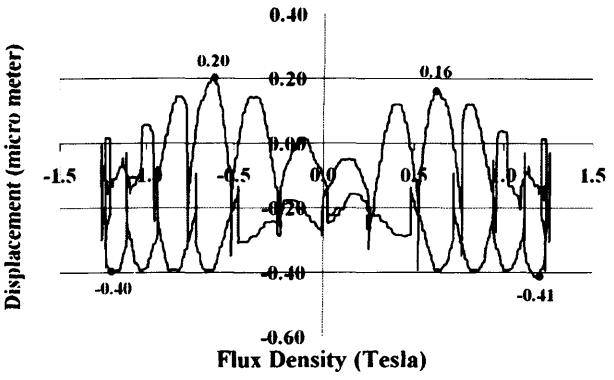

Fig. 5-77 Horizontal displacement at point 4 under PWM voltage excitation, $m_a = 0.7$, $f_s = 3$ kHz, $f = 100$ Hz, $B_{peak} = 1.3$ T

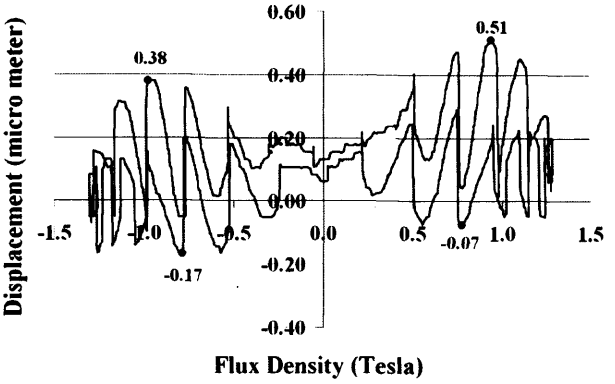

Fig. 5-78 Horizontal displacement at point 4 under PWM voltage excitation, $m_a = 0.8$, $f_s = 3$ kHz, $f = 100$ Hz, $B_{peak} = 1.3$ T

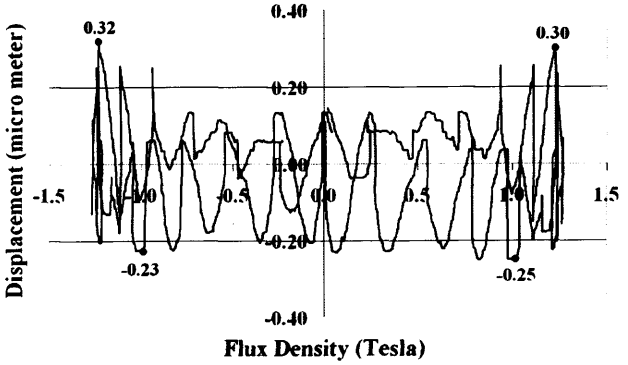

Fig. 5-79 Horizontal displacement at point 4 under PWM voltage excitation, $m_a = 1.0$, $f_s = 3$ kHz, $f = 100$ Hz, $B_{peak} = 1.3$ T

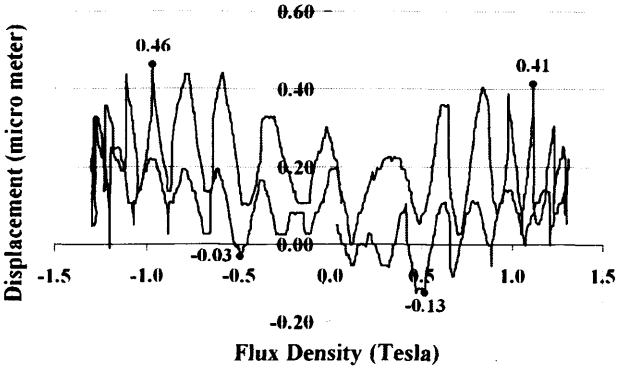

Fig. 5-80 Horizontal displacement at point 4 under PWM voltage excitation, $m_a = 1.2$, $f_s = 3$ kHz, $f = 100$ Hz, $B_{peak} = 1.3$ T

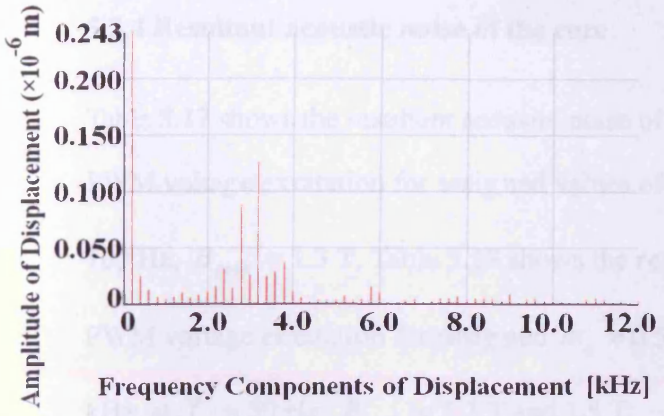

Fig. 5-81 Harmonic components of horizontal displacement at point 4 under PWM voltage excitation, m_a = 0.7, f_s = 3 kHz, f = 100 Hz, B_{peak} = 1.3T

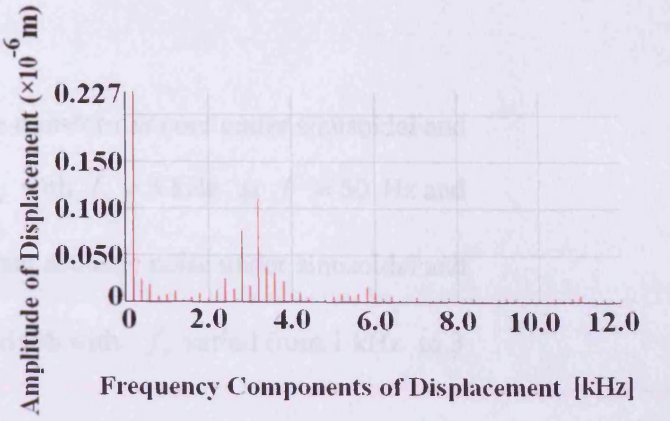

Fig. 5-82 Harmonic components of horizontal displacement at point 4 under PWM voltage excitation, m_a = 0.8, f_s = 3 kHz, f = 100 Hz, B_{peak} = 1.3T

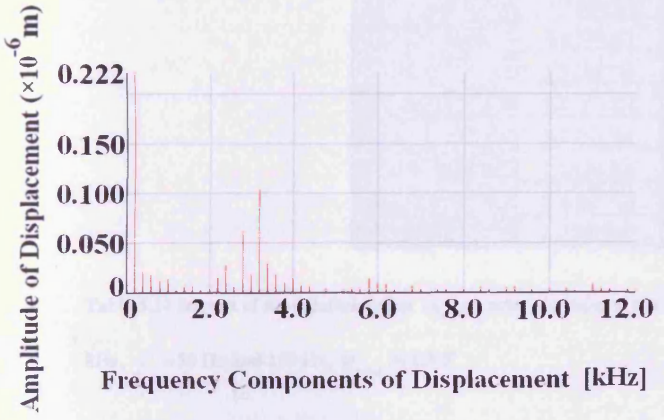

Fig. 5-83 Harmonic components of horizontal displacement at point 4 under PWM voltage excitation, m_a = 1.0, f_s = 3 kHz, f = 100 Hz, B_{peak} = 1.3T

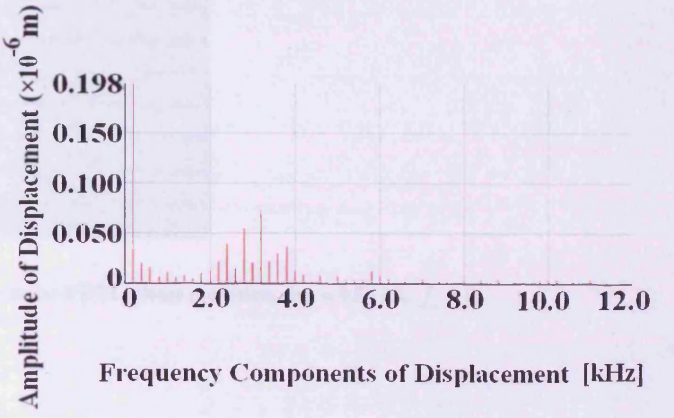

Fig. 5-84 Harmonic components of horizontal displacement at point 4 under PWM voltage excitation, m_a = 1.2, f_s = 3 kHz, f = 100 Hz, B_{peak} = 1.3T

5.3.4 Resultant acoustic noise of the core

Table 5.17 shows the resultant acoustic noise of the transformer core under sinusoidal and PWM voltage excitation for assigned values of m_a with $f_s = 3$ kHz, at $f = 50$ Hz and 100 Hz, $B_{peak} = 1.3$ T. Table 5.18 shows the resultant acoustic noise under sinusoidal and PWM voltage excitation for assigned $m_a = 0.5$ and 0.6 with f_s varied from 1 kHz to 3 kHz, at $f = 50$ Hz, $B_{peak} = 1.3$ T and 1.5 T.

Magnetisation frequency [f]	Modulation index m_a [OV %]	Average acoustic noise SPL [dBA]
sine 50 Hz	--	36.7
PWM 50 Hz	0.5 [40 %]	49.8
	0.6 [50 %]	48.6
	0.7 [60 %]	47.4
	0.8 [70 %]	46.6
	1.0 [80 %]	45.8
	1.2 [90 %]	45.0
PWM 100 Hz	0.7 [60 %]	53.2
	0.8 [70 %]	52.4
	1.0 [80 %]	51.3
	1.2 [90 %]	50.5

Table 5.17 Impact of modulation index m_a on acoustic noise of the core under PWM voltage excitation, $m_a = 0.5$ - 1.2, $f_s = 3$ kHz, $f = 50$ Hz and 100 Hz, $B_{peak} = 1.3$ T

Magnetisation frequency [f]	Modulation index m_a [OV %]	Switching frequency [f_s] [kHz]	Average acoustic noise SPL [dBA]	
			1.3 T	1.5 T
sine 50 Hz	--	--	36.7	39.5
PWM 50 Hz	0.5 [40 %]	1	51.7	53.6
		2	50.6	52.3
		3	49.8	51.5
	0.6 [50 %]	1	50.7	52.8
		2	49.4	51.6
		3	48.6	50.8

Table 5.18 Impact of switching frequency f_s on acoustic noise of the core under PWM voltage excitation, $m_a = 0.5$ and 0.6 with f_s varied from 1 kHz to 3 kHz, at $f = 50$ Hz, $B_{peak} = 1.3$ T and 1.5T

5.4 Analysis and discussion

5.4.1 Acoustic noise and vibration of the core under sinusoidal and PWM voltage excitation for assigned m_a

Fig. 5-5 shows that the acoustic noise and corresponding peak-to-peak vertical displacement at point 1 on the core surface under PWM voltage excitation were reduced with increasing value of m_a at f_s = 3 kHz, which was due to the lower harmonic content of the core flux density at the higher value of m_a (table 5.19) that caused a reduction of harmonic content in the displacement (table 5.1). It was also found that the acoustic noise and corresponding peak-to-peak vertical displacement, at a low m_a = 0.5, were around 4.0 *dBA* (10.0%) and 0.7 μm (28.3%) respectively greater than that at a high m_a = 1.2 (fig. 5-5), because over-modulation index reduces harmonic distortion in core flux density (table 5.19).

Fig. 5-12 and table 5.3 display the acoustic noise and corresponding peak-to-peak vertical displacement fall with increasing m_a when the magnetisation frequency was set to 100 Hz for the same reason (table 5.19). At 100 Hz, it was found that the acoustic noise and corresponding displacement, at m_a = 0.7 (f_s = 3 kHz), were around 3.0 *dBA* (5.9%) and 0.5 μm (12.8%) respectively larger than that at m_a = 1.2 (f_s = 3 kHz).

Similar trends to fig. 5-5 and fig. 5-12 of acoustic noise were found above the other measurement points (table 5.4, table 5.9, table 5.11 and table 5.15), and similar trends to fig. 5-5 and table 5.3 of displacement were also found at the other measurement points (table 5.5, table 5.10, table 5.12 and table 5.16) for the same reason (table 5.19).

Magnetisation frequency [f]	Modulation index m_a [OV %]	THD[%] of core flux density $B(t)$
sine 50 Hz	--	1.12
PWM 50 Hz	0.5 [40 %]	8.62
	0.6 [50 %]	7.83
	0.7 [60 %]	6.57
	0.8 [70 %]	5.54
	1.0 [80 %]	4.36
	1.2 [90 %]	3.78
PWM 100 Hz	0.7 [60 %]	7.46
	0.8 [70 %]	6.38
	1.0 [80 %]	5.15
	1.2 [90 %]	4.42

Table 5.19 Variation THD[%] of core flux density $B(t)$ under sinusoidal and PWM voltage excitation, m_a = 0.5 - 1.2, f_s = 3 kHz, f = 50 Hz and 100 Hz, B_{peak} = 1.3 T

Points 2 and 3 were the same distance from point 1. The beha vior of acoustic noise and corresponding vertical displacement at point 2 and point 3 were similar (table 5.4 to table 5.10) and therefore data measured from point 2 was used for analysing.

Fig. 5-13 to fig . 5-18 sh ow plots of vertical displacement against flux density at point 2 under PWM voltage excitation for assig ned m_a with f_s = 3 kHz , at f = 50 Hz. It can be seen that the displacement decreases with increasing m_a , and also it can be observed in fig. 5-19 to fig . 5-24 th at at a low m_a = 0.5 (f_s = 3 kHz), the amplitude of harmonic components and the harmonic contents of the displacement were higher than that at a high value of m_a = 1.2 (f_s = 3 k Hz), which was du e to the hig her amplitude of harmonic components and the hig her harmonic contents in the core flux density waveform at m_a = 0.5 (table 5.19 and fi g. 5-85 to fig . 5-90). Fig. 5-85 to fig . 5-90 displa y the frequency domain of the cor e flux density $B(t)$ under PWM voltage excitation for assi gned values of m_a with f_s = 3 kHz, at f = 50 Hz, B_{peak} = 1.3 T.

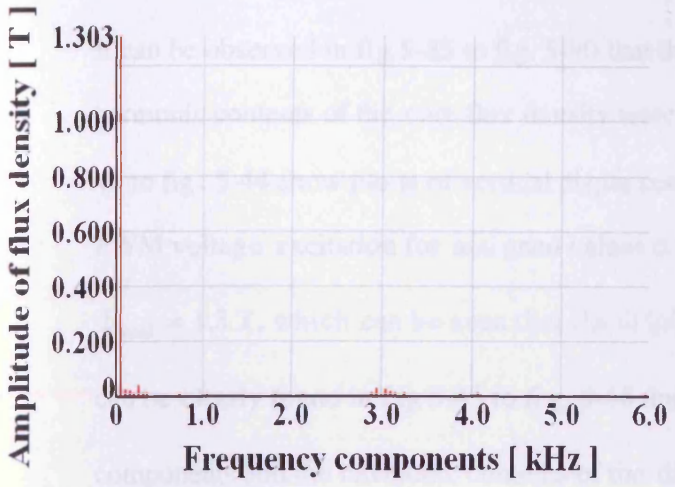

Fig. 5-85 Harmonic components of the core flux density under PWM voltage excitation, f = 50 Hz, m_a = 0.5, f_s = 3 kHz, B_{peak} = 1.3 T

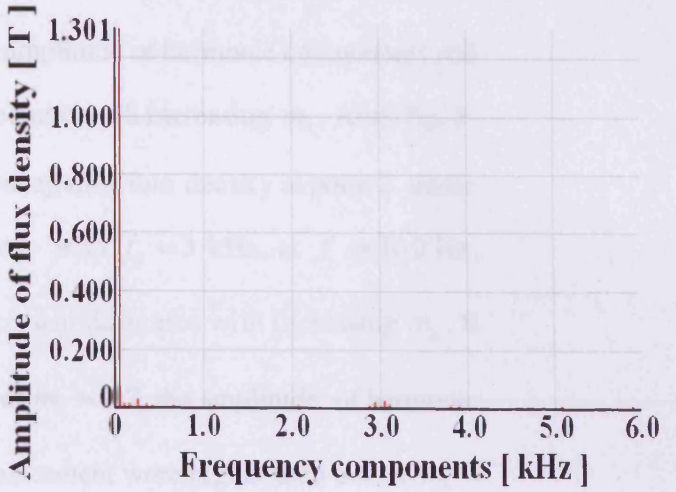

Fig. 5-86 Harmonic components of the core flux density under PWM voltage excitation, f = 50 Hz, m_a = 0.6, f_s = 3 kHz, B_{peak} = 1.3 T

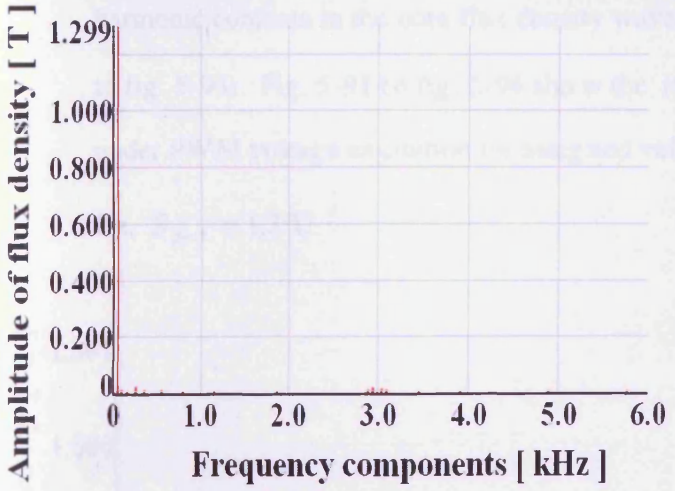

Fig. 5-87 Harmonic components of the core flux density under PWM voltage excitation, f = 50 Hz, m_a = 0.7, f_s = 3 kHz, B_{peak} = 1.3 T

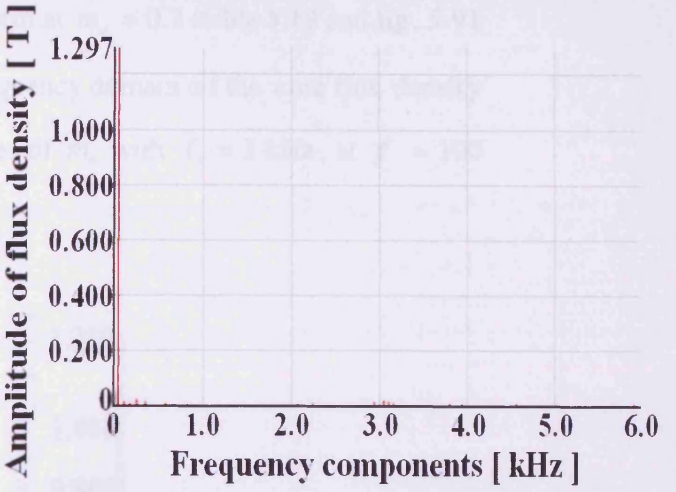

Fig. 5-88 Harmonic components of the core flux density under PWM voltage excitation, f = 50 Hz, m_a = 0.8, f_s = 3 kHz, B_{peak} = 1.3 T

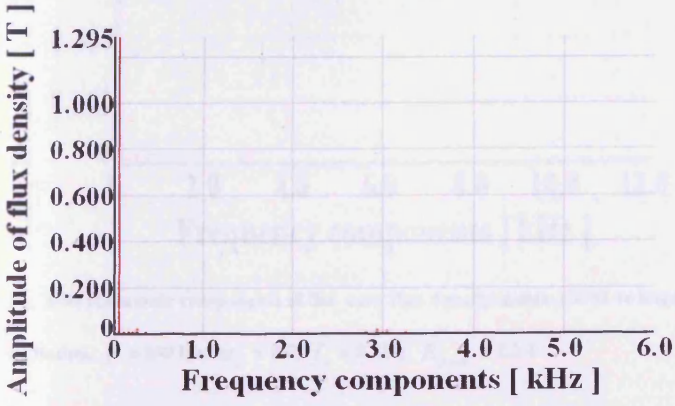

Fig. 5-89 Harmonic components of the core flux density under PWM voltage excitation, f = 50 Hz, m_a = 1.0, f_s = 3 kHz, B_{peak} = 1.3 T

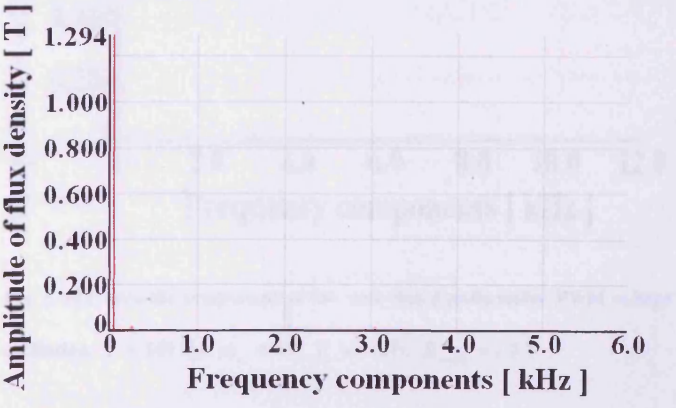

Fig. 5-90 Harmonic components of the core flux density under PWM voltage excitation, f = 50 Hz, m_a = 1.2, f_s = 3 kHz, B_{peak} = 1.3 T

It can be observed in fig.5-85 to fig. 5-90 that the amplitude of harmonic components and harmonic contents of the core flux density were reduced with increasing m_a. Also, fig. 5-41 to fig. 5-44 show plots of vertical displacement against flux density at point 2 under PWM voltage excitation for assigned values of m_a with $f_s = 3$ kHz, at $f = 100$ Hz, $B_{peak} = 1.3$ T, which can be seen that the displacement decreases with increasing m_a. It can be clearly found in fig 5-45 to fig. 5-48 that at $m_a = 0.7$, the amplitude of harmonic components and the harmonic contents of the displacement were higher than that at $m_a = 1.2$, which was also due to higher amplitude of harmonic components and higher harmonic contents in the core flux density waveform at $m_a = 0.7$ (table 5.19 and fig. 5-91 to fig. 5-94). Fig. 5-91 to fig. 5-94 show the frequency domain of the core flux density under PWM voltage excitation for assigned values of m_a with $f_s = 3$ kHz, at $f = 100$ Hz, $B_{peak} = 1.3$ T.

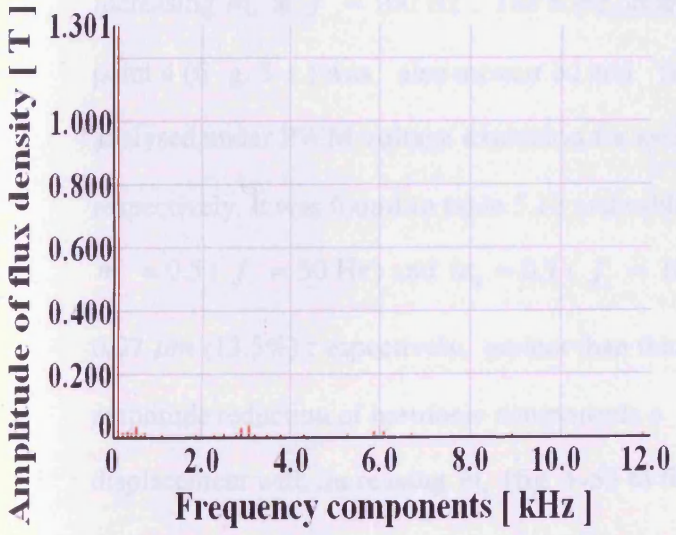

Fig. 5-91 Harmonic components of the core flux density under PWM voltage excitation, $f = 100$ Hz, $m_a = 0.7$, $f_s = 3$ kHz, $B_{peak} = 1.3$ T

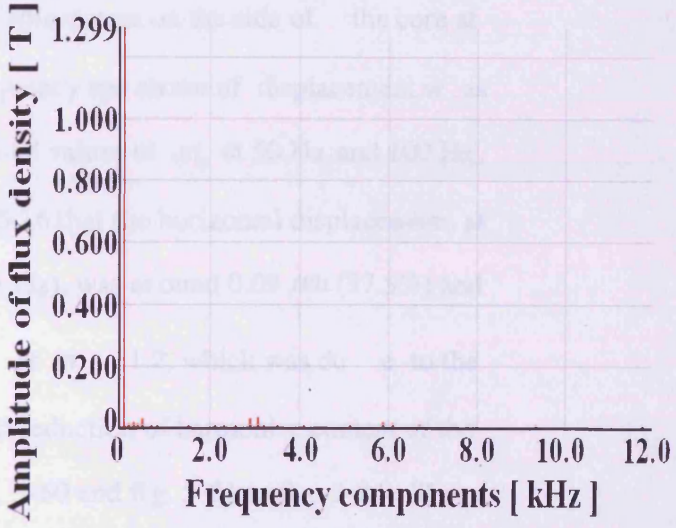

Fig. 5-92 Harmonic components of the core flux density under PWM voltage excitation, $f = 100$ Hz, $m_a = 0.8$, $f_s = 3$ kHz, $B_{peak} = 1.3$ T

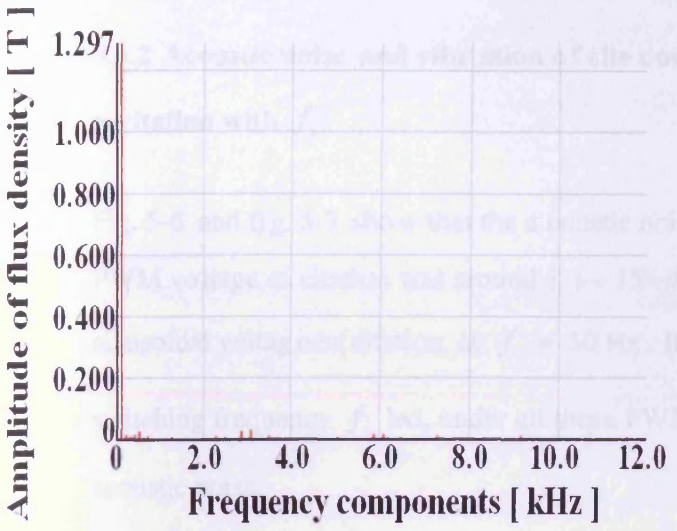

Fig. 5-93 Harmonic components of the core flux density under PWM voltage excitation, f = 100 Hz, m_a = 1.0, f_s = 3 kHz, B_{peak} = 1.3 T

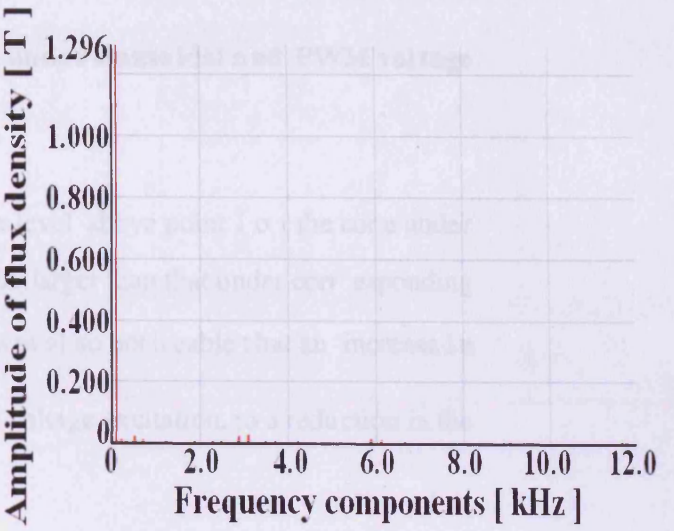

Fig. 5-94 Harmonic components of the core flux density under PWM voltage excitation, f = 100 Hz, m_a = 1.2, f_s = 3 kHz, B_{peak} = 1.3 T

It was also observed in fig. 5-91 to fig. 5-94 that, the similar trend of the amplitude of harmonic components and harmonic contents of the core flux density were decreased with increasing m_a at f = 100 Hz . The horizontal displacement on the side of the core at point 4 (fig. 5-1) was also measured and frequency spectrum of displacement was analysed under PWM voltage excitation for assigned values of m_a at 50 Hz and 100 Hz, respectively. It was found in table 5.12 and table 5.16 that the horizontal displacement, at m_a = 0.5 (f = 50 Hz) and m_a = 0.7 (f = 100 Hz), was around 0.09 μm (37.5%) and 0.07 μm (13.5%) respectively, greater than that at m_a = 1.2, which was due to the amplitude reduction of harmonic components and reduction of harmonic content of the displacement with increasing m_a (fig. 5-55 to fig. 5-60 and fig. 5-81 to fig. 5-84). These results present the benefit on the performance of the transformer core at high value of m_a.

5.4.2 Acoustic noise and vibration of the core under sinusoidal and PWM voltage excitation with f_s

Fig. 5-6 and fig. 5-7 show that the acoustic noise level above point 1 of the core under PWM voltage excitation was around 11 – 15 *dBA* larger than that under corresponding sinusoidal voltage excitation, at f = 50 Hz. It was also noticeable that an increase in switching frequency f_s led, under all these PWM voltage excitation, to a reduction in the acoustic noise.

It was demonstrated in fig. 5-8 to fig. 5-11 that the corresponding peak-to-peak vertical displacement at point 1 under PWM voltage excitation were higher than that under corresponding sinusoidal condition and also the displacement was reduced with increasing f_s from 1 kHz to 3 kHz. This was due to the higher harmonic contents of the core flux density under PWM voltage excitation than that under corresponding sinusoidal condition, and the lower harmonic content of the core flux density with an increase in f_s (table 5.20), which caused a harmonic content reduction of the displacement (table 5.2).

At m_a = 0.5, B_{peak} = 1.5 T, it was found that the acoustic noise and the corresponding peak-to-peak vertical displacement, at a low f_s = 1 kHz, were around 2.0 *dBA* (3.8%) and 0.6 μm (18.2%) respectively, greater than that at a high f_s = 3 kHz (fig. 5-7 and fig. 5-8 to fig. 5-11).

Magnetisation frequency [f]	Modulation index m_a [OV %]	Switching frequency [f_s] [kHz]	THD[%] of core flux density $B(t)$	
			1.3 T	1.5 T
sine 50 Hz	--	--	1.12	1.68
PWM 50 Hz	0.5 [40 %]	1	10.45	11.74
		2	9.53	10.58
		3	8.62	9.49
	0.6 [50 %]	1	9.79	10.72
		2	8.71	9.64
		3	7.83	8.56

Table 5.20 Variation THD[%] of core flux density $B(t)$ under sinusoidal and PWM voltage excitation, m_a = 0.5 and 0.6 with f_s varied from 1 kHz to 3 kHz, at f = 50 Hz, B_{peak} = 1.3 T and 1.5T

Fig. 5-25 to fig . 5-32 sh ow plots of vertical displacement a gainst flux de nsity at point 2 under sinusoidal and PWM voltage excitation for assigned m_a = 0.6 with f_s varied in the range of 1 kHz to 3 kHz , at f = 50 Hz, B_{peak} = 1.3 T and 1.5 T. It can b e seen th at the displacement r esults ob tained under PW M vol tage ex citation we re l arger than that corresponding measur ement results made unde r sinusoidal condition; and also under al l these PWM voltage excitation, the displacement results were decreased with an increasing in f_s.

It can be obse rved in fig 5-33 to fig . 5-40 that under PW M voltag e ex citation, the amplitude of harmonic c omponents and the ha rmonic contents of th e displacement we re higher than that unde r corresponding sinusoidal conditions. It w as also n oticed that at a low f_s = 1 kHz, the amplitude of harmonic com ponents and the harmonic co ntents of the displacement w ere hi gher t han t hat at a hi gh f_s = 3 kHz . This was due t o the hi gher amplitude of h armonic components and the hi gher h armonic contents i n the core flux density w aveform under PW M voltag e excitation than that under correspondin g sinusoidal conditions, a nd was also due to the reduction of amplitude of harmonic components and reducti on of harm onic contents in the core flux densit y waveform with an increase in f_s (table 5.20 and fig. 5-95 to fig. 5-102).

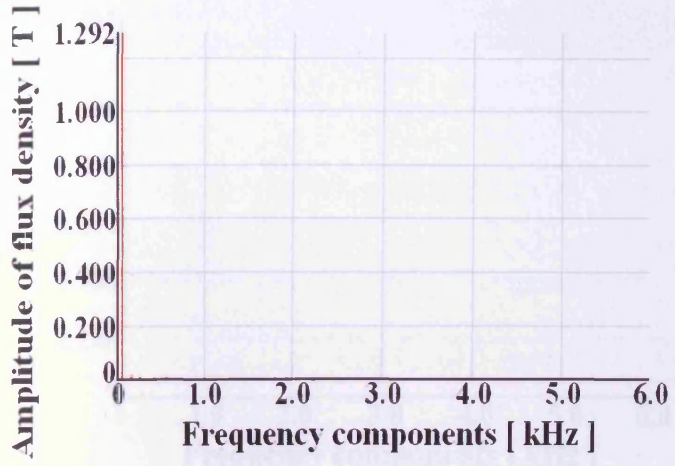

Fig. 5-95 Harmonic components of the core flux density under sinusoidal voltage excitation, f = 50 Hz, B_{peak} = 1.3 T

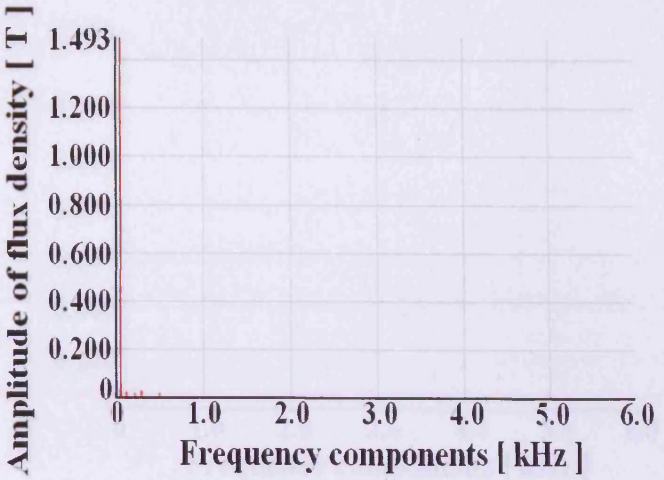

Fig. 5-96 Harmonic components of the core flux density under sinusoidal voltage excitation, f = 50 Hz, B_{peak} = 1.5 T

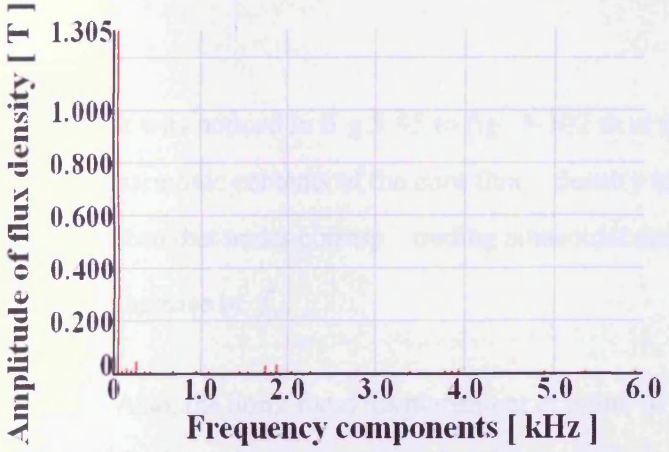

Fig. 5-97 Harmonic components of the core flux density under PWM voltage excitation, f = 50 Hz, m_a = 0.6, f_s = 1 kHz, B_{peak} = 1.3 T

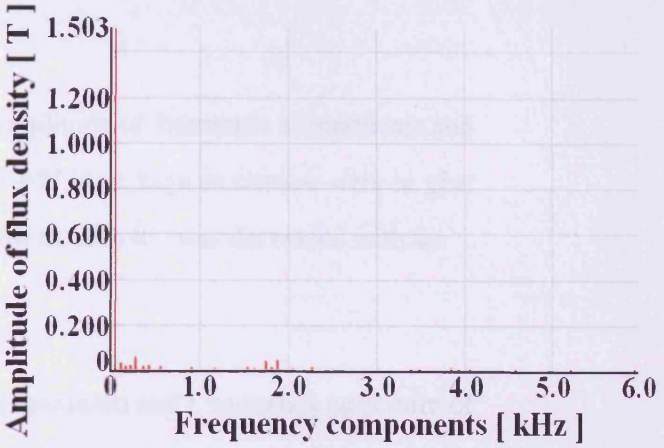

Fig. 5-98 Harmonic components of the core flux density under PWM voltage excitation, f = 50 Hz, m_a = 0.6, f_s = 1 kHz, B_{peak} = 1.5 T

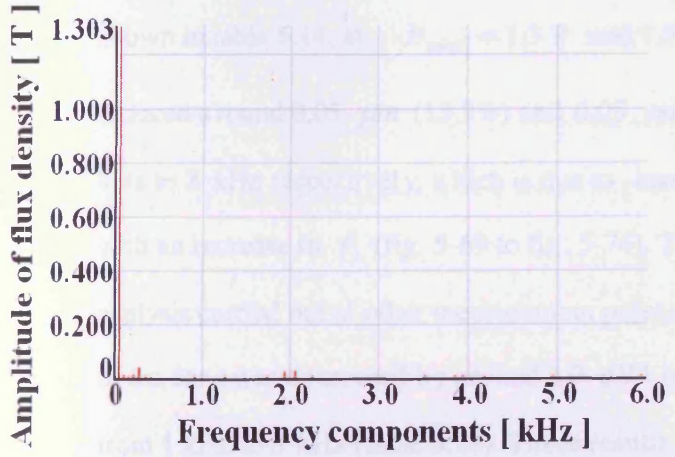

Fig. 5-99 Harmonic components of the core flux density under PWM voltage excitation, f = 50 Hz, m_a = 0.6, f_s = 2 kHz, B_{peak} = 1.3 T

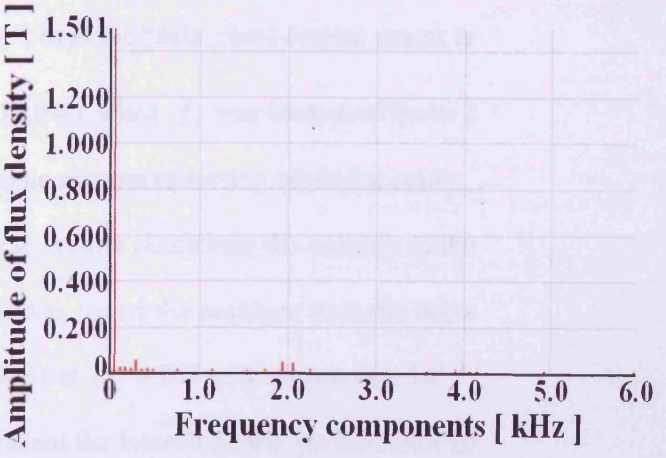

Fig. 5-100 Harmonic components of the core flux density under PWM voltage excitation, f = 50 Hz, m_a = 0.6, f_s = 2 kHz, B_{peak} = 1.5 T

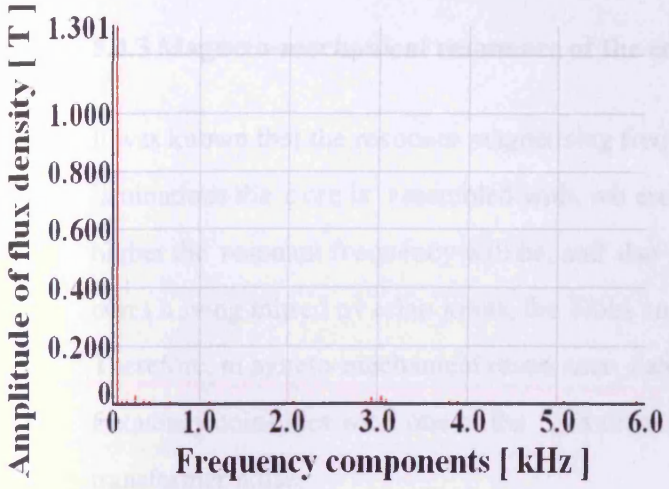

Fig. 5-101 Harmonic components of the core flux density under PWM voltage excitation, f = 50 Hz, m_a = 0.6, f_s = 3 kHz, B_{peak} = 1.3 T

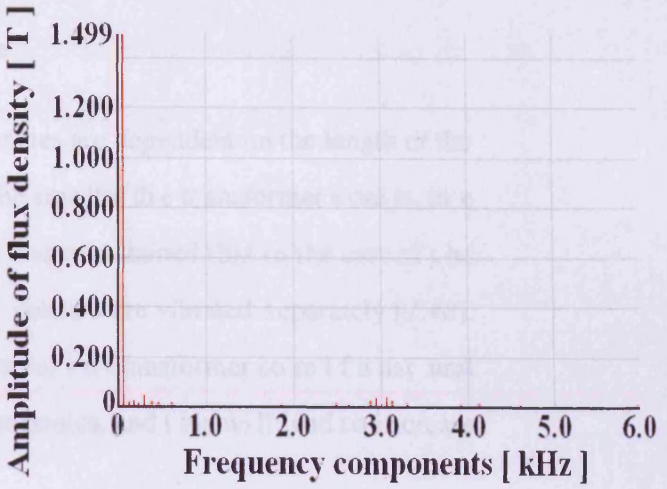

Fig. 5-102 Harmonic components of the core flux density under PWM voltage excitation, f = 50 Hz, m_a = 0.6, f_s = 3 kHz, B_{peak} = 1.5 T

It was noticed in fig.5-95 to fig. 5-102 that the amplitude of harmonic components and harmonic contents of the core flux density under PWM voltage excitation were higher than that under corresponding sinusoidal conditions, also it was decreased with an increase in f_s.

Also, the horizontal displacement at point 4 was measured and frequency spectrum of displacement was analysed under sinusoidal and PWM voltage excitation for assigned value of m_a = 0.6 with f_s varied in the range of 1 kHz to 3 kHz, at f = 50 Hz. It is shown in table 5.14, at B_{peak} = 1.3 T and 1.5 T, that the horizontal displacement is reduced around 0.05 μm (13.9%) and 0.05 μm (8.5%) when f_s was increased from 1 kHz to 3 kHz respectively, which is due to harmonic content reduction of displacement with an increase in f_s (fig. 5-69 to fig. 5-76). These results confirmed the validity of the analysis carried out at other measurement points. It was found the resultant acoustic noise of the core was decreased by around 2.0 dBA (4.0%) at m_a = 0.6 with an increase in f_s from 1 kHz to 3 kHz (table 5.18). These results present the benefit on the performance of the transformer core at a high f_s.

5.4.3 Magneto-mechanical resonance of the core

It was known that the resonant magnetising frequencies are dependent on the length of the laminations the core is assembled with, where the smaller the transformer core is, the higher the resonant frequency will be, and also it was maintained that in the case of the cores having mitred overlap joints, the limbs and yokes were vibrated separately [*1.48*]. Therefore, magneto-mechanical resonance can occur in transformer core if a natural frequency coincides with one of the vibration harmonics, and this will lead to increase transformer noise.

The dimensions of limb and yoke laminations assembled the transformer core are shown in fig. 5-1. Thereafter, the resonant frequency f_n in the limb and yoke laminations of the core could be inferred by equation (2.2), where the assumed modulus of elasticity E = 110 GPa (table 2.2) and the calculated results are shown in table 5.21.

Lamination	Length inner / outer l (m)	Calculated inner / outer f_n [kHz]
Yoke	0.38 / 0.6	2.5 / 1.6
Limb	0.33 / 0.55	2.9 / 1.7

Table 5.21 Calculated resonance frequencies f_n in the limb and yoke laminations of the core

It is noticed in table 5.21 that the calculated resonant frequency f_n at inner part of limb lamination, which was about 2.9 kHz, was similar to the measured value, which was around 3 kHz. This was due to the switching frequency at f_s = 3 kHz, where its higher harmonics in the core flux density occurred close to the resulting limb resonant frequency.

Comparing the frequency spectra of the core flux density with displacement, it was clearly observed in fig. 5-19 to fig. 5-24 and fig. 5-55 to fig. 5-60 that the frequency

spectra of the displac ement at measuremen t p oints under PW M vo ltage excitation for assigned v alues of m_a with $f_s = 3$ kHz , the harmonic components at around 3 kHz had high amplitude of vibrat ion that was due to low values of cor e flux densit y at a round 3 kHz, which are displa yed in fig . 5-85 to fig. 5-90, could cause high displacement indicating magneto-mechanical resonance.

The similar resonant phenomena were also found of the core subjected to i dentical PWM voltage excitation for a ssigned valu es of m_a with $f_s = 3$ kHz when m agnetisation frequency f was set to 100 Hz. It was also noticed in fig. 5-45 to fig. 5-48 and fig. 5-81 to fig . 5-84 that the hi gh f requency co mponents cluster at around 3 k Hz had hig her amplitude of displacement, which was also due to the low values of cor e flux densit y cluster at around 3 kHz and that w as cl early sho wn in fi g. 5 -91 to fi g. 5 -94, also could cause hi gh vibration be cause of reson ance. Moreover, in the frequency spectra figures of vibration, it was observed that the ampli tude of higher frequency components, which was clustered around multiple inte gers of f_n (2.2) at approximate 6 kHz , was i ncreased. This was due to even smaller values in core flux density cluster at around 6 k Hz, which were displayed in fig. 5-91 to fig . 5-94, al so could cau se high vibration due to 2^{nd} harmonic of resonance.

It w as mentioned in section 5.4.2 that the reduction of the acoustic noise and corresponding vibration with an increase in f_s from 1 kHz to 3 kHz, was due to reduction of amplitude of harmonic components and reduction of harmonic contents in the core flux density with increasing f_s (table 5.20 and fig. 5-97 to fig. 5-102). Nevertheless, at $f_s = 3$ kHz, it was clearly noticed in fig. 5-39, fig. 5-40, fig. 5-75 and fig. 5-76 that the amplitude of high frequency component at around 3 kHz w as greater than that at $f_s = 1$ kHz and 2 kHz, which was shown in fig . 5-35 to fi g. 5-38 and fig . 5 -71 to fig . 5-74, indicating magneto-mechanical resonance. This was du e to the low values o f flux density presented

at around 3 kHz (fig. 5-101 and fig. 5-102) when $f_s = 3$ kHz and could cause high vibration because of resonance. However, at f_s = 1 kHz and 2 kHz, there was no high frequency components of core flux density presented at the resonant frequency (fig. 5-97 to fig. 5-100).

The measurement results represent the benefit on the performance of the core under PWM voltage excitation for assigned values of m_a with a high f_s. Nevertheless, the resultant acoustic noise of the core under PWM voltage excitation was reduced around 2.0 *dBA* with an increase in f_s from 1 kHz to 3 kHz because of magneto-mechanical resonance at $f_s = 3$ kHz, which in core laminations was a possible cause of increased vibration and acoustic noise.

By equation (2.2), the resonant phenomenon would be similar in other electrical steel laminations, which were used to assemble the transformer core, since thickness, texture, grain size have no effect whereas density, modulus of elasticity and laminations length variable with composition would have some influence. Although this vibration experiment was conducted on a model three- phase three-limb transformer core (fig. 5-1), similar effects would be expected in other transformer cores but with different resonant frequencies. Large acoustic noise and vibration could be generated if the switching frequency f_s of the PWM inverter coincides with a resonant frequency of the transformer core.

Also, extrapolation of the results to other larger cores suggest that the resonant phenomenon could possibly occur in cores with different length of laminations (fig. 2-7) leading to variability of acoustic noise output and vibration according to how close the magnetising frequency or predominant harmonic components are to the resonant frequency.

5.4.4 Out-of-plane forces of the core

It is known that a global attractive interlaminar force P_Z, which is due to the global normal flux component B_Z of induction that somewhat higher values arise locally at joint regions of the core, is given by equation (5.3), which yields additional sources of vibration that propagate to the entire core [*1.44*] [*2.44*].

$$P_Z = \frac{0.5B_Z^2}{\mu_0} \qquad [\text{Pa}] \qquad [2.44] \qquad (5.3)$$

where μ_0 is permeability of free space (4×10^{-7} H/m).

P_Z yields a 100 Hz (f = 50 Hz) oscillation of the interlaminar gap length g_z in the joint region (fig. 5-103), where g_z (5.4) can be estimated by means of the effective elasticity modulus E_Z [*1.44*][*2.44*].

$$g_z = \frac{P_Z}{E_Z} \qquad [\mu m/m] \qquad [2.44] \qquad (5.4)$$

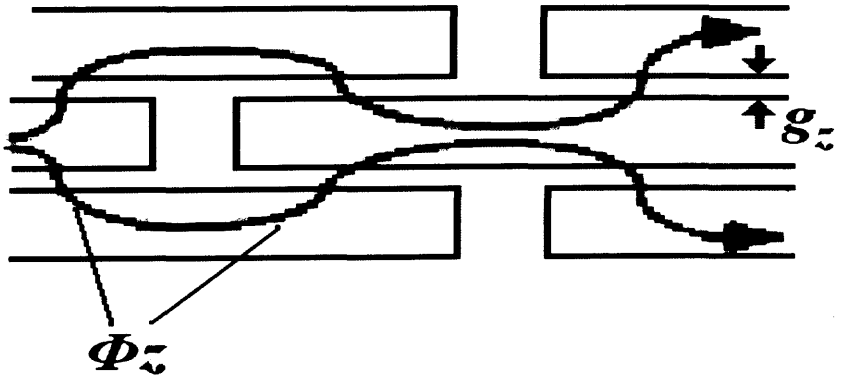

Fig. 5-103 Normal flux distribution in the overlap regions [*2.44*]

then, the normal vibration $_z$ could be estimated by equation (5.5), which would increase linearly with increasing a stack of lamination number k [*1.44*] [*2.44*].

$$_z = k \; g_z \qquad [\mu m] \qquad [2.44] \qquad (5.5)$$

therefore, by equations (5.4) and (5.5), the value of normal vibration $_z$ is proportional to the attractive interlaminar force P_Z.

Also, the correspondin g peak attractive interlami nar force $\hat{P}_Z$ at different re gions of the core und er sinusoidal a nd PW M voltag e excitation for a ssigned va lues of m_a with f_s varied in the ran ge of 1 kHz to 3 kH z can be obtained by (5.3), where the peak values of normal flux density $\hat{B}_z$ at different regions of the core are shown in table 4.4.

Table 5.22 shows th e corresponding peak force $\hat{P}_Z$ and the variation average THD [%] of force at different regions of the co re under sinusoidal and PW M voltage ex citation for assigned m_a = 0.5 with f_s varied from 1 kHz to 3 kHz, at f = 50 Hz, B_{peak} = 1.5 T.

Magnetisation frequency [f]	Modulation index m_a [OV %]	Switching frequency [f_s] [kHz]	Limbs and Yokes		T-joints		Corners	
			$\hat{P}_Z$ [Pa]	THD [%]	$\hat{P}_Z$ [Pa]	THD [%]	$\hat{P}_Z$ [Pa]	THD [%]
sine 50 Hz	--	--	0.4	10.2	5.2	17.3	20.1	21.9
PWM 50 Hz	0.5 [40 %]	1	1.3	15.4	10.8	27.8	35.2	35.2
		2	1.0	14.8	9.6	25.2	33.0	31.6
		3	1.0	13.9	8.8	22.8	30.8	29.5

Table 5. 22 V ariation of $\hat{P}_Z$ and THD [%] of force a t d ifferent r egions of t he core u nder s inusoidal and PWM vo ltage excitation, m_a = 0.5 with f_s varied from 1 kHz to 3 kHz, at f = 50 Hz, B_{peak} = 1.5 T

Table 5.22 shows that a t limb and yoke r egions, even unde r the most distorted PW M voltage ex citation (m_a = 0.5, f_s = 1 kHz), the value of force $\hat{P}_Z$ is only around 1.3 Pa, which was small and can be n eglected. The v alues of v ertical vibration a t points 2 and 3

(table 5.5, table 5.7 and table 5.10) are greater than that at point 1 (fig. 5-5, fig. 5-8 to fig. 5-11 and table 5.3), which was due to the normal component B_z arising to considerably higher local flux values in joint regions (table 4.4) that could generate higher attractive interlaminar force P_Z (table 5.22). This could be assumed to explain that the acoustic noise above point 2 and point 3 (table 5.4, table 5.6 and table 5.9) was around 1 – 2 *dBA* larger than that above point 1 (fig. 5-5 to fig. 5-7 and fig. 5-12).

In table 5.22, it is shown that at joint corner regions, the attractive peak force $\hat{P}_Z$ and the corresponding average $THD[\%]$ of force are reduced with an increase in f_s. Therefore, we could assume that it could to be linked with amplitude reduction of fundamental harmonic component and less distortion of vibration at point 2 and point 3 with an increase in f_s (table 5.7, table 5.8 and fig. 5-33 to fig. 5-40), which could be a possible reason that the acoustic noise was reduced around 2.0 *dBA* with increasing f_s from 1 kHz to 3 kHz. Although, the magneto-mechanical resonance occurred at f_s = 3 kHz, due to the resulting inner part of limb resonance, the trend of acoustic noise was reduced with an increase in f_s.

References to Chapter 5:

[5.1] B rüel & Kjae r T ype 4955 Us er's Manual, *Brüel & Kjaer North America Incorporated.*

[5.2] Brüel & Kjaer 2692C User's Manual, *Brüel & Kjaer North America Incorporated.*

Chapter 6 Conclusions and Future Work

6.1 Conclusions

Results showed that the peak-to-peak magnetostriction of grain-oriented, 3% silicon electrical steel sample in the form of Epstein strips cutting along rolling direction, under PWM voltage excitation were greater than that under corresponding sinusoidal voltage excitation, which was due to an integer multiple of the switching frequency f_s being close to the mechanical resonant frequency of the sample. Even a small value of flux density could cause a high magnetostriction if resonance occurred. Although the experiment was conducted on a single strip, similar effects would be expected in the transformer cores but with different resonant frequencies. High acoustic noise and vibration could be generated if the f_s of the PWM inverter coincides with a resonant frequency of the transformer core.

Results showed that core loss subjected to PWM voltage excitation decreased with increasing modulation index m_a as found previously. However, at a given modulation index m_a, the loss dropped with an increasing in switching frequency f_s. This improvement was due to the significant reduction in eddy-current component losses. The benefit at high m_a with high f_s impacted on loss was not apparent, which was due to improved harmonic spectra in flux density waveforms. Also, in high power applications consisting of current-source inverters, high switching frequencies were not applicable to thyristors, the primary choice when dealing with high voltages and currents. An increase in PWM switching frequency in the low range led to a substantial improvement of the performance of steel in transformer cores, owing to a significant reduction of the eddy-current component loss.

Results from the acoustic noise output of transformer core operating under PWM voltage excitation were around 8-15 *dBA* greater than that under corresponding sinusoidal voltage excitation due to higher results of core vibration under PWM voltage excitation. Also, the results represented the benefit on the noise performance of the core under PWM voltage excitation for assigned values of m_a with a high value of f_s, where the reduction of acoustic noise was around 2 *dBA* with an increase in f_s from 1 kHz to 3 kHz. Nevertheless, the magneto-mechanical resonance phenomenon at f_s = 3 kHz was observed, which was close to

the resonance frequency in core laminations that was a possible cause of deterioration of a transformer core performance by increasing vibration and acoustic noise.

Extrapolation of the results inferred that resonance phenomenon could possibly occur in large cores, with different length laminations leading to variability of acoustic noise output according to how close the magnetising frequency or predominant harmonics were to the resonant frequency. Also, the results implied that the resonant phenomenon was indeed the cause of excessive noise and vibration found in transformer cores operating under distorted PWM voltage excitation. The high vibration and acoustic noise in the resonant state could lead to possible core failure. Therefore, more care should be taken in such case to control or avoid the resonant phenomenon.

6.2 Suggestion for future work

The present investigation has given rise to a number of specific experimental areas worthy of further investigations. The measurement of magnetostriction in the form of Epstein strips under PWM voltage excitation with stress will be carried out. After analysing measurement results, then it could to investigate the PWM parameters, i.e. modulation index m_a and switching frequency f_s affect the magnetostriction under stress condition.

The present acoustic noise and vibration investigation could give rise to extend approximately approach in predicting magneto-mechanical resonance for large cores made from materials used in this investigation. The single-point laser Doppler vibrometer has an advantage in ease using to measure vibration, but laser vibrometer could only measure vibration on core surface. Therefore, it will be valuable to use strain sensors to measure the in-plane displacement within the laminations and normal displacement between the laminations of the core under PWM voltage excitation. Displacement measured from strain sensors will eliminate most of the external vibrations that a laser vibrometer would measure in addition to displacement.

In present investigation, the results showed the beneficial impact on the loss performance of the transformer core under PWM voltage excitation at a high value of f_s. However, in the future, the impact of higher switching frequencies on power semiconductor losses of PWM inverter must also be studied thoroughly, due to their effect on the overall efficiency.

Due to the limitation of the laboratories, the total power losses of the core were measured under PWM voltage excitation at no-load condition. It is also important to study the total power loss of transformer core operating under PWM voltage excitation at loaded condition, which will be the future work.

So far, the performance of acoustic noise and vibration has been investigated on a bare model transformer core operating under PWM voltage excitation. Therefore, if practically possible, future research will be continued to determine the influence of windings, oil and tanks etc.

Appendix A: Repeatability of the magnetostriction of the sample in the form of Epstein strips using single-point laser Doppler vibrometer under sinusoidal and PWM voltage excitation

The peak-to-peak magnetostriction of grain-oriented, 0.27 mm thickness, 3% silicon electrical steel sample in the form of Epstein strips, annealed after cutting along rolling direction, has been measured using single-point laser Doppler vibrometer. For the test sample, it was magnetised in a single sheet tester under sinusoidal and PWM voltage excitation for assigned modulation index m_a with different switching frequency f_s, at f = 50 Hz and 100 Hz, B_{peak} = 1.3 T and 1.5 T. The measurements have been repeated five times at each voltage excitation condition. All the magnetostriction have been measured and then averaged over all five measurements.

Appropriated graphs are shown in the following figures. Colourful lines represent the peak-to-peak magnetostriction characteristics averaged from five measurements under each voltage excitation condition. Black vertical lines represent the error bars at each measured point.

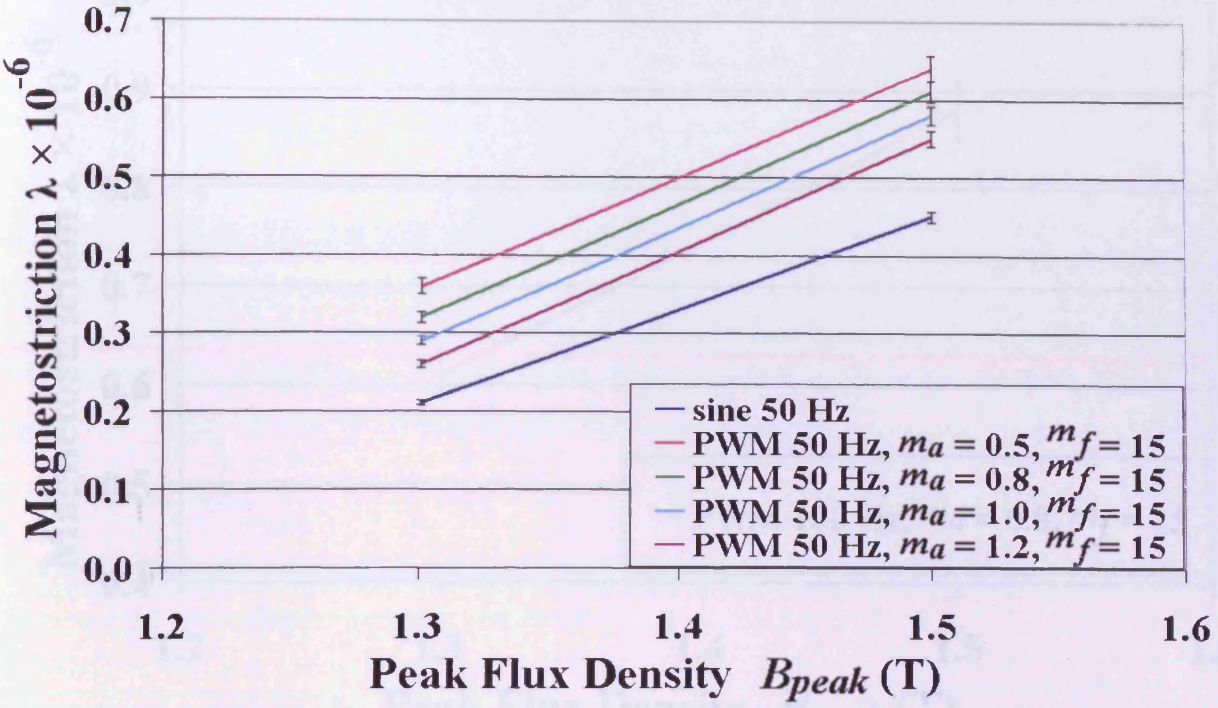

Fig. A-1 Peak-to-peak magnetostriction versus magnetic peak flux density under sinusoidal and PWM voltage excitation, at f = 50 Hz

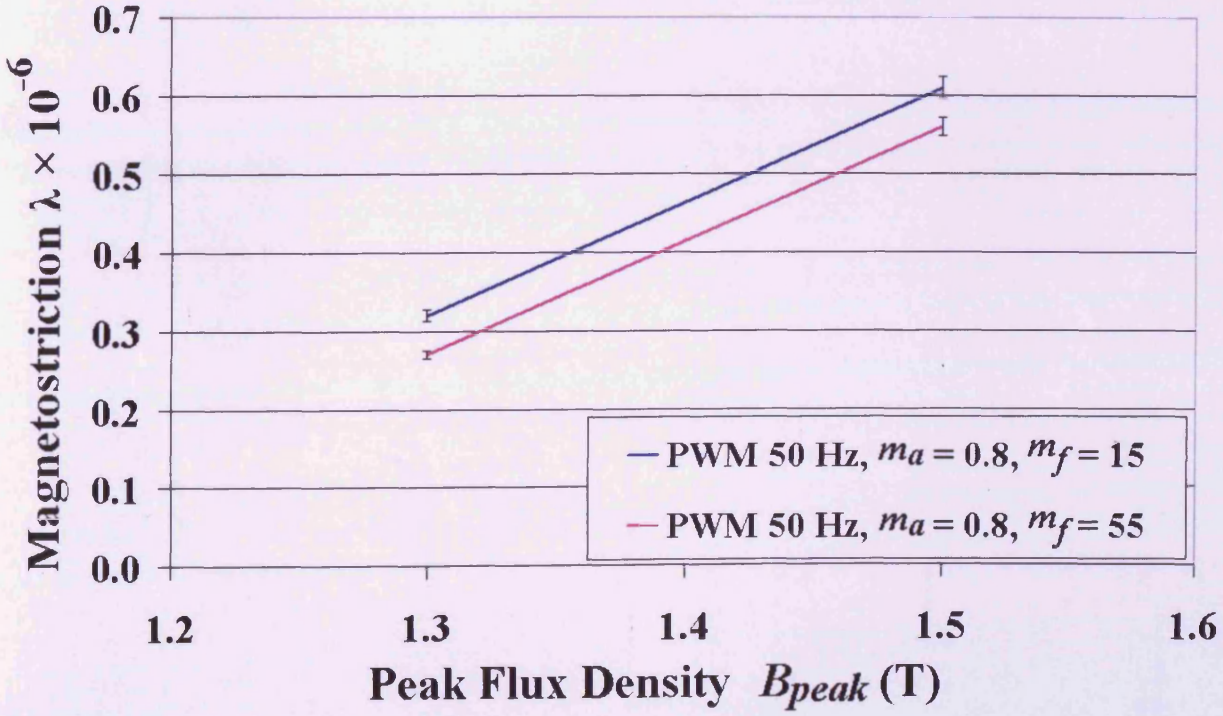

Fig. A-2 Peak-to-peak magnetostriction versus magnetic peak flux density under PWM voltage excitation, m_a = 0.8, m_f = 15 and 55, f = 50 Hz

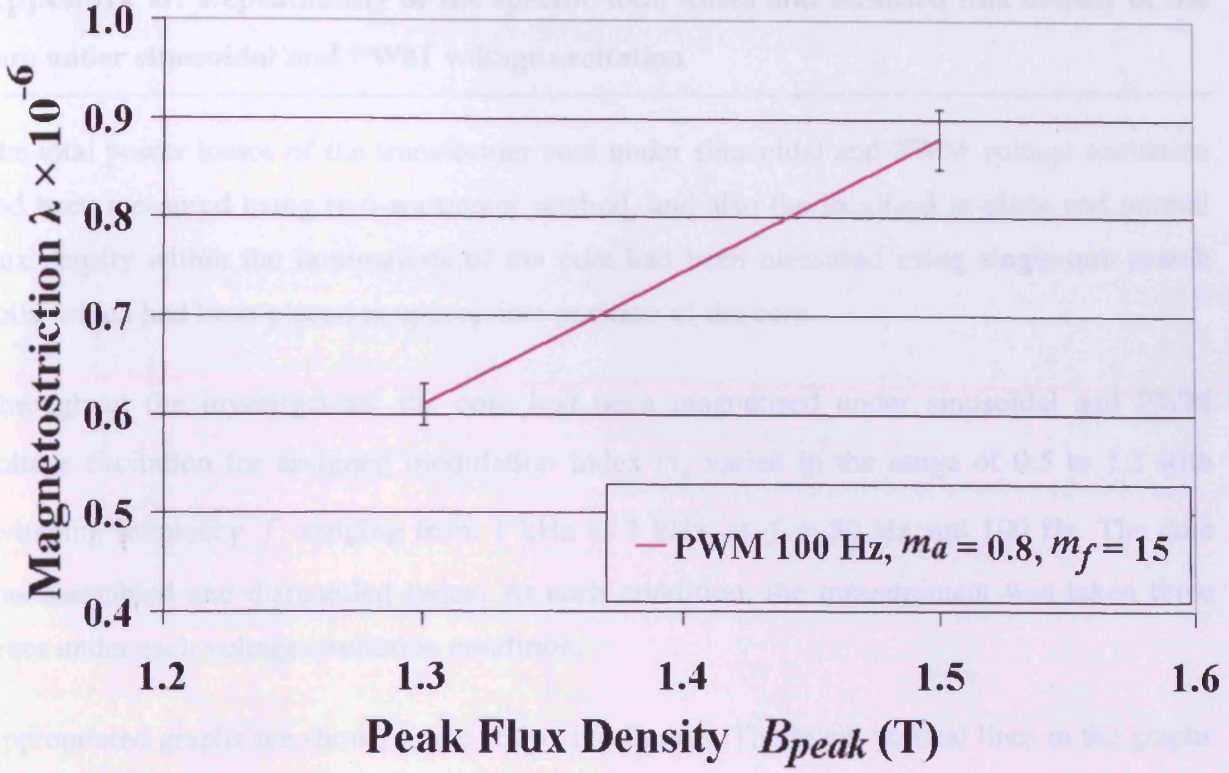

Fig. A-3 Peak-to-peak magnetostriction versus magnetic peak flux density under PWM voltage excitation, at f = 100 Hz

Appendix B: Repeatability of the specific total losses and localised flux density of the core under sinusoidal and PWM voltage excitation

The total power losses of the transformer core under sinusoidal and PWM voltage excitation had been measured using two-wattmeter method, and also the localised in-plane and normal flux density within the laminations of the core had been measured using single-turn search coils, which had been placed at appropriate position of the core.

Throughout the investigation, the core had been magnetised under sinusoidal and PWM voltage excitation for assigned modulation index m_a varied in the range of 0.5 to 1.2 with switching frequency f_s ranging from 1 kHz to 3 kHz, at f = 50 Hz and 100 Hz. The core was assembled and dismantled twice. At each condition, the measurement was taken three times under each voltage excitation condition.

Appropriated graphs are shown in the following figures. The black vertical lines in the graphs represent the error bars at each measurement condition.

1). Repeatability of the total power losses of the core

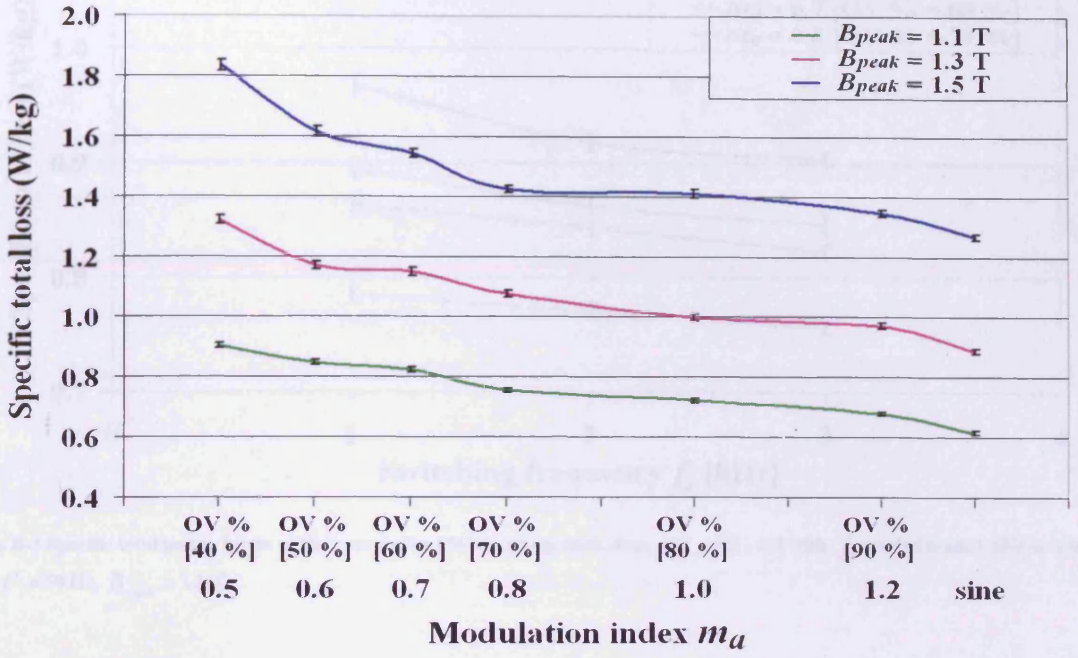

Fig. B-1 Specific total power losses of the core under sinusoidal and PWM voltage excitation, m_a = 0.5 -1.2 with f_s = 3 kHz, at f = 50 Hz, B_{peak} = 1.1 T, 1.3 T and 1.5 T

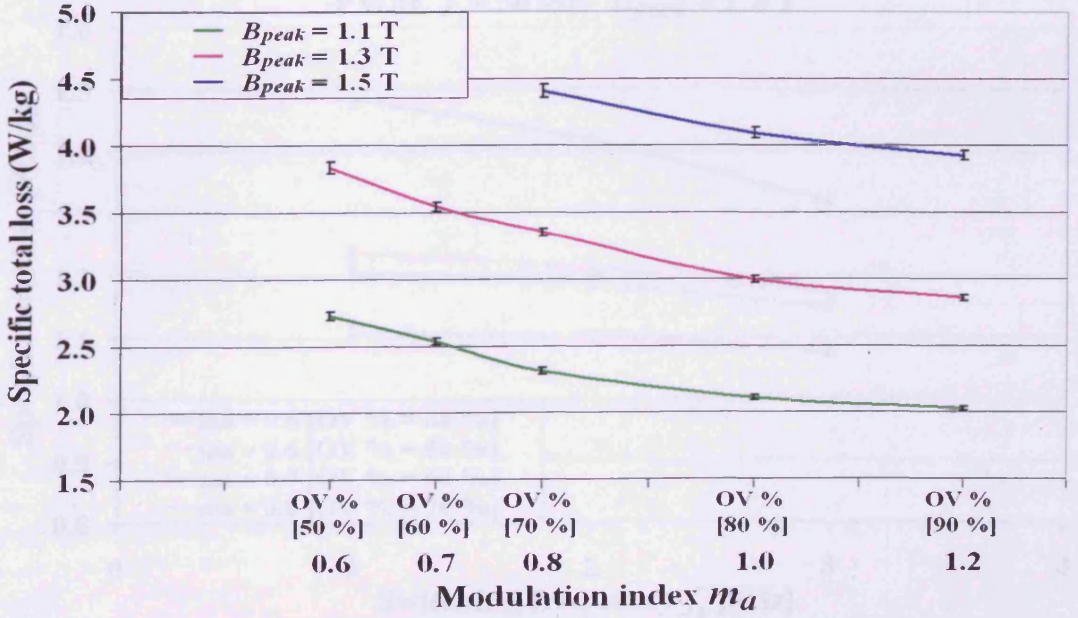

Fig. B-2 Specific total power losses of the core under PWM voltage excitation, m_a = 0.6 -1.2 with f_s = 3 kHz, at f = 100 Hz, B_{peak} = 1.1 T, 1.3 T and 1.5 T

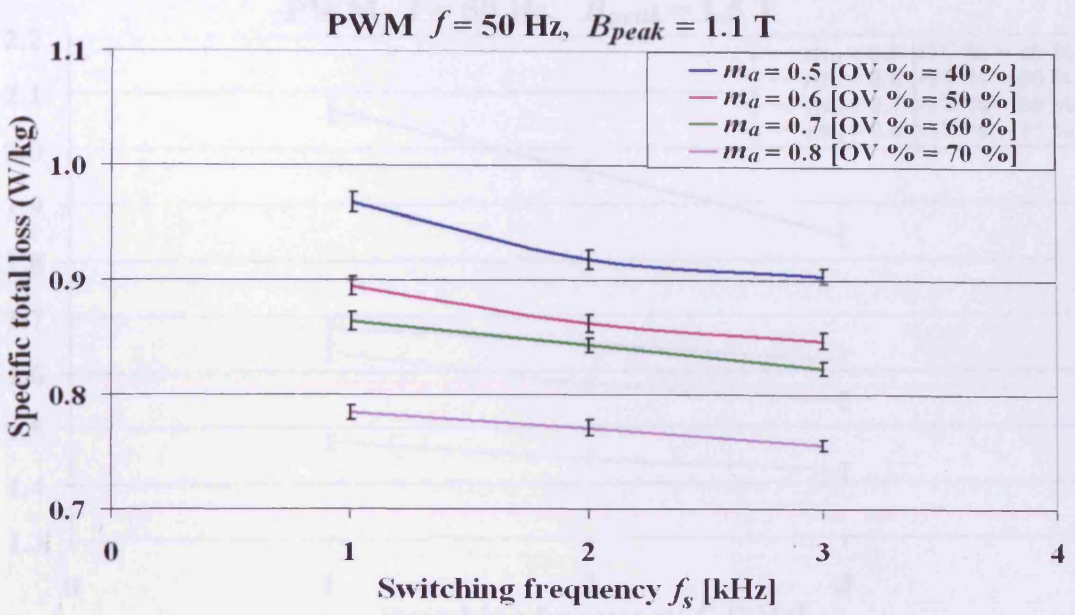

Fig. B-3 Specific total power losses of the core under PWM voltage excitation, m_a = 0.5 - 0.8 with f_s varied from 1 kHz to 3 kHz, at f = 50 Hz, B_{peak} = 1.1 T

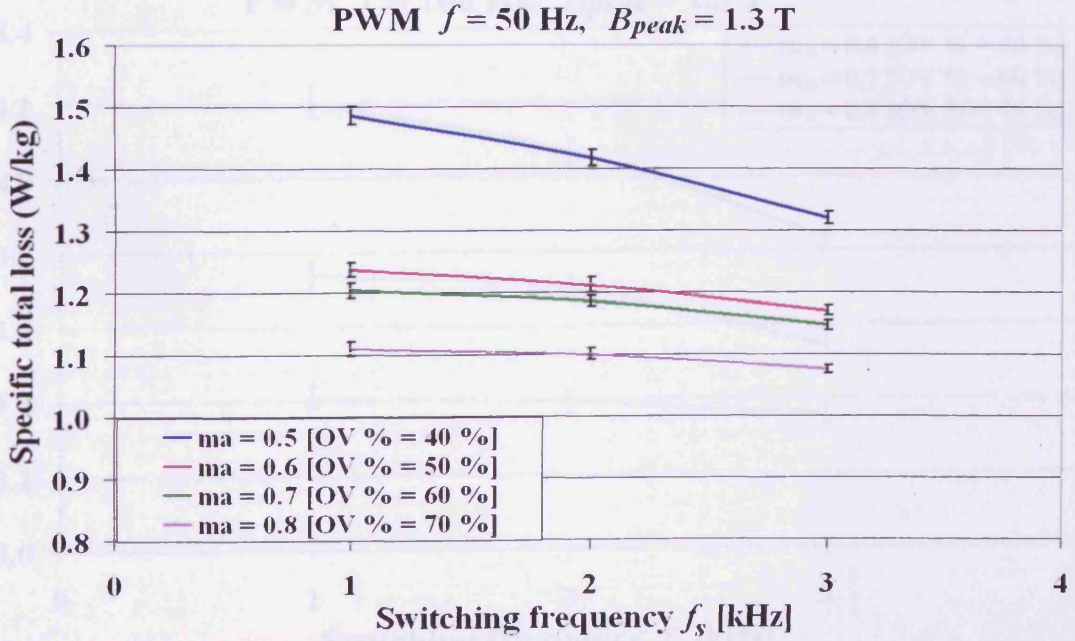

Fig. B-4 Specific total power losses of the core under PWM voltage excitation, m_a = 0.5 - 0.8 with f_s varied from 1 kHz to 3 kHz, at f = 50 Hz, B_{peak} = 1.3 T

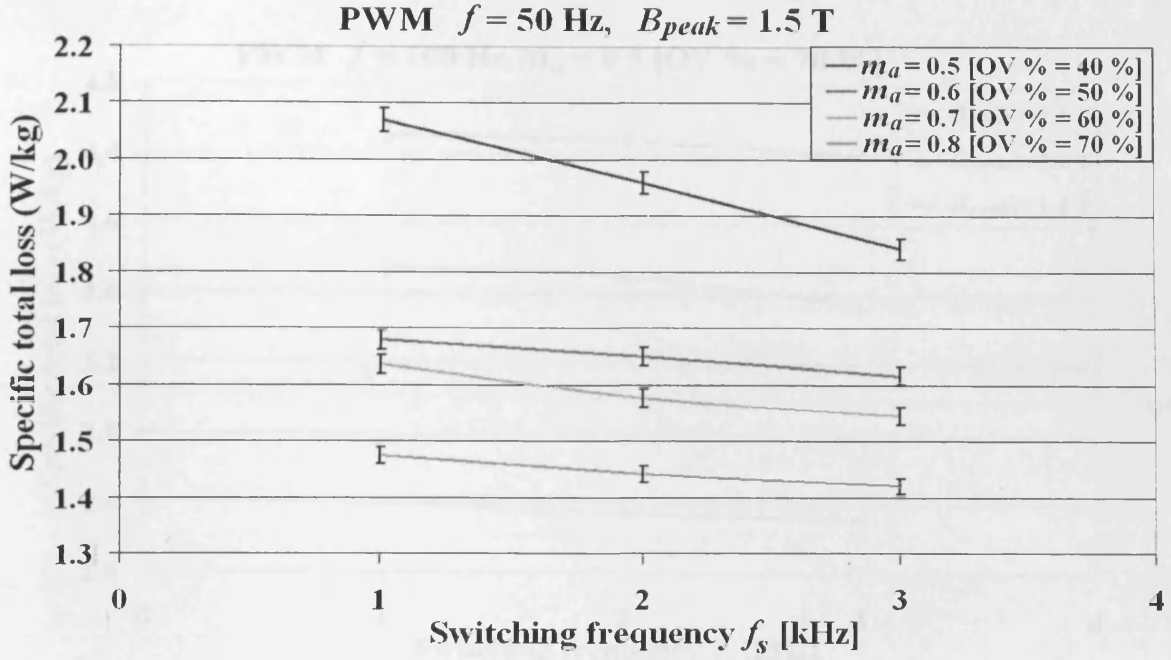

Fig. B-5 Specific total power losses of the core under PWM voltage excitation, m_a = 0.5 - 0.8 with f_s varied from 1 kHz to 3 kHz, at f = 50 Hz, B_{peak} = 1.5 T

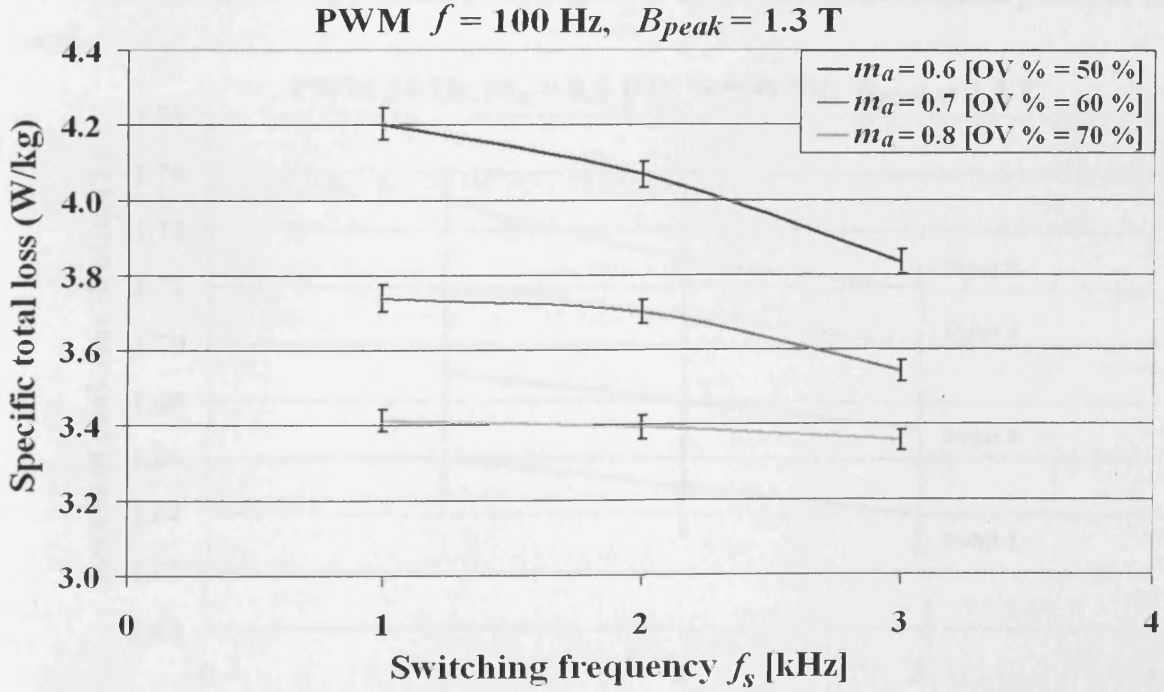

Fig. B-6 Specific total power losses of the core under PWM voltage excitation, m_a = 0.6, 0.7 and 0.8 with f_s varied from 1 kHz to 3 kHz, at f = 100 Hz, B_{peak} = 1.3 T

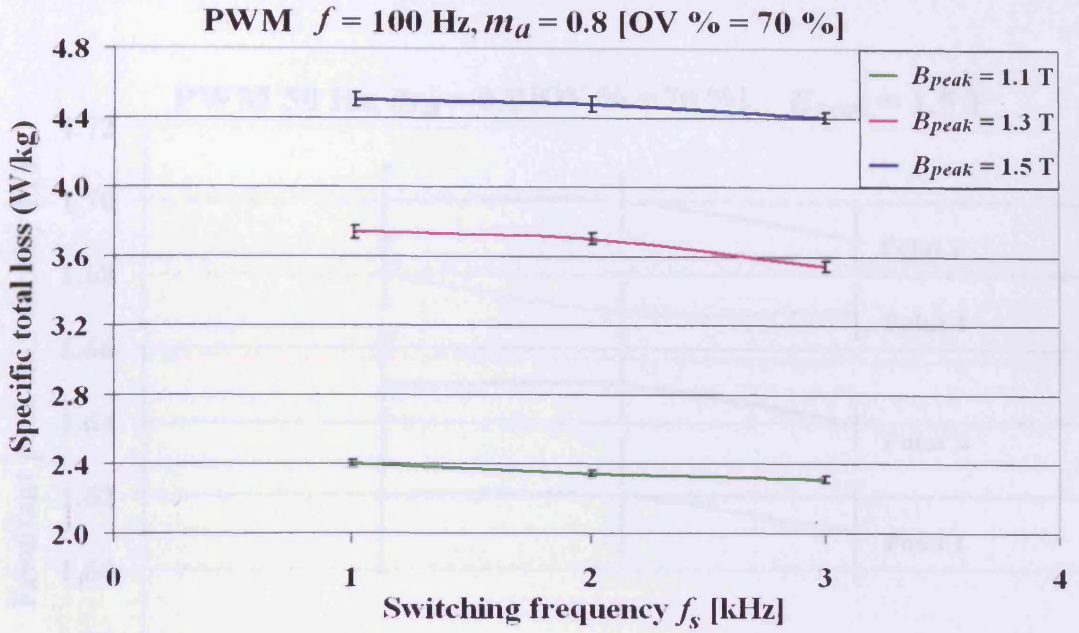

Fig. B-7 Specific total power losses of the core under PWM voltage excitation, m_a = 0.8 with f_s varied from 1 kHz to 3 kHz, at f = 100 Hz, B_{peak} = 1.1 T, 1.3 T and 1.5 T

2). Repeatability of the resultant peak in-plane flux density at investigated points of the core

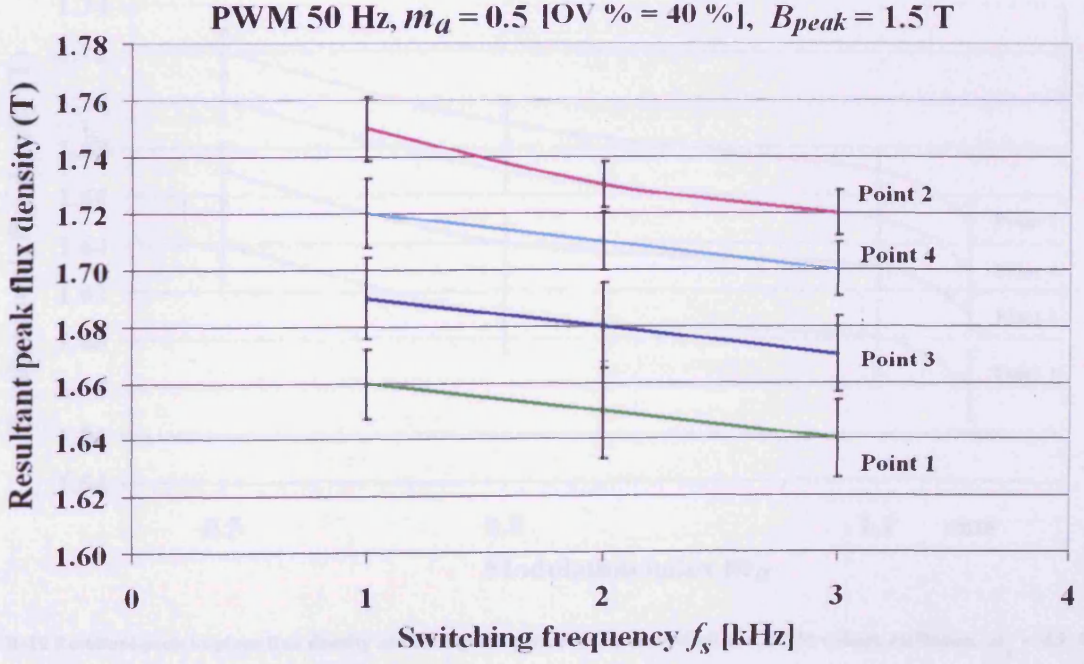

Fig. B-8 Resultant peak in-plane flux density at investigated points under PWM voltage excitation, m_a = 0.5 with f_s varied from 1 kHz to 3 kHz, at f = 50 Hz, B_{peak} = 1.5 T

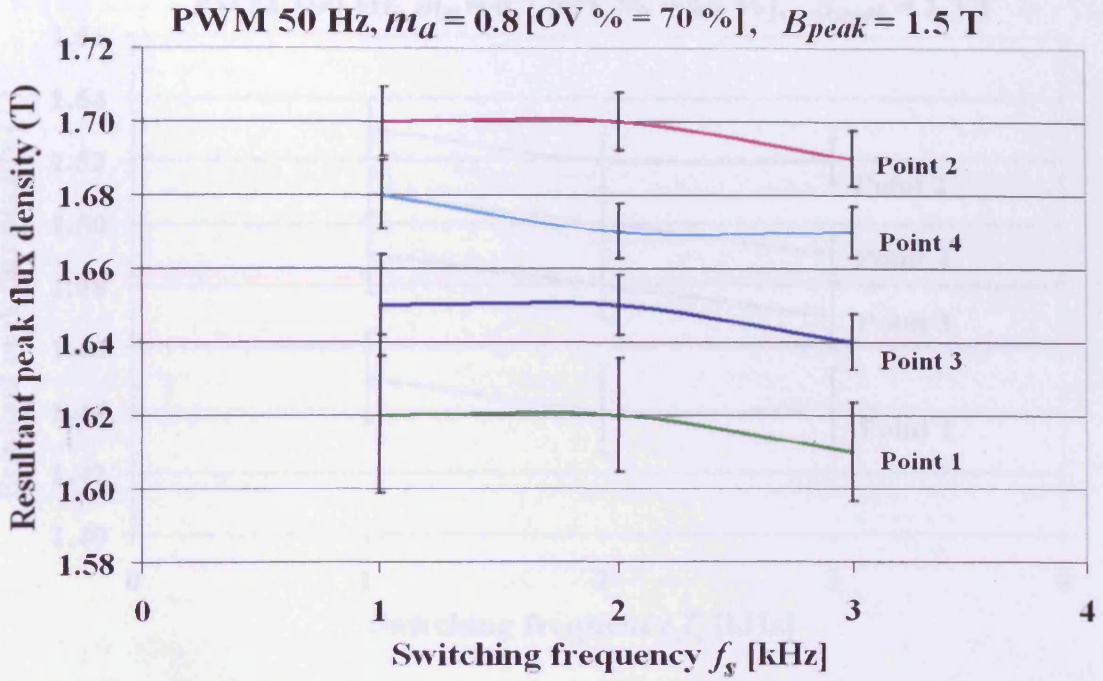

Fig. B-9 Resultant peak in-plane flux density at investigated points under PWM voltage excitation, m_a = 0.8 with f_s varied from 1 kHz to 3 kHz, at f = 50 Hz, B_{peak} = 1.5 T

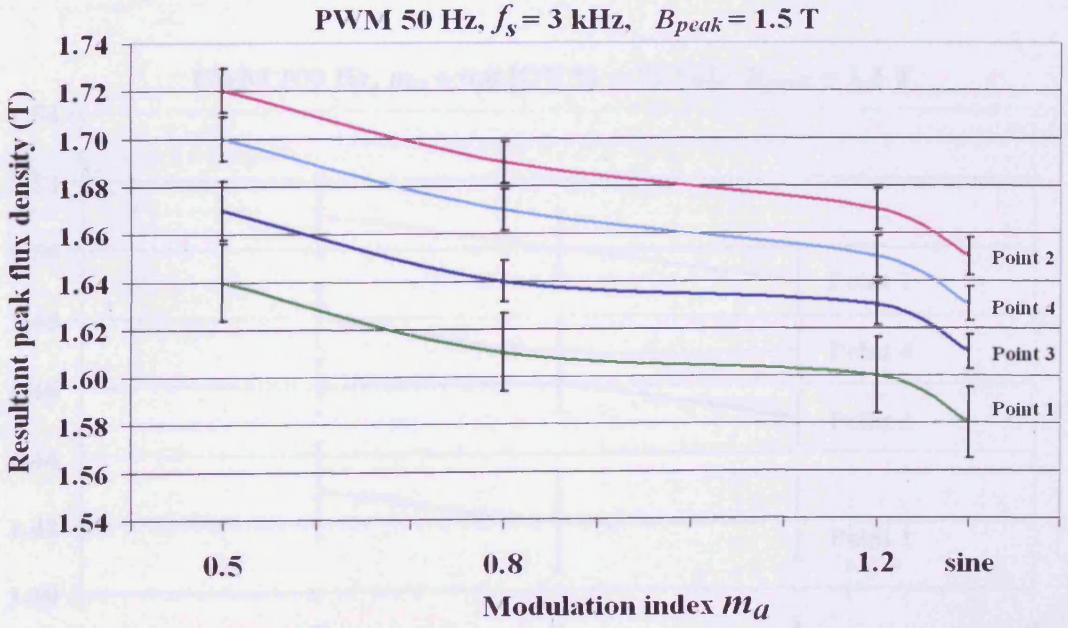

Fig. B-10 Resultant peak in-plane flux density at investigated points under sinusoidal and PWM voltage excitation, m_a = 0.5, 0.8 and 1.2 with f_s = 3 kHz, at f = 50 Hz, B_{peak} = 1.5 T

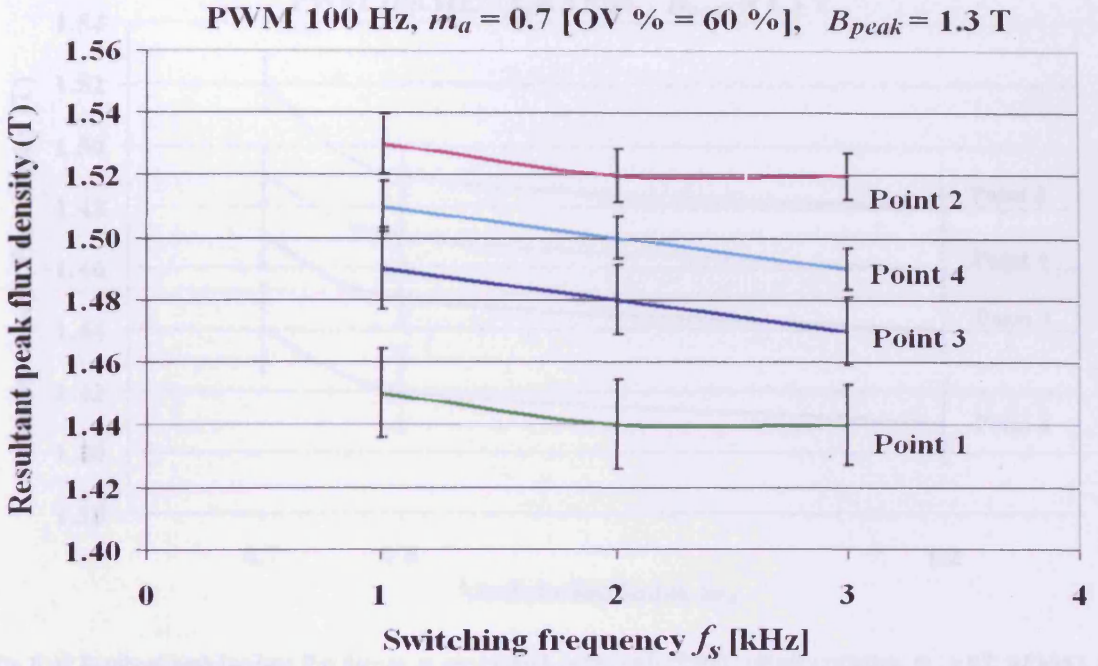

Fig. B-11 Resultant peak in-plane flux density at investigated points under PWM voltage excitation, m_a = 0.7 with f_s varied from 1 kHz to 3 kHz, at f = 100 Hz, B_{peak} = 1.3 T

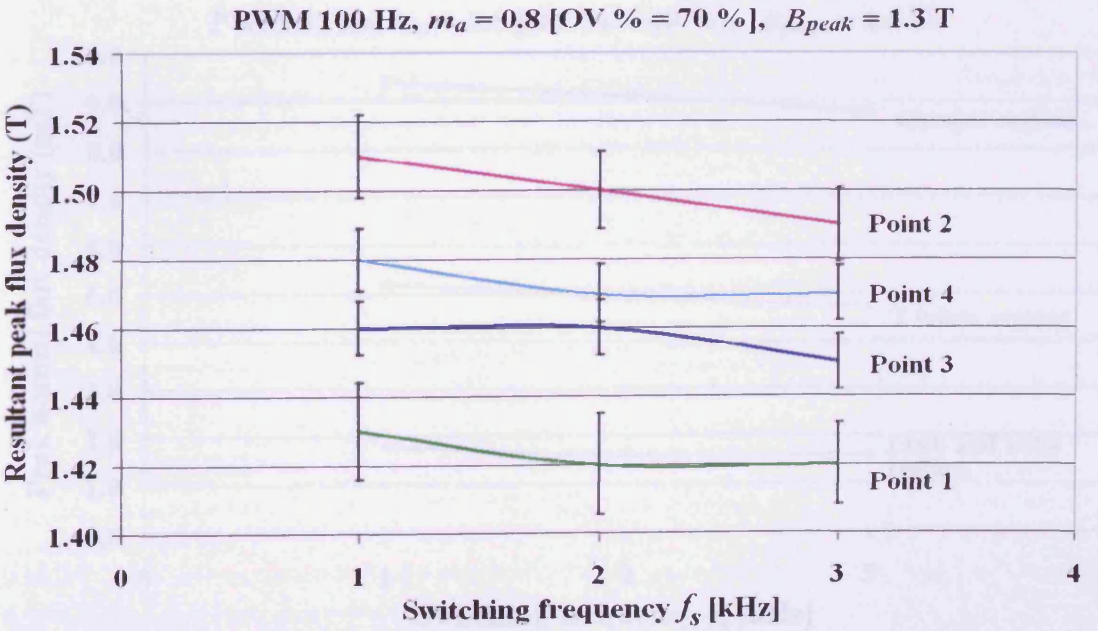

Fig. B-12 Resultant peak in-plane flux density at investigated points under PWM voltage excitation, m_a = 0.8 with f_s varied from 1 kHz to 3 kHz, at f = 100 Hz, B_{peak} = 1.3 T

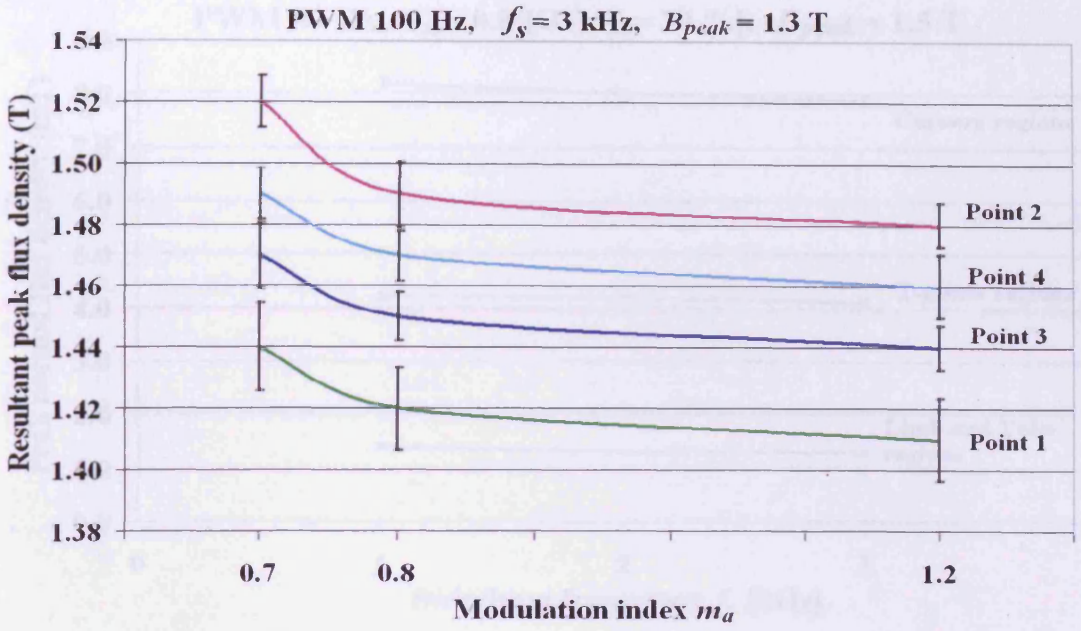

Fig. B-13 Resultant peak in-plane flux density at investigated points under PWM voltage excitation, m_a = 0.7, 0.8 and 1.2 with f_s = 3 kHz, at f = 100 Hz, B_{peak} = 1.3 T

3). Repeatability of the mean peak normal flux density at different regions of the core

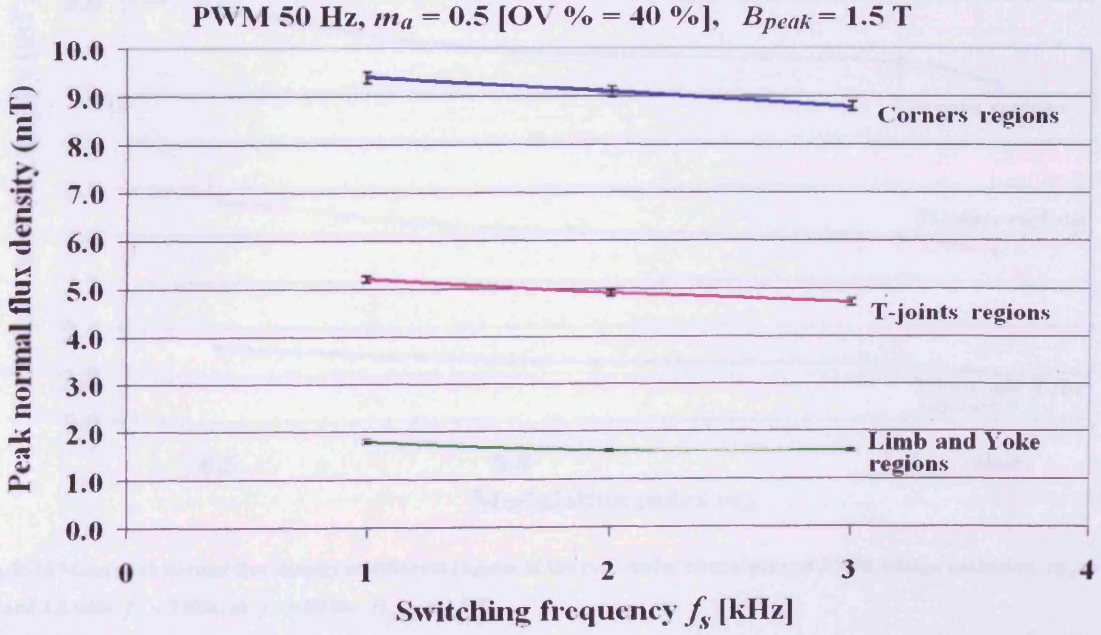

Fig. B-14 Mean peak normal flux density at different regions of the core under PWM voltage excitation, m_a = 0.5 with f_s varied from 1 kHz to 3 kHz, at f = 50 Hz, B_{peak} = 1.5 T

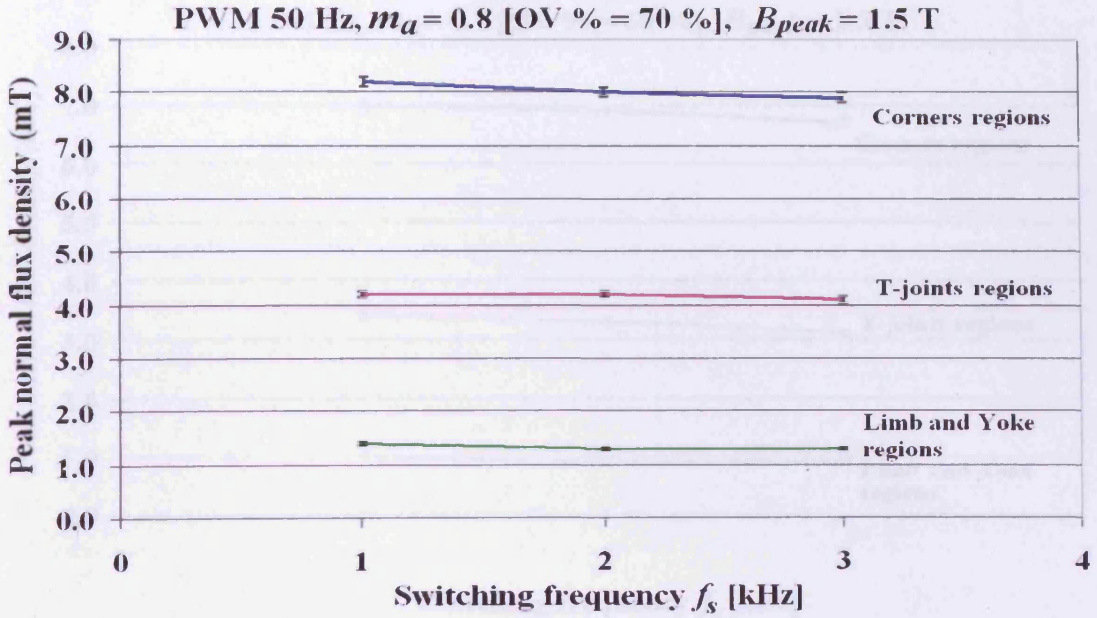

Fig. B-15 Mean peak normal flux density at different regions of the core under PWM voltage excitation, m_a = 0.8 with f_s varied from 1 kHz to 3 kHz, at f = 50 Hz, B_{peak} = 1.5 T

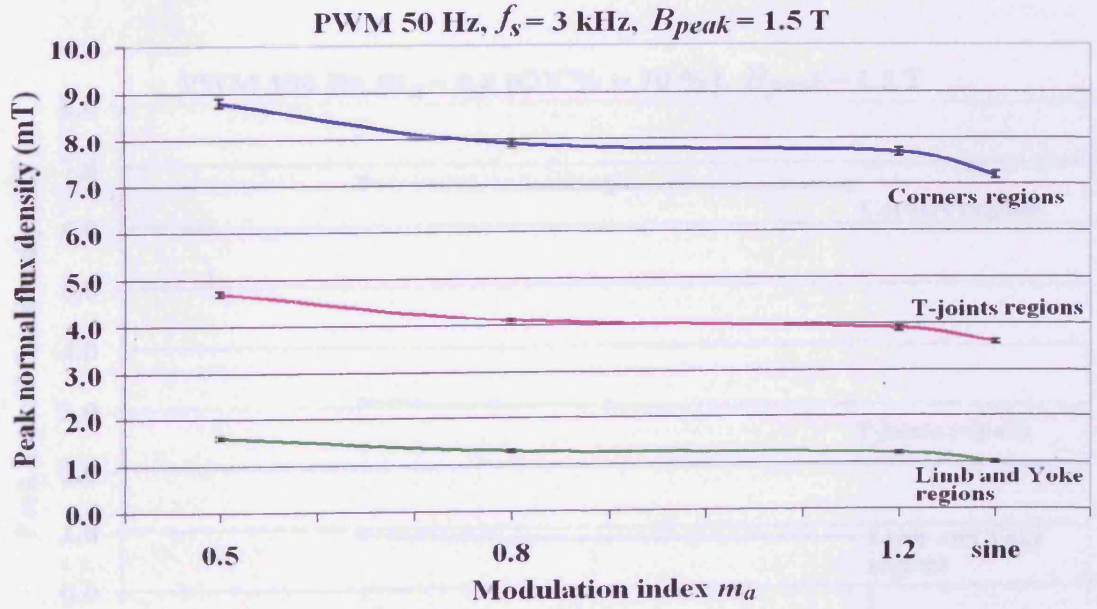

Fig. B-16 Mean peak normal flux density at different regions of the core under sinusoidal and PWM voltage excitation, m_a = 0.5, 0.8 and 1.2 with f_s = 3 kHz, at f = 50 Hz, B_{peak} = 1.5 T

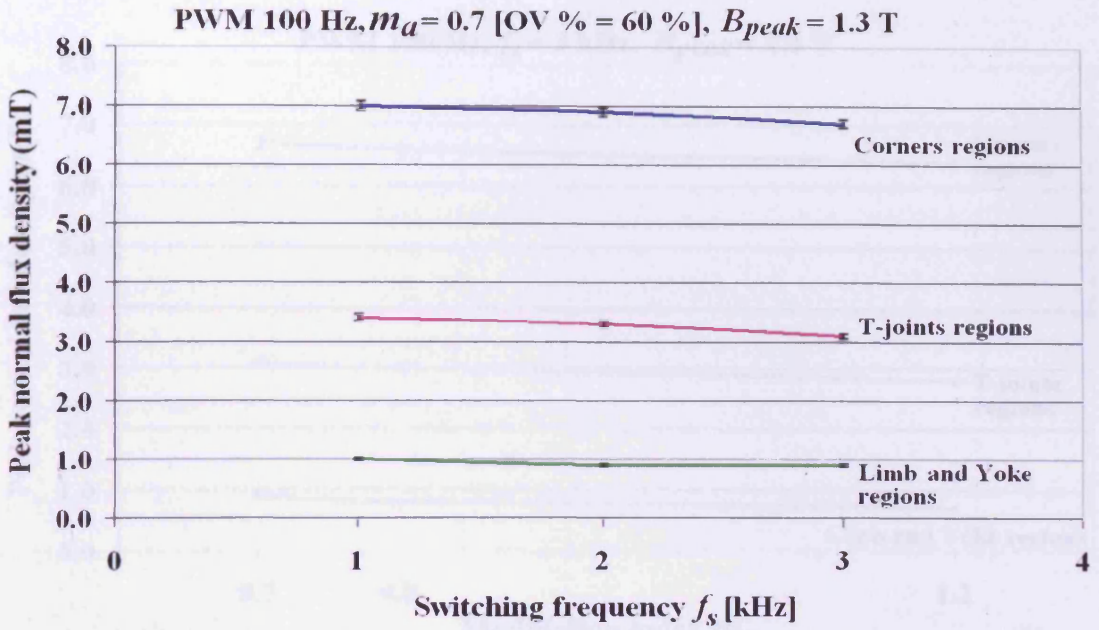

Fig. B-17 Mean peak normal flux density at different regions of the core under PWM voltage excitation, m_a = 0.7 with f_s varied from 1 kHz to 3 kHz, at f = 100 Hz, B_{peak} = 1.3 T

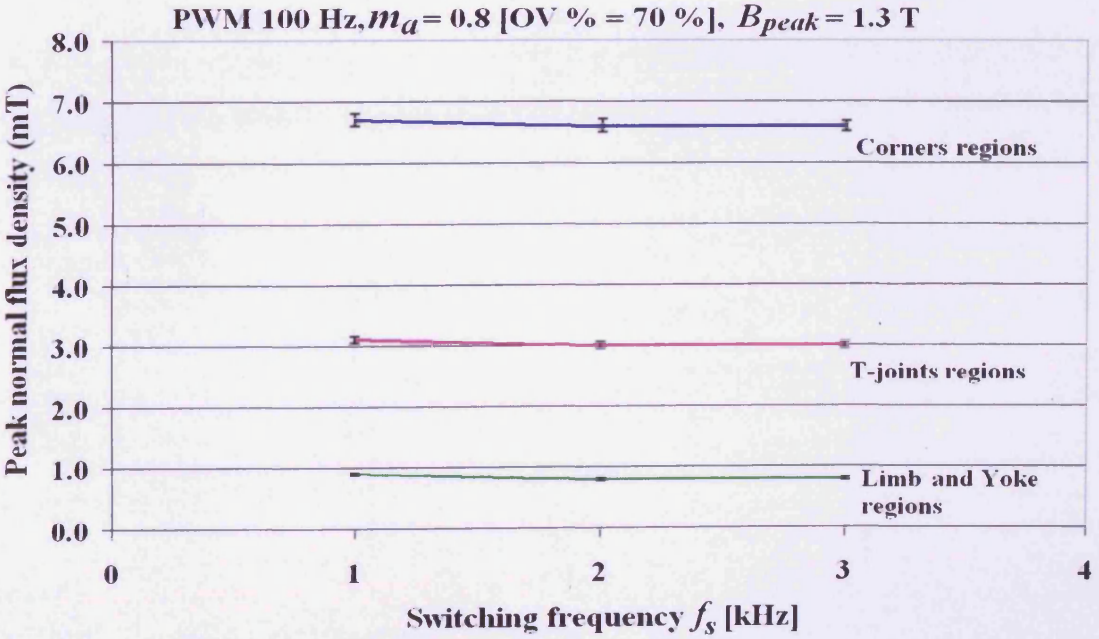

Fig. B-18 Mean peak normal flux density at different regions of the core under PWM voltage excitation, m_a = 0.8 with f_s varied from 1 kHz to 3 kHz, at f = 100 Hz, B_{peak} = 1.3 T

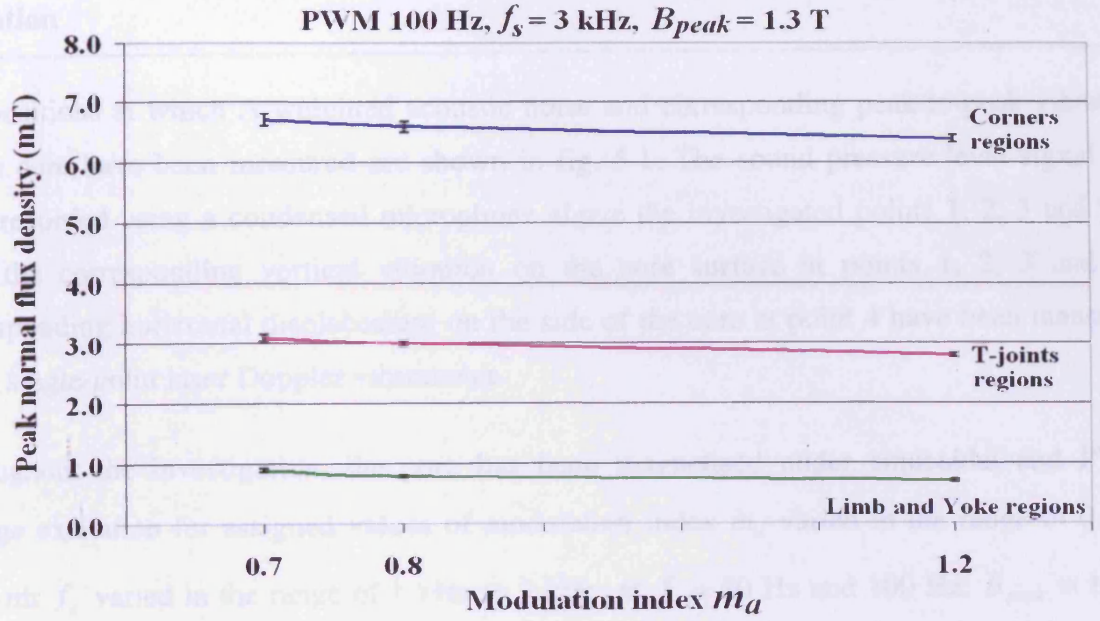

Fig. B-19 Mean peak normal flux density at different regions of the core under PWM voltage excitation, m_a = 0.7, 0.8 and 1.2 with f_s = 3 kHz, at f = 100 Hz, B_{peak} = 1.3 T

Appendix C: Repeatability of the resultant acoustic noise and corresponding peak-to-peak vibration at investigated points of the core under sinusoidal and PWM voltage excitation

The positions at which A-weighted acoustic noise and corresponding peak-to-peak vibration of the core have been measured are shown in fig. 5-1. The sound pressure level signal has been recorded using a condensed microphone above the investigated points 1, 2, 3 and 5 in turn, the corresponding vertical vibration on the core surface at points 1, 2, 3 and the corresponding horizontal displacement on the side of the core at point 4 have been measured using single-point laser Doppler vibrometer.

Throughout the investigation, the core has been magnetised under sinusoidal and PWM voltage excitation for assigned values of modulation index m_a varied in the range of 0.5 to 1.2 with f_s varied in the range of 1 kHz to 3 kHz, at f = 50 Hz and 100 Hz, B_{peak} = 1.3 T and 1.5 T. The core was assembled and dismantled twice. Each measurement was taken three times at each investigated point under each voltage excitation condition. Resultant acoustic noise of the core was presented as a mean value of the noise obtained opposite points 1, 2, 3 and 5.

Appropriated graphs are shown in the following figures. The black vertical lines in the graphs represent the error bars at each measurement condition.

1). Repeatability of the resultant acoustic noise of the core

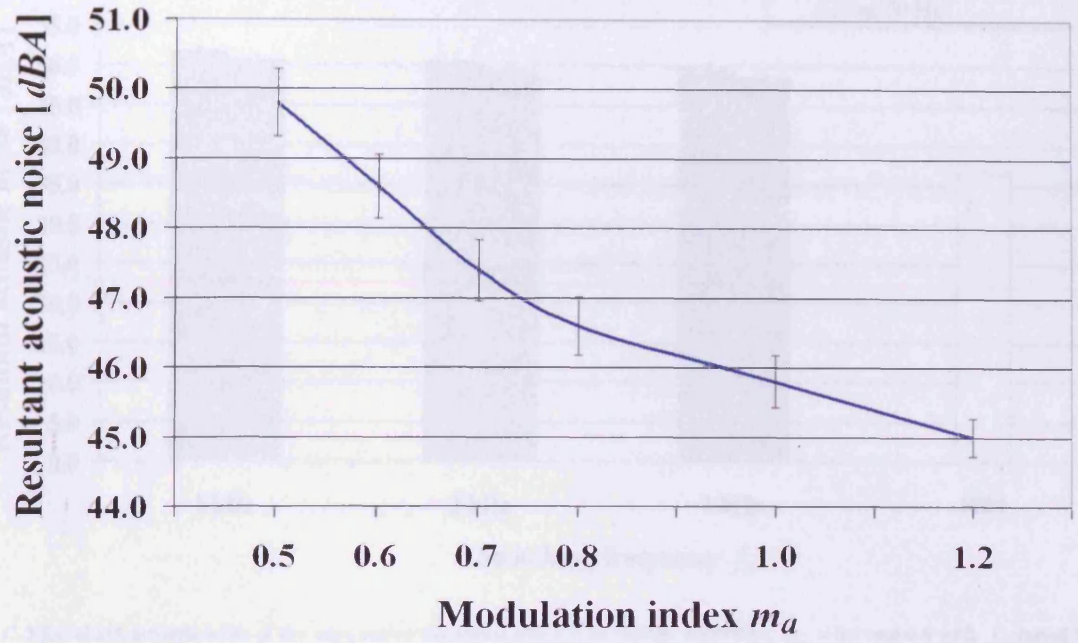

Fig. C-1 Resultant acoustic noise of the core under PWM voltage excitation, m_a = 0.5 - 1.2 with f_s = 3 k Hz, at f = 50 Hz, B_{peak} = 1.3 T

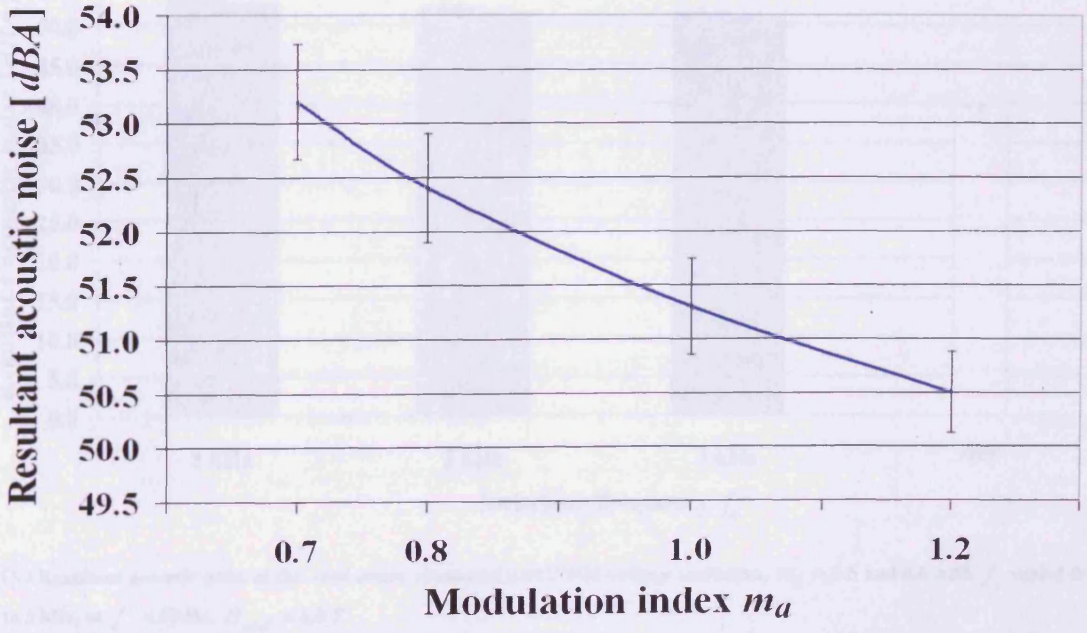

Fig. C-2 Resultant acoustic noise of the core under PWM voltage excitation, m_a = 0.7 - 1.2 with f_s = 3 k Hz, at f = 100 Hz, B_{peak} = 1.3 T

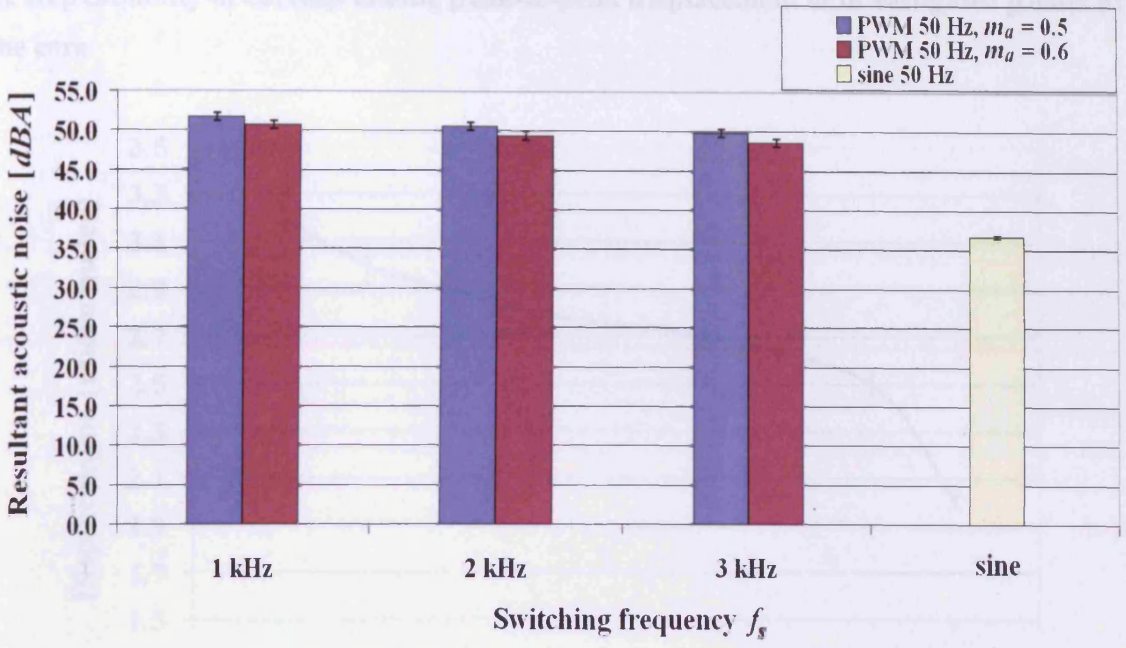

Fig. C-3 Resultant acoustic noise of the core under sinusoidal and PWM voltage excitation, m_a = 0.5 and 0.6 with f_s varied from 1 kHz to 3 kHz, at f = 50 Hz, B_{peak} = 1.3 T

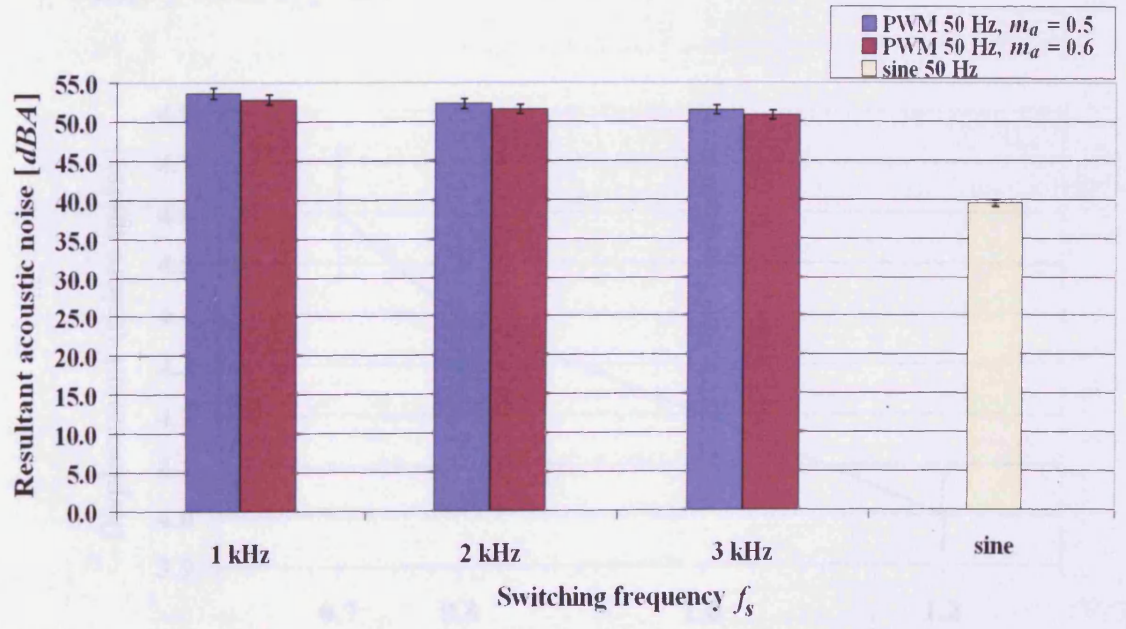

Fig. C-4 Resultant acoustic noise of the core under sinusoidal and PWM voltage excitation, m_a = 0.5 and 0.6 with f_s varied from 1 kHz to 3 kHz, at f = 50 Hz, B_{peak} = 1.5 T

2). Repeatability of corresponding peak-to-peak displacement at investigated points of the core

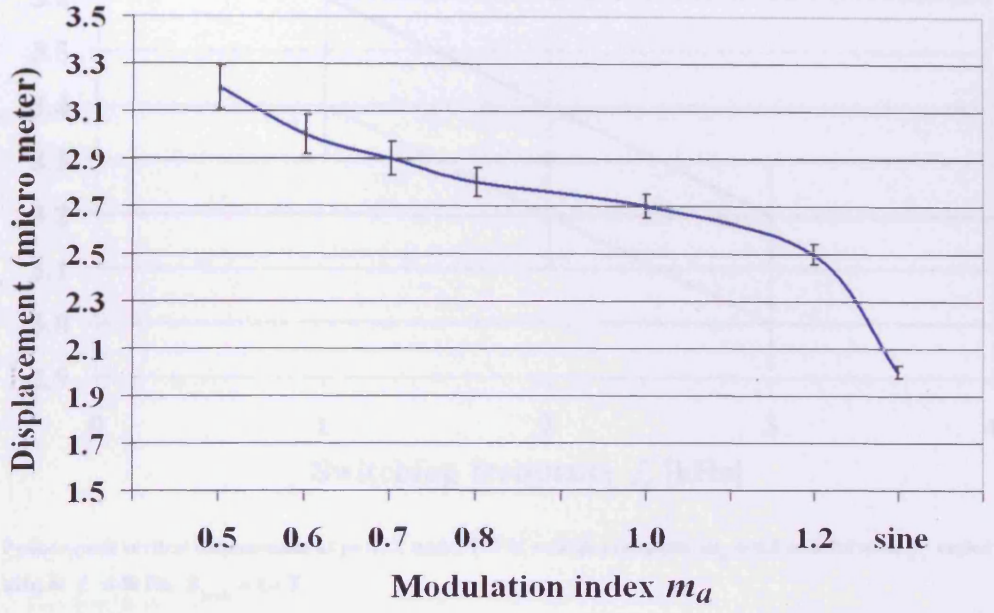

Fig. C-5 Peak-to-peak vertical displacement at point 2 under sinusoidal and PWM voltage excitation, m_a = 0.5 - 1.2 with f_s = 3 kHz, at f = 50 Hz, B_{peak} = 1.3 T

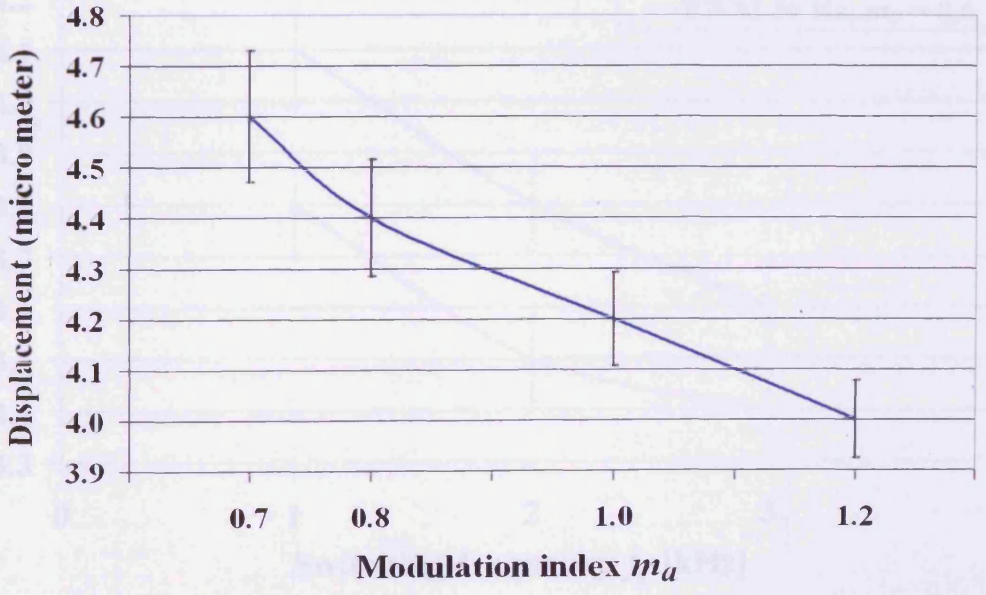

Fig. C-6 Peak-to-peak vertical displacement at point 2 under PWM voltage excitation, m_a = 0.7 - 1.2 with f_s = 3 kHz, at f = 100 Hz, B_{peak} = 1.3 T

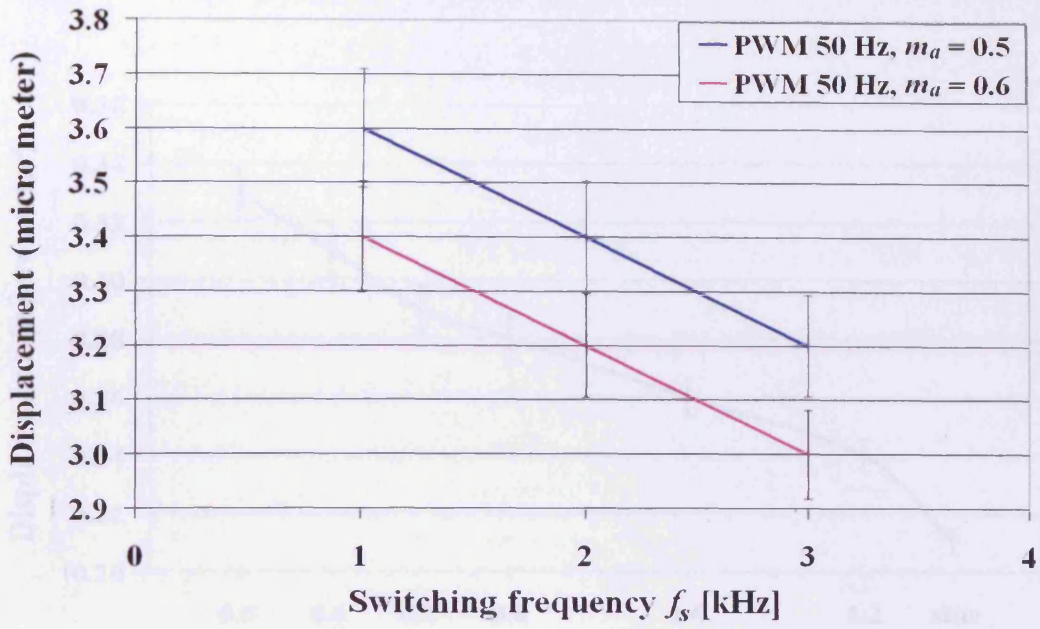

Fig. C-7 Peak-to-peak vertical displacement at point 2 under PWM voltage excitation, m_a = 0.5 and 0.6 with f_s varied from 1 kHz to 3 kHz, at f = 50 Hz, B_{peak} = 1.3 T

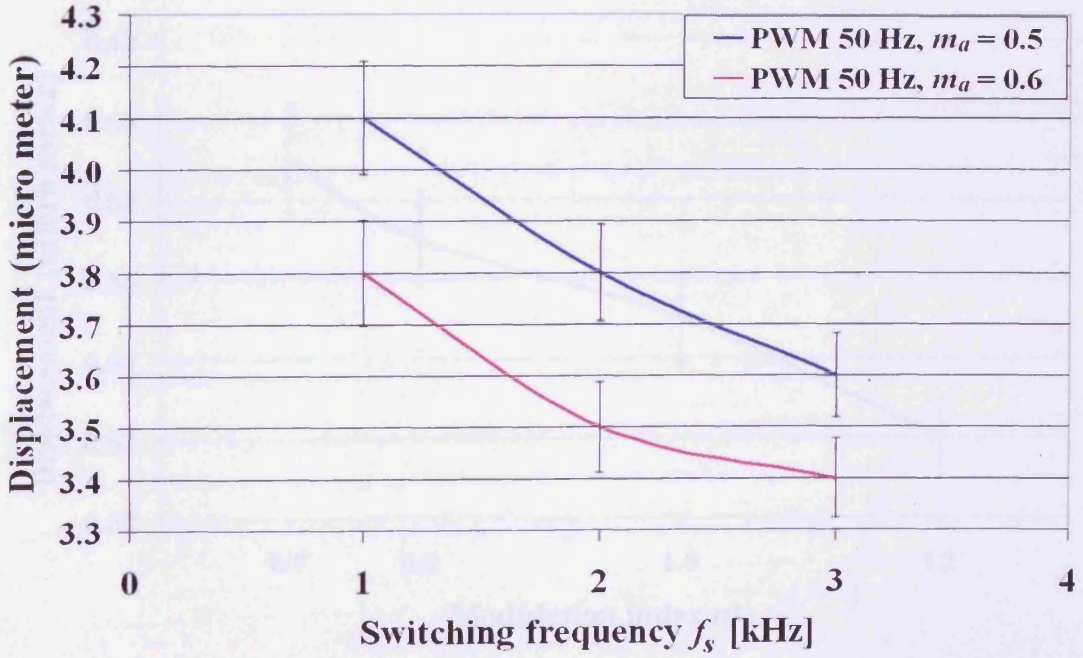

Fig. C-8 Peak-to-peak vertical displacement at point 2 under PWM voltage excitation, m_a = 0.5 and 0.6 with f_s varied from 1 kHz to 3 kHz, at f = 50 Hz, B_{peak} = 1.5 T

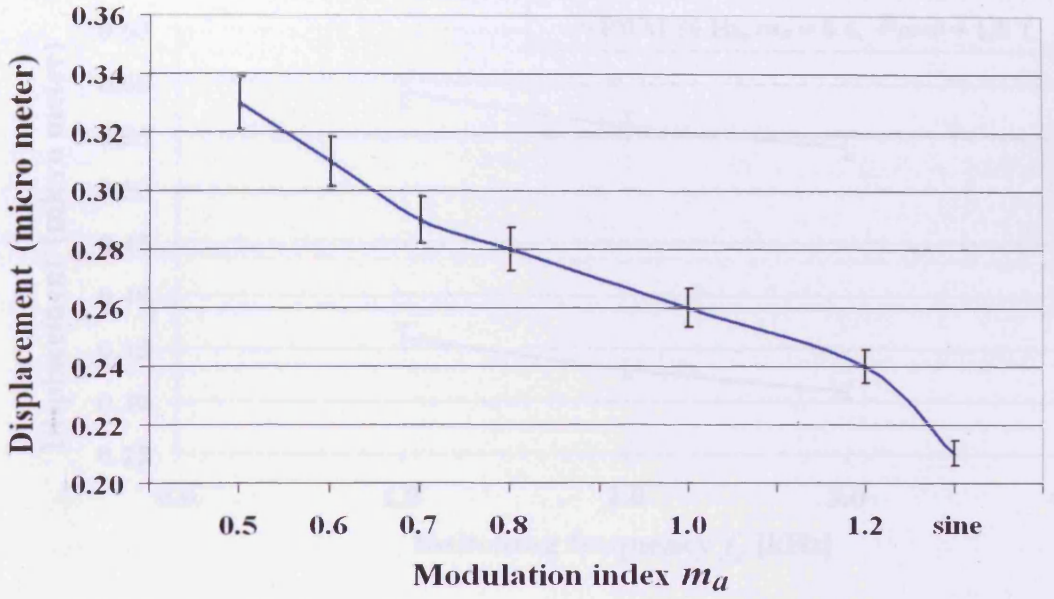

Fig. C-9 Peak-to-peak horizontal displacement at point 4 under sinusoidal and PWM voltage excitation, m_a = 0.5 - 1.2 with f_s = 3 kHz, at f = 50 Hz, B_{peak} = 1.3 T

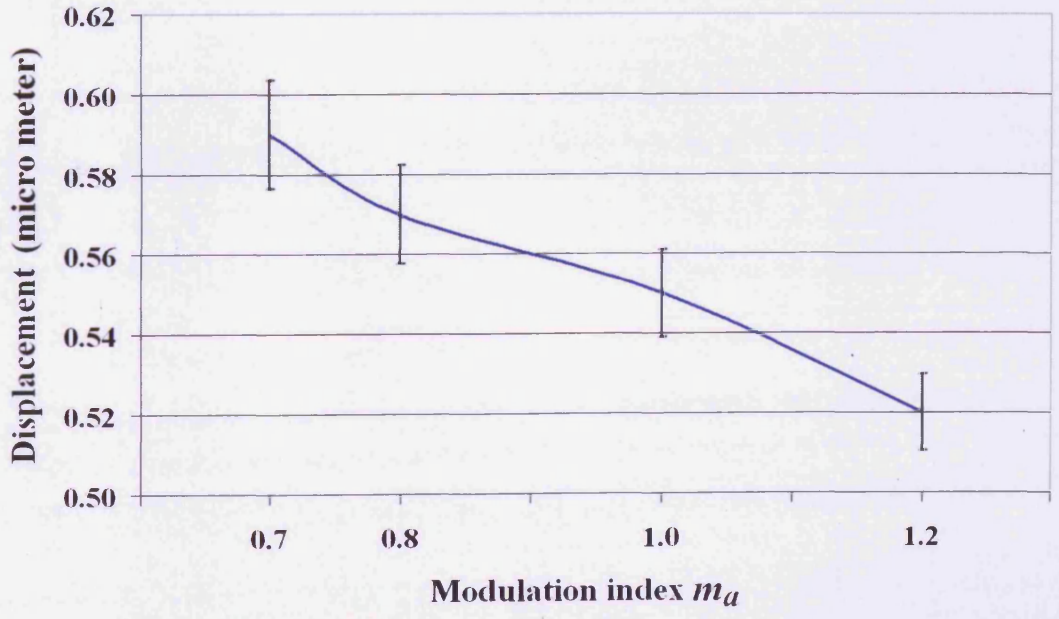

Fig. C-10 Peak-to-peak horizontal displacement at point 4 under PWM voltage excitation, m_a = 0.7 - 1.2 with f_s = 3 kHz, at f = 100 Hz, B_{peak} = 1.3 T

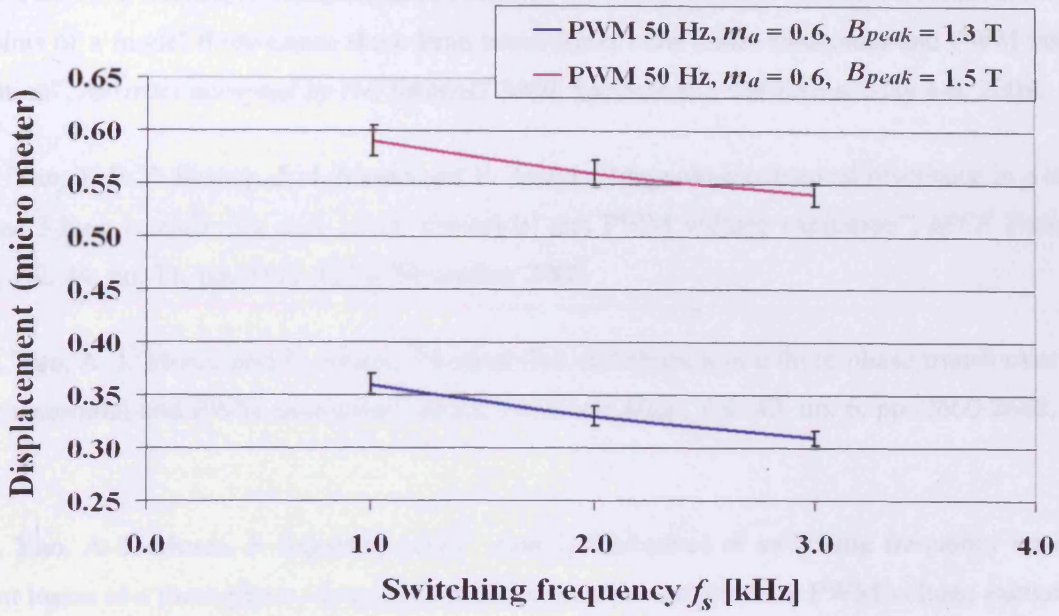

Fig. C-11 Peak-to-peak horizontal displacement at point 4 under PWM voltage excitation, m_a = 0.6 with f_s varied from 1 kHz to 3 kHz, at f = 50 Hz, B_{peak} = 1.3 T and 1.5 T

Appendix D: List of publications

1. **X. G. Yao**, A. J. Moses, S. Somkun and F. Anayi, "Rotating flux and estimation rotational loss in the joints of a model three-phase three-limb transformer core under sinusoidal and PWM voltage excitation", *Abstract accepted by INTERMAG 2009*, Sacramento, California, May 4-8, 2009.

2. **X. G. Yao**, T. P. P. Phway, A. J. Moses and F. Anayi, "Magneto-mechanical resonance in a model 3-phase 3-limb transformer core under sinusoidal and PWM voltage excitation", *IEEE Trans. on Mag.*, vol. 44, no. 11, pp. 4111-4114, November 2008.

3. **X. G. Yao**, A. J. Moses and F. Anayi, "Normal flux distribution in a three-phase transformer core under sinusoidal and PWM excitation", *IEEE Trans. on Mag.*, vol. 43, no. 6, pp. 2660-2662, June 2007.

4. **X. G. Yao**, A. J. Moses, J. Sagarduy and F. Anayi, "Influence of switching frequency on eddy-current losses in a three-phase, three-limb transformer core subjected to PWM voltage excitation", *International Conference on Power Engineering, POWERENG 2007*, pp. 324-329, Setubal, Portugal, April 12-14, 2007.

5. **X. G. Yao**, T. P. P. Phway, A. J. Moses and F. Anayi, "Acoustic noise and displacement analysis of a 3-phase transformer core under sinusoidal and PWM excitation", *VII International Conference on Electrical Machines, ICEM 2006*, Chania, Crete, Greece, September 2-5, (2006) 514 OTM 4-4.

6. M. C. Huang, A. J. Moses, F. Anayi and **X. G. Yao**, "Shaft position correction scheme comparison for sensorless control PWSM based space state-estimation between α-β variance adjustment and d-q angle PI regulation", *32nd Annual Conference on IEEE Industrial Electronics, IECON 2006*, pp. 1469-1474, November 2006.

7. M. C. Huang, A. J. Moses, F. Anayi and **X. G. Yao**, "Linear Kalman filter (LKF) sensorless control for permanent magnet synchronous motor based on orthogonal output linear model", *International Symposium on Power Electronics, SPEEDAM 2006*, pp. 1381-1386, May 2006.

8. M. C. Huang, A. J. Moses, F. Anayi and **X. G. Yao**, "Reduced-order linear Kalman filter (RLKF) theory in application of sensorless control for permanent magnet synchronous motor (PMSM)", *1st IEEE Conference on, Industrial Electronics and Applications*, pp. 1-6, May 2006.